UNIVERSITÀ DEGLI STUDI FIRENZE

DOTTORATO DI RICERCA IN SCIENZE CHIMICHE

CICLO XXX

COORDINATORE Prof. Piero Baglioni

ELECTRODEPOSITION, CHARACTERIZATION AND MODELING OF TECHNOLOGICALLY INTERESTING FILMS

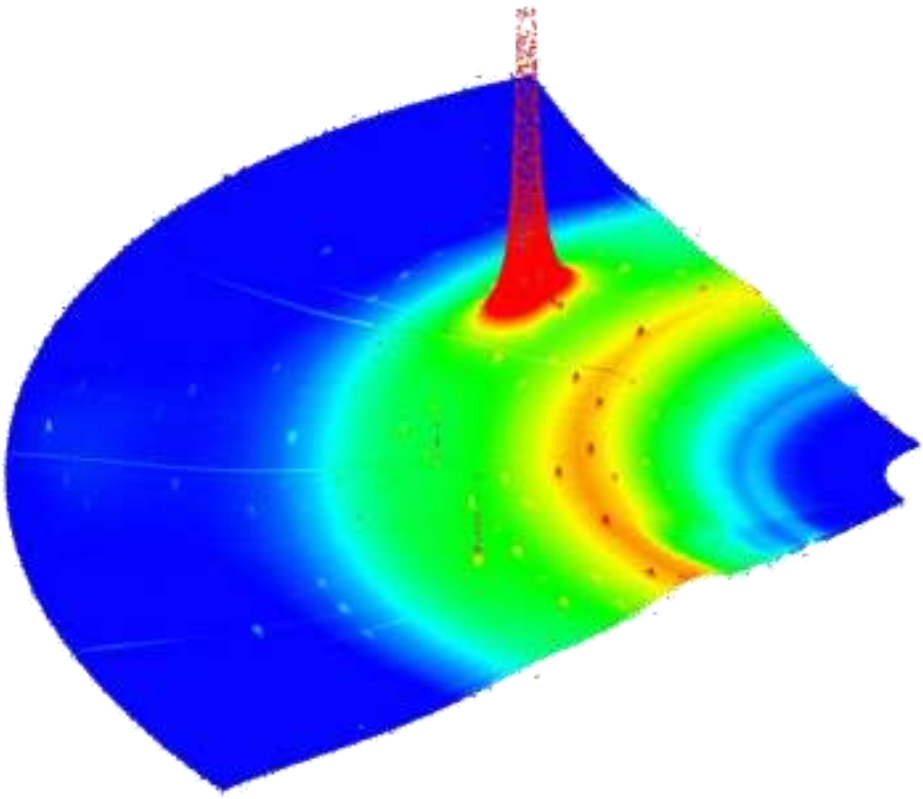

Dottorando
Dott. Andrea Giaccherini

Tutore
Prof. Massimo Innocenti

Co-tutore
Prof. Francesco Di Benedetto

Co-tutore
Dr. Stefano Caporali

UNIVERSITÀ
DEGLI STUDI
FIRENZE

DOTTORATO DI RICERCA IN SCIENZE CHIMICHE

CICLO XXX

COORDINATORE Prof. Piero Baglioni

ELECTRODEPOSITION, CHARACTERIZATION AND MODELING OF

TECHNOLOGICALLY INTERESTING FILMS

Settore Scientifico Disciplinare CHIM/01

Dottorando
Dott. Andrea Giaccherini

_____
(firma)

Tutore
Prof. Massimo Innocenti

_____
(firma)

Co-tutore
Prof. Francesco Di Benedetto

_____
(firma)

Co-tutore
Dr. Stefano Caporali

_____
(firma)

Coordinatore
Prof. Piero Baglioni

_____
(firma)

Anni 2014/2017

Science is always wrong. It never solves a problem without creating ten more.

George Bernard Shaw

Make things as simple as possible, but not simpler.

Albert Einstein

Aknowledgments

This study was carried out in the Department of Chemistry at the University of Florence during the years 2014-2017. I am grateful to my principal supervisor Professor Massimo Innocenti, for his support and guidance during this work. I also thank him for the opportunity to work in this exciting research field in the Applied Electrochemistry group. I am also grateful to my supervisors Professor Francesco Di Benedetto and Stefano Caporali for their ideas and guidance in my research work. I wish to thank the colleagues of the CNR Giordano Montegrossi and Alessandro Lavacchi since they constitute an unceasing source of ideas. The former also courteously provided the figure in the cover of this thesis. I would like to thank the staff of the Department of Chemistry for their support. In particular Antonio De Luca, Ferdinando Capolupo, Emanuele Salvietti and Maurizio Passaponti for their assistance with the laboratory activity. I thank all the researchers at ESRF for their support and for the pleasant working atmosphere during the synchrotron light experiments. Especially, I thank Francesco Carlà and Roberto Felici whose friendship, constant help and tremendous expertise made most of the activity at the synchrotron possible. I thank my colleagues and ex-colleagues Enrico Berretti, Stefano Martinuzzi, Luca Conti, Serena Cinotti, Claudio Zafferoni and Patrick Marcantelli for the mutual support and the profound academic and non-academic discussions we shared.

I want to express my gratitude to my parents Adriano, Elisabetta and my sister Valentina whose caring attention helped me in overcoming the hardest moments, I also thank all my relatives and friends for their support and friendship during these years.

During the development of this research I grew as man and as researcher thanks to all these people, but I wouldn't probably even started this process without the encouragement and love of Serena Bucelli.

Firenze December, 2017 Andrea Giaccherini

Contents

1. Introduction

Over the past four decades, semiconducting materials covered a wide range of applications from photovoltaic technology to informatics. In principle we can grow these materials starting from the atoms and molecules and assembling them exploiting their chemical properties (bottom up approach) or we can carve out the devices from a homogeneous material (top down approach). Nowadays the only industrially available methods are based on the second approach. In all technological fields where semiconducting materials have been applied, a constant development have been carried to: 1) reduce the size, 2) improving the structural quality of these materials and 3) reducing the impact from either the energetic and environmental standpoints. These developments highlighted some of the limits of the top-down approach.

1.1.1. The nanoelectronics industry

The overwhelming majority of the electronic components market is covered by the silicon-based microelectronics (or nanoelectronics) devices. This market has been remarkably conservative, in the sense that it limited the exploitation of available chemical elements to a very small fraction of the periodic table involving always silicon as main element. For a long time, after all, the industry focussed more on reducing the size of devices, to sustain their increases of performances as they were scaled down than in studying new devices and semiconducting materials. Lately, size reduction cannot deliver anymore the necessary increases in performance anymore. Thus, the exploitation of more elements in the semiconducting devices could be a solution to this stagnation of performances.

Reducing the size of the devices features in the deep sub-100-nm regime, forces the industry to face enormous technological and fundamental challenges for the conventional scaling methods[1–3]. For instance, problems such the device size fluctuations may affect dramatically key parameters such as the threshold voltage and on/off currents. Another issues is related to the possible reduction of the structural quality of the materials during the fabrication process which can make the transport properties inefficient. Additionally, the implementation of suitable lithography techniques and traditional operating facilities might also create an economic barrier to continued increases in the capabilities of conventional processor and memory chips[1–3]. Hence, the traditional production techniques present also economic obstacle to their further developments.

1.1.2. The light emission diode industry

The light emission diode industry have underwent a tremendous increase of its production during the last years. Lately, the vast markets of house lightning, computer monitors and TV shifted mostly to LED as the lightning part of their products. Thus, these markets stimulated the mass production of LED.

Similarly to the nanoelectronics industry, LEDs are carved out from wafers of layered semiconducting materials constituting the p-n junctions exploited for their electroluminescent properties. On the contrary, compare to the nanoelectronics industry, a wider variety of chemical elements are involved in the production of LED, depending on the properties required for the device. Usually, compound semiconductors from In, Ga based phosphide and arsenide represent the main materials for LEDs mass production. Hence, after all, the industry is mainly focused on earth-rare elements.

Although, in 2015 the market suffered by overproduction issues, the mass production process of LEDs shows several limitations from a sustainability standpoint. The wafer of semiconducting materials are cut from an ingot produced by pressurized melting and blending of the involved elements. Then the wafer is doped by means of liquid phase epitaxy or molecular beam epitaxy obtaining. Several doping layers can be added to the wafer obtaining the final p-n junction that will be processed to carve out the LEDs. In conclusion, the process is indeed energy-hungry and results in the loss of an amount of non-earth abundant elements.

1.1.3. The solar devices industry

The energy predicament due to the impending Hubbert's Peak Oil, combined with the environmental consequences of CO_2 emissions, indicate the need for a rapid transition from fossil fuels to renewable and sustainable energy sources to power the social and economic global metabolism[4,5]. The growing demand of energy represents the main driving force of the growth of photovoltaics industry. As found for to nanoelectronics industry the market is dominated by silicon based devices. These are manufactured exploiting energy-hungry technology as well. Alternative devices based on semiconducting compounds i.e. Ga and In arsenide and chalcogenides show a high efficiency but they involve non-earth abundant elements. In this context several issues are raised:

- the consciousness of the limits of the actual resources (fossil fuel, Ga and In)

- the need of improving the Full Life Cycle Assessment (FLCA) establishing environmentally friendly and sustainable productions (i.e. FLCA of Si based devices)

In recent years, kesterites, $Cu_2ZnSn(S,Se)_4$, and related materials, attracted a worldwide interest as promising materials for energy conversion devices (PV applications), encompassing reduced production costs and low environmental risks, in agreement with the above mentioned goals[6–10]. Indeed, many improvements were reached in the kesterite thin film technology, mainly concerning the solar cell conversion efficiency, as reviewed by Delbos[11], with the overall best result obtained by Wang et al. et al.[12] and by Matsumura group for the electrodeposited kesterite[13,14]. A systematic effort, in progress since some years, is also paid 1) to reduce the high temperatures, conventionally needed to obtain the byproducts for kesterite thin film technology[15], 2) to establish a synthetic protocol scalable up to the industrial production[16], 3) to tune the physical proprieties[17].

1.1.4. Advantages of the bottom up approach

We could think the bottom up approach would be the favorite approach for the future nanofabrication techniques. Unfortunately, the processes based on this approach present severe limitation to the uniformity and perfection of bottom up synthesized nanostructures if compared to electronic devices carved out of silicon crystals using conventional techniques[18]. However, the advantage of the bottom-up approach is the possibility to involve a larger part of the periodic table with more flexibility. This leads to devices and fabrication strategies impossible with top-down methods. Many technological and economic advantages are thus gained. At this point, the enormously challenging problem still remain: we will be able to develop bottom up method able to organize this nanostructures and to integrate them into useful systems?

We can imagine that electronics obtained through the bottom-up approach with an atomic-level control of material composition and structure may solve most of this thermodynamic conundrum. To be suitable, these techniques should ensure a high structural control for the engineering of nanostructures such as quantum dots, quantum well, superlattices and thin films still preserving the crystalline properties of the bulk material. Although the bottom-up approach is renowned as very favourable for the synthesis of such materials in the form of dispersed nanoparticles from molecular precursor, it usually involves several steps and the addition of surfactants to the reaction environment. Since most of these products, obtained following these pathways, are in form of powders, the production of solid state devices requires several steps. In this context, electrodeposition has the advantage of the direct production of the films from

the molecular precursors. In any case, due to the already mentioned thermodynamic limits, electrodeposition hardly results in highly ordered materials. Still, in specific conditions electrodeposition enables the assemblage of atomic layers by means of surface limited reactions (SLR). SLRs gives the opportunity of exploiting layer by layer deposition of different atomic layers, leading to one of the most clean and energy saving approaches, Electrochemical Atomic Layer Epitaxy (ECALE)[19], for the growth of heterostructures. ECALE could be also referred in general as E-ALD (Electrochemical Atomic Layer Deposition) since in some cases the growth, though based on underpotential deposition (UPD) processes or on any SLR, cannot be rigorously considered epitaxial. Hence, E-ALD joins highly ordered products with the direct access to the final material in the context of the bottom-up approach in a very clean reaction environment. E-ALD has been proven to be very effective for the electrodeposition of ultra-thin films of semiconducting materials[20]. In recent years, thin films of binary[21–24]and ternary semiconductors[25–28] were successfully obtained. E-ALD requires very low energy consumption, diluted solutions, room temperature and atmospheric pressures. In principle, these characteristics of the process enable it to be employed for the sustainable large-scale production of these materials. This is particularly interesting for application in photovoltaics, where the improvements of the FLCA is considered a crucial aspect for the possible large-scale production of new materials. In this context, the growth mechanism together with a detailed analysis of the structural features of the resulting thin films requires an appropriate study and understanding. For this purpose, surface analysis techniques play an important role. Among them, Surface X-Ray Diffraction (SXRD), with high brilliance synchrotron sources, enables the operando structural analysis in electrochemical environment during the ECALE growth, and discloses the structural features of such systems during the deposition process. The process has been found to epitaxially grow high quality crystal on single crystal surfaces.

We could say that E-ALD has a good chance to be able to grow and organize nanostructures integrating them into useful systems in an easy and sustainable way. Starting the exploration of this chance is one of the aims of this work.

2. State of the art

2.1. Rise of UPD and ECALE

The Under Potential Deposition (UPD), is a Surface Limited Reaction (SLR) involving a surface limited deposition of a particular elements on an electrodic surface. Such reaction deposits matter in the range between a fraction of a monolayer and up to more than an atomic layer depending on the elements and the conditions involved. UPD has been the subject of investigation for over 50 years. Most of the published works at the time have been devoted to the investigations of metal ad-atomic layers on foreign metals, in particular the flat faces of single-crystal Ag, Au, and Pt. The first indications for the UPD phenomenon were given by Haissinsky in his research on the deposition of radioactive materials in 1933[29]. This author [30–33] argued that UPD was due to lattice sites of the substrate presenting large adsorption energies (so called "active centers"). Far from the upd current denomination, at that time the process was addressed as deposition of small metal traces from extremely diluted solutions[31,34]. In the 1950s, other authors started research on this topic, as for example Rogers[35–37], Kolthoff[38], Haenny [39,40] and Bowles[41–45]. These pioneering works regarded the deposition of less noble metals on more noble metals. During the 1980s the study of the UPD of chalcogenides on Au began to gather attention[46]. It was soon established that the deposition of these metals or chalcogenides traces was very sensitive to the substrate material. Several authors, during the 1990s ex-situ and in-situ STM studies confirmed that the UPD on the surfaces of metal single crystals appears to take place with the formation of regular surfaces structures at sub- and full-monolayer coverage [47–50]. In the case of small lattice mismatch between the adsorbate and the substrate, the resulting structures are often commensurate, on the contrary systems with a large lattice mismatch are generally incommensurate, especially when reaching the monolayer coverage. Repeating different SLRs to deposit alternatively atomic sub- or full-monolayer of different elements we can define the electrochemical atomic layer deposition (E-ALD). A simplified scheme is reported in Figure 2-1.

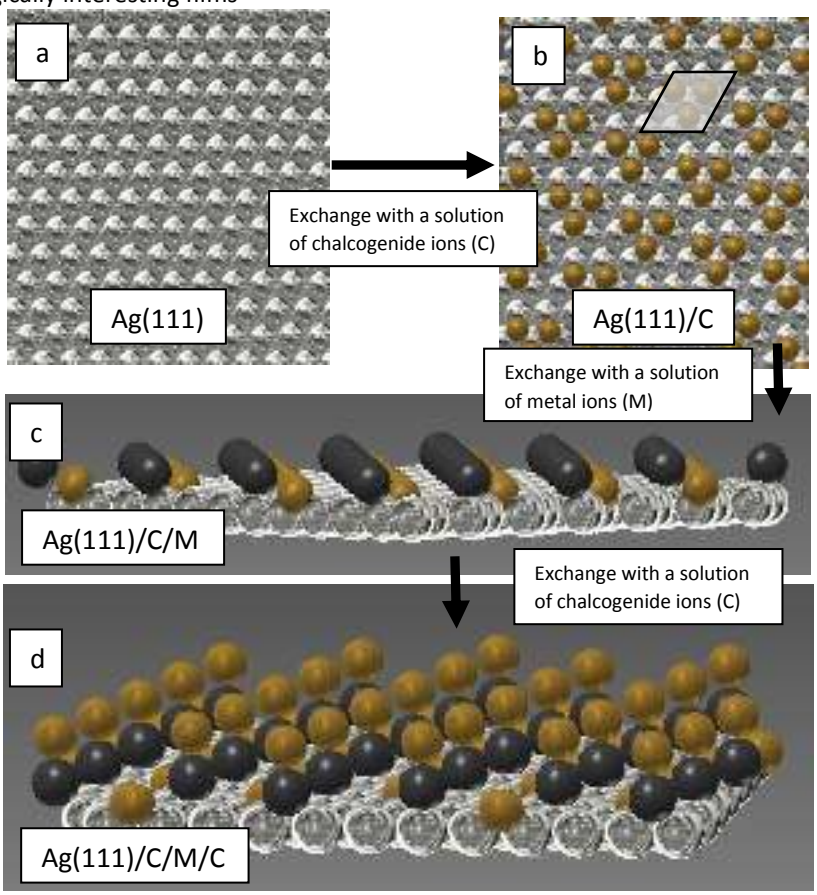

Figure 2-1 Pictorial representation of the main mechanism for the first stages of the E-ALD growth of a general MC_x chalcogenides: a) the Ag(111) surface, b) the chalcogen layer (dark yellow) atoms on the Ag(111) depicted on the basis of a typical geometry for a S_{ad}, the black parallelogram showing the repetition motive for a S_{ad}, c) the deposition of the metal atoms (black) and d) the growth of the second chalcogen layer.

Being performed at room temperature and pressure, this approach results very effective for the epitaxial growth of metal chalcogenides and more efficient compared to vacuum-based techniques. When the thin film growth can be rigorously considered epitaxial the E-ALD method is referred as Electrochemical Atomic Layer Epitaxy (ECALE). In 1991 the concept of E-ALD was introduced by Stickney regarding the ECALE growth of CdTe on a flame annealed polycrystalline gold surface[35]. In the following years, several works reported the growth of binary and ternary metal chalcogenides on Au an Ag single crystals by means of E-ALD.

2.2. Sulphides

E-ALD technique has been successfully used to fabricate ultrathin films of metal sulfides on silver electrodes, by alternating the underpotential deposition of metal and sulfur. These compounds include cadmium sulfide (CdS)[21,51,52], zinc sulfide (ZnS)[21], nickel sulfide (NiS)[23], lead sulfide (PbS)[53], copper sulfides (Cu_2S)[24], and tin sulfides (Sn_xS)[54]. A typical E-ALD cycle includes the underpotential deposition of sulfur followed by the surface limited reaction (SLR) of metal on S-covered Ag. The UPD of sulfur on crystalline and polycrystalline silver have been extensively investigated in the past [48,55,56]. Electrochemical measurements on Ag(110), Ag(100), and Ag(111) show that sulfur UPD deposition processes differ significantly on the three silver surfaces and in situ STM experiments have evidenced the presence of differently ordered sulfur structures depending on substrate orientation. The formation of the first layer of S (S_{ad}) on Ag(100) and Ag(110) occurs at a potential of E=-0.8 V in pH 13 solutions, whereas on Ag(111) it was obtained at E=-0.68 V in ammonia buffer (pH 9.6).Proceeding towards more positive potentials in the presence of sulfide ions resulted in bulk sulfur deposition. Cyclic voltammogramms performed in Na_2S solutions revealed two distinct behaviors. While on Ag(100) only two broad anodic peaks at -1.32 V and -1.15 V were observed, cycling the potential on the other two faces resulted in a more complex behavior, with a sharp anodic peak occurring at E=-1.06 V and E=-0.78 V on Ag(110) and Ag(111), respectively. The charges associated with the UPD deposition of S in the first layer, as calculated from chronocoulometry experiments, were 137μC cm^{-2} for Ag(100), 163 μC cm^{-2} for Ag(110) and 189 μC cm^{-2} for Ag(111). Interestingly, different coverage has been reckoned for the S_{ad} on Ag(111) according to the potential applied. Although the growth of M_xS_y on silver electrodes follows an oxidative-reductive behavior in all cases, SLR of metal layers depends on the semiconductor type and solution conditions.

2.2.1. E-ALD of PbS and NiS

Lead sulfide (PbS) and nickel sulfides (NiS) are binary semiconductors that have received considerable attention for a variety of applications, such as detectors[57], sensing materials and solar cells[58]. A complete electrochemical study of PbS multilayers has been reported by Fernandes et al.[53]. The Pb_{ad} (lead adlayer) cannot be formed on S-covered silver electrodes because of partial re-dissolution of sulfur. So the first layer is the Pb_{ad} deposited on Ag(111), this was obtained from 5.0 mM $Pb(NO_3)_2$ solutions in acetic buffer at pH 5 by scanning the potential from -0.2 V to -0.45 V. Two well-defined

peaks were observed at - 0.35 V and at -0.29 V for the deposition and the dissolution of Pb monolayer, respectively. Next, the underpotential deposition of S on Pb-covered Ag(111) was obtained by scanning the potential from -1.0V to -0.70V in 2.5 mM Na_2S solutions in ammonia buffer. The constancy of the anodic stripping of Pb deposited at -0.45V and at different accumulation times ensures the process is surface limited, giving rise to a charge of 332 μC cm^{-2} for the first layer. Successive sulfur and lead layers resulted in a linear growth with an average charge per cycle of approximately 83μC cm^{-2}. Morphological analysis by ex-situ AFM measurements revealed the deposits consisted of homogeneous films of PbS small clusters.

Differently from lead, underpotential deposition of nickel on bare Ag(111) is not possible due to weak adhesion with the electrode substrate and competing surface phase transformations[59]. On the contrary nickel presents a well-defined surface limited reaction on S-covered Ag(111), showing cathodic and anodic peaks at -0.52 V and -0.22 V, respectively. UPD layers of nickel were obtained from $NiCl_2$ in boric acid solutions (pH 6.5) at E=-0.6 V. The amount of sulfur, as determined by separate anodic stripping experiments, was found to linearly increase with the number of the deposition cycles. Conversely, the stripping of nickel was less precise due to the formation of oxide and hydroxide films with the increase in layer number[60]. Despite these limitations the charges of both Ni and S showed a quasi-linear layer-by-layer growth with slopes of 53 μC cm^{-2} for Ni and 58 μC cm^{-2} for S. Morphological analysis by AFM indicated a decrease of average roughness (smoothing) with aging, thus suggesting the formation of a passivation layer (oxide/hydroxide) with time, which was later confirmed by XPS analysis.

2.2.2. E-ALD of CdS, ZnS, Sn_xS and Cu_2S

Cadmium, tin, zinc, and copper are metals that form strong interactions with sulfur ions, thus generating binary semiconductors with peculiar transport and electrical properties. Cadmium and zinc sulfides have been among the first binary semiconductors to be deposited by means of E-ALD, due to favorable electrochemical features.

UPD deposition of CdS has been investigated by means of in-situ Surface X-Ray Diffraction (SXRD) experiments on silver single crystals exhibiting different orientations, i.e. Ag(111), Ag(110), and Ag(111)[51,52,55]. The structure of the S_{ad} drives the epitaxial deposition of the subsequent Cd layer leading to the formation of multidomain growth of greenockite ($P6_3mc$ [61]) or hawleyte ($F43m$ [61]) depending on the symmetry of the surface. After washing out the sulfur ions in excess, UPD of cadmium is performed by

holding the potential at -0.68 V on S-Ag (111) and at E=-0.6 V on the other two faces. The procedure used to obtain further alternated layers of S and Cd is identical to that used for the Ag/S/Cd structure. The average values of the charge deposited in each E-ALD cycle were 103 μCcm^{-2} for Ag(100), 85 μCcm^{-2} for Ag(110), and 70 μCcm^{-2} for Ag(111). Ex situ XPS analysis confirmed the presence of cadmium and sulfur in a 1:1 stoichiometric ratio[60]. However, Carlà et al. reckoned the thickness of the film by means of X-Ray Reflectivity. The results suggest that the overall growth of the film follow a layer by layer involving the deposition of half layer of greenockite or hawleyite per each E-ALD cycle[51].

Similarly to cadmium sulfide, E-ALD of ZnS thin film were grown on silver electrodes by first depositing sulfur at E=-0.70 V from Na_2S solution, and then injecting $ZnSO_4$ solution while keeping the electrode at the same potential to underpotentially deposit Zn. Plots of the charges for Zn and S measured in the stripping of ZnS deposits were linear, with a slope of 67 $\mu C\ cm^{-2}$ for Zn and 75 $\mu C\ cm^{-2}$ for S[53].

In a different way from CdS and ZnS, the other two metal sulfides (Cu_2S and Sn_xS) exist in different stoichiometry; their interest in E-ALD growth relies on the tunable transport and electronic properties by changes in composition, x and y[62,63].

The surface limited reaction of Sn_xS has been thoroughly studied by Innocenti et al.[54] both on bare and on S-covered silver substrates. Electrodeposition of tin on bare silver showed two anodic peaks, E_{c1}=-0.70 V and E_{c2}=-0.48 V, the latter ascribed to the formation of Sn(IV) hydroxides. Differently, on S-covered Ag(111) the reduction peak was seen at lower potentials, Ec=-0.61 V, thus suggesting true underpotential deposition mechanism. Independently from the deposition time, the charge involved in the oxidative process remained nearly constant, thus confirming a surface limited process.

Thin films of copper sulfides were fabricated on silver substrates through E-ALD. Interestingly, the surface limited layer-by-layer growth of Cu_2S was found not to be a true UPD process like for the other metal sulfides. As reported by Innocenti et al.[24] the electrochemistry of copper on S-covered Ag (111) is quite complex. Cyclic voltammograms as obtained by sweeping the potential between -0.05 V and -0.55 V in 1 mM Cu(II) solutions in ammonia buffer revealed the presence of two cathodic peaks, E1= -0.39 V and E2=-0.42 V. While the latter was easily associated to the bulk reduction of Cu(II) to Cu(0), the nature of the first cathodic peak is still under debate, except for the fact that it precedes bulk deposition. More-in-depth electrochemical analysis suggests the process is surface limited in the range -0.3/-0.38V and it involves the formation of Cu(0) through the two-step reduction of cupric cation and the subsequent conproportionation reaction:

$$Cu^{2+} + e^- \Rightarrow Cu^+$$

$$Cu^+ + e^- \Rightarrow Cu$$

$$Cu^{2+} + Cu \Rightarrow 2Cu^+$$

The amount of Cu deposited in a given number of cycles was determined by measuring the charge involved in the anodic stripping. The authors found the charges were linearly increasing with the number of deposition cycles with a slope of 44μC cm^{-2}. XPS results confirmed the valence states of copper and sulfur as Cu(I) and S(-II) respectively, although a possible fraction of S(-I) in the form of disulfide anion was not excluded. The experimental Cu/S ratio observed in the XPS characterization was later attributed to the covellite phase, where positive holes allow Cu ions to be stabilized in their monovalent state[64].

2.2.3. E-ALD of ternary M_xN_yS

The interest in the ternary compounds has increased in the last twenty years due to the possibility to have a fine control over the band gap energy of solar cell devices[64–66]. At this stage it should be clear that E-ALD can effectively grow binary compound semiconductors, but it is able to grow also ternary compounds? This question have been raised by the scientific community in the infancy of the E-ALD studies. This was just not merely a scientific question but it has natural technological follow-up. The answer to question is partially reported by Foresti et. al regarding the successful deposition of Cd_xZn_yS [66], Cu_xZn_yS [67] and Cu_xSn_yS [64]. These semiconductors were prepared by sequential deposition of the corresponding binaries; for instance alternate deposition of Cu_2S and Sn_xS was carried out to form Cu_xSn_yS. Recalling the importance of the quaternary sulphides discussed in paragraph 1.1.3, we should notice that because of the large variety of the possible (x:y) combinations research on E-ALD of multinary kesterite group thin films, although challenging, can be explored. Depending on the adopted sequence profile only certain combinations were attainable, thus limiting the possible metal-to-metal stoichiometries. The electrochemical behavior of Cu_xSn_yS, Cu_xZn_yS, and $Cd_xZn_{1-x}S$ thin films is separately discussed below.

Di Benedetto et al. [64] investigated the electrodeposition of Cu_xSn_yS thin films exploiting different sequences of E-ALD cycles, that is $Ag/S[(Cu/S)_k/(Sn/S)_j]_n$ with k=1, j=1, 2, and 1<n<60. Surface limited deposition of Cu and Sn occurred respectively at E=-0.37 V and E=- 0.68 V in ammonia buffer containing EDTA. As already reported for binary sulfides

S_{UPD} layers on Ag(111) and on metal were obtained by keeping the potential at E=-0.68 V in Na_2S ammonia solutions. Stripping analysis of the ternary sulfides yielded a large and well- defined peak centered at E=-0.22 V (Cu stripping), preceded by a broader peak at -0.43 V (Sn stripping). Charges involved in the stripping of both metals (Sn+Cu) and S allowed defining the effective layer-by-layer formation of a ternary compound with a slope of 42 μC cm^{-2}, which is very close to the value obtained from the stripping of the binary CuS compound [24]. The chemical composition of $Ag/S[(Cu/S)_k/(Sn/S)_j]_n$ deposits were analyzed by means of SEM, XPS, and TOF-SIMS[28]; the ex-situ characterizations have highlighted the nominal stoichiometry is not respected leading to Sn/Cu ratio equal to 1/13 and 1/9 for j=1, and 2, respectively. Independently from Sn/Cu ratio the morphology of the growing films, as revealed by AFM measurements, were found to be homogeneous and similar to the bare Ag(111). Conversely the band gap values, carried out by diffuse reflectance spectroscopy, decreased with the increase in thickness and Cu/Sn ratio ranging from 2.12 for n=60, j=2 to 2.43eV for n=20, j=1.

As for the Cu–Sn–S system the experimental conditions to grow ternary cadmium and zinc sulfides on Ag(111) with the E-ALD were by alternating the underpotential deposition of the corresponding binaries (CdS and ZnS) [60]. The potential chosen for the deposition of S and Zn was -0.65 V, whereas different series of experiments were carried out depositing Cd in correspondence to the first (-0.5 V) or to the second UPD (-0.65 V). The authors investigated the electrodeposition of $Cd_xZn_{1-x}S$ thin films exploiting different sequences of E-ALD cycles, that is Ag/S[(Cd/S)k/(Zn/S)j]n with k=1, j=1, 2, 5 and 1<n<20. The charge involved in the stripping increases linearly with the number of deposition cycles. Yet, the slope of the plot decreases while increasing the number of ZnS cycles per CdS cycles, i.e 89 μC cm^{-2}, 67 μC cm^{-2}, and 52 μC cm^{-2} for j=1, 2, and 5, which reflect the higher percentage of Zn in the deposit. The chemical composition of $Cd_xZn_{1-x}S$ thin films, as analyzed by XPS have highlighted the nominal stoichiometry is not respected leading to Zn/Cu ratio equal to 1/3, 1/2, and 2 for j=1, 2, and 5 respectively. However, regardless of the stoichiometry of the obtained ternary compound, the charge involved in cathodic stripping was equal to the charge involved in the anodic one, thus indicating the right 1:1 stoichiometric ratio[68].

The low contribution of Zn in $Cd_xZn_{1-x}S$ compounds was also found to occur in the Cu-Zn-S system. Ternary Cu_xZn_yS compounds were obtained through the E-ALD method by alternating deposition of Cu_2S and ZnS layers. Innocenti et al. [66] studied the electrochemical and compositional behavior of $Cd_xZn_{1-x}S$ thin films by applying the general sequence Ag/S/[(Cu/S)j/(Zn/S)k)]n with j=1, k=1, 5, 9, and 1<n<60. As for other binary and ternary compounds UPD sulfur layers were obtained by keeping the electrode potential at E = -0.68 V for either on bare Ag(111) or on Ag(111) already

covered by a metal layer. Deposition of Cu and Zn occurred in ammonia buffer at -0.37V and -0.85V, respectively. Stripping analysis revealed the charge involved in (Cu+Zn) deposition followed a non-linear increase with the number of cycles. Moreover, samples containing higher percentage of Zn had lower slope, thus indicating a lower extent of deposition in each cycle; a Cu/Zn ratio of about 6 was found for j=1, k=1, and n=40. By means of extrapolation, the authors reported that the 1:1 ratio can be achieved with n = 13 meaning a strong deficiency of Zn in the sulfides. Independently from the Cu/Zn ratio, ex-situ investigations highlighted at least two prevailing morphologies, the first one homogeneously covering the Ag(111) surface, and the second one consisting of random network of nanowires of variable length [27,67].

2.3. Selenides

The E-ALD of metal selenides (M_xSe_y) on monocrystalline surfaces usually starts with the deposition of a selenium monolayer by using selenite, Se(IV), as a precursor salt. Differently from sulfur deposition the oxidative UPD of Se is not allowed due to the low stability of selenite solutions. According to the work by Rajeshwar et al. the electrochemistry of Se(IV) is quite complex. The direct reduction of Se(IV) to Se(0) is attributed to the formation of the electroinactive gray Se (hexagonal selenium – $P3_121$ No 152[69]), which forms a stable deposit:

$$H_2SeO_3 + 2\ H_2Se \Rightarrow 3\ Se + 3\ H_2O$$

Instead, the electroactive form of Se(0), usually referred as red Se (amorphous selenium), is obtained through a first reduction of Se(IV) to Se(-II) followed by a comproportionation reaction[70]:

$$H_2SeO_3 + 4\ H^+ + 4\ e^- \Rightarrow Se + 3\ H_2O$$

$$H_2SeO_3 + 6\ H^+ + 6\ e^- \Rightarrow H_2Se + 3\ H_2O$$

In ammonia buffer (pH 9.13) the presence of the electroactive red Se is evident for E<-0.95V through the reduction Se(0) → Se(-II), and around E=-0.8V through the oxidation Se(0) → Se(IV). Adlayers of Se on the electrode surface, Se_{ad}, are formed through a two-step procedure involving the deposition of an excess of Se(0) from Se(IV) solutions, followed by the reduction of bulk Se at sufficiently negative potential (E≈-0.95V). The reduction must be performed in the absence of Se(IV) to avoid the comproportionation reaction with Se(-II) leading to a massive formation of Se(0).

The STM investigation at potential more negative than that of the bulk reduction peak has shown two distinct structures. The layer at more positive potential values has a (√7 x √7) R19.1° structure, with an associated charge of 65 μC cm^{-2}, whereas at more negative potentials it has a (2 √7 x 2 √7) R19.1° structure, with an associated charge of 48 μC cm^{-2}.

2.4. Tellurides

The E-ALD of metal tellurides, M_xTe_y, on monocrystalline surfaces starts with the deposition of tellurium. As in the case of selenite, telluride solutions are not stable, so the oxidative UPD is not allowed. Te(IV) reduction occurs following two possible schemes[71,72]. A stable Te deposit is formed upon direct reduction of Te(IV)

$$HTeO_2^+ + 5H^+ + 6e^- \rightarrow H_2Te + 2H_2O$$

or through a two-step process involving the reduction of Te(IV) to Te(-II) followed by a comproportionation reaction.

$$HTeO_2^+ + 2H_2Te \rightarrow 3Te + 2H_2O + H^+$$

$$HTeO_2^+ + 3H^+ + 4e^- \rightarrow Te + 2H_2O$$

The TeO_2 in ammonia buffer solutions (pH 8.5) on Ag(111) shows a large reduction peak at E=-0.4 V, which is only observed during the first scan from -0.1 to -0.9 V. Integration of the peak yields a charge of about 370 μC cm^{-2}. Due to the high irreversibility of the system, the reoxidation of the underpotentially deposited Te is prevented by silver oxidation, so the Te UPD peak disappears in the successive CV scans. Towards more negative potentials the deposited Te(0) is reduced to Te(-II). The reduction process at about -1.1 V only involves bulk deposited Te(0), since the Te UPD layer is more strongly bound to the silver substrate and therefore it starts to reduce at potentials more negative than -1.5 V. So, the Te_{ad} can be obtained through UPD reduction before bulk deposition or in a two-step process: deposition at a potential of -0.6 V of small excess of bulk Te, followed by the reduction of bulk Te (but not Te_{ad}) at a potential of -1.4 V.

2.5. The open questions

In the contemporary literature about E-ALD, in particular when developed on Ag(111) substrate, several new materials has been successfully growth in the form of ultra-thin films (thickness lower than 50 nm). Interestingly, several results are reported lately for some binary compound and ternary compounds:

- Zn deficiency discussed for both the Cu_xZn_yS, $Cd_{1-x}Zn_xS$ and the Sn deficiency for Cu_xSn_yS.
- the complex morphology revealed by the Cu_xZn_yS and less evidently by Cu_2S
- the thickness of CdS films
- Uncertain composition of the copper sulphides

These results raise several questions about the growth mechanism and the structural, chemical and physical properties of the thin films obtained by means of E-ALD. In order to fully grasp those questions, it should be notice that the literature assumed the films grow by the scheme reported in Figure 2-1, repeating the same process for an arbitrary number of cycles. On this ground, these results are interesting because they cannot be explained in such theoretical framework, hence the actual growth mechanism underlying E-ALD is unknown. Layer-by-layer process, at the beginning of the growth could be thought to be effectively well described only by SLRs. Intuitively, at a certain growth stage it could change, for instance when the solutions interact with a semiconducting surface with proprieties differing from the initial Ag(111) metal substrate. Moreover, a general discussion of the thermodynamic behind the E-ALD process will expect several other factors involved in the determination of the final product of each step (Chapter 3). Hence, the overall E-ALD process is likely to be more complex than the results of several consecutive surface process whose outcome does not depend on the growth stage. Although, the mechanism at the beginning of the E-ALD has been verified to be driven by the interaction of the surface, even at an atomistic level [48,52,55], the mechanistic characterization of the whole process is completely lacking. Under these considerations, one of the aim of this work is to improve the comprehension of the complexity underlying the E-ALD process.

To this aim, a more thorough characterization of the products has to be developed. It should be noticed that at the beginning of this research work there was a complete lack of knowledge about the structure of most of this compounds, which has only been reckoned for CdS. Although, a complete clarification of the structure is limited by the extremely low thickness of the thin films and the interference of the substrate. Still, any

information about the structure of some of these films can be important *per se* but can help in addressing the questions raised by recent studies.

Eventually, understanding the structure and the growth process of these films is necessary to establish a solid ground where we could explore the actual possibilities of the E-ALD. Specifically, to answer the question raised by paragraph 1.1.4: will be E-ALD able to grow directly nanostructures with a bottom approach and to integrate them into useful systems?

3. Thermodynamics of the E-ALD process

For the sake of simplicity and clarity, we will develop the thermodynamics an epitaxial E-ALD process (ECALE) with the steps constituted by UPD. In the following, the considered exemplar process is the growth of CdS on Ag(111) by means of ECALE.

3.1. Thermodynamics of UPD

Chemically, ECALE exploits UPD to grow the semiconductor compounds on a selected surface. For instance, the oxidative deposition of an atomic layer of sulfur atoms on top of Ag(111) surface is:

$$Ag(111) - S_{ad} + 2e^- \leftrightarrows Ag(111) + S^{2-}$$

where S_{ad} refers to the sulfur adlayer. The UPD provide a surface limited deposition process characterized by a potential more cathodic than the bulk deposition process. The latter is defined by means of the Nernst equation:

$$E_{S^{2-}/S} = E^0_{S^{2-}/S} + \frac{RT}{2F} ln\left(\frac{a_S}{a_{S^{2-}}}\right) \qquad 3\text{-}1$$

Considering the experimental observation of the potential shift provided by a UPD process, an intuitive knowledge of this UPD process can be gained by proposing an heuristic (and rough) extension of Nernst by writing:

$$E_{S^{2-}/S_{ad}} = E^0_{S^{2-}/S} + \frac{RT}{2F} ln\left[\frac{a_{S_{ad}}(\theta)}{a_{S^{2-}}}\right] \qquad 3\text{-}2$$

where $a_{S_{ad}}(\theta)$ is the activity of S atoms adsorbed on Ag(111) as a function of the coverage θ. On this basis, we can define the quantity ΔE_{UPD} called underpotential shift[73]:

$$\Delta E_{UPD} = E_{S^{2-}/S_{ad}} - E_{S^{2-}/S} = \frac{RT}{2F} ln\left[\frac{a_{S_{ad}}(\theta)}{a_S}\right] \qquad 3\text{-}3$$

On this ground, we should expect a ΔE_{UPD} independent from the activity of the sulphides anions. However, because of several reasons this is not the case. In fact, there are some process not considered in this heuristic approach:

1. the lateral and vertical binding energies between metallic adatoms in nanostructures and the binding energy between adatoms and the substrate
2. the energetic influence of local surface defects of the substrate
3. the binding energies between solvent dipoles and the metallic substrate/ nanostructure system
4. the binding energies of solvated anions with Ag(111) and the S adlayer.

Still, this heuristic extension of the Nernst equation (equation **3-2**) enables an intuitive thermodynamic description of the UPD process. A more accurate description of the UPD thermodynamics can be formulated in the framework of the ideal polarized electrode. In this scheme, the substrate (i.e. Ag(111)) on which UPD takes place is in contact with the electrolyte solution (sol) containing S^{2-}, $Na^{+}$and X^{-} ions and solvent (H_2O). Thus, it appears an interphase (IP) between the Ag(111) surface and the solution (sol). From a theoretical standpoint, the electrolyte solution can be considered in contact with a reference electrode reversible with respect to a general anion X^{-}. The phases relevant for the present analysis are the Ag(111) surface, the interphase (IP) and the solution (sol). Each of them, say the j^{th} phase, is described thermodynamically by an energy equation of the type:

$$G^j = G^j\left(T^j, P^j, A^{IP}, N_i^j\right) \qquad 3\text{-}4$$

where G^j is the Gibbs free energy of the system as a function of the variables T^j(temperature), P^j (pressure), A^{IP} (interfacial area) and N_i^j (amount of matter of the i-th species). The total derivative of the energy equation has the well-known form[73]:

$$dG = \sum_j dG^j = \gamma^{IP} dA^{IP} + \sum_{j,i} S^j dT^j - V^j dP^j + \mu^j dN_i^j \qquad 3\text{-}5$$

Where γ^{IP} is the surface tension of the interphase, S^j the entropy, V^j the volume and μ^j the chemical potential. In a solution of Na_2S in NaOH buffer solution (i.e. pH=13) at constant T^j, P^j, when only the following charge transfer equilibrium is present:

$$S_{sol}^{2-} \leftrightarrows S_{el}$$

where *sol* refers to the liquid phase and *el* refers to the electrode. The corresponding electrocapillary equation is[74].

$$-d\gamma^{IP} = \Gamma_{S^{2-}}^{IP} d\mu_{S^{2-}}^{sol} + \Gamma_{OH^-}^{IP} d\mu_{OH^-}^{sol} + \Gamma_S^{IP} d\mu_S^{el} - q_{ion} dE \qquad 3\text{-}6$$

Where E is the potential referred to the reference electrode and defined by means of the chemical potential of $\Gamma_{Na^+}^{IP} d\mu_{Na^+}^{sol}$. According to this latter definition, $q_{ion}$is the surface excess of electric charge density:

$$q_{ion} = \left(\frac{\partial \gamma^{IP}}{\partial E}\right)_{(\mu_{S^{2-}}^{sol}, \mu_{OH^-}^{sol}, \mu_S^{el})} \quad 3\text{-}7$$

This equation is renowned as Lippmann equation. Eventually, $\Gamma_{OH^-}^{\mathrm{IP}}$, $\Gamma_{S^{2-}}^{\mathrm{IP}}$ and Γ_S^{IP} are the relative excess of Na^+ and $S^{2-}$with respect to $\mathrm{H_2O}$ (solvent):

$$\Gamma_{S^{2-}}^{IP} = \frac{1}{A^{IP}}\left[N_{S^{2-}}^{IP} - \frac{N_{S^{2-}}^{sol} N_{H_2O}^{IP}}{N_{H_2O}^{sol}}\right] \quad 3\text{-}8$$

Noticeably, equation 8, in the Gibbs theoretical framework, is not a mere change of variable. In fact the amounts of matter ($\mathrm{N_i^{IP}}$) are dependent on the arbitrary definition of the interface while the relative excess of matter (Γ_i^{IP}) are independent from the area and the thickness of the interface. It should be noticed that in this theoretical framework the contribution the formation of the S adlayer is described by the term $\mathrm{d}\gamma^{IP}$. Using the following equation for the chemical potential in the case of complete dissociation:

$$\mu_{S^{2-}}^{\mathrm{sol}} = \mu_{S^{2-}}^{0,\mathrm{sol}} + RT \ln a_{S^{2-}} \quad 3\text{-}9$$

$$\mu_{OH^-}^{\mathrm{sol}} = \mu_{OH^-}^{0,\mathrm{sol}} + RT \ln\ a_{OH^-} \quad 3\text{-}10$$

$$\mu_S^{el} = \mu_S^{el} + RT\ ln\ \theta_S \quad 3\text{-}11$$

Where a are the activities in the liquid phase and θ is the fractional amount in the solid phase. The relationship between activities and surface tension is well represented by the following.

$$\Gamma_{S^{2-}}^{IP} = \frac{1}{RT}\left(\frac{\partial \gamma^{IP}}{\partial\ ln\, a_{S^{2-}}}\right)_{(a_{OH^-}^{sol}, \theta_S^{el}, q_{ion})} \quad 3\text{-}12$$

$$\Gamma_{OH^-}^{IP} = \frac{1}{RT}\left(\frac{\partial \gamma^{IP}}{\partial\ ln\, a_{OH^-}}\right)_{(a_{S^{2-}}^{sol}, \theta_S^{el}, q_{ion})} \quad 3\text{-}13$$

$$\Gamma_S^{IP} = \frac{1}{RT}\left(\frac{\partial \gamma^{IP}}{\partial\ ln\, \theta_S}\right)_{(a_{S^{2-}}^{sol}, a_{OH^-}^{sol}, q_{ion})} \quad 3\text{-}14$$

$$E = \left(\frac{\partial \gamma^{IP}}{\partial q_{ion}}\right)_{(a_{S^{2-}}^{sol}, a_{OH^-}^{sol}, \theta_S^{el})} \quad 3\text{-}15$$

Hence the surface tension depend on the activity of the chemical species:

$$\gamma = \gamma_{\left(a_{S^{2-}}^{sol}, a_{OH^-}^{sol}, \theta_S^{el}, q_{ion}\right)} \quad 3\text{-}16$$

Therefore, upon the integration of equation 3-6, an extension of the Nernst equation can be obtained substituting equations *3-9* - 3-11 in equation 3-16:

$$E = E^0 + \frac{\Gamma_{S^{2-}}^{IP} RT}{q_{ion}} ln\, a_{S^{2-}} + \frac{\Gamma_{OH^-}^{IP} RT}{q_{ion}} ln\ a_{OH^-} + \frac{\Gamma_S^{IP} RT}{q_{ion}} ln\ \theta_S + \frac{1}{q_{ion}} \left[\gamma_{\left(a_{S^{2-}}^{sol}, a_{OH^-}^{sol}, \theta_S^{el}, q_{ion}\right)} - \gamma^0 \right] \quad \textit{3-17}$$

Where:

- E^0 is the standard potential of the electrode with respect to the reference electrode
- $\frac{\Gamma_{S^{2-}}^{IP} RT}{q_{ion}} \ln a_{S^{2-}}$ takes into account the effect of the activity
- $\frac{\Gamma_{OH^-}^{IP} RT}{q_{ion}} \ln\ a_{OH^-}$ takes into account the effect of the pH (in a buffer solution this activity is constant)
- $\frac{\Gamma_S^{IP} RT}{q_{ion}} \ln\ \theta_S$ if no compound is formed with the electrode the equilibrium with a new phase (bulk Sulfurs) can be described considering $\theta_S = 1$. When considering the formation of an adlayer its physical meaning is the coverage of the surface of the electrode.
- $\frac{1}{q_{ion}} \left[\gamma \left(a_{S^{2-}}^{sol}, a_{OH^-}^{sol}, \theta_S^{el}, q_{ion} \right) - \gamma^0 \right]$ this term takes into account the interaction with the Ag(111) surface

It should be noticed that $q_{ion} \propto 2F$(for the oxidation of S^{2-}). Eventually, we should state that equation 3-11, in principle, takes into account all the effects neglected by equation 3-2. However, equation 3-11 describes the equilibrium of a system with 4 constituents (S^{2-}, S , OH^- and Na^+) with one charge transfer equilibrium. Thus, the phase rule allows only 3 variables hence equation 3-17 reduces to different Nernst equations according to the conditions of the system considered. The equilibrium of an ad-layer with our reference solution (Na_2S in NaOH buffer 0.1M) can be described by 3 variables while the other two can be considered constant. Experimental observations suggest that the potential of the UPD process of sulfur depends on the concentration of sulfur atoms ($a_{S^{2-}}$), the pH (a_{OH^-}) and the coverage of the ad-layer (θ_S).

3.2. Thermodynamics of the E-ALD growth

The thermodynamics framework used to describe the E-ALD growth could be design as an extension of the formalism developed for the UPD. In the following, we will refer to the epitaxial E-ALD (or ECALE) process for the growth of CdS on Ag(111). Clearly, since the composition of the solution changes according to the E-ALD scheme, every step will have a specific set of thermodynamic variables in the energy equation. For instance, the energy equation for a general n-th cycle depends on a set of chemical potential and

relative excess Γ_i^{IP}. Moreover, it should include additional terms with respect to the UPD of the first atomic layer on the substrate (i.e. S/Ag(111)):

1. Chemical potential and amount of CdS
2. Strain energy due to the epitaxial relationship with the substrate (Ag(111))
3. Displacement energy, for instance the plastic deformation relaxing the epitaxial strain

Resulting in the following formulation[75,76]:

$$dG \quad = \gamma^{IP} dA^{IP} + \sum_{j,i} S^j dT^j - V^j dP^j + \mu^j dN_i^j + \varepsilon \otimes \sigma + dG_{DS} \quad \text{3-18}$$

Where ε is the strain tensor and σ stress tensor. Their inner product is in general the strain energy of the film. G_{DS} is the energy term due to the formation of displacement relaxing the strain. This latter is related to the plastic deformation occurring in the film including the formation of defects. In particular the formation of dislocations in the film describes roughly the transition from a pseudomorphic layer to a commensurate epitaxial layer. In this context the critical thickness can be computed by means of this recursive transcendent equation[75]:

$$h_c = \frac{K_1}{f_m} \ln(K_2 h_c) \qquad \textit{3-19}$$

Where K_1 is a constant dependent on the properties of the film and K_2 on the properties of the dislocations. Eventually, $f_m$is the epitaxial mismatch, as expected, inversely proportional to critical thickness which is usually a few nanometers. However, UPD processes enabled the growth of adlayers of different coverage that cannot be considered pseudomorphic. Such trend be modelled by means of the hereby presented dislocations approach expecting a very low critical thickness? Moreover, what is the thermodynamic effect of the stress on the morphologies and structures of the resulting thin films? Although the effect of the stress accumulated during the growth by means of E-ALD is fostered in equation 3-18, these are still open questions. However, in paragraphs 5.1 and 5.2 it is showed that the E-ALD growth of Ag(111)/ Cu_2S and Ag(111)/Cu_xZn_yS occurs with a structural and morphology changes observed while increasing the thickness of the film.

4. Methods

4.1. Materials and electrodes

Solutions

The measurements and preparation were performed using analytical grade reagents without further purification. $HClO_4$ 65% and NH_4OH 28% (VWR Chemical) were used to prepare the 50 mM [$HClO_4$] and 100 mM [NH_4OH] ammonia buffer at pH 9.13. $CuCl_2 \cdot 2H_2O$, Merck $ZnSO_4 \cdot 7H_2O$, $3CdSO_4 \cdot 8H_2O$ and Aldrich $Na_2S \cdot 3H_2O$ were used as sources of Cu, Zn, Cd and S respectively to prepare 0.5 mM solution of each element in ammonia buffer. The solutions were freshly prepared just before the beginning of each series of measurements.

Electrodes

The measurements reported in this study are based on the exploitation of the silver single crystals for both ex-situ and operando electrochemical preparations and characterization. However, the operando experiments require a higher surface quality. Specifically, it is required a more strict crystallographic orientation, a smaller roughness and the absence of facets. In all the case reported in this thesis, the Ag(111) electrodes were initially prepared according to the Bridgman technique in our laboratory and polished by a CrO_3 based procedure[77–79]. When the electrodes were used to perform operando experiments an additional step of sputtering-annealing in ultra-high vacuum before each operando measurement. In particular, the electrode surface was cleaned under Ultra High Vacuum (UHV) conditions by performing several cycles of Ar+ sputtering at 1kV followed by annealing at 900 K for about 1 min. The cycles were repeated until a sharp Low Energy Electron Diffraction (LEED) pattern was observed and no contamination was observable by X-ray Photoelectron Spectroscopy (XPS).

Automated systems

All the synthesis were performed exploiting two automated deposition apparatus one located at the department of chemistry and on the ID03 beamline at ESRF synchrotron (Grenoble)[80]. Both the automated systems, share a common design consisting of Pyrex reservoirs, solenoid valves, a distribution valve and a flow-cell. The software driving these systems are based on different programming languages, the one in Florence is connected to a computer by a Labview software[21]. Conversely, the one in Grenoble is connected to the control room by means of the SPEC system following the standards of the ESRF synchrotron. Moreover, the two apparatus has different the electrolytic cell

designs. Specifically, the ex-situ experiments carried at the department of chemistry of the University of Florence is more robust but it is not suitable for the operando experiment with synchrotron light. The paragraph 4.4 is dedicated to a thorough description of the cells designed for the operando experiments at ESRF. Concerning the electrolytic cell exploited at the department of chemistry of the University of Florence, it consists of a Teflon cylinder (with an internal diameter of about 7 mm and a 42 mm outer diameter), whose inner volume was 0.5 ml. The working electrode, Ag(111), was on one side and the counter electrode (gold or glassy carbon) on the other side. The exposed area of the silver single crystal working electrode is 0.785 cm^2. The inlet and the outlet for the solutions were placed on the side walls of the cylinder. The reference electrode (RE) was Ag/AgCl saturated in KCl, placed on the outlet tube. This cell design with the counter electrode facing the working electrode ensures a high homogeneity of the deposits and a low ohmic drop.

4.2. Surface X-Ray Diffraction

An electromagnetic wave (EW) interacting with a surface will be reflected, diffracted, transmitted and absorbed. Surface X-ray diffraction (SXRD) and X-ray Reflectivity (XRR) exploit respectively the diffracted and reflected EW to reckon several physical information about the surface and its modification. However, it should be noticed that the two phenomena are related in the sense that their effect can be located in the same position of the space, with comparable intensity and energy. Hence, they can be detected with the same experimental setup depending on the experimental protocol applied to the measurement.

This paragraph delves into the theory of SXRD and the following paragraph (4.3) in the theory of XRR. In each paragraph, the focus will be on the separation between the physical effect of the X-rays interaction with matter and the information we can obtain detecting such effects.

Every object (not only a crystal) could be an X-ray scatterer and every object could provide a diffraction signal reckoning the whole information about the shape of the scatterer, i.e. the inverse Fourier transform of the diffraction signal coming from a frog could (in principle) reconstruct the exact shape of the frog. Hence, also the inverse transform of the signal diffracted by an infinite set of finite and defective iso-orientated crystals can deliver more information than the atomic structure of the crystals. This idea constitutes the background for the development of a basic comprehension of the origin

of the Crystal Truncation Rod (CTR), which represents one of the most interesting features studied by SXRD. The CTR can be seen as an extreme broadening of Bragg peaks caused by finite size of the crystals.

4.2.1. X-Ray Diffraction: Theory of the diffraction by crystals

Electromagnetic waves scattered by free electrons

Let consider a free electron (charge e and mass) on the origin of the coordinate system in the vacuum and a monochromatic plane EW propagating in the positive direction towards the electron, the former described by the following:

$$E_i = E_{0i} e^{2\pi i \nu \left(t - \frac{x}{c}\right)} \qquad 4\text{-}1$$

where E_{0i} is the amplitude of the wave and E_i is the value of the field at position x at time t. The field induces on the particle a periodic acceleration perpendicular to the propagation of the EW:

$$a = eE_i/m = \frac{e}{m} E_{0i} e^{2\pi i \nu \left(t - \frac{x}{c}\right)} \qquad 4\text{-}2$$

with frequency ν, generating a secondary EW (diffracted EW) with the same frequency (elastic scattering) or a different frequency (inelastic scattering). The former is the Thomson or elastic scattering while the latter is the Compton or inelastic scattering. The wave generated by the two types of scattering can be respectively described by one of the following equations at the position pointed by vector $\boldsymbol{r}$:

$$E_d = E_{0d} e^{2\pi i \nu \left(t - \frac{|\boldsymbol{r}|}{c}\right) - i\alpha} \qquad 4\text{-}3$$

$$E_d = E_{0d} e^{2\pi i (\nu + \Delta\nu) \left(t - \frac{|\boldsymbol{r}|}{c}\right) - i\alpha} \qquad 4\text{-}4$$

where α is the phase lag and $\Delta\nu$ the change of frequency due to exchange of energy between the electron and the EW. Thomson scattering, involving a set of electrons, generates coherent EWs while Compton scattering generates incoherent EWs, hence the former could lead to constructive interference between EWs diffracted by the set of electrons while the latter cannot. On this basis, we while develop the constructive interference conditions for a plane EW diffracted by two electrons. Two electrons are at O and at O' the secondary EW are interfering spherical waves. In the meanwhile, let $\boldsymbol{k_{in}}$ and $\boldsymbol{k_{out}}$ be the unit vectors associated with the direction of propagation respectively

of the primary EW and secondary EW (Figure 4-1 Definition of the reciprocal space vectors.

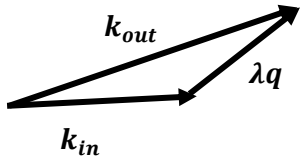

Figure 4-1 Definition of the reciprocal space vectors.

The phase difference between the secondary and primary EWs is:

$$\delta = 2\pi\, \boldsymbol{q} \cdot \boldsymbol{r} \qquad 4\text{-}5$$

where $\boldsymbol{q} = \frac{1}{\lambda}(\boldsymbol{k_{out}} - \boldsymbol{k_{in}})$, thus if the ratio $\frac{|\boldsymbol{r}|}{\lambda} \to 0$ also $\delta \to 0$ and there will not be any appreciable interference phenomena. In the case of molecular and atomic crystals $|\boldsymbol{r}|$ is the typical length of chemical bond (1-4 Å). Hence, the most suitable EWs for the diffraction of crystals are the X-rays. If there are N electrons along the path of the primary EW the total intensity scattered by the electrons is:

$$F(\boldsymbol{q}) = \sum_{j=1}^{N} f_j\, e^{2\pi i \boldsymbol{q}\cdot\boldsymbol{r_j}} \qquad 4\text{-}6$$

Where $|F(\boldsymbol{q})|^2 = \frac{I_T}{I_{eTh}}$ is the structure factor of the set of N electrons, I_T is the total diffracted intensity by the set of electrons and I_{eTh} is the intensity diffracted by a free electron. The latter is constant with an analytical expression called Thomson formula. $|F(\boldsymbol{q})|^2 = \frac{I_T}{I_{eTh}}$ is just a practical way of representing the diffracted intensity of system of electrons easily related to the experimental intensity by I_{eTh}. $f_j$is the amplitude of the wave scattered by the electrons at $\boldsymbol{r_j}$, i.e. f_j is related to the number of electrons at $\boldsymbol{r_j}$. When considering a continuum distribution of charges (i.e. an atom) equation 4-6 has the following integral form:

$$f_a(\boldsymbol{q}) = \int_V f(\boldsymbol{r}) e^{2\pi i \boldsymbol{q}\cdot\boldsymbol{r}}\, dV \qquad 4\text{-}7$$

Electromagnetic waves scattered by atoms

Although both Thomson and Compton scatterings are simultaneously occurring during the interaction between EM and atomic electrons, only the coherent intensity is relevant for the diffraction by crystals. Hence, we will focus on the calculation of the amplitude due to the Thomson scattering. In the quantum mechanical picture, an electron can be

represented by its distribution function $\rho_j(\boldsymbol{r}) = |\psi_j(\boldsymbol{r})|^2$, where $\psi(\boldsymbol{r})$ is the wave function of the j_{th} electron of an atom. In this context, the sum:

$$f(\boldsymbol{r}) = \sum_{j=1}^{Z} \rho_j(\boldsymbol{r}) dV \qquad 4\text{-}8$$

is the scattering factor of the atomic electrons at position $\mathbf{r}$. Hence, substituting equation 4-8 equation 4-7, the atomic scattering factor (or atomic form factor) is:

$$f_a(\boldsymbol{q}) = \int_V \sum_{j=1}^{Z} \rho_j(\boldsymbol{r}) e^{2\pi i \boldsymbol{q}\cdot\boldsymbol{r}} dV = \mathcal{F}[f(\boldsymbol{r})] \qquad 4\text{-}9$$

Where $\mathcal{F}[f(\boldsymbol{r})]$ represent the Fourier transform of the electron density of the atom.

Electromagnetic waves scattered by an infinite crystal

An infinite crystal can be represented by a Bravais lattice and a motif (i.e. the unit cell). The Bravais lattice is defined by a set of translation operations repeating the unit cell to map the whole crystal. The unit cell is an arrangement of atoms with symmetry properties compatible with the related Bravais lattice. In the adopted formalism a Bravais lattice is represented by a sum of Dirac deltas:

$$L(\boldsymbol{r}) = \sum_{u,v,w=-\infty}^{+\infty} \delta(\boldsymbol{r} - \boldsymbol{r_{u,v,w}}) \qquad 4\text{-}10$$

Where $r_{u,v,w}$ are the positions of the Dirac's deltas in the coordinate system u, v, w (generic lattice vector in the direct space). On the other hand, the charge density of a unit cell is (ρ_{UC}):

$$\rho_{UC}(\boldsymbol{r}) = \sum_{l=1}^{N} \sum_{j=1}^{Z} \rho_{j,l}(\boldsymbol{r}) \qquad 4\text{-}11$$

The charge density of a crystal (ρ_C) is the convolution of equations 4-10 and 4-11:

$$\rho_C(\boldsymbol{r}) = L(\boldsymbol{r}) * \rho_{UC}(\boldsymbol{r}) \qquad 4\text{-}12$$

On this ground, the structure factor of the unit cell (f_{UC}) is represented by the sum of the atomic form factor of the atoms in the unit cell:

$$f_{UC}(\boldsymbol{q}) = \sum_{l=1}^{N} f_{a,l} = \int_V \sum_{l=1}^{N} \sum_{j=1}^{Z} \rho_{j,l}(\boldsymbol{r}) e^{2\pi i(\boldsymbol{q}\cdot\boldsymbol{r})} dV = \mathcal{F}[\rho_{UC}(\boldsymbol{r})] \qquad 4\text{-}13$$

Finally, the crystal can be considered as an infinite motif. Hence, according to equation 4-13 the Fourier transform of $\rho_C(\boldsymbol{r})$ is the structure factor (F_C), namely the amplitude of the EW scattered by the whole crystal:

$$F_C(\boldsymbol{q}) = \mathcal{F}[\rho_C(\boldsymbol{r})] = \mathcal{F}[L(\boldsymbol{r})]\mathcal{F}[\rho_{UC}(\boldsymbol{r})] = f_{UC}(\boldsymbol{q_{h,k,l}}) \sum_{h,k,l=-\infty}^{+\infty} \delta(\boldsymbol{q} - \boldsymbol{q_{h,k,l}}) \qquad 4\text{-}14$$

$\boldsymbol{q_{h,k,l}} = h\boldsymbol{a}^* + k\boldsymbol{b}^* + l\boldsymbol{c}^*$is a generic vector of the lattice represented in the reciprocal space. The structure factor of a finite crystal is just the scattering factor for a unit cell in the space repeated in the space by the translation rules defined by the lattice.

Hence, the structure factor for a crystal is non-zero only in specific positions defined by the lattice .

Electromagnetic waves scattered by an infinite set of isoorientated finite crystals

Let consider a crystal with finite size and a generic form, namely the habitus. The habitus of the crystal is rigorously described by the form factor $\Phi(\boldsymbol{q})$ [81]:

$$\Phi(\boldsymbol{r}) = \begin{cases} \Phi(\boldsymbol{r}) = 1 \; when \; \boldsymbol{r} \; is \; points \; inside \; the \; crystal \\ \Phi(\boldsymbol{r}) = 0 \; when \; \boldsymbol{r} \; is \; points \; outside \; the \; crystal \end{cases} \quad 4\text{-}15$$

Thus the electron density of a finite crystal is:

$$\rho_{FC}(\boldsymbol{r}) = \Phi(\boldsymbol{r}) \, \rho_C(\boldsymbol{r}) \quad 4\text{-}16$$

Consequently the scattering for a finite crystal is:

$$F_{FC}(\boldsymbol{q}) = \mathcal{F}[\rho_{FC}(\boldsymbol{r})] = \mathcal{F}[\Phi(\boldsymbol{r})] * \mathcal{F}[\rho_C(\boldsymbol{r})] = f_{UC}(\boldsymbol{q_{h,k,l}}) \sum_{h,k,l=-\infty}^{+\infty} D(\boldsymbol{q} - \boldsymbol{q_{h,k,l}}) \quad 4\text{-}17$$

Thus the resulting scattering factor for a finite crystal can be non-zero also outside the specific points in the space defined by the lattice.

Electromagnetic waves scattered by a defective finite crystal

The effect of a random distribution of defects on a crystal structure can be described by a set of non-correlated displacements of atoms positions[82,83]. Hence for the i^{th}atom in the crystal the position is $R_i = r_{u,v,w} + u_i$. Similarly to equation **4-17**, the resulting structure factor can be non-zero also outside the specific points defined by the lattice as depicted by Figure 4-2.

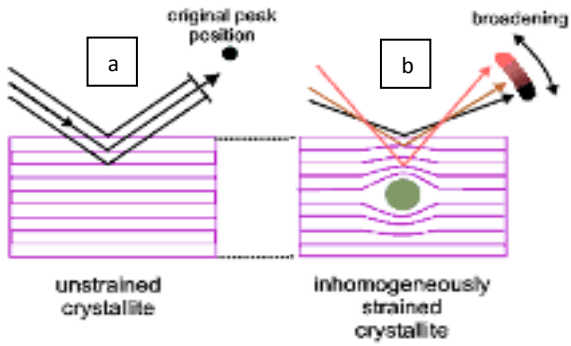

Figure 4-2 Scheme of the diffraction from (a) perfect crystal (b) randomly defective crystal

Electromagnetic waves scattered by an infinite set of finite crystals

The interaction with an infinite set of finite crystals (namely the crystallites) with different orientations can be described as all the interaction averaged over the random orientations described by three Euler's angles (ϕ_1, ϕ_2, ϕ_3). To describe the statistical weight of each orientation the orientation, its distribution function $ODF(\phi_1, \phi_2, \phi_3)$ is introduced as the volume fraction of crystallites with a certain orientation:

$$\frac{1}{8\pi^2} ODF(\phi_1, \phi_2, \phi_3) sin\phi_2 d\phi_1 d\phi_2 d\phi_3 = \frac{dV(\phi_1, \phi_2, \phi_3)}{V} \qquad 4\text{-}17$$

By definition:

$$\int_V \frac{1}{8\pi^2} ODF(\phi_1, \phi_2, \phi_3) sin\phi_2 d\phi_1 d\phi_2 d\phi_3 = \int_V \frac{dV(\phi_1, \phi_2, \phi_3)}{V} = 1 \qquad 4\text{-}18$$

For randomly oriented crystallites the $ODF(\phi_1, \phi_2, \phi_3)$ is:

$$ODF(\phi_1, \phi_2, \phi_3) = 1 \qquad 4\text{-}19$$

For a set crystallites equally oriented according to the Euler's angles $(\phi_1^f, \phi_2^f, \phi_3^f)$:

$$\begin{cases} (\phi_1, \phi_2, \phi_3) = (\phi_1^f, \phi_2^f, \phi_3^f) : , ODF(\phi_1, \phi_2, \phi_3) = 1 \\ (\phi_1, \phi_2, \phi_3) \neq (\phi_1^f, \phi_2^f, \phi_3^f) : , ODF(\phi_1, \phi_2, \phi_3) = 0 \end{cases} \qquad 4\text{-}20$$

Then in the first case the diffracted intensity is evenly distributed leading to the well-known Debye-rings, while for the second case the diffracted intensity is discrete as expected from equation 4-17. Thus, the diffracted intensity obtained from the second case it is equivalent to a single crystal.

Peaks broadening and profile analysis

The ideal interaction diffraction of a crystal is defined by the four following hypothesis:

1) non-defective crystal
2) infinite crystal
3) purely monochromatic EW
4) ideal detector

The resulted diffracted intensity would be registered by the detector at specific points. After the last paragraphs, it should be clear that the world is cruel and we none of the above hypothesis holds in real experiment. Hence, the diffracted intensity will be distributed around the points established by the ideal crystal structure. Its profile, namely the Bragg peaks' profile is determined by the following effects corresponding to each one of the hypothesis above:

1) strain of the crystallites
2) crystallites finite size
3) spectral purity of the EW
4) detector response

In the following discussion, we will assume that points 3 and 4 (instrumental effects) negligibly affect the profile of the Bragg peaks, which will be related only to the sample characteristics. The last three paragraphs developed the theoretical framework to describe the arising of sample-related broadening of the Bragg peaks profile (or Debye rings).
Intuitevely, interplanar distances close to the surface are different with respect to the interplanar distances in the bulk: this difference generates the peaks broadening. Recalling equation 4-17 for the scattering factor of a finite crystal, the contribution to the peak broadening is completely described by the term $D(\boldsymbol{q}-\mathbf{q}_{\boldsymbol{h},\boldsymbol{k},\boldsymbol{l}})$[84]:

$$F_{FC}(\boldsymbol{q}) = \mathcal{F}[\rho_{FC}(\boldsymbol{r})] = \mathcal{F}[\Phi(\boldsymbol{r})] * \mathcal{F}[\rho_C(\boldsymbol{r})] = f_{UC}(\boldsymbol{q}_{\boldsymbol{h},\boldsymbol{k},\boldsymbol{l}}) \sum_{h,k,l=-\infty}^{+\infty} D(\boldsymbol{q}-\boldsymbol{q}_{\boldsymbol{h},\boldsymbol{k},\boldsymbol{l}}) \quad \textit{4-21}$$

Similarly, the random distribution of defects changes locally the interplanar distances leading to the broadening of the peaks profile.

4.2.2. Surface X-Ray Diffraction: Theory

Diffraction from ordered surfaces

A truncated crystal can be described by a layer with finite thickness (t) and the bulk of the crystal treated as an infinite crystal. The layer has infinite sizes along two directions on the surface plane (in-plane) and finite along the direction perpendicular to the

surface plane (out-of-plane). The scattering factor of the truncated crystal can be obtained by the sum of the scattering factor from the surface ($F_S(\boldsymbol{r}^*)$) and the one from the bulk ($F_C(\boldsymbol{r}^*)$). The form factor (see 4.2.1) of the surface depends only on the components along the direction perpendicular to the surface (z):

$$\Phi(z) = \begin{cases} 0 < z < t;\ \Phi(z) = 1 \\ 0 > z\ and\ z > t;\ \Phi(z) = 0 \end{cases} \qquad 4\text{-}22$$

Hence its electron density will be:

$$\rho(\boldsymbol{r}) = \rho_{UC}(\boldsymbol{r}) * L(\boldsymbol{r})\Phi(z) \qquad 4\text{-}23$$

The scattering factor of the surface is its Fourier transform:

$$F_S(\boldsymbol{r}^*) = T[\rho_{UC}(\boldsymbol{r})]T[L(\boldsymbol{r})] * T[\Phi(z)] \qquad 4\text{-}24$$

The term $\mathcal{F}[\Phi(z)]$ is:

$$\mathcal{F}[\Phi(z)] = \int_x \int_y \int_z \Phi(z)\, e^{2\pi i(\boldsymbol{r}^* \cdot \boldsymbol{r})} dx\, dy\, dz = \delta(x^* - h)\delta(y^* - k) \int_{-\infty}^{\infty} \Phi(z) e^{2\pi lzi} dz \quad 4\text{-}25$$

The $\delta(x^* - h)\delta(y^* - k)$ term shows that the positions of the diffracted intensity in the plane is the same that the positions of the Bragg peaks. The term $\int_{-\infty}^{+\infty} \Phi(z) e^{2\pi lzi} dz$ should be elaborated a little bit more:

$$\int_{-\infty}^{+\infty} \Phi(z) e^{2\pi lzi} dz = \int_0^t e^{2\pi lzi} dz = i + sin(2\pi lt) - i\, cos(2\pi lt) \qquad 4\text{-}26$$

Considering equations 4-23 - 4-25 we easily obtain the following:

$$F_S = f_{UC}\left(\boldsymbol{r}^*_{\boldsymbol{h},\boldsymbol{k},\boldsymbol{l}}\right) \sum_{h,k,l=-\infty}^{+\infty} \delta(x^* - h)\delta(y^* - k)\, \{i + sin[2\pi(z^* - l)t] - i\, cos[2\pi(z^* - l)t]\} \qquad 4\text{-}27$$

This result shows that the intensity scattered from the surface is localized on the plane in the positions of the Bragg peaks while out-of-the plane is not. This is due to the truncation of the film which impairs the Fourier transform of the shape factor out of the plane. Hence the diffracted intensity from the surface will be equally distributed along the direction perpendicular to the surface as represented by Figure 4-3a.

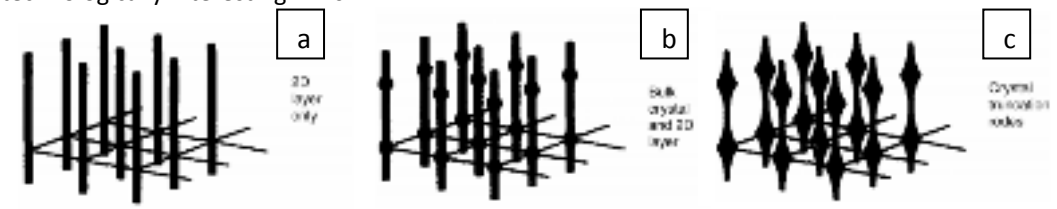

Figure 4-3 Schematic of the diffraction from a 2D layer on a truncated crystal. The 2D rods of reciprocal space are indicated as bars (a), 3D points of reciprocal space are indicated as circles (b). From Robinson and Tweet (1992)[85].

Figure 4-3b shows the point of where the Braggs peaks are located in the reciprocal space and Figure 4-3c shows the sum of the profile of the Braggs centered on the points marked by Figure 4-3b, namely, the crystal truncation rods (CTR). The diffraction from a truncated crystal is sensitive to the structure of the surface through the term $F_S(\boldsymbol{r}^*)$. The diffracted intensity of the surface can be tuned by species adsorption of species (changes the electron density of the surface), the roughness of the surface that can be thought as defective surface or modulated structures on the surface (i.e. haring bones of Au(111)). Thus, CTR are particularly sensitive to the change of the surface structure and chemistry. A simple rule of thumb the most surface sensitive positions are at the position on the CTR that is furthest from the bulk Bragg peaks, where the contribution of the bulk crystal to the diffraction is negligible[85–87].

Grazing incident

SXRD strongly employs grazing incidence geometries to enhance the ratio between the diffracted intensity from the surface and the bulk. This means that the incident beam, the exit beam, or both make a very small angle with the surface to be measured. The description of the diffraction under grazing incidence conditions falls of the kinematical theory due to the partly reflection from the surface and slight refraction as it crosses to the interior of the crystal. The effect, described by classical optics by Born and Wolf (1999)[88], is negligible until the incidence angle becomes comparable with the critical angle for total external reflection, (a few tenths of a degree for most situations). In this cases, only an evanescent wave continues inside with a K vector parallel to the surface. This reduces the penetration depth of the EW down to the order of 10–20 nm.

Six circles diffractometer and detector

A 6-circles diffractometer configuration is considered an excellent instrumentation to perform SXRD at a synchrotron source[89,90]. Compared to a ''2+2 configuration'' (2 circles for the sample and 2 circles for the detector)[91], the redundancy of a 6-circle configuration allows much easier sample alignment and scanning of the incident and outgoing beam directions. A specific argument in favor of the redundancy of 6-circles diffractometer for the electrochemical operando SXRD experiment is that an electrochemical cannot be rotated freely from the vertical position. The axes of reciprocal space are chosen to lie along convenient directions within the reciprocal lattice of the substrates. Commonly two axes are chosen to be laying on the plane of the sampled surface (in-plane), whereas the third direction is assumed to be perpendicular to the same surface (out-of-plane).

The diffracted intensity has been registered by means of a MAXIPIX fast readout areal detector[92]. This areal detector hosts a grid of 1024x1024 pixels dived on four Si wafers. The diffracted intensities collected by the detector have been treated off-line using the Binoculars package: this procedure enables a correct evaluation of the Bragg peak intensities and the meshing in the reciprocal space of the detector responses[93–95]. A typical arrangement is presented in Figure 4-4:

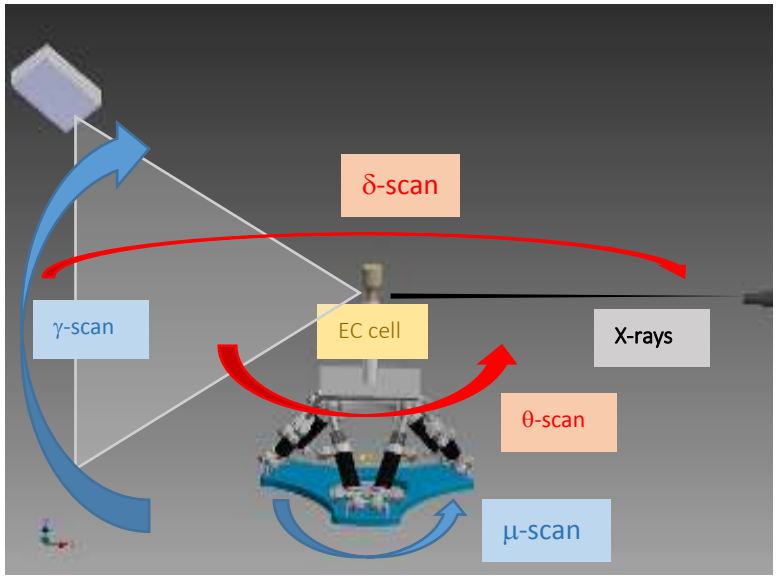

Figure 4-4 *This is a typical SXRD setup involving an hexapod for positioning and moving the sample. The arrow represent the main movement used to collect data, the red*

arrow are on the plane and the blue are out of the plane. μ and θ move the sample while γ and δ move the detector.

Orientation of the electrodes

The diffracted intensity has been collected in a space parameterized with respect to a coordinate system referred to the surface unit cell of the Ag (111) substrate. According to this convention, the correspondence between the standard fcc bulk Ag unit cell and the metric of the surface pseudo-hexagonal cell (a_1, a_2, c, α, β, γ)- where a_1 and a_2 vectors lay on the sample surface, while c is perpendicular to that surface- is determined by the following relations:

$$\alpha = \beta = 90° \qquad 4\text{-}28$$

$$\gamma = 120° \qquad 4\text{-}29$$

$$|c| = \sqrt{3}a_0 \qquad 4\text{-}30$$

$$|a| = |b| = \frac{a_0}{\sqrt{2}} \qquad 4\text{-}31$$

Where a_0 is the lattice parameter of the cubic fcc cell of Ag. Having adopted this convention for the a_1, a_2 and c vectors, the reciprocal space is parameterized by the fundamental reciprocal vectors of the pseudohexagonal Ag structure, a_1*, a_2* and c*. Where a_1 and a_2 are respectively the $[½ \; -½ \; 0]$ and the [0 ½ −½] standard fcc vectors and define the plane parallel to the sample surface (referred as "in-plane") and c is the the standard fcc [1 1 1] vectors and perpendicular to the sample surface ("out of plane"). Any vector in the reciprocal space is represented by the h, k and l coordinates, respectively, corresponding to the vectors component along the a_1^*, a_2^* and c^* axis, distances in the same space are expressed using reciprocal lattice units (rlu).

Peaks profiles analysis

One of the first successful attempt of peaks profile analysis was carried out by Scherrer[96]. He assumed that the whole profile is described by a Gaussian function and that its width is inversely proportional only to the finite size of the crystallites. Successively, this approach was evaluated as underestimating the size of strained crystallites[97].

Warren and Avenbach[98] reported the first successful general description of the diffraction peaks broadening by means of a method based on the Fourier decomposition of multiple independent peaks. This method does not assume any functional form for the peak profiles and it provides the contribution of both size and strain effects. Even if this method can be considered, the most rigorous to describe the peaks broadening, its

need for several independent peaks often impairs its use, especially when the exploration of the reciprocal space is limited by experimental conditions.

A simplified method can be obtained, if the functional form of the profile is assumed. Among others, one of the most used is the Voigt single line profile analysis proposed by Langford[99]. Moreover, exploiting modern setups, especially at synchrotron sources, we can safely assume that only the sample has a non-negligible contribution to the broadening of the peak. In this context, the effects of size and strain distribute the diffracted intensity according to Lorentzian and Gaussian functions respectively. On this ground, the profiles of the peaks are well described by the convolution of Lorentzian and Gaussian functions, namely, the Voigt function:

$$V_{A,wG,wL,x_c}(x) = A\int_{-\infty}^{\infty} \frac{e^{-\frac{(t-x_c)^2}{2wG^2}}}{wG\sqrt{2\pi}} * \frac{wL}{\pi(x-x_c-t)^2+wL^2}\, dt \qquad 4\text{-}32$$

A is the area of the function, x_c center of the function, wG is the Gaussian width and wL is the Lorentzian width. There are several approximations known to compute and fit $V_{A,\sigma,\gamma,x_c}(x)$, still those are different with respect to the widely used Pseudo-Voigt function defined by a weighted sum of one Lorentzian and one Gaussian functions. $V_{A,\sigma,\gamma,x_c}(x)$ can rewritten in the form:

$$V_{A,\sigma,\mu,x_c}(x) = A\frac{\int_{-\infty}^{\infty} \frac{e^{-t^2}}{\mu^2+\left(\frac{x-x_c}{\sigma}-t\right)^2}dt}{\int_{-\infty}^{\infty}\frac{e^{-t^2}}{\mu^2+t^2}\,dt} \qquad 4\text{-}33$$

Where σ is proportional to the Gaussian width and μ to the ratio of Lorentzian and Gaussian widths:

$$wG = 2\sqrt{ln(2)}\,|\sigma| \qquad 4\text{-}34$$

$$wL = 2|\sigma|\mu \qquad 4\text{-}35$$

This form of the Voigt function enables to compute it according to the numerical approximation proposed by Wells and Olivero[100,101]. Equations 4-34 and 4-35 clearly show the correlation between wG and wL, hence the fit resulting from this method have to be carefully considered. Specifically, in case of strong correlation the error can be overestimated. This algorithm has been implemented in the Origin and Fytk softwares used to fit the profile of the peaks in this thesis[102].

According to Langford[99] the wG and wL are related to crystallite size and strain through the following equations:

$$\epsilon = \frac{\lambda}{wG} 4\, tan\theta \qquad 4\text{-}36$$

$$D = \frac{\lambda}{wL} cos\theta \qquad 4\text{-}37$$

Where ϵ is the wavelength of the EW, $\epsilon = \left\langle \frac{\Delta(r_i - r_j)}{(r_i - r_j)} \right\rangle$ is the average crystallites' strain, D is the average size of the crystallites and θ is the Bragg angle.

4.3. X-Ray Reflectivity

X-ray reflectivity is the analysis of the reflected beam as resulting from the interaction between the surface and the X-ray at very low incident angle. It can deliver information on the thickness and density of the layers in a layered thin film as well as the roughness of the interfaces.

4.3.1. X-Ray Reflectivity: Theory

Reflectivity at interfaces

The EW propagating in a medium is reflected and refracted when reaching the interface with another medium. The reflection and refraction phenomena are related by the Snell's law:

$$n \cos\theta = n' \cos\theta' \qquad 4\text{-}38$$

Where n, n' are the refraction indexes of the two media and θ, θ' are the angles represented in Figure 4-5:

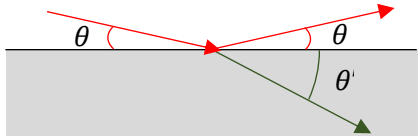

Figure 4-5 Schematic of the reflection and transmission of a EW from an interface between two different phases.

For an incident beam with high enough energy (i.e. every X-ray beam) the refraction index is always lower than 1 and $\theta' < \theta$. Consequently, at a certain angle (θ_C) the refracted intensity is zero. The refractive index of the medium is related to the electron density of the interaction volume by the following equation 4-39:

$$n = 1 - \delta + i\beta \qquad 4\text{-}39$$

Where $1-\delta$ describes the contribution of the dispersion and β the absorption effect occurring during the interaction between the EW and the surface. These components are related to the electron density by the following equations 4-40 and 4-41:

$$\delta = \left(\frac{r_e \lambda}{2\pi}\right) \frac{N_0 \rho}{M} 10^{-2} \sum_i x_i f_i' \quad 4\text{-}40$$

$$\beta = \left(\frac{r_e \lambda}{2\pi}\right) \frac{N_0 \rho}{M} 10^{-24} \sum_i x_i f_i'' \quad 4\text{-}41$$

Considering r_e the classic radius of the electron (2.818 10^{-5} Å), λ the wavelength of the EW (Å), N_0 is the Avogadro constant, ρ the density of the material, M is the molar mass of the material, $x_i$is the fractional molar amount of the i^{th} atom with scattering factor $f_i'$and f_i''. On this ground, the critical angle is:

$$\theta_C = \sqrt{2\delta} \quad 4\text{-}42$$

Reflectivity of homogeneous layered materials

The reflection of X-Rays on layered and ideally flat surfaces gives a reflectivity profile whose features are related to multiple reflection on the interfaces lying on the optical path of the X-Ray beam. The intensity profile is defined by the interference of all the reflected beam crossing the surface as depicted in Figure 4-6:

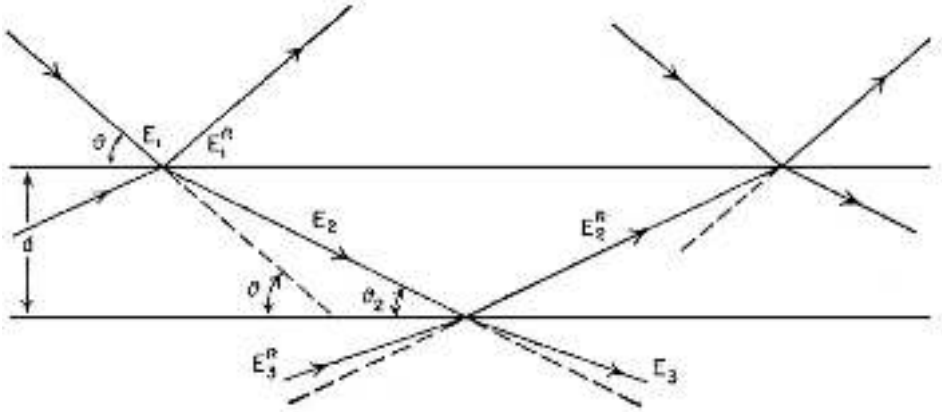

Figure 4-6 Scheme of the multiple reflection occurring in a layered surface E_1, E_2 and E_3 are the EWs propagating respectively in medium 1,2 and 3 while $E_{R,1}$, $E_{R,2}$ and $E_{R,3}$ are the EWs reflected by the corresponding interfaces.

The reflectivity is usually computed as the ratio between the amplitude of the EW reflected and the amplitude of the incident beam:

$$R = \frac{||E_1||}{||E_R||} = \sqrt{\frac{I_1}{I_R}} \quad 4\text{-}43$$

where $||E_R||$ is the amplitude of the interference signal involving all the reflected beams (i.e. in Figure 4-6 $E_R = E_{R,1} + E_{R,2} + E_{R,3}$). In this context, the function $R = R(\theta)$ can be defined according to a recursive formula describing the reflectivity at the J^{th} layer R_j:

$$R_j = \frac{R_{j+1}+F_j}{R_{j+1}F_j+1} a_j^4 \quad 4\text{-}44$$

considering:

$$F_j = \frac{g_j - g_{j+1}}{g_j + g_{j+1}} \quad 4\text{-}45$$

$$a_j = e^{-i\pi g_j d_j} \quad 4\text{-}46$$

$$g_j = n_j sin\theta \quad 4\text{-}47$$

$$g_{j+1} = \sqrt{n_{j+1}^2 + n_j^2 cos\theta} \quad 4\text{-}48$$

Where d_j is the thickness of the j^{th} layer and F_j is called the Fresnel coefficient. In the case of an infinitely thick substrate the recursive formula cannot be used to calculate the reflectivity of the interface between the last layer of the film and the substrate (R_n) which is:

$$R_n = F_n a_n^4 \quad 4\text{-}49$$

Starting from equation 4-50 the recursive formula 4-44 can be used for each layer and finally to obtain the S to take into account the roughness of the interfaces, the Fresnel coefficient can be corrected:

$$F_j = \frac{g_j - g_{j+1}}{g_j + g_{j+1}} e^{\left(-\frac{8\pi g_j g_{j+1}\sigma_{j+1}^2}{\lambda^2}\right)} \quad 4\text{-}50$$

Where σ_{j+1}^2 is the surface roughness estimated as the root mean square of the heights of the interfaces.

4.3.2. X-Ray Reflectivity: Experimentals methods

The operando XRR curves obtained can be exploiting the same setups of the SXRD measurements when changing the μ and γ accordingly. Their interpretation is carried by fitting the reflectivity measurements with a layered model of the sample surfaces calculated with specific software based on the theory explained in paragraph 4.3.1.

Figure 4-7 shows the dependence of the simulated reflected intensity of a Cu_2S thin film (50 Å) on top of an Ag substrate. The amplitude of the oscillations depend mainly on the difference between the density of the materials composing the film and the density of the substrate. Moreover, the density of the film changes also the critical angle for the total reflection (Figure 4-7(a)). Otherwise, the thickness modulates the period of the oscillations (Figure 4-7(b)). Specifically, it is evident that thicker the film smaller the period of the oscillations.

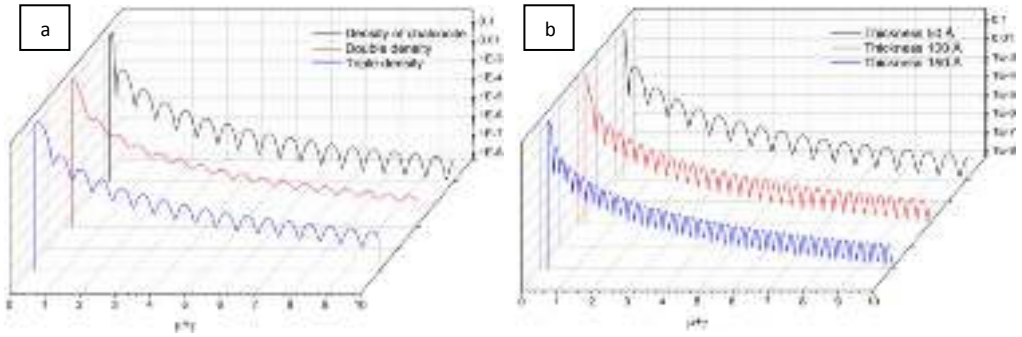

Figure 4-7 Reflectivity curves simulated for different density (a) and thickness of the overlayer (b). Simulated with GenX [103].

Figure 4-8 shows the effect of both the overlayer and the substrate interface on the reflected intensity. In both cases higher the roughness to thickness ratio more the damping of the oscillations. The effect of the overlayer interface roughness (Figure 4-8(a)) is higher than the substrate interface roughness (Figure 4-8(b)).

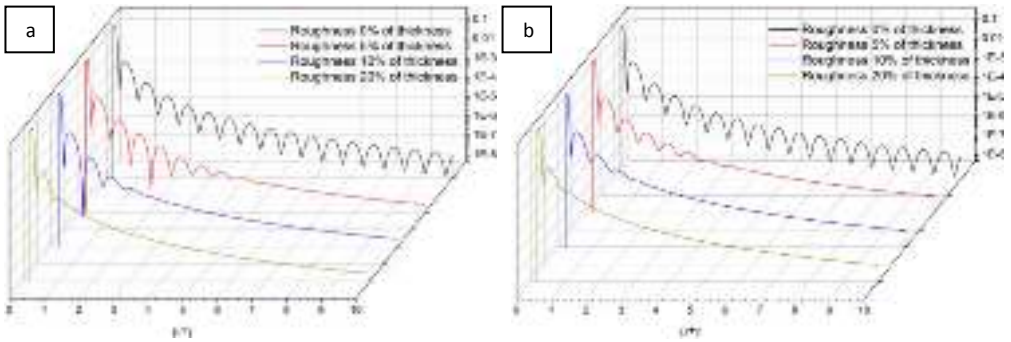

Figure 4-8 Reflectivity curves simulated for different roughness of the overlayer (a) and of the interface with the substrate (b). Simulated with GenX [103].

4.4. Operando experimental setups

In this paragraph I will present the electrochemical flow cell specifically design to perform E-ALD operando experiment with synchrotron light (Table 4-1):

Label	Characteristics	Year
EC2006	Deeply buried electrode	2006
EC2017	Thin layer	2017

Table 4-1 Summary of the operando electrochemical cell used in this thesis.

4.4.1. Standard EC for operando experiment (EC2006)

The thin-layer cells usually involved in electrochemical operando experiments are design and realized with replaceable elastic window, usually made of Mylar, ensuring the maximum transmission but disabling the exchange of solutions needed for the E-ALD process. In order to overcome this limitation, in 2006 Foresti et al.[104] designed a cell with suitable windows and flow channels enabling the fast exchange of the solutions without impairing the SXRD measurements. The working electrode sealed the cell in the bottom part of internal vessel. The body of the cell is directly fastened to the sample holder of the diffraction beamline front end. This setup resulted particularly convenient for the alignment of the electrode surface and for exposure to the X-ray radiation. The cell can be in principle built with Teflon, Kelef or other chemically resistant plastics. During the last years several materials has been tested for this cell and polyether ether ketone (PEEK) became the standard for our SXRD measurement due to its resistance to hard X-ray radiation and higher machinability. However, PEEK suffers for the presence of some crystalline domains and without an adequate design of the cell walls, the powder and amorphous patterns from the cell windows can hinder the X-ray signal from the sample itself. As depicted by Figure 4-9, the internal vessel is a cylinder with an internal diameter of 6.7 mm and a height of 40 mm. The working electrode on one side and the counter electrode on the other side delimited the electrochemical cell volume (1.5 mL). The inlet and the outlet for the solutions were placed on the side walls of the cylinder. The counter electrode used for our measurements is a glassy carbon cylinder, and the reference electrode made of a small Ag/AgCl (KCl sat) and placed in the outlet pipe. The attenuation of the X-rays along the path for an SXRD experiment can be estimated considering the absorbed radiation through a typical optical path as reported in Figure 4-9. Considering an incident angle with the electrode very close to 0°, Figure 4-10 reported different thickness and material for the X-ray window in the cell, maintaining a optical path in the electrolyte in the different setups taken into consideration. The X-ray

beam propagates through two plastics walls and roughly 10 mm of solution. For the first CdS experiment, the cell was made of Teflon, with wall of 1 mm[104] while for the experiment on the Cu_2S growth the cell was made of PEEK with a wall of 100 μm. At 20 keV, for the EC2006 setup Figure 4-10 reports an overall transmission across the X-ray windows and electrolyte of roughly 40%, which is well matching the data reported in literature (50%)[104]. PEEK ensure a lower attenuation of diffracted signal[105].

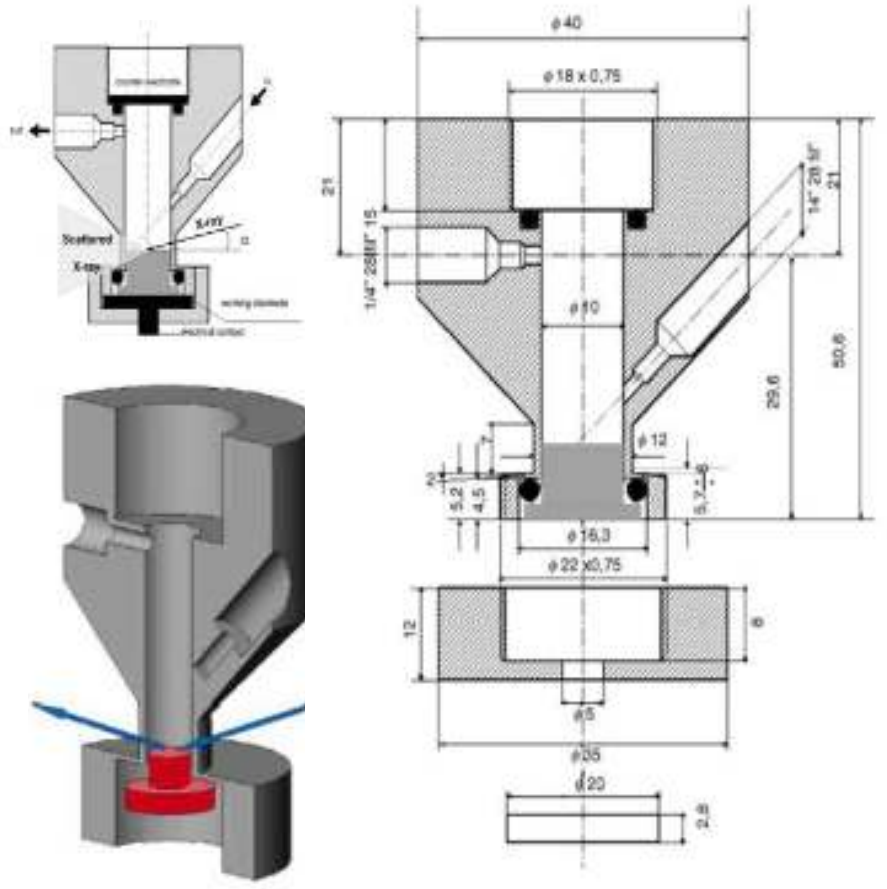

Figure 4-9 Technical specification for the operando electrochemical flow cell EC2006.

Moreover, PEEK windows can be reduced to 100μm thanks to its better mechanical properties. Hence, as depicted in Figure 4-10, this setup ensure a transmission very close to 70% at 24 keV. It is worth to notice that PEEK has a strong X-ray diffraction, reducing the thickness of the X-ray window by a factor of 10, makes completely undetectable the signal diffracted by PEEK.

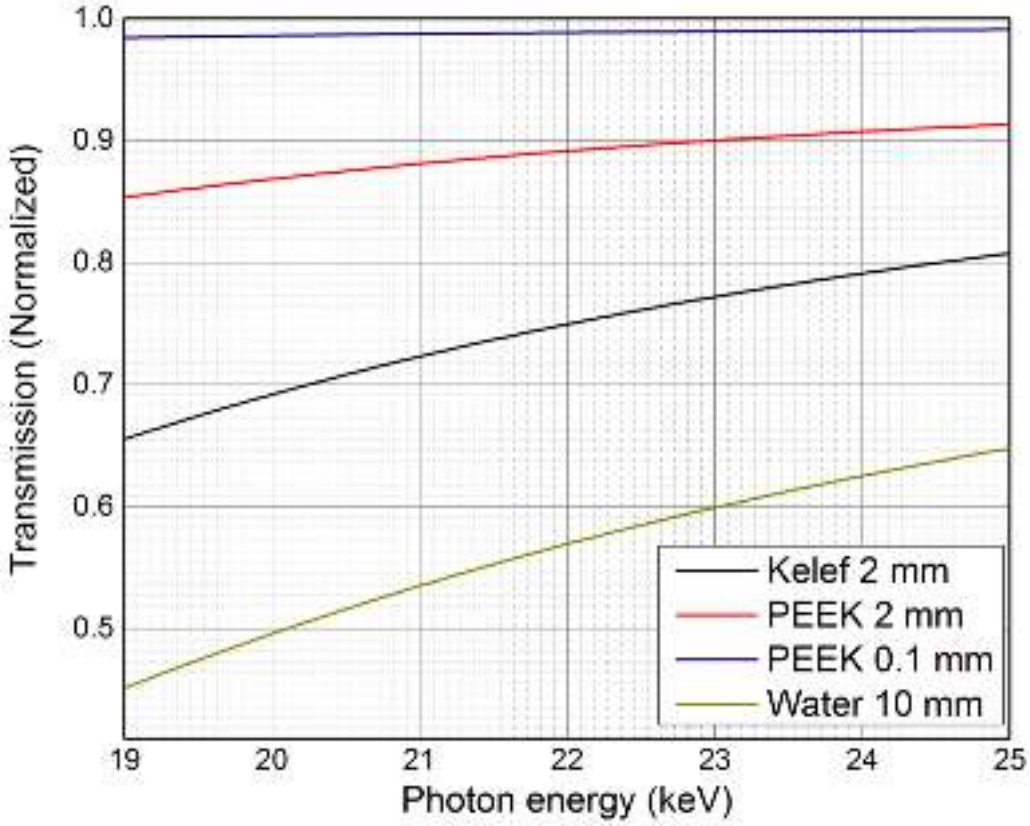

Figure 4-10 *Transmission of X-ray at different energy through different surfaces* [105].

4.4.2. Novel thin layer EC flow cell for operando experiment (EC2017)

Although the electrochemical flow cell specifically designed for operando SXRD allowed several successful experiments it showed its limitations in detecting diffracted intensity from a few atomic layers of deposit, especially when enriched in lighter elements. As it will be reported in the paragraph 5.1, we encountered this problem for the acquisition of SXRD data on the first stages of the growth of Cu_2S, while for CdS data have been acquired from the first cycles of growth[104]. To overcome this issue, we designed a new thin-layer flow electrochemical cell aiming to reduce the optical path in solution. The new design of the thin layer cell is reported in Figure 4-11:

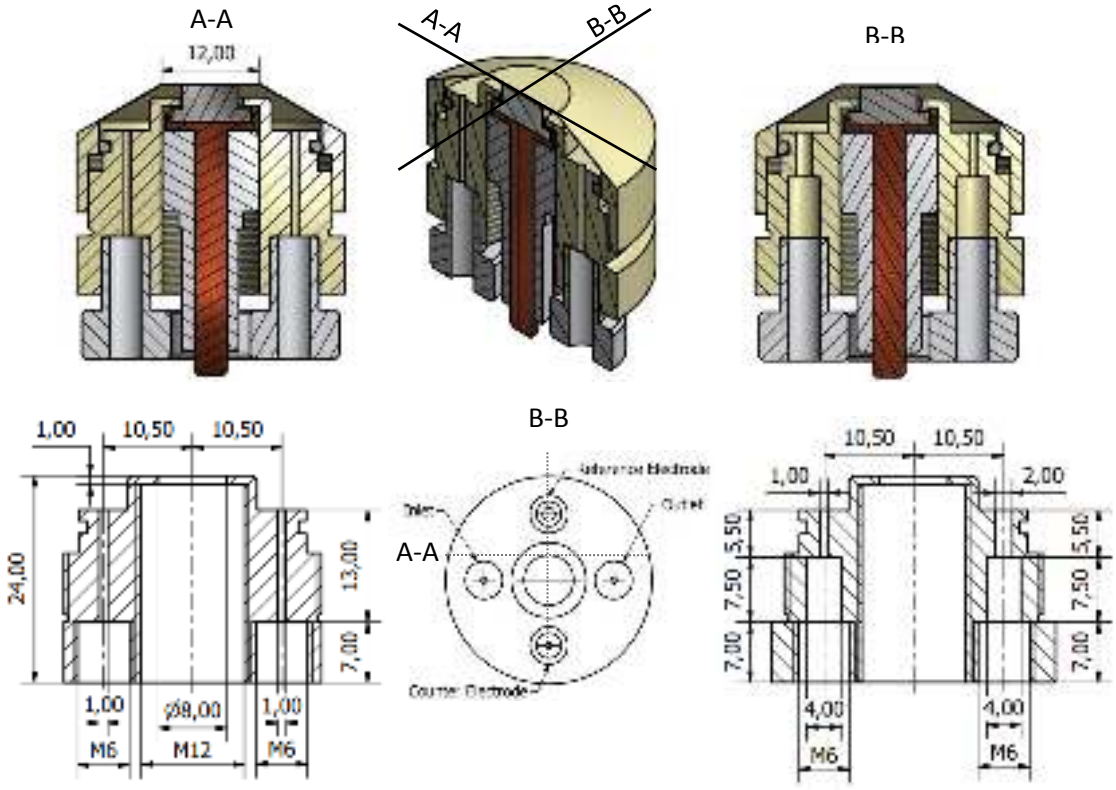

Figure 4-11 Technical specification for the operando electrochemical flow cell EC2017.

The cell consists of 2 blocks, the head and the body with one screw to hold the working electrode and 4 fittings to hold the counter/reference electrodes and the inlet/outlet tubes. The electrolyte occupies a small disk with an internal diameter of 12 mm while the height can be tuned by means screwing the threads between the external shell and the main block. The electrochemical cell is delimited by the reference electrode on one side and the counter electrode on the other side. The inlet and the outlet for the solutions were placed on the side walls of the cylinder. The counter electrode is a glassy carbon cylinder, and the reference electrode is made of a thin Ag wire (0.3 mm) coated with AgCl in saturated KCl solution. Considering an incident angle with electrodic surface of 10°, the X-ray beam propagates for roughly 80 μm in solution, while with the EC2006 design the optical path in solution is 10.15 mm. These are the conditions making the EC2017 setups outperforming the EC2006 setup. For very low values of the incident (μ) and take off (γ) angles the two setups work comparably well, with the EC2006 design slightly outperforming the EC2017 setup by 2.5% at μ=γ=1°. Figure 4-12 compares the transmission of the two setups at 24 KeV for a typical XRR (μ=γ) and SXRD (μ=0.1°) measurements for different values of γ. Strictly regarding the XRR measurements, most

information about the reflectivity is acquired for $\gamma = \mu < 3°$, hence the two setup works comparably well. However, for the SXRD at 10° it ensures a 15% improvement on the transmitted signal with respect to the old one.

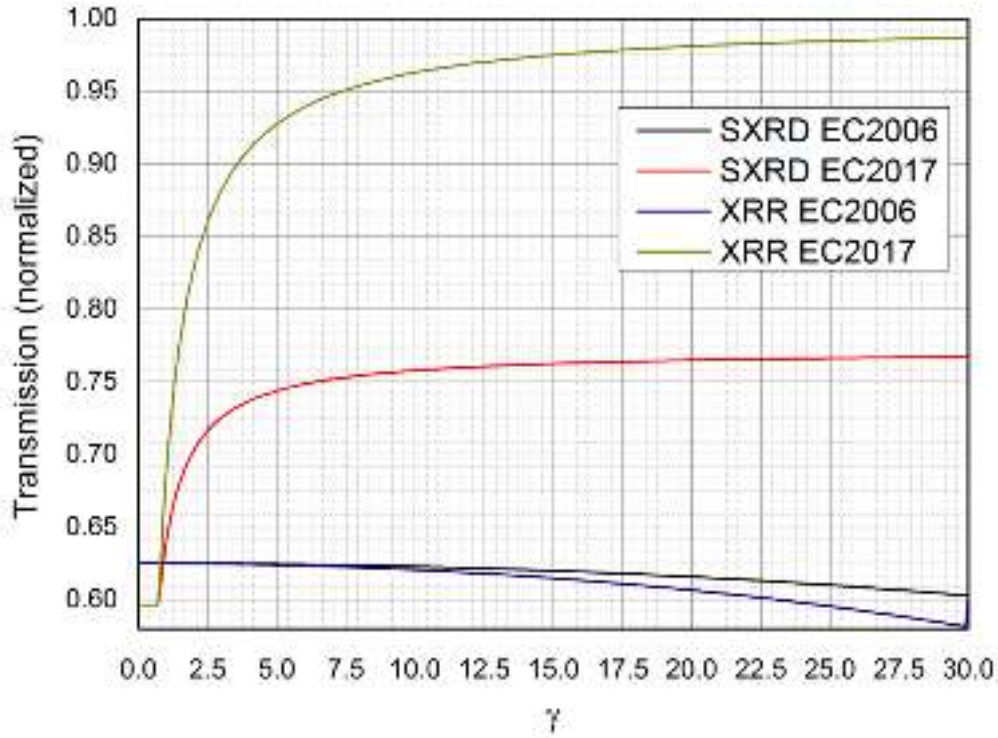

Figure 4-12 Transmission of X-ray at different γ angles for a typical XRR and SXRD experiments for both electrochemical flow cell EC2006 and EC2017 [105].

4.5. Chemical speciation modelling

We performed our calculation under the *phreeqc* formalism[106], taking into account aqueous species equilibria in a reference database. The solid phases are considered through dissolution/precipitation reactions, and their stability is reported as the logarithm of equilibrium constant of formation (log K) at standard temperature and pressure condition (i.e. 25°C and 1.0132 bar) from the master species[107,108]. Only one master species is associated to each element or element valence state (for instance Fe^{3+} for ferric iron), one to the hydrogen ion, one to water and (formally) one to the aqueous electron. The master species are the "building blocks" used in the *phreeqc* formalism to write all chemical equations: they are related to the secondary species, in fact, by means of formation reactions involving the master species as a reactant (e.g. $Cu^{2+} + e^- = Cu^+$, S^{2-}

= S + 2 e^- etc.) and the relative equilibrium constant logarithms are included in the calculation (as a function of temperature). These species are present in a single phase, an aqueous solution. On this ground, the aim of the *phreeqc* formalism is the definition of a system of algebraic homogeneous equations describing the equilibrium conditions for different thermodynamics variables such as the activities of aqueous species (including water), ion-exchange species, surface-complexation species, gas-phase components, solid solutions, pure phases, aqueous charge balance, gas-phase equilibria and ionic strength. Such algebraic system is assembled taking into account all the residual functions (denoted by *f*) describing the relevant equilibria. The residual functions are defined as the difference between a global constant and the combination of specific variables for each species or phases. Hence, for each set of values of the thermodynamics variables, defining a certain state of the system, the residual functions describe the "distance" of the state from the equilibrium. On this basis, the equilibrium condition corresponds to the set of values for the thermodynamics variables that let all the residual functions equal to zero. To compute the results, each residual function is reduced to contain a minimum number of variables (called the unknown masters), so that the number of functions equals the number of variables. The unknown masters for aqueous solutions are the natural log of the activities of master species ($\ln a_m$), the natural log of the activity of water ($\ln a_{H_2O}$), the ionic strength (μ), and the mass of solvent water in an aqueous solution (W_{aq}). The system is then computed and solved by means of the Newton-Raphson technique, which proceeds through the assembling of a Jacobian matrix containing the derivatives of the residual functions by the unknown master. Thus, this matrix describes the thermodynamics of the multi-equilibria system and its diagonalization leads to the equilibrium conditions. The analytic expression of each residual function and of the related derivatives has been developed and implemented in the *phreeqc* software. For instance, the equilibrium between the aqueous phase and pure solid phases is described under the following assumptions:

1) The activity of the pure phase is 1.0
2) The additional unknown master for each pure solid phase is the mole of the pure phase present in the system (n_p where p refers to the p^{th} phase)
3) The mass-action law holds

Under this assumptions the pure phase equilibria are described by the mass-action law:

$$K_p = \prod_m^{M_{aq}} a_m^{C_{m,p}} \qquad 4\text{-}51$$

Where K_p is the equilibrium constant with the p^{th} phase, $c_{m,p}$ is the stoichiometric coefficient of the aqueous master species (positive if the product of the desorption

reaction and negative otherwise), a_m is the activity of the m[th] species (it is an unknown master). Eventually, M_{aq} is the number of aqueous master species. On this basis a new residual function can be defined:

$$f_p = \ln K_p - \sum_m^{M_{aq}} C_{m,p} \ln\ a_m \qquad 4\text{-}52$$

The total derivative of the residual function in terms of the unknown master is:

$$df_p = \sum_m^{M_{aq}} c_{m,p}\ d \ln a_m \qquad 4\text{-}53$$

Chemical speciation in aqueous solutions is not uniquely defined but depends on the theoretical formulation of mass-action equilibria and activity coefficients (e.g. Davis, Pitzer or Debye-Huckel activity model)[106]; in other words, the numerical solution of the system is model-dependent. In some cases, aqueous speciation can be analytically determined, but operational definitions and assumptions are still unavoidable. Accordingly, the equilibrium is computed with a reaction-path calculation, i.e. a sequence of mass-transfer calculations that follows defined phase (or reaction) boundaries during incremental steps of reaction progress. In this study, the considered gas species, i.e. $H_{2(g)}$ and $O_{2(g)}$, are computed defining the corresponding partial pressures, and in the database are present the dissolution reactions (e.g. $O_{2(g)} = O_{2(aq)}$) and the corresponding constants. Accordingly, the presence of oxygen or hydrogen in any redox reaction is linked to their partial pressures. These latter are monitored as the result of an evolving chemical system in any given thermodynamic conditions.

4.5.1. Modelling of the predominance charts

In the present study, the relationships between the main phases of the compositional field (involving always an aqueous solution) are studied through the use of Eh versus pH (or "*Pourbaix*") diagrams, calculated according to the point-by-point mass balance method [23,35]. Under this approach, the predominant charts are computed identifying the predominant species at each given point of potential and pH, taking into account other variables such as presence of ligand(s), temperature and pressure[35]. The predominant species is identified as the one with the highest content (absolute amount) of the considered element, without any discrimination between aqueous and solid species.

We performed our point-by-point mass balance calculation under the *phreeqc* formalism [106]. Aqueous species equilibria are taken into account in a reference database file that include also aqueous complex formation. The solid phases are considered in the same database through dissolution/precipitation reactions, and their stability is reported as the logarithm of equilibrium constant of formation (log K) at standard temperature and pressure condition (i.e. 25°C and 1.0132 bar) from the master species[107,108].

The considered gas species, i.e. $H_{2(g)}$ and $O_{2(g)}$, are computed defining the corresponding partial pressure, and in the database are present the dissolution reactions (e.g. $O_{2(g)} = O_{2(aq)}$) and the corresponding constants. Accordingly, the presence of oxygen or hydrogen in any redox reaction is linked to their partial pressure. The latter and can be the result of an evolving chemical system or used to constrain the redox potential. The distribution of dissolved components among free ions, ion pairs, and complexes, namely the aqueous speciation, is obtained by solving simultaneously all the equilibria selected from the database. For example, dissolved Cu in the aqueous environment can be present as $Cu^{2+}_{(aq)}$, $Cu^{+}_{(aq)}$, $Cu(OH)_2$, etc.; among them, $Cu^{+2}_{(aq)}$ act as master species, while the others are defined as secondary species by means of formation reactions from the master species (e.g. $Cu^{2+} + 2OH^- = Cu(OH)_2$, $Cu^{2+} + e^- = Cu^+$, etc.) and their equilibrium constant logarithms (as a function of temperature) are included in the calculation. These species are present in a single phase, an aqueous solution.

Aqueous speciation is not uniquely defined but depends on the theoretical formulation of mass-action equilibria and activity coefficients (e.g. Davis, Pitzer or Debye-Huckel activity model)[106]. In other words, it is model-dependent. Some aqueous speciation assemblages can be analytically determined, but operational definitions and assumptions are still unavoidable. According to this consideration, the equilibrium is computed with a reaction-path calculation, i.e. a sequence of mass-transfer calculations that follows defined phase (or reaction) boundaries during incremental steps of reaction progress. To solve the system that arise writing down all the involved reaction for aqueous and gas species and solid phases, the model proceeds through the creation of a Jacobian matrix that starts from the master species of the involved elements (Cu, Zn, Sn, C, O and H) and contains all the involved reactions. The matrix representing the chemical system is diagonalized, obtaining the concentrations that satisfy the simultaneous solutions to all the considered equilibria. Numerical models for the chemical speciation require comprehensive thermodynamic databases.

For this purpose, it is necessary to mention that the thermodynamic properties of the chemical species relevant to our models are already present in the *phreeqc* wateq4f.dat database [109].

4.5.2. Modelling of the E-ALD process

In order to clarify the thermodynamics of the concurrent reactions possibly underlying the E-ALD process, it is useful to stress the definition of its fundamental blocks. To this aim, the example reported in Figure 4-13 and Table 4-2 refers to the growth Cu_xZn_yS. The deposition of an atomic layer and the subsequent renovation of the buffer solution in the electrochemical cell (for instance the first two rows in Table 4-2) at room pressure and temperature, are labelled as E-ALD steps. The E-ALD cycle is the basic repeating unit of the E-ALD process (for instance the first eight row in), in the sense that every E-ALD cycle is a defined sequence of E-ALD steps. Table 4-2 reports the potential and the solution involved in the part of the E-ALD process modeled in this work, while Figure 4-13 depicts the time span of the same part of the process.

#Cycle	# Step	E-ALD steps	Conc. (mM)	Time (s)	Pot (V)
1	**1**	**Na_2S/ Buffer**	**0.5**	**60**	**-0.68**
		Buffer	**N/D**	**60**	**-0.68**
	2	**CuCl2/ Buffer**	**0.5**	**120**	**-0.38**
		Buffer	**N/D**	**60**	**-0.38**
	3	**Na2S/Buffer**	**0.5**	**60**	**-0.68**
		Buffer	**N/D**	**60**	**-0.68**
	4	**$ZnSO_4$/ Buffer**	**0.5**	**120**	**-0.85**
		Buffer	**N/D**	**60**	**-0.85**
2	5	Na_2S/ Buffer	0.5	60	-0.68
		Buffer	N/D	60	-0.68
	6	$CuCl_2$/ Buffer	0.5	120	-0.38
		Buffer	N/D	60	-0.38

Table 4-2 The first 8 rows, in bold, constitute the periodic part of the E-ALD process for Cu_xZn_yS.

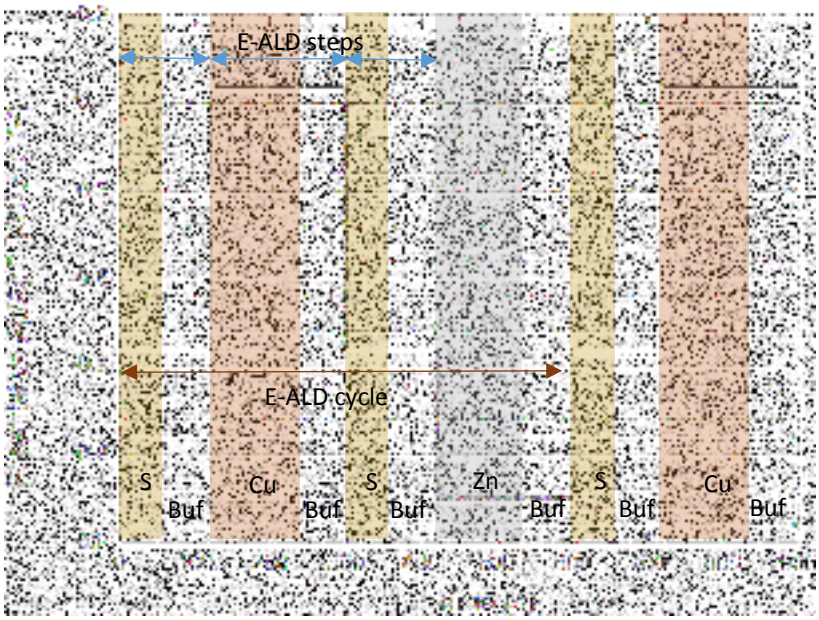

Figure 4-13 Time span of the part of the E-ALD process considered in this work. The blue and brown arrows highlight the E-ALD steps and cycles, respectively. S represent the presence of the Na_2S solution inside the electrochemical cell, B the buffer solution, Cu the $CuCl_2$ and Zn the $ZnSO_4$ solutions.

The deposition of the first Sulfur adsorbed atomic layer (briefly S-adlayer) on the Ag(111) surface requires some observations: 1) in the S-adlayer, since the surface cell of the Ag-S interface includes 3 sulfur and 6 silver atoms [48], the apparent stoichiometry of the surface is Ag_2S. Such stoichiometry corresponds to the mineral acanthite [61]. 2) an excess of free energy, corresponding to the estimation of the surface excess of free energy obtained by Aloisi et. al [48], is needed to model the deposition step of the S-adlayer. Thus, the modelling procedure was carried out as follows:

a) Modelling of the formation of the S-adlayer by precipitation of Ag_2S (acanthite) driven by the additional surface free energy.
b) Modelling of the subsequent steps using the thermodynamic data for the bulk phases. As a starting condition of each step, we considered the amount of solid phases obtained at the equilibrium of the previous step in contact with fresh solutions under the proper potential.

The solution is changed, between two following E-ALD steps, while keeping a constant applied potential. This part of the process is intrinsically dynamic, and its rigorous modelling would require including the transport properties and the kinetics of the chemical process involved. However, in order to assure a complete change of the chemical environment inside the electrochemical cell, the volume of fluxed solution is

several times the volume of the cell (roughly 30 times). Then, every equilibria leading to the dissolution of a solid species would be extremely favorited by the fluxing of the solution. Conversely, in the modelling of E-ALD, the solution, volumes are kept constant at the value of the cell volume, thus largely underestimating the effect of the dissolution processes. This calculation is referred as *constant volume model*. A further calculation can be carried out under the assumption that the moderately soluble phases are completely dissolved while fluxing the washing solution: this model overestimates the effect of the dissolution processes. This last calculation is referred as *total depletion model*. In this context, it is evident that the *total depletion model* has to be defined after having identified the most soluble species in the *constant volume model*.

4.6. Scanning Electron Microscopy

4.6.1. Scanning Electron Microscopy: Theory

The Scanning Electron Microscopy (SEM) exploits the interaction between the surface of a sample and a focused electron beam (constituted by the Primary Electrons – PE). The latter can be deflected to scan the surface and recover a raster representation of the morphology. With respect to optical microscopy SEM has a higher field depth and lower theoretical Abbe limit (4 nm against 250 nm). The interaction of the electron beam with the surface leads to the emission of different signals collected by means of different detectors:

- Secondary Electrons (SE)
- Back-Scattered Electrons (BSE)
- X-rays
- *Auger* Electrons (AE)

SE are generated by the deflection of PE due to the interaction with the electronic density down to 50 nm below the surface. Thus, the collection of SE reproduce the sample's morphology. The intensity of the SE signal is related to the atomic number.

BSE have energy well higher than 50 eV coming from the multiple and single scattering of PE with the atoms of the samples. This signal is more sensitive to the average atomic number than the SE signal[110].

A fraction of the X-rays collected in a SEM measurement is generated by the relaxation of an excited state induced by the ionization of an atom by means of the interaction of the PE with the core electrons. The other fraction of X-rays is due to the slowing of the PE when interacting with the surface leading to the *Bremsstrahlung,* which Is a white emission of X-rays.

AE are electron generated by the relaxation of an excited state induced by the ionization of an atom by means of the interaction of the PE with the core electrons.

The interaction of the electron beam with the surface of an insulator lead to the accumulation of charge density on the sampled spot. In this condition focusing the electron beam on the sample becomes impossible. Hence, the SEM cannot be implemented directly for an insulating surface. In these cases, the best practice is to coat the sample with a conducting material such as gold or graphite. Exploiting the sputtering-coating techniques the morphology of the surface is essentially unchaged.

4.6.2. Scanning Electron Microscopy: Experimental setup

A typical SEM is constituted by the following:

- source of the PE
- electromagnetic lenses
- deflection coils
- focusing lens
- signal detectors

Interestingly, the cheaper source is just a tungsten filament emitting the PE due to the thermoionic effect. The PE are accelerated by a potential usually in the range 1-30 kV.

The focusing lens is responsible of the reduction of the beam diameter down to 0.01-20 μm depending on the setup.

The deflection coils deflect the beam to interact with different spots on the surface concurring to the scan of the morphology of the sample's surface.

During the measurement the SEM acquisition chamber is kept under ultra high vacuum condition.

4.7. X-ray photoelectron spectroscopy

4.7.1. X-ray photoelectron spectroscopy: Theory

X-ray photoelectron spectroscopy (XPS) exploits the detection of photoemitted electrons due to the absorption of monochromatic X-rays. Electron photoemission occurs only when the energy of the incident radiation is higher than the workfunction of a certain orbital:

$$\phi = h\nu_t \qquad 4\text{-}54$$

The energy excess is the kinetic energy of the photoemitted electrons:

$$h\nu = \phi + \frac{1}{2}m_e v^2 \qquad 4\text{-}55$$

m_e and v are the electron mass and speed. The electronic kinetic energy is E_k and it is directly measured during and XPS experiment. Thus the bonding energy that the detected electrons had in the orbital (E_b) can be reckoned by means of the following:

$$E_b = h\nu - E_k - w \qquad 4\text{-}56$$

w is an experimental correction factor due to the XPS setup.

Usually the photoemission process is described by means of a three steps mechanism [111]:

1. Absorbance of the X photon and emission of the electron
2. Migration of the electron through the solid matrix
3. Expulsion of the electron through the surface

During step 1 the X rays are usually able to penetrate form several μm, hence large part of the sample is involved in the photoemission process. However, step 2 and 3 of the mechanism are crucial for the effectively detected photoelectron, in the sense that during the migration and expulsion the photoelectron interacts with the solid matrix and with a very high probability is absorbed. Hence, the auto-absorption process allows to detect photoelectrons only if coming from 1-20 nm under the surface of the sample.

XPS spectrum can be used to obtain both quantitative and qualitative information on the sample. A wide range XPS spectrum is usually a low resolution (1-2eV) plot of the

count per second against the bonding E_b tipically in the range 0-1250 eV. Wide range spectra are useful tools to perform a qualitative analysis. The qualitative analysis it is not restricted to the determination of the elemental composition of the surface but also the oxidation states of the elements present in the sample can be identified. Often, differences in valence electrons and bond type change the bonding energy (chemical shifts) by several units of electronvolt. Another very useful analysis of the wide range spectra is to find the most informative subranges (usually 5-10 eV wide). These, can be exploited to acquire high resolution (<1 eV) spectra, which are necessary to perform a quantitative analysis.
On this regard, we have to take into account that each element can have several orbitals with E_b in the scanned energy range. Thus, it is quite common to have superposition of peaks associated with different elements. Hence, not always the primary peaks (most intense) can be used to perform a quantitative analysis.

4.7.2. X-ray photoelectron spectroscopy: Experimental setup

XPS spectrometer are mainly constituted by the following:

- X-ray source
- analyzer
- detector

The most common X-ray sources at the lab-scale are the Coolidge tubes with aluminum or magnesium targets and suitable filter to obtain a monocromatic radiation. Typically, such sources have a very small bandwidth are in the range of 0.8-0.9 eV.

The analyzer is device constituted by collecting lens enabling the separation of the electrons by means of their kinetic energy (Figure 4-14). More specifically the electromagnetic lens deflects the electron forcing them to follow a curved trajectory towards the detector. The radius of the curved trajectory is dependent on the kinetic energy of the electrons.

The most commonly used detectors are multichannel solid state trasductors constituted by glass tube doped with lead or vanadium. This particular setup enables the contemporary acquisition of photoemitted electrons of different energy allowing a fast acquisition of the spectra[110].

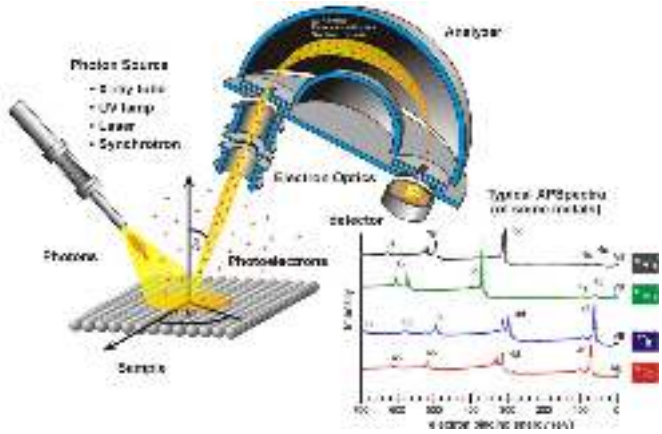

Figure 4-14 Experimental setup and some typical wide range XPS spectra.

5. Results and discussion

5.1. Ag(111)/Cu_2S

5.1.1. Preparation of the samples and analysis

The samples have been prepared according to the synthesis developed in our laboratory by Bencistà et al.[24]. Table 5-1 presents the electrochemical synthesis performed for this study.

Label	Method	Deposition sequence
OpCuS10	*E-ALD operando at ESRF*	*$Ag/(S/Cu)_{10}/S$*
OpCuS60	*E-ALD operando at ESRF*	*$Ag/(S/Cu)_{60}/S$*
ExCuS	*E-ALD ex-situ at UNIFI*	*$Ag/(S/Cu)_{60}/S$*

***Table 5-1** list of the electrochemical synthesis presented in this paragraph.*

We first adopted the cell EC2006 cell to gather information about the position of the main peaks and to follow their changes during the growth. However, to study the early E-ALD cycles we were forced to adopt the EC2017 cell in order to follow the main peaks during the growth of Cu_2S. The following paragraphs report the results according to the growth stages of the film and not to the time of their collection.

The following paragraphs report the results according to the growth stages of the film and not the history of their collection.

5.1.2. Operando analysis of the growth

As reckoned from the following experiments, the position of the most intense peak (0.73, 0.73, 2.09) provides the ideal position for the analysis of the growth. Hence, we followed the first stages of the growth recording small 3D maps centered on this position in the reciprocal space parametrized as presented in paragraph 4.2.3. To ensure the detectability of the signal from the first cycles of growth, we exploited the improved design of the electrochemical cell (EC2017) for the first 10 cycles. Figure 5-1 shows the projection of the 3D maps on the h-k plane. Figure 5-2 shows the same 3D maps projected on the h-l plane, in this case the 3D plot is proposed to highlight the signal diffracted out of the plane. Figure 5-2 shows that at 2^{th} cycle the diffracted signal is not a Bragg peak but probably a CTR fading in the background.

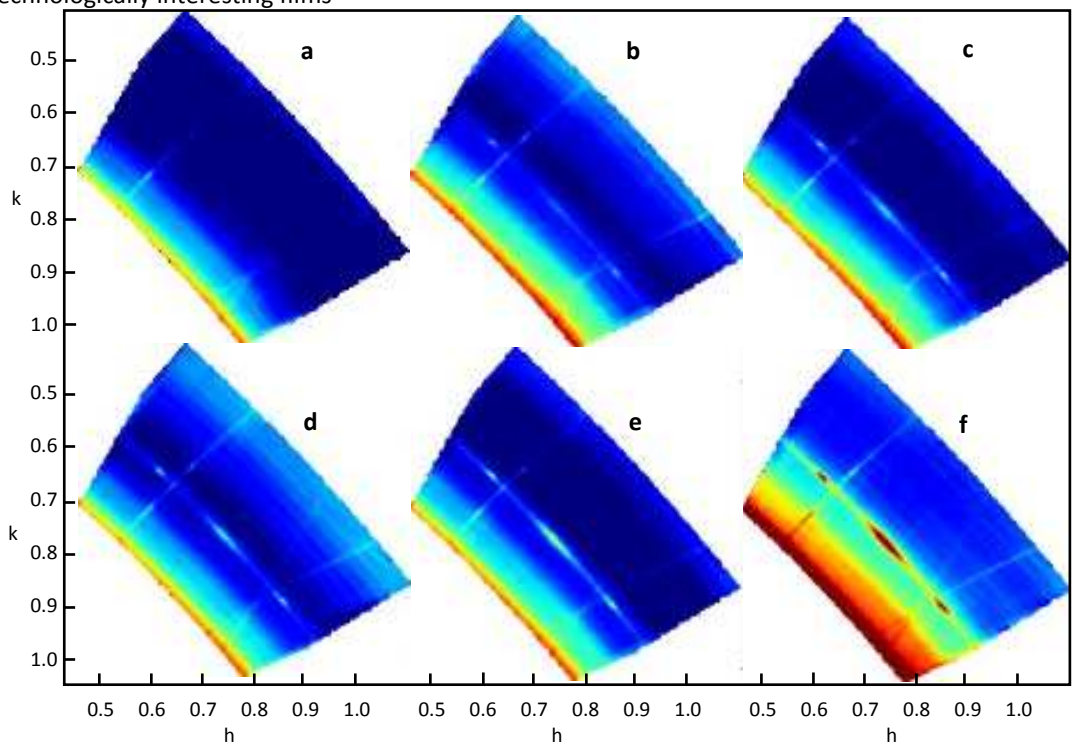

Figure 5-1 2D reciprocal space maps on the plane at 0 (a),2 (b),4 (c),6 (d),8 (e) and 10 (f) growth cycles.

As previously stated, from the 12th cycle onward the results have been collected using the EC2006 setup. Finite size fringes, characteristic of very well defined thicknesses and of abrupt interfaces, are not visible neither in the l scan crossing the Bragg peak nor in any extended XRR measurement. This is an indication for a quite rough growth, in agreement with the morphological analysis (paragraph 5.1.5) and the XRR analysis.

Starting from the 12th cycle the profiles of the Bragg peak along the *l* and *h=k* reciprocal directions have been registered (Figure 5-3). The peak is very sharp along the in-plane *h=k* direction (full width at half maximum, FWHM, ~0.02 h *rlu*). As discussed in paragraph 4.2.3 the profiles of the Bragg peaks can be described by the convolution of a Gaussian profile with a Lorentzian profile. The best fit is obtained fixing the Gaussian width to the value of 0.005 rlu resulting in a narrow Lorentzian width (Figure 5-3a). The latter clearly indicate a quite large crystallites size while the former suggests a quite small number of defects, keeping the concentration constant during the growth.

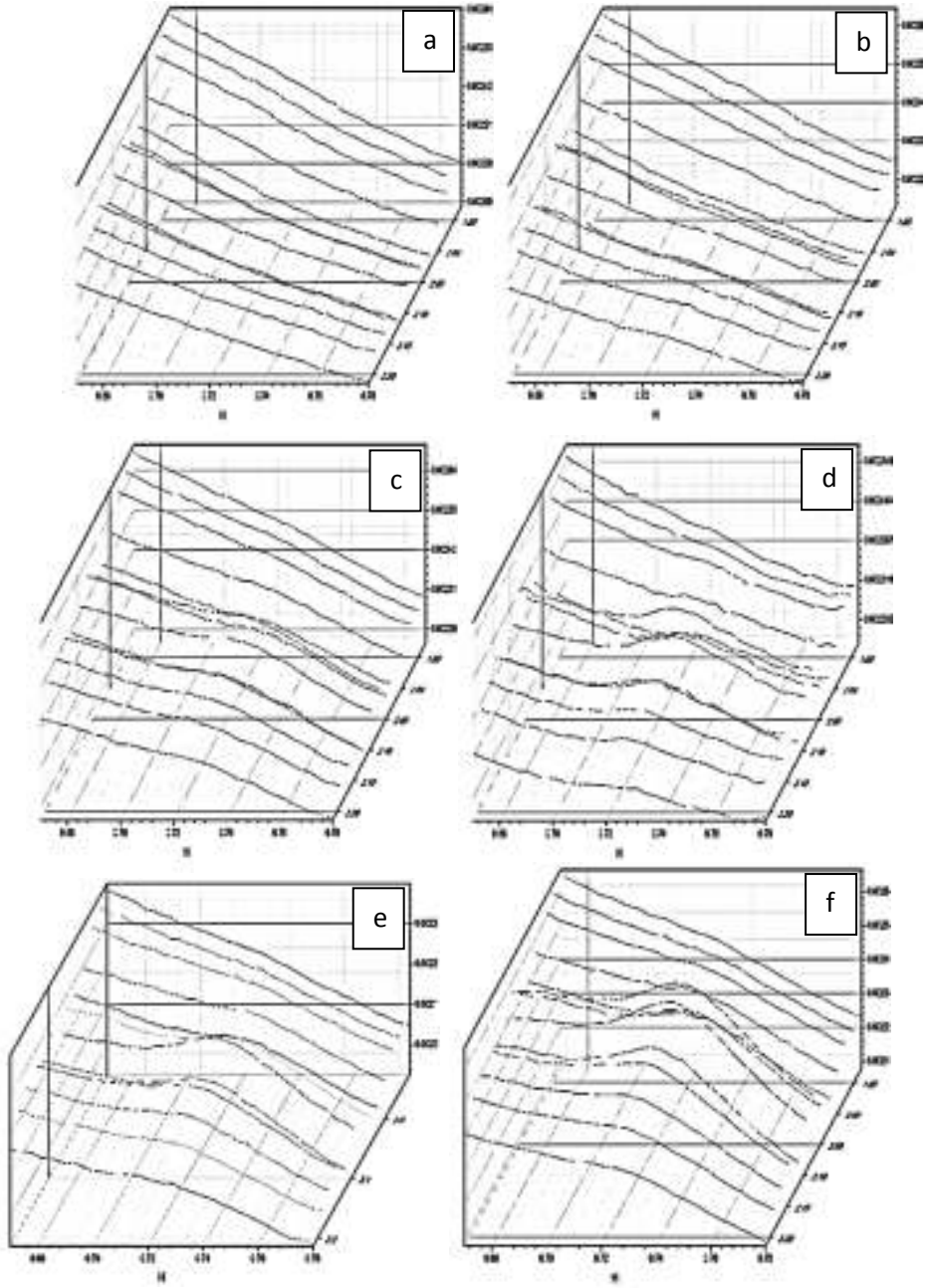

Figure 5-2 *Projection on the a^*, c^* plane. The use of 2D maps is not suitable to show the intensity along the c^* direction at (a) 0, (b) 2, (c) 4, (d) 6, (e) 8 and (f) 10 E-ALD cycles.*

Figure 5-3b show that the profile along *l* is broader (FWHM ~0.1 *l rlu*) and better fitted by means of a Lorentzian function since the contribution of the Gaussian width to the

Voigt function is negligible. Hence, the profile along the *l* direction is determined by the finite size of the film, while the contribution of the crystallite strain cannot be reckoned.

The results of the best fit at different stages of the growth is reported in Figure 5-4, providing several information on the evolution of the structural features of the film.

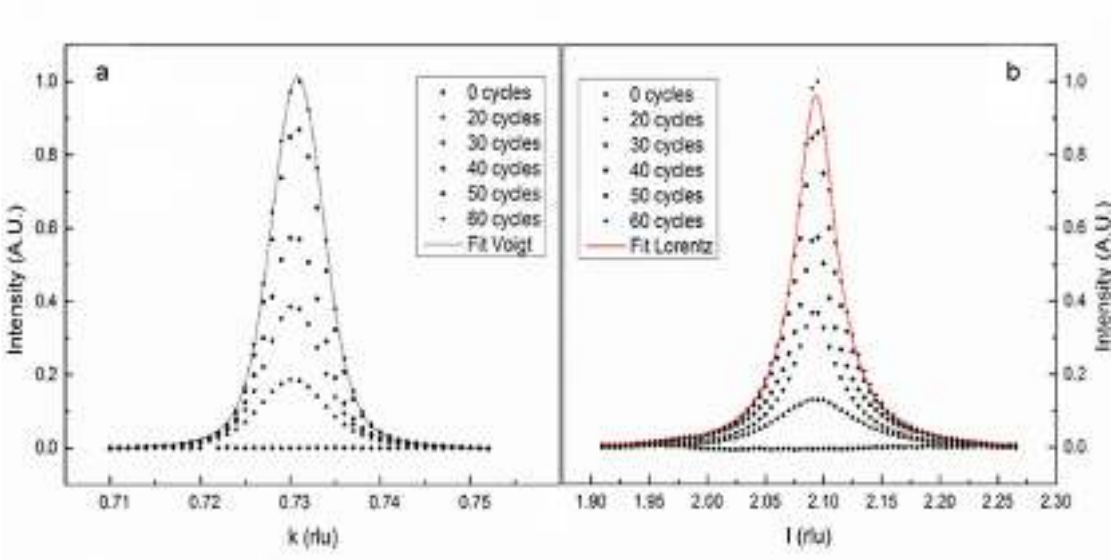

Figure 5-3 *Scans along (h, h, 2.09) (a) and along (0.73, 0.73, l) (b) at different stages of growth.*

Figure 5-4a and Figure 5-4b show that between the 12th and 18th cycle the position of the Bragg peak is not well defined, the data seem indicating that the structure is quite stressed with an expanded in-plane lattice parameter and compressed out-of-plane one. Then the structure is set starting from the 20th, with a small increase of the position along the out-of-plane direction. However, the cell volume is constant along all the observable growth process from 18 deposition cycles onward (Figure 5-5).

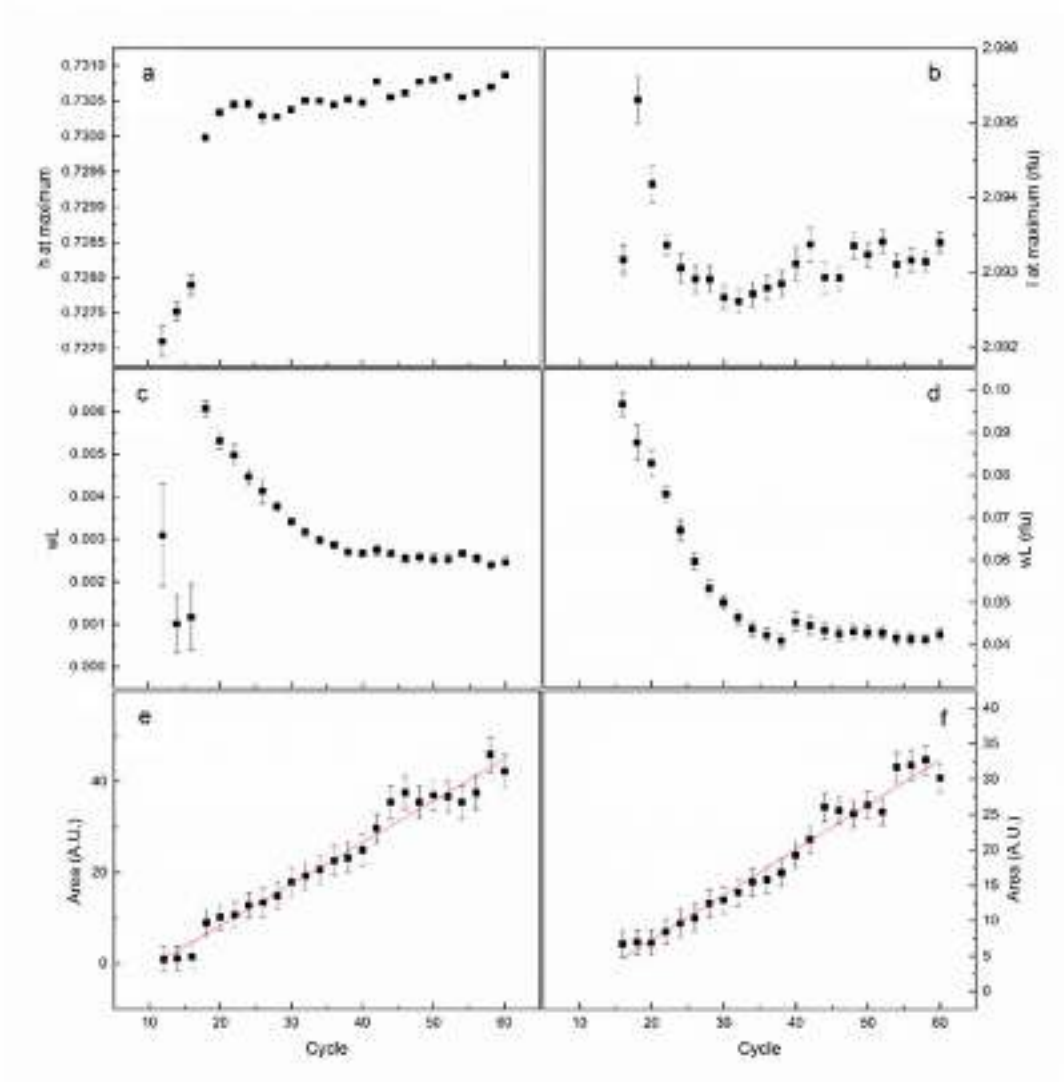

Figure 5-4 *Growth curves for the position at the maximum of the peak, for the Lorentzian breadth (wL) and for the peak area along (h, h, 2.09) (a,c,e) and along (0.73, 0.73, l) (b,d,f), respectively. The experimental uncertainties are plotted as error bars corresponding to 3σ.*

Figure 5-4c and Figure 5-4d depict the Lorentzian widths versus the growth cycles along the in-plane and out-of-plane directions, respectively. The plots in Figure 5-4e and Figure

5-4f show that the amount of deposited material goes linearly with the deposition cycles and no saturation is present.

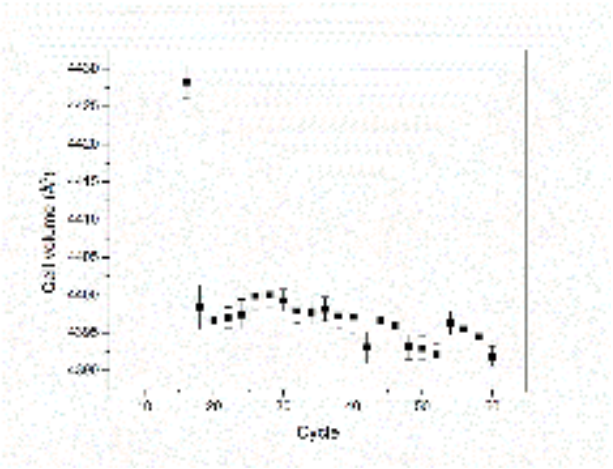

Figure 5-5 *Cell volume in Å^3 during the growth of the film. The experimental uncertainties are plotted as error bars corresponding to 3σ.*

5.1.3. Operando analysis at the end of the growth

At the end of the growth the reciprocal space maps of the grown films measured in the *hk* planes at different *l* values are shown in Figure 5-6. They have been operando recorded keeping the electrode at the potential of -0.680 V in buffer solution. The maps show a number of well-defined diffraction peaks arranged according to an apparent pseudohexagonal symmetry (Figure 5-6). The *a* hexagonal cell parameter can be estimated in 27.76 Å, considering the shortest distance between two adjacent Bragg reflections in the map. Interestingly, the unitary vectors of this pseudohexagonal pattern are rotated by 30° with respect of the chosen pseudohexagonal silver frame (Figure 5-6). The most intense Bragg reflections, among those registered in our collections, occur at (0.73, 0.73, l), (0.73, 0, l), (0, 0.73, l) and at position characterized by doubling the h and/or k values. This suggests that one of the most relevant structural fragments has a 3.96 Å periodicity, which closely corresponds to the S-S distance in the CuS_3 triangular groups, identified as building units in all the $Cu_{2-x}S$ structures. Our data are thus consistent in showing that the Cu_2S films grown by E-ALD have strong similarities to the chalcocite structural arrangement. However, the (h,k) maps of Figure 5-6 definitely point to the occurrence of a new crystal structure.

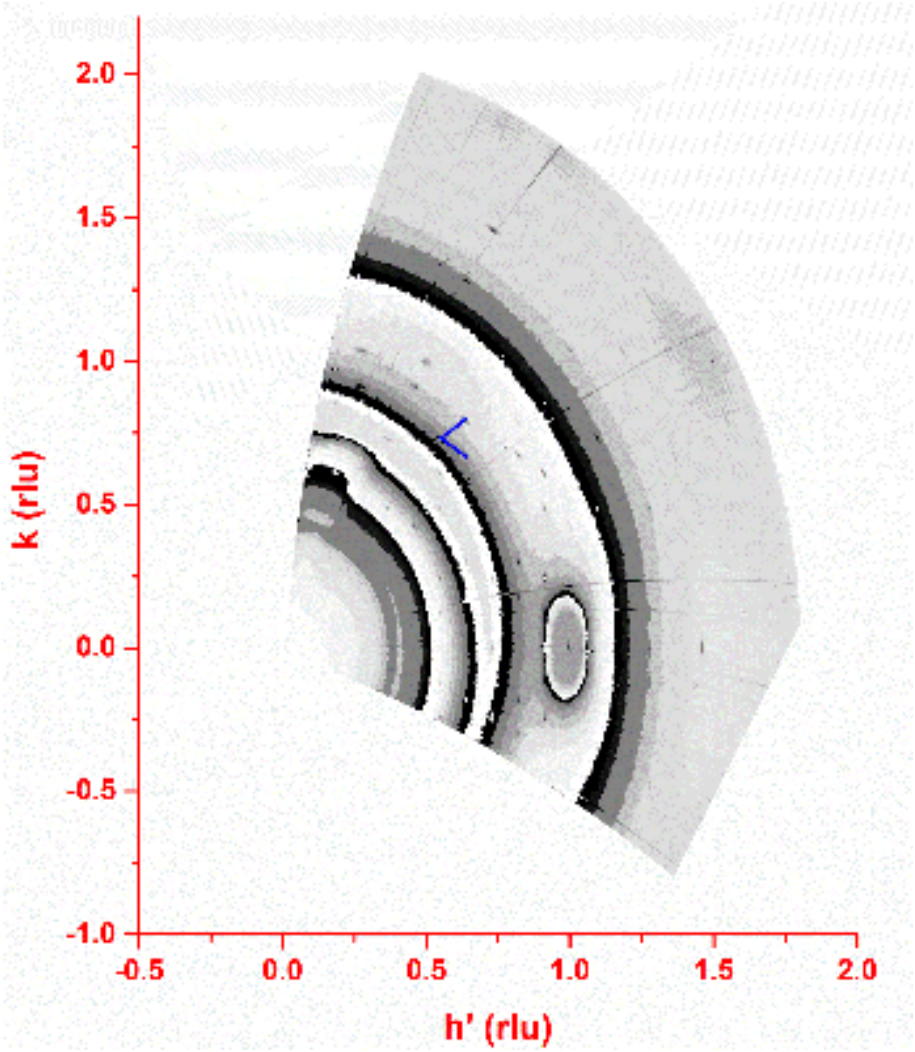

Figure 5-6 (h,k,1.05) reciprocal space map of the thin film. Units are expressed in the metrics of the pseudohexagonal silver lattice. The h' values are related to the h values by the relation: h' = h + k cos 60°. The blue segments are the unitary vectors of the hexagonal periodicity of the diffraction effects of the film.

To confirm this, we projected the pseudo-orthorhombic unit cell, derived from the known structure of low chalcocite, normal to the c* direction (not shown). The measured diffraction pattern looks very different from the expected low chalcocite structure even assuming the presence of multiple domains induced by the pseudo 6-fold symmetry of the top Ag(111) surface. The present data strongly support the occurrence of a new phase in the Cu_2S-CuS join, characterized by an in-plane periodicity based on of 7x7 triangular CuS_3 units of the hexagonal-close-packed sulfur framework. A detailed

refinement of its structure is prevented because the present set of reflections is not large enough, and because of the interference of the diffuse scattering from the solution.

The XRR curves have been collected in the same condition at the end of the growth and the fitted with the following stack model: Water/High density layer/Substrate (Table 5-2). Figure 5-7 shows the XRR experimental data and the related best fits. Consistently with the roughness reckoned by Bencistà et al. [24] interference fringes cannot be present in the XRR scan impairing the direct determination of the total thickness of the film. However, the fit suggests the formation of a film with an optical density slightly lower than theoretical density (0.0219A^{-3}), high roughness and a very low roughness at the Cu_2S/Ag(111) interface.

		Model 1		
Roughness of the substrate	(Å)	3.25	±	0.02
Thickness of the bottom layer	(Å)	18,84	±	0.08
Density of the bottom layer	($Å^3$)	0.0178	±	0.0001
Roughness of the bottom layer	(Å)	6.54	±	0.08
Thickness of the top layer	(Å)	-		-
Density of the top layer	($Å^3$)	-		-
Roughness of the top layer	(Å)	-		-

Table 5-2 Result of the fit of the XRR data using the stack model 1.

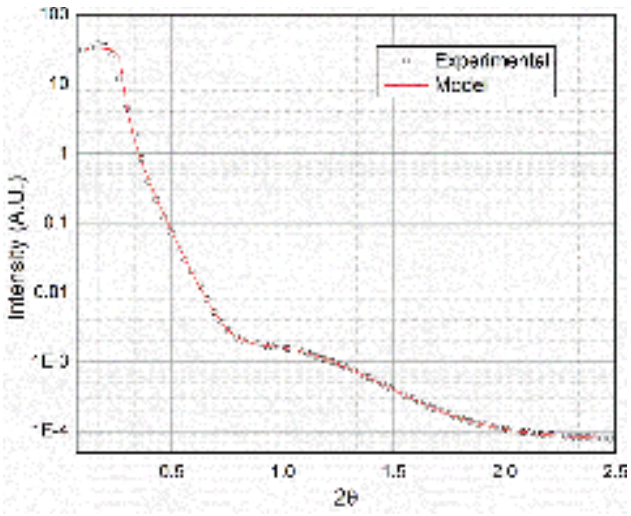

Figure 5-7 Comparison of the experimental XRR data (open circles) and the model used to fit it (continuous lines).

5.1.4. Ex-situ analysis at the end of the growth

A mention about the structural stability of the films has to be made. The removal of the electric potential, applied to the working electrode, leads to a structural transition (Figure 5-8a and Figure 5-8b). This transition results reversible when the pristine electric potential value is re-set up (Figure 5-8c).

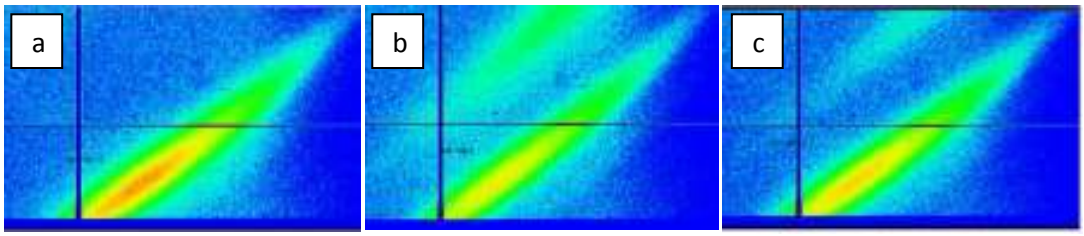

Figure 5-8 the evolution of the (0.73, 0.73, 2.09) peak when the voltage is removed. Corresponding the potential referred to the subfigures are chronologically arranged: (a) -0.680V, (b) open circuit potential and (c) -0.680 V.

The reciprocal space maps in Figure 5-9 were acquired after removing the sample from the electrochemical cell and putting the electrode on the sample holder of the diffraction beamline. When compared with the maps of Figure 5-6, the appearance of further other ordered phases due to removal of the sample from the electrochemical cell is clear. Figure 5-10a and 5-10b depict a small area reciprocal space map of OpCuS60 centered at (0.66, 0.25, 2.09) respectively ex-situ and operando.

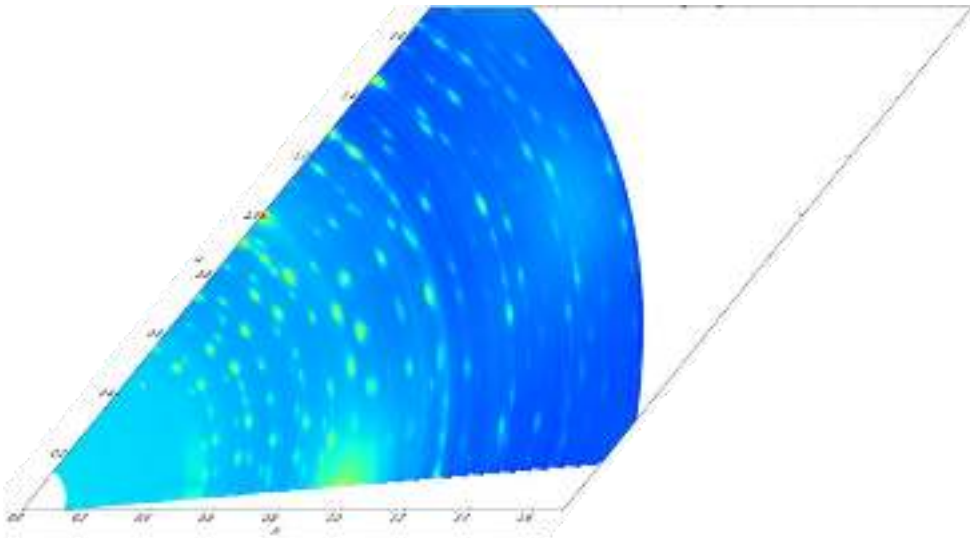

Figure 5-9 Large area reciprocal space map at l=1.05 for ex-situ OpCuS60.

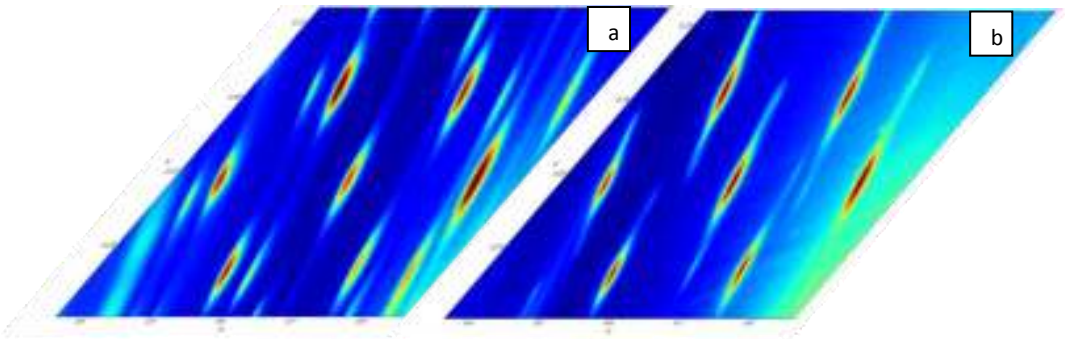

Figure 5-10 Small area reciprocal space map centered at (0.66, 0.25, 1.05) for OpCuS60 (a) operando and (b) ex-situ.

5.1.5. Micromorphology and semi-quantitative analysis

The micromorphology and semiquatitative analysis has been carried on the ExCuS sample. The micrographs in Figure 5-11 show that the Cu_2S surface is characterized by two main morphologies:

- a flat surface with some holes
- several small worm-like structures overgrowing the flat surface

The worm-like structure are randomly distributed and the reach easily the micrometric scale. Still, they seem to grow from the surface where the contact with the surface is in the range of hundreds of nanometers. These microstructures do not show any evidence of ordered phases. Eventually, their number are lower near the edges of the electrode.

	S	Cu	Ag	Conditions
Spectrum 1	9	19	75	Wide area 840X
Spectrum 2	11	18	72	Wide area 840X
Spectrum 3	14	25	60	One point on worm-like structure
Spectrum 4	4	7	89	One point on the flat surface
Average	**9**	**16**	**74**	

Table 5-3 Composition of the sample ExCuS in at% rounded considering 1% of error.

Regarding the EDX analysis, we assumed a 1% error threshold, the composition of the worm-like structure is equivalent to the flat surface. Under, these assumption the composition is consistent with a Cu:S ratio of 2.

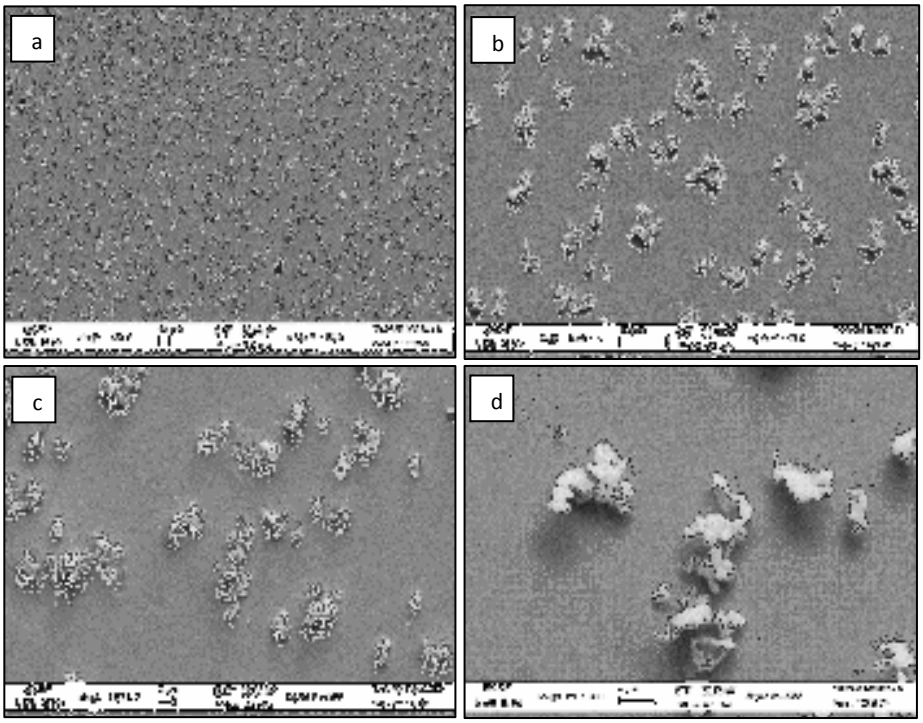

Figure 5-11 *Micrograph of a representing portion of the sample ExCuS at 1000X (A), 3000X(b), 10000X(c) and 15000 (d) .*

5.1.6. Discussion

The main achievement of this part of the work is the observation of the growth of Cu sulfide over Ag(111) by E-ALD and its first structural characterization.

Clearly, the film exhibits a Bragg's pattern supporting the idea of a new phase of the Cu-S system, having an apparent pseudohexagonal structural arrangement with unprecedented metrics [112,113] derived from that of chalcocite's structure. It has strong similarities with the one of the low chalcocite, Particular attention was dedicated to the low chalcocite Cu_2S structure refined by Evans [112,114] which crystallizes in a monoclinic cell (a=15.246 Å, b=11.884 Å, c=13.494 Å, β=116.35°). The structural model can be described as a hexagonal arrangement of sulphides ions perpendicular to the c axis, with the Cu ions partially filling the triangular sites in the hexagonal plane of sulphide anions, and the triangular sites between two successive planes. This second type of Cu ions is intrinsically characterized by a high mobility in the (a, b) plane [115]. These structural results are in agreement with recent EXAFS studies, revealing a chalcocite-like local structure for copper sulphides in similar systems obtained by means of E-ALD [67].

The measured periodicity along the *c* axis is 6.75 Å [116], very close to half of the periodicity along *c* observed by Evans[112,114]. This metrics corresponds to a distance between two

adjacent sulfur layers of 3.37 Å. In the Cu-S compositional field this value is related to the stoichiometry. Thus, we can extrapolate that the stoichiometry of our deposited film is Cu_2S[113], which is consistent with the result of the EDX study reported in Table 5-3.

Considering the orientation of the film with respect to the substrate it possible to define only one non-trivial epitaxial relationship (11x2) with a strain lower than 5% (-0.8%). Moreover, the structural relationship between low chalcocite and the high symmetry Cu_2S structure reported in this study involves the planarization of the CuS_3 fragments. Such distortion is likely due to a substrate-induced straining which can be considered as an epitaxial effect as well. Hence, the SXRD data suggest the commensurate growth of a new Cu_2S phase, by means of an epitaxial process involving linear and angular straining of the in-layer Cu-S bonds of a chalcocite structure.

The Lorentzian width of the in-plane peaks profile showed that the domains keep increasing in size until 40 cycles, reaching the remarkably average size of 1000±100 Å. Out of the plane, the width of the purely Lorentzian width is much larger resulting in domains size of ~140±14 Å after the 40^{th} cycle. Thus, the expected value of the film thickness is at least 140 Å. The asymptotic trend towards a constant value of the width (Figure 5-4d), namely the saturation value, might also be an indication of a multidomains growth along the *l* direction. However, the absences of the XRR fringes, while confirming the high roughness of the film, hinders the precise analysis of the thickness of the deposit. The XRR data analysis has to take into account the lower boundary of the film established by the Lorentzian width. This allowed to define an additional two layer models:

Model 1: Water/High density layer/Substrate

Model 2: Water/Low density layer/High density layer/Substrate

For the last model two almost equally good fits have been obtained. To confirm the existence of a lower density top layer we compared Model 1 and Model 2 (Table 5-4) where Model 2 has been fitted with fixed parameters in order to have the same number of estimated parameters. The estimated uncertainties of the two fits in Table 5-4 show that they can be considered comparably accurate. The relative scattering lengths are reported in Figure 5-12, confirming the existence of a lower density top layer. This confirms that the crystallites' size is compatible with the thickness reckoned by XRR data. On these basis, the pseudo single crystal pattern showed by the reciprocal space maps, the high optical density of the bottom layer and the low optical density of the top layer

suggests the emerging of separated crystallites from a "wetting layer" resembling a Stranski-Krastanov growth mechanism.

		Model 1	Model 2
Roughness of the substrate	(Å)	3.25 ± 0.02	3.25 ± N/D (Fixed)
Thickness of the bottom layer	(Å)	18,84 ± 0.08	18.84 ± N/D (Fixed)
Density of the bottom layer	($Å^3$)	0.0178 ± 0.0001	0.0178 ± N/D (Fixed)
Roughness of the bottom layer	(Å)	6.54 ± 0.08	6.54 ± N/D (Fixed)
Thickness of the top layer	(Å)	- -	82.59 ± 0.06
Density of the top layer	($Å^3$)	- -	0.0120 ± 0.0007
Roughness of the top layer	(Å)	- -	22.42 ± 0.05

Table 5-4 Comparison between the results of the fitting of the XRR data with the two stack models.

Although the relevant expected compressive epitaxial relationship would support this hypothesis, there are not experimental evidences of the growth of a wetting layer in the analysis of the Bragg peaks. Accordingly, this layer could be induced by the release of strain occurring at a certain stage of the growth, likely at the saturation of the increasing of the domain size.
The micrographs in paragraph 5.1.5 present worm-like structures which could be related to the islands that are expected to be growing at the end of the process. However, the density of the top layer is the 67 % of chalcocite's crystallographic density, while the coverage of the electrodic surface due by the worm-like structures is less than 25%. However, their size at the contact with the flat part of the sample is probably of the order of the crystallite size.

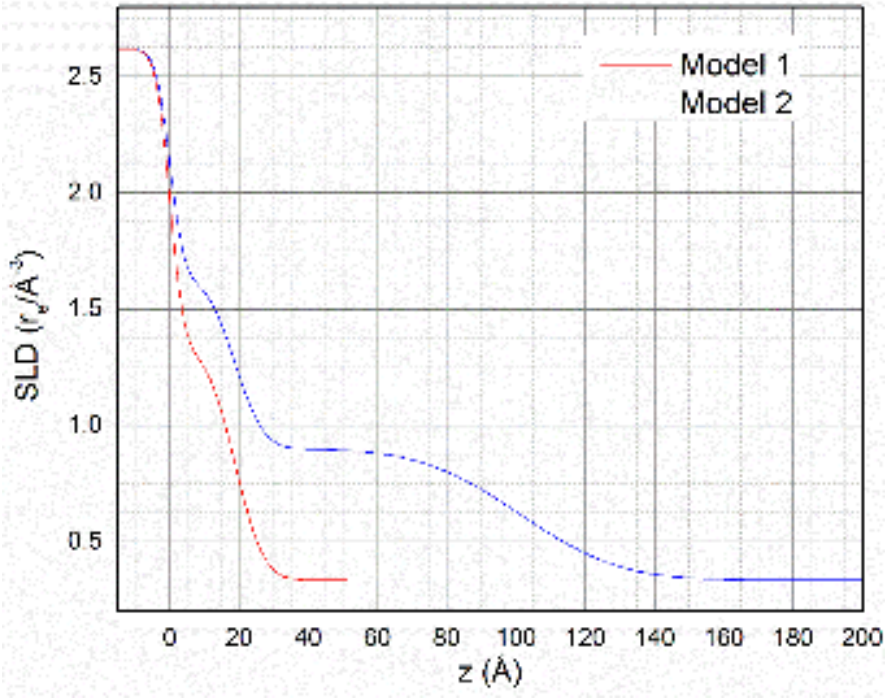

Figure 5-12 *Scattering length densities of the two models fitting the XRR data. A dramatic difference is present for distance higher than 30 Å along z.*

Moreover, these structure are clearly polycrystalline in contrast with the absence of Debye rings in the reciprocal space maps. On this ground, we can exclude that they can grow to the last part of the E-ALD process. Since in the ExCuS it has been observed both other epitaxial phases and Debye-rings, the worm-like structure are likely to be grown when the electrode is removed from the cell. It is still not clear if their growth occurs contemporarily to the structural changes observed when the potential is removed or when the electrode is removed from electrochemical cell, in the latter case not comparable with the operando SXRD data.

Hence, while the growth of the worm-like structure is not understood, we can exclude that they concur to the process observed by means of any operando measurement. From the whole set of operando data and related consideration we can infer a four stages growth mechanism (Figure 5-13) for the epitaxial phase:

1) The deposition of the S_{ad} occurs through the formation of S atoms triplets capping the Ag(111) surface[55] with a periodic array.

2) The first Cu monolayer occurs through the thermodynamically driven formation of pseudomorphic Cu-S layer. As suggest by Pattrick et al. [117] the building blocks

of these sulphides are the CuS_3 units, which can be inferred to form the 2D planar structures.

3) From the 4th to 40th E-ALD cycle the formation of a relaxed (not pseudomorphic) compact layer dominates the growth. The crystallites have probably a ratio between the in-plane and out-of-plane dimensions of the order of 10. The grain boundaries could include hexagonal triple junctions.

4) Finally accumulated strain in the wetting layer is released forming coherent islands which developed the final microcrystalline structure with constant lateral size from the 40th cycle.

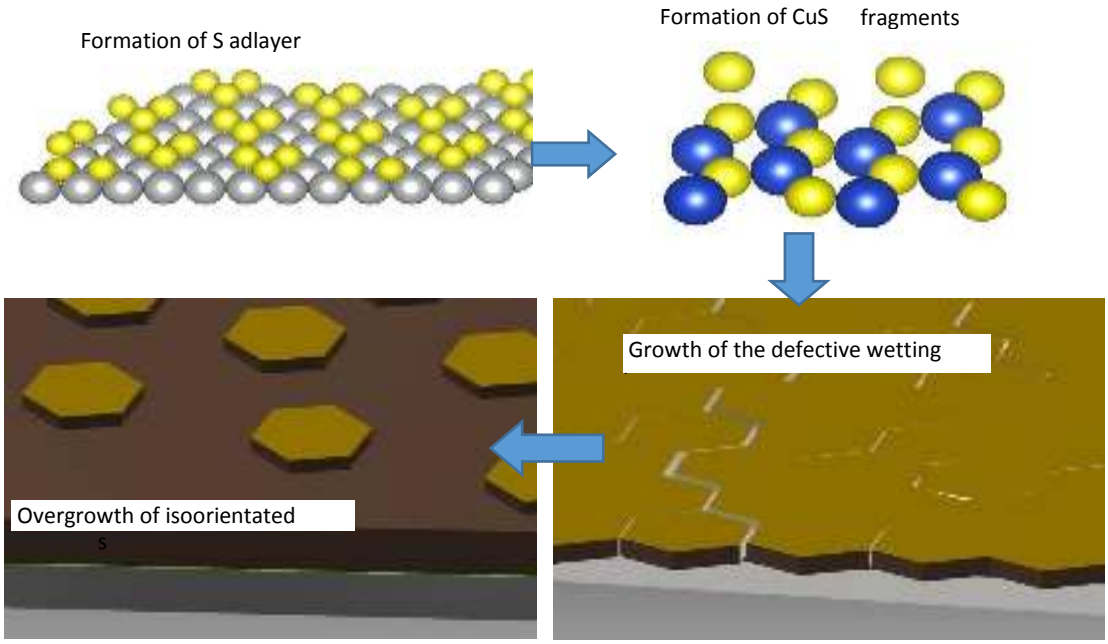

Figure 5-13 *Pictorial representation of the proposed mechanism for the E-ALD growth of Cu_2S.*

5.2. Ag(111)/Cu_xZn_yS

5.2.1. Preparation of the samples

The samples have been prepared according to synthesis developed in our laboratory by Cinotti et al. [27]. Table 5-5 presents the electrochemical synthesis performed for this study according to this protocol.

Label	Method	Deposition sequence
Op1:1	*E-ALD operando at ESRF*	$Ag/(S/Cu/S/Zn)_{60}/S$
Ex20	*E-ALD ex-situ at UNIFI*	$Ag/(S/Cu/S/Zn)_{20}/S$
Ex40	*E-ALD ex-situ at UNIFI*	$Ag/(S/Cu/S/Zn)_{40}/S$
Ex60	*E-ALD ex-situ at UNIFI*	$Ag/(S/Cu/S/Zn)_{60}/S$

Table 5-5 *List of the electrochemical synthesis presented in this paragraph.*

5.2.2. Operando analysis of the growth

For the Op1:1 we detected both Debye rings and Bragg peaks patterns, revealing the presence of a disordered phase and an epitaxial phase in the film. Hence, during the growth, the Debye rings pattern has been collected by means of azimuthal scans (δ-scans see paragraph 4.2.3) while the study of the Bragg peak followed the same strategy applied in the characterization of Cu_2S (paragraph 5.1).

The δ-scans were performed on the Op1:1 sample at different stages of growth (0, 15, 30, 45 and 60 cycles). The δ-scans of the sample Op1:1 at 60 cycles is shown in Figure 5-14a. All reflections can be indexed according to the structure of monoclinic chalcocite (space group $P2_1/c$ [112]), the barely detectable discrepancies (Figure 5-14b) are compatible with wurtzite structure (space group $P\ 6_3mc$ [61]). Under the limit of the method (1 wt%), no other reflections due to spurious products or relics of the precursors are evident (Figure 5-14b). The R-Bragg values for the Rietveld fits are in the range of 4-10. The δ-scans are presented in Figure 5-14c after the removal of the background signal from the diffuse scattering. The δ-scans show a monotonic growth of the disordered phase which seem to increase rapidly between the 45th and 60th cycles. This trend is quantitatively confirmed by the results of the Rietveld quantification, as illustrated by Figure 5-14d, where we report the scale factor (i.e. a factor proportional to the total amount of chalcocite) *versus* a function of the number of E-ALD cycles. Apparently, the

growth of chalcocite proceeds with a higher rate between the 15th and 30th and between the 45th and the 60th cycle, than between the 30th and the 45th deposition cycle. The growth process is studied by following the trends for the fit parameters obtained by single line profile analysis of the Bragg peaks in the Op1:1 sample. The Bragg peaks match the ones of the Cu_2S chalcocite-like crystal structure previously described (paragraph 5.1). In the following, the growth parameters related to the peak at (0.73, 0.73, 4.19) are presented in Figure 5-15. Among the most intense, this peak has no overlapping with other signals and provides very reliable information. The peak profiles registered at the different number of deposition cycles are shown in the Figure 5-15a, together with the least-squares best fit curves obtained using a Voigt function (paragraph 4.2.3). There is a small change in the Bragg's peaks position during the growth (in the range 4.194-4.204 rlu) and with respect to the Cu_2S grown by means of the binary scheme (4.19 rlu) (see paragraph 5.1). These discrepancies are in the range 0.1%-0.4%, thus comparable to the uncertainties of the positioning and the fit. Hence, the position can be considered constant during the process, although slightly changed with respect to Cu_2S (paragraph 5.1.2). The evolution of the most relevant parameters is shown in the graphs of Figure 5-15b: wL decreases until the cycle 45 and then increases slightly: this can be related to an increase of crystallite size at least up to the 45th cycle. The trend for wG is exactly the opposite, thus pointing to an increase of strain of the film until 45 cycle. The scale parameter A, which is related to the amount of deposited material, grows up to 45 cycle and then decreases slightly.

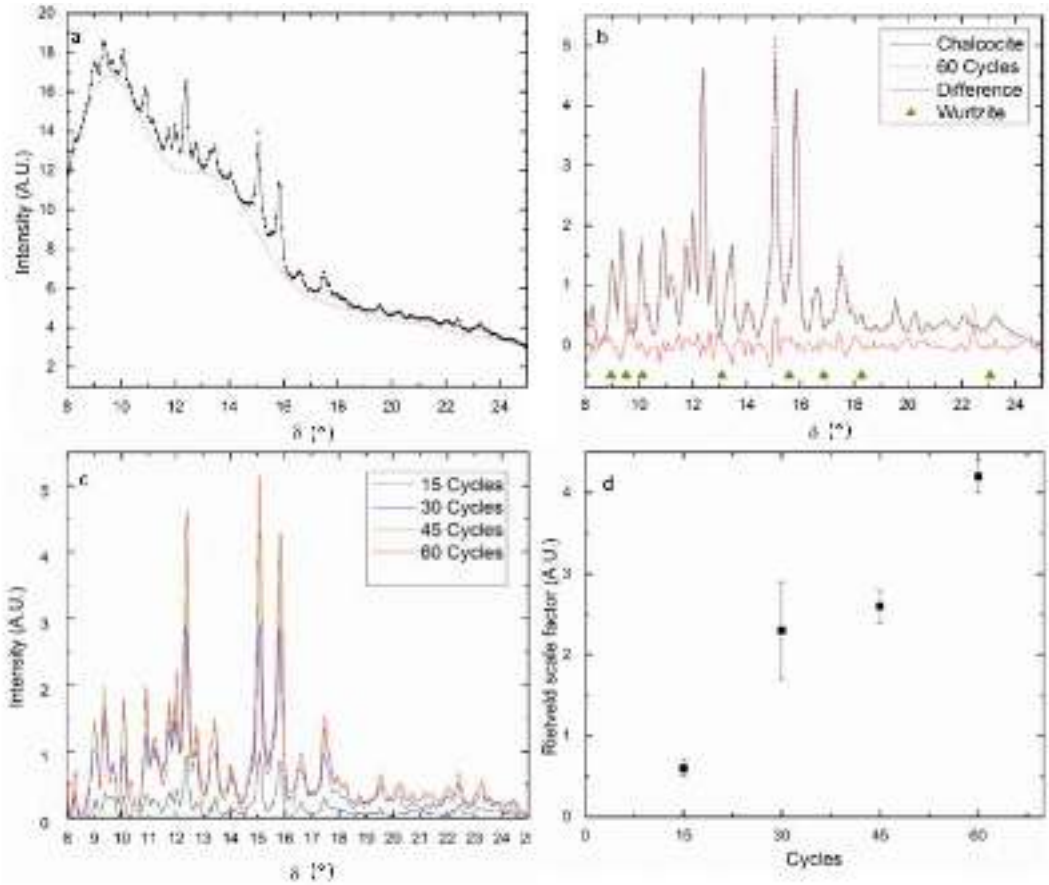

Figure 5-14 (a) Raw in-plane XRPD pattern of the Op1:1 sample at 60 cycles the fit (continuous line) is superimposed to the experimental points, (b) background subtracted in-plane XRPD pattern of the Op1:1 sample at 60 cycles compared with the best fit of the Rietveld analysis and the position of the wurtzite reflections, (c) in plane XRPD patterns of the Op1:1 sample and (d) Rietveld scale factors at different growth stages.

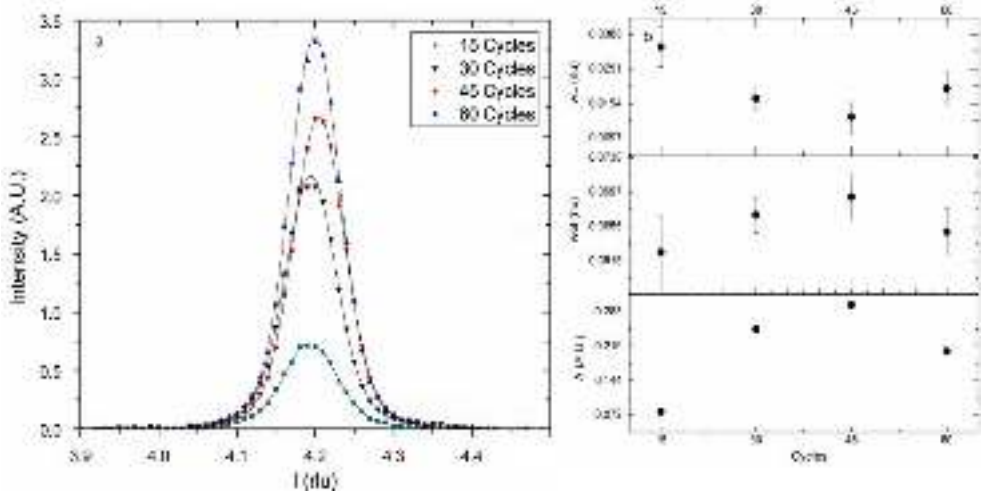

Figure 5-15 Results of the Bragg peaks analysis for the Operando 2D-maps at (0.73, 0.73, 4.19). (a) the Bragg peaks with the related best fits and (b) the parameters resulting from the best fits.

5.2.3. Operando analysis at the end of the growth

The different peaks analyzed during the sample growth can be observed in the (h, k) intensity map measured at a constant L value of 1.045 rlu. The maps of Op1:1 reveal an apparent pseudo single crystal hexagonal pattern (Figure 5-16), and the presence of rings. The dependence of the intensity along the l direction shows that the rings are due to phases almost perfectly oriented along the [0 0 1] direction. The reflections present as Bragg peaks have a periodicity and structure comparable to an ordered phase of Cu_2S (see paragraph 5.1). We also registered the presence of the characteristic Bragg peaks in the positions expected for wurtzite, i.e. (0 0.75 1.13). However, these Bragg peaks are very close to the peaks of the Cu_2S, i.e. (0 0.73 1.045). Accordingly, the proximity of ZnS and Cu_2S reflections prevented a quantitative analysis. Eventually, superimposed to the Bragg reflections, a set of Debye rings can be identified (Figure 5-16).

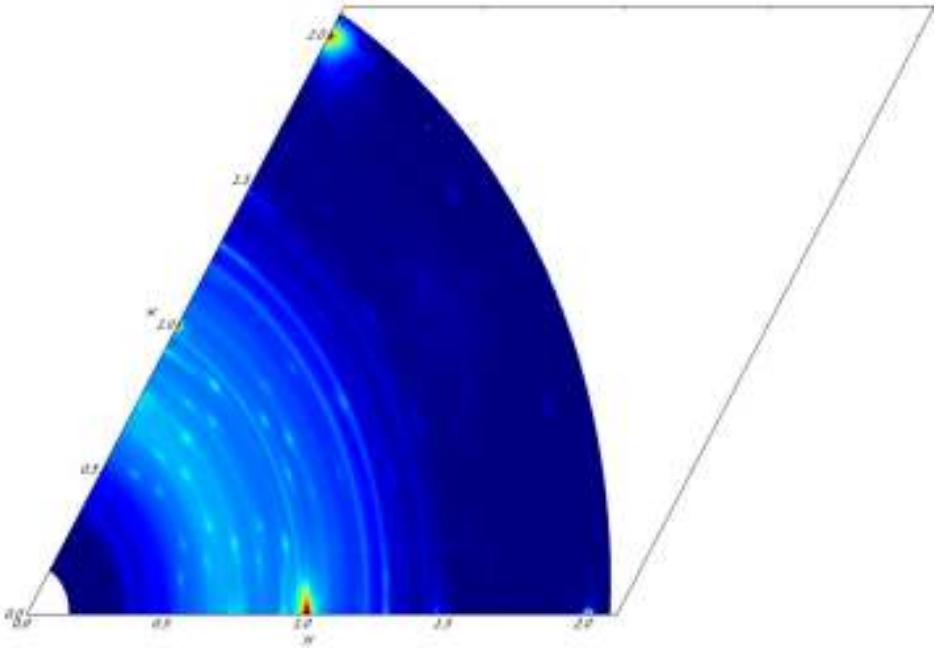

Figure 5-16 Operando h,k intensity maps at l=1.05 measured for the Op1:1 sample.

5.2.4. Micromorphology and semi-quantitative analysis

The SXRD analysis of sample Op1:1 points to the growth of at least one polycrystalline phase on the top of the sample. Figure 5-17 shows the morphology of the Ex20, Ex40 and Ex60 samples corresponding to different stages of growth for the Op1:1. After 20 deposition cycles, the surface is no longer smooth similarly for the ex-situ Cu_2S film (paragraph 5.1). The film is covered by several grains stepping ahead from its surface. After 40 cycles, these structures are replaced by nanowires with the length of the order of 1-2 microns, and the thickness in the range of few tens of nanometers. After 60 cycles, the number, density and length of the nanowires is definitely increased, whereas the wire thickness has remained almost the same than before, in full agreement with previous studies on this type of film[67,118]. These evidences suggest that at a certain stage of the growth an intermediate step of reorganization occurs, stimulating the formation of thread-like structures. With the increasing number of deposition cycles, the morphology of the ternary compound becomes more complex, leading to the formation of thread-like structures with length of several μm and sub-micrometric diameter.

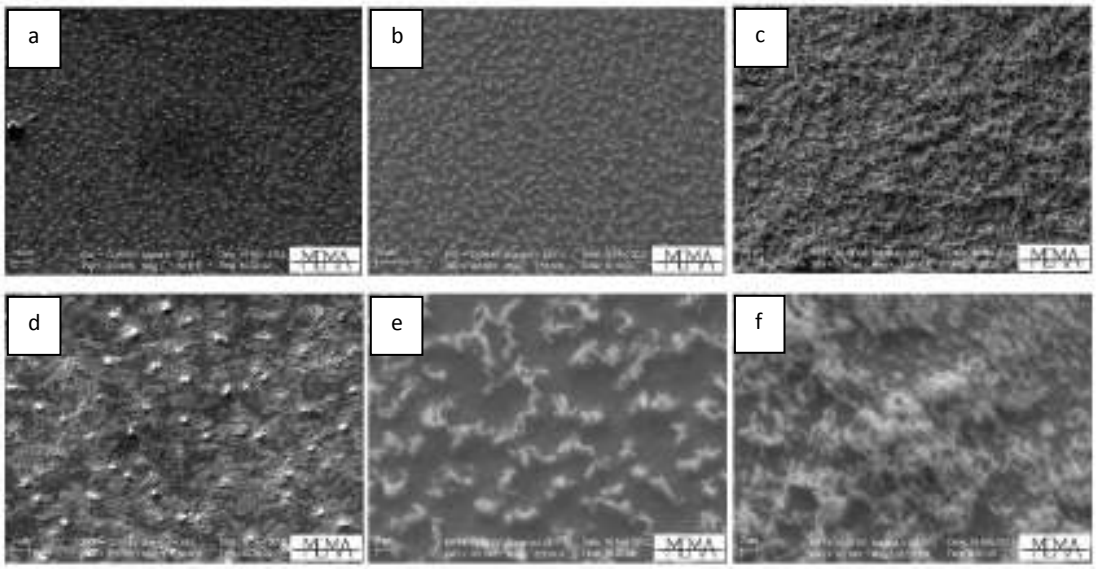

Figure 5-17 Morphological analysis of the Cu_xZn_yS 1:1 at 1000X (a),(b),(c) and at 6500X (d),(e),(f). (a) and (d) refer to Ex20, (b) (e) Ex40 while (c) (f) Ex60 [119].

5.2.5. Predominance charts of the Cu-Zn-S-O-H system

This system represents a solution of Zn and Cu salts in ammonia buffer (50mM of NH_3 and 25mM of $HClO_4$) at the equilibrium with the solid phases. On the ground set by the review of the known literature, no Cu-Zn-S ternary compound were included to the wateq4f.dat, since none of them is generally accepted as a thermodynamically stable phase at room temperature [120]. When considering the following concentration: [Zn]=5 10^{-4} mol/kgw [Cu]=5 10^{-4} mol/kgw [S]=5 10^{-3} mol/kgw, the Pourbaix diagram of this system constitutes a general description of the chemical environment where the synthesis of the Cu_xZn_yS is performed. The main difference with E-ALD environment is the formal concentration of S which is 5 10^{-3} mol/kgw. The excess of sulfur formal concentration with respect to metals is a common practice to compute the predominance charts within the *phreeqc* framework, to prevent sulfur from acting as a limiting species for the precipitation of sulphides. In order to clarify which is the most stable phase for each element at given thermodynamic conditions, Figure 5-18, Figure 5-19 and Figure 5-20 depict the predominance charts specific for each relevant element (respectively Cu, S and Zn). Figure 5-18 depicts the predominance charts of the copper-bearing species. It is worth noting that chalcocite results as the most stable sulfide phase. Figure 5-18 reports the predominance chart for copper-bearing species in the E-ALD environment. As elsewhere reported for other environments [121], in the lower part

of the plots (more reducing conditions) copper sulphide phases dominate the charts. In the upper part of the plots copper oxides are the most abundant phases. The only region where solid phases are lacking occurs at very low pH in oxidizing conditions, where Cu^{2+} is the main aqueous species. The inset in Figure 5-18 Predominance charts for the copper bearing phases, assuming [Zn]=5 10-4 mol/kgw [Cu]=5 10-4 mol/kgw [S]=5 10-3 mol/kgw., roughly depicts the range of pH and potential where the whole E-ALD occurs, giving an insight about the most stable solid phases involved in the growth of Cu_xZn_yS: these species result elemental copper and chalcocite.

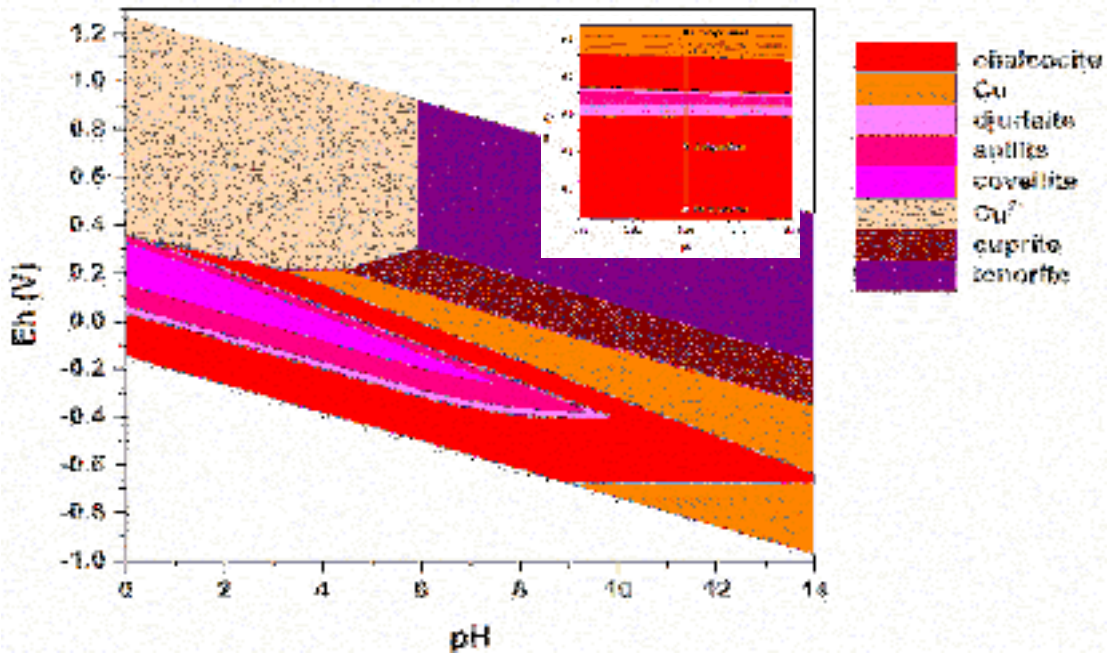

Figure 5-18 Predominance charts for the copper bearing phases, assuming [Zn]=5 10^{-4} mol/kgw [Cu]=5 10^{-4} mol/kgw [S]=5 10^{-3} mol/kgw.

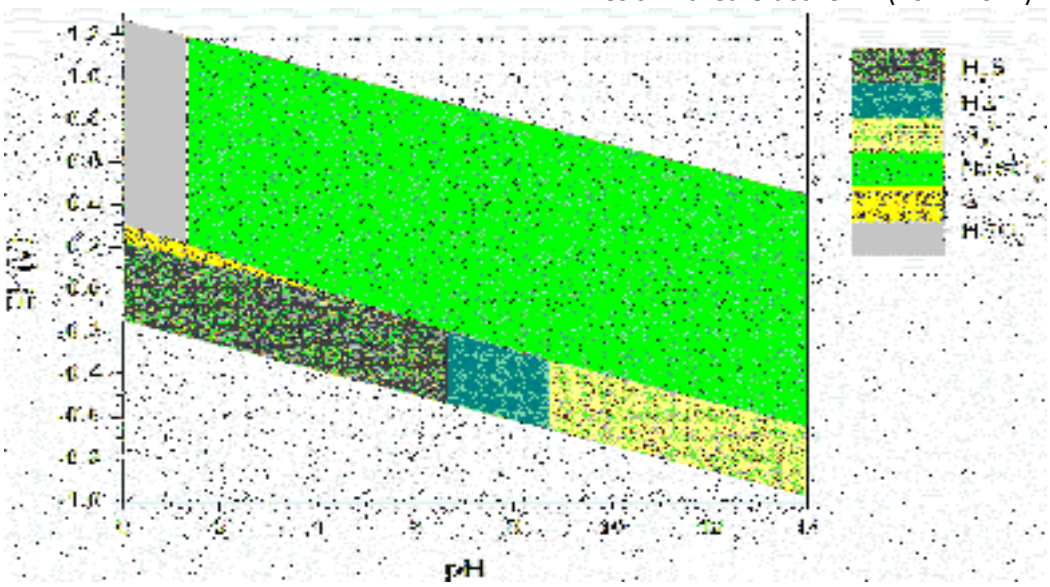

Figure 5-19 Predominance charts for the sulfur bearing phases, assuming [Zn]=5 10^{-4} mol/kgw [Cu]=5 10^{-4} mol/kgw [S]=5 10^{-3} mol/kgw.

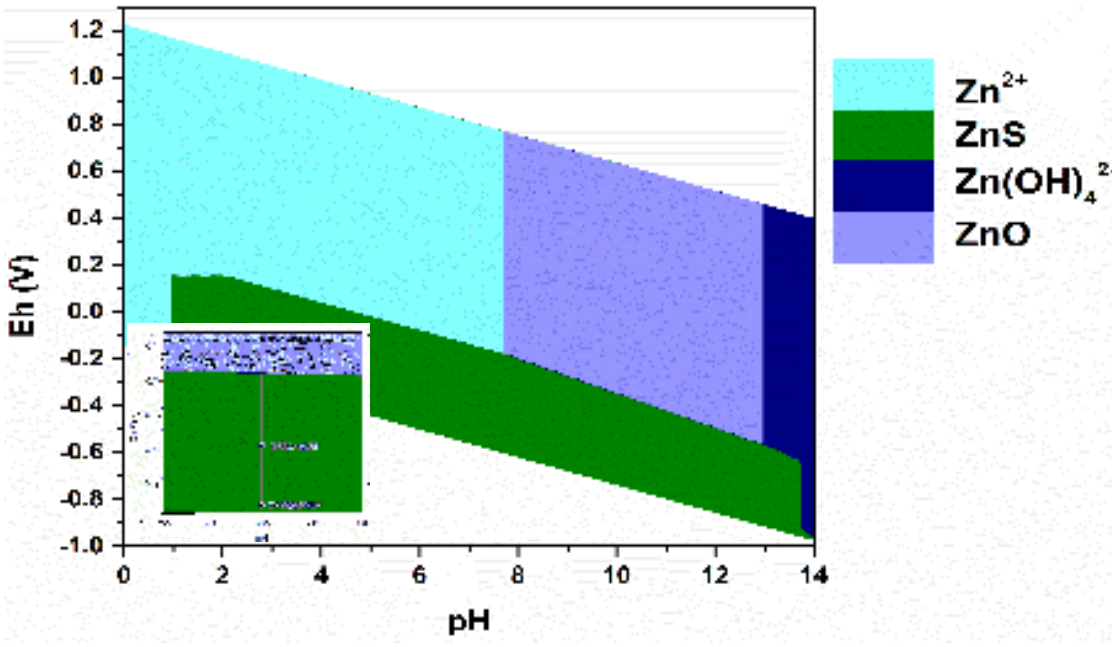

Figure 5-20 Predominance charts for the zinc bearing phases, assuming [Zn]=5 10^{-4} mol/kgw [Cu]=5 10^{-4} mol/kgw [S]=5 10^{-3} mol/kgw.

Figure 5-19 shows the predominance charts of the sulphur-bearing species. A comparison with the Pourbaix diagrams of the Cu-S system reported by Peters [122] and Huang (2016) [123] shows that the only difference is the reduced stability of elemental sulfur. The absence of reduced aqueous sulfur species is evident in the upper part of our diagram. These discrepancies with Cu-S system have to be accounted for the presence of competitive equilibria involving also the precipitation of zinc and copper sulphides as well as other redox equilibria in the liquid phase. Figure 5-20 depicts the predominance charts for the zinc-bearing species. It should be noticed that the potentials at which we perform the E-ALD steps (inset in fi Figure 5-20) is across the ZnO/ZnS stability boundary.

5.2.6. Modelling of the E-ALD cycles

Paragraph 5.2.5 showed clearly that the only solid phases precipitating during the process (except the first step) are chalcocite, sphalerite, Cu and zincite. This result is confirmed in this paragraph while two models are applied to the E-ALD process.

Constant volume model

Figure 5-21 shows the plot of the cumulative molar amount of the main solid phases as a function of the number of E-ALD steps. A transient regime of the chemical speciation for the first 20 steps is apparent. Successively, the system reaches a pseudo-periodic regime. Further detail on the transient regime is given in the inset to Figure 5-21, where a close-up on the first 6 E-ALD steps is shown. In general, the cleaning steps after each deposition step do not affect the amount of precipitated phases. To achieve more readable graphs we didn't report the amount of acanthite in Figure 5-21 and Figure 5-23, however we find that the first step deposits the S-adlayer as expected, due to the excess of free energy added to the acantite species to model the strong interaction with the Ag(111) surface. While none of the 4 relevant solid phases are not present after the first step due to the formation of acantite, the second step (reduction of copper) results in the precipitation of metallic copper. The third step (oxidation of sulfur) leads to the complete sulfidization of the metallic copper, converted completely to chalcocite. The fourth step leads to the deposition of the zinc as zincite and the desulfidization of chalcocite leading to the formation of sphalerite and metallic copper. The fifth step leads to the complete sulfidization of metallic copper and zincite converted respectively in chalcocite and sphalerite. The sixth step of this sequence is the deposition of copper. At this stage, the formation of chalcocite apparently occurs at the expenses of sphalerite, probably due to the higher stability of the former. Although the sixth step leads clearly

to a diminishing of total Zn in the solid phases, unexpectedly the extended trend over 120 steps (depicted in Figure 5-21) shows the steady growth of chalcocite and sphalerite over zincite and metallic copper. The apparent excess of sphalerite over chalcocite is removed when considering the amounts normalized over the metal atoms per unit formula (0.0146 chalcocite and 0.010 sphalerite).

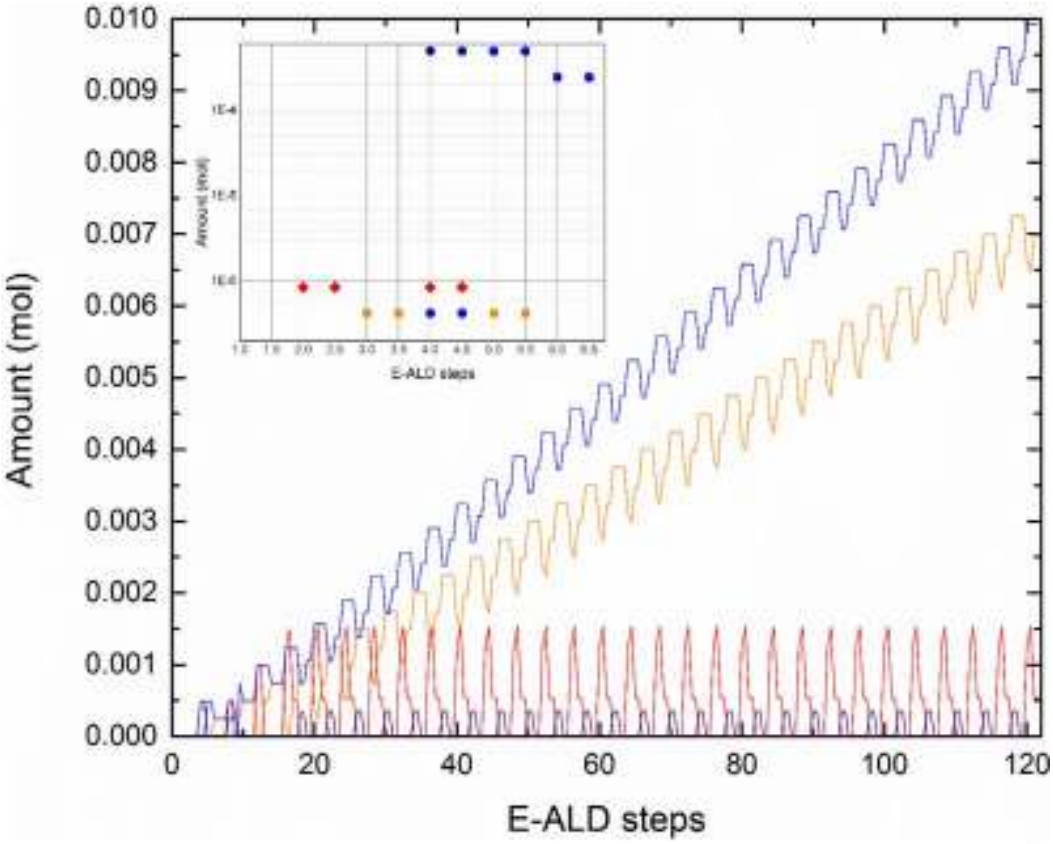

Figure 5-21 Amount of the solid species as computed by means of the constant volume model. In the inset and the main plot the blue, red, yellow and blue curves represents the total amounts of sphalerite, chalcocite, copper and zincite respectively.

During the pseudo-periodic regime (after 20 steps) every time copper is deposited, the total amount of zinc in the solid phase is reduced (Figure 5-22a), while during the whole process there is no net diminishing of copper in the solid phases (Figure 5-22b). Moreover, Figure 5-21 confirms zincite as the less stable solid phase when the reduction of the amount of Zn in the solid phase occurs (during the deposition of copper).

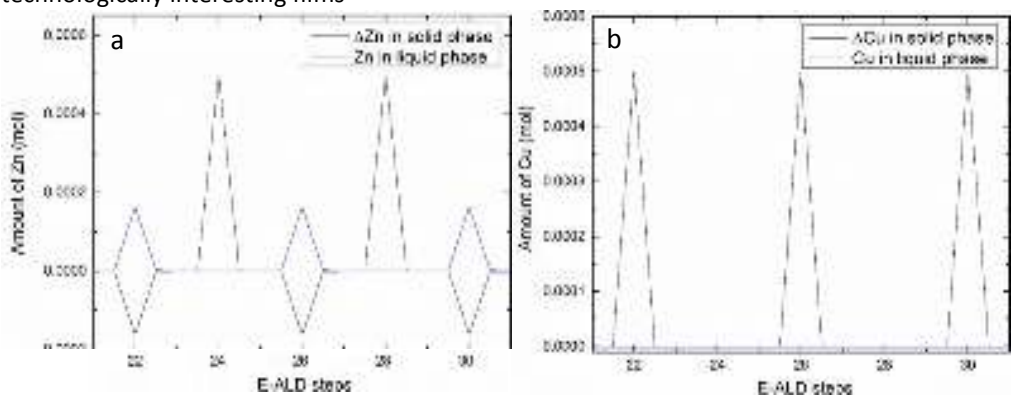

Figure 5-22 Amount of the total metal ions in the liquid phase compared to the change of the amount of solid phases (constant volume model).

Total depletion model

It should be considered that the constant volume model could not describe the effect induced by the exchange of solution, underestimating the Cu/Zn ratio. As discussed in paragraph 4.5.2, the total depletion model provides a description of the maximized consequences of the solution exchange. On the ground established by paragraph 4.5.2, the total depletion model for Cu_xZn_yS has been developed under the assumption that during the flux of the copper solution inside the cell (fluxing a volume several times bigger than the cell volume, to change the solution) zincite is completely depleted. The results of such model are depicted in Figure 5-23, one can observe that the only species able to establish a growing trend is chalcocite. Conversely, sphalerite slowly decreases after the 20^{th} cycle. Thus, the Cu/Zn ratio at the end of the process is by far larger than the ratio obtained with the constant volume model (18.9).

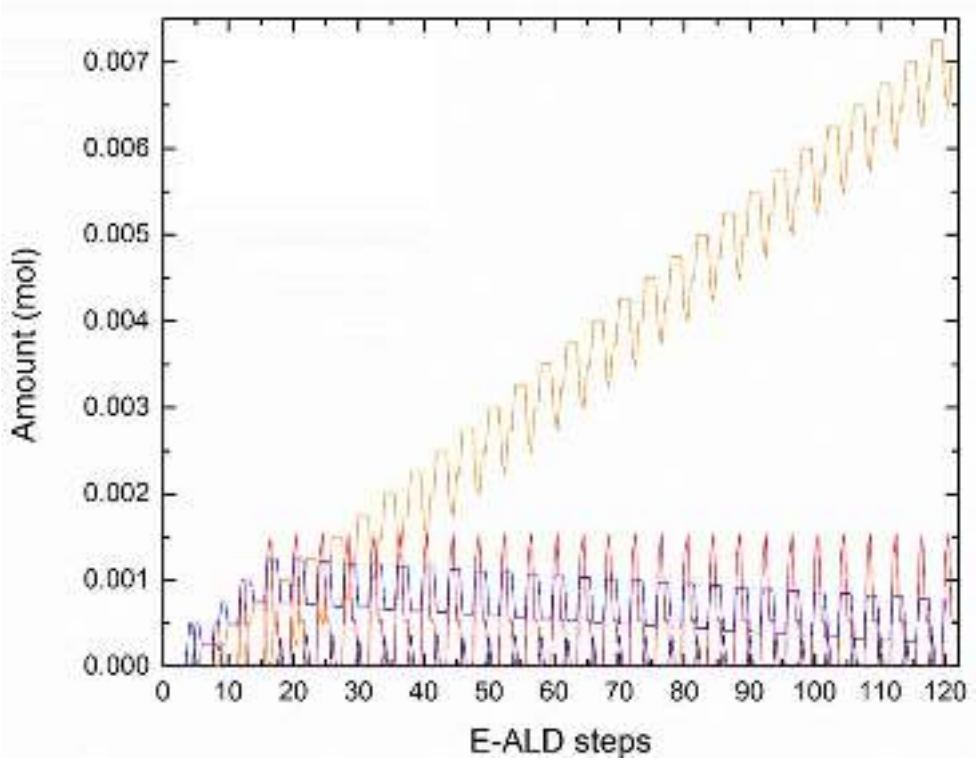

Figure 5-23 Amount of the solid species as computed by means of the total depletion model. In the plot the blue, red, yellow and blue curves represents the total amounts of sphalerite, chalcocite, copper and zincite respectively.

Recalling that Figure 5-21 and Figure 5-23 depict the main results of the constant volume and total depletion models, respectively, Table 5-6 shows the comparison of the expected Cu/Zn ratio with the experimental data after 120 steps [17-19].

	Cu/Zn	REF
Constant volume	1.46	This study
Total depletion	18.9	This study
Experimental Ex60	6	[118]

Table 5-6 Comparison between the theoretical and experimental Cu/Zn ratios.

5.2.7. Discussion

The whole set of the experimental data obtained in this part of study highlights, and confirms, the previous findings on the E-ALD films realized on the Cu-Zn-S system [18,19]. The data (Figure 5-15 and Figure 5-16), point out that ordered (pseudo-single crystal) and disordered polycrystalline phases are occurring in the sample Op1:1, as well as that the final product do contains two different Cu_2S phases, with different structural arrangements, and wurtzite ZnS. This evidence apparently contrasts what already observed on other binary sulphides, including the Cu_2S itself [20,21], and the ternary Zn-Cd-S films [17,22].

The set of pseudo-single crystal Bragg reflections has been assigned to the Cu_2S (chalcocite type) phase already reckoned during the *operando* SXRD study of the E-ALD grown binary copper sulphide (see paragraph 5.1)56. The growth of the ordered phase is simultaneously accompanied by the formation of a disordered Cu_2S phase, this latter fully coincident with the natural low temperature chalcocite polymorph, the presence of which is also confirmed by the Debye rings present in the map of Figure 5-16. The final assignment of this disordered phase was confirmed by means of Rietveld analysis (Figure 5-14). Concerning ZnS, our data point to two possible phases in the sample, i.e. certainly a pseudo single crystal wurtzite and possibly a polycrystalline wurtzite. This result can be considered in line with other studies [67,118], in fact, the presence of two phases Cu_2S and ZnS was derived from XAS spectroscopy. These authors have attributed ZnS either to wurtzite or to sphalerite polymorphs, with preference to the latter, but they were not able to finally solve this issue because of the short-range structural environment investigated by the XAS technique around Zn. The study of the trends of the Cu_2S crystallites strain and size (Figure 5-15a) depicts an even more complex situation occurring during the crystal growth. These trends suggest a growth less ordered than the one for Cu_2S samples analyzed in paragraph 5.1. The crystallite strain and size along the c-axis increase with the deposition cycles until the 45^{th} cycle and then abruptly decreases; the same trend is followed by the value A, which is related to the amount of the ordered Cu_2S deposited. It is worth to notice that after the 45^{th} cycle, the amount of the polycrystalline phase increases, whereas that of the epitaxial phase decreases. Since the intercalation of cycles dedicated to the deposition of Zn-S layers is the only difference between the E-ALD scheme for the direct growth of Cu_2S (paragraph 5.1), the effect of the Zn deposition step emerges clearly. The data confirmed that the accumulation of the stress as well as the growth of the nanowires are straight related to the effect of the deposition of Zn. Moreover, the analysis of the data suggests that the release of the stress leads to the abrupt increase of the amount of the polycrystalline phase during the

last part of the growth. An opposite trend is recorded for the disordered pattern, for which the Rietveld scale factor obtained from the δ-scans increases abruptly from the 45th cycle to the 60th cycle (Figure 5-16b). The micrographs for the ex-situ samples registered the abrupt increase of a very complex net of nanowires between the 40th and 60th cycles (Figure 5-17). Since no other diffraction signals were recorded on this system, the nanowires are attributed to the disordered phase observed by the δ-scans, i.e. to Cu_2S chalcocite. Hence, the micrographs allow a visual confirmation of the abrupt increase of the disordered phase in the last part of the growth. From the early stages of the growth, at least two phase are clearly present: an ordered phase (pseudo-single crystal) and a disordered (polycrystalline) phase, as confirmed by morphological and structural data. In general, the growth of the Cu_xZn_yS by means of E-ALD seems to be driven by the occurrence of copper-sulphides structures, as expected from recent studies that revealed a strong Zn deficiency [118]. No other phases involving zinc sulphides, but wurtzite, are present. However, recent studies have suggested the occurrence of the cubic ZnS polymorph, sphalerite[67]. Regarding the current assignment of the ZnS structure in the Cu_xZn_yS, the performed diffraction investigation properly deal with the long range arrangement of the structure.

The SXRD allowed the characterization of the changes in the features of the crystallites of the pseudo-single crystal and in the scale factors of both the pseudo-single crystal and the polycrystalline phase. After the 45th cycle, most of the stress is released by increasing the amount of disordered phase, likely by means of a structural rearrangement or re-crystallization. Comparing the growth of Op1:1 with the direct growth of Cu_2S [21] we reckoned a general increase of the strain, revealing a high concentration of randomly distributed structural defects in the Cu_2S epitaxial phase. The hypothesis is that Cu vacancy or Zn inclusion in a defective Cu_2S structure explain the increased strain. In this context, the effect of the Zn deposition step emerges clearly, leading to accumulation of stress that seems to drive the growth of the nanowires, hence leading the abrupt increase of their amount during the last part of the growth.

These results points to the occurrence of a complex growth process involving an oriented and strained phase with a randomly oriented, polycrystalline phase growing on top of it jointly with and the Zn-deficiency. Our modelling approach aimed to understand, from a thermodynamic standpoint this complex mechanism. The calculation performed in the Phreeqc framework reproduced the experimental trends, giving a clear (although qualitative) insight in the growth process, confirming the link between the Zn-deficiency, the arising of the thread-like structure and the dissolution of Zn during the Cu deposition step.

The relevance of the main species has been reckoned by a preliminary study of the predominance chart and confirmed also by the calculation of the E-ALD steps, carried by means of the two extremes models:

1) “Constant volume”: where the volume of solution is considered constant. Hence, the effect of the exchange of solution in the cell is not considered.

2) “Total depletion”: where the solution is considered to be changed several times at fixed potential leading to the complete dissolution of the less stable phase (zincite).

In this context, the pursued computational approach demonstrated that the expected dominant phase in the bulk of the grown material is chalcocite.

- Regarding the Zn-deficiency: Table 5-6 shows that the experimental Cu/Zn is 6:1, hence between the two extremes value of 18.9:1 (total depletion model) and 1.46:1 (constant volume model). Such values point out that we successfully implemented two extreme models for the E-ALD growth of Cu_xZn_yS. Since the theoretical value is not perfectly matching the experiments, we suggest that the depletion of zincite during the reduction of copper is not complete as we assumed for the “total depletion model”. We consider such incomplete depletion as related to the following factors: the contemporary growth of a surface driven epitaxial phase, the kinetics of the redissolution processes and the convective transport of dissolved species during the renewal of the solution. However, we found a net decrease of zinc (between 0.3% and 1% even in the constant volume model), suggesting that the periodic interconvertion of Zn between sulfidized and oxidized species, and the preferential dissolution of zincite are the cause of the Zn-deficiency in the E-ALD growth of Cu_xZn_yS.
- Regarding the overgrown thread-like structure: both our models forecast a prevalent amount of chalcocite. Since most of the polycrystalline phase in the Cu_xZn_yS is chalcocite[15], we suggest that the occurrence of the thread-like structure is related to the precipitation/dissolution equilibria involving the 4 relevant species when depositing copper. In these conditions, the net results is the precipitation of bulk chalcocite at the expense of sphalerite (involving sphalerite to zincite dissolution-precipitation reactions and partial zincite dissolution).

To explain in deeper details the process we propose a mechanism ground on the following five competing equilibria guessed on the basis of the complete simultaneous equilibria system described in paragraph 5.2.5:

$$Cu^{2+} + 2\,e^- \Leftrightarrow Cu_{(s)} \quad \textbf{5-1}$$

$$Zn^{2+} + 2OH^- \Leftrightarrow ZnO + H_2O \quad \textbf{5-2}$$

$$2\,Cu_{(s)} + OH^- + HS^- \Leftrightarrow Cu_2S_{(s)} + H_2O + 2\,e^- \quad \textbf{5-3}$$

$$ZnO_{(s)} + HS^- \Leftrightarrow ZnS_{(s)} + OH^- \quad \textbf{5-4}$$

$$ZnO_{(s)} + H_2O \Leftrightarrow Zn(OH)_{2(aq)} \quad \textbf{5-5}$$

Equilibria $Cu^{2+} + 2\,e^- \Leftrightarrow Cu_{(s)}$ **5-1** and $Zn^{2+} + 2OH^- \Leftrightarrow ZnO + H_2O$ **5-2** are mainly involved during the steps leading to the deposition of Cu and zincite. Equilibria $2\,Cu_{(s)} + OH^- + HS^- \Leftrightarrow Cu_2S_{(s)} + H_2O + 2\,e^-$ **5-3** and $ZnO_{(s)} + HS^- \Leftrightarrow ZnS_{(s)} + OH^-$ **5-4** are involved in the deposition of sulfur, leading to the sulfidization of Cu and zincite. Starting from the sixth step, everytime that a solution of Cu^{2+} is kept at -0.18 V, the presence of solid sulphides enables the formation of chalcocite at the expense of sphalerite through the competition of equilibria $Cu^{2+} + 2\,e^- \Leftrightarrow Cu_{(s)}$ **5-1** - $ZnO_{(s)} + HS^- \Leftrightarrow ZnS_{(s)} + OH^-$ **5-4**, resulting also in a partial conversion of sphalerite to zincite. Moreover, equilibrium 5 is responsible for the decrease of the total Zn content in the solid phases (at a rate in the range 0.3-1% per cycle) through the dissolution of zincite.

5.3. Ag(111)/Cu_xZn_yS/CdS

5.3.1. Preparation of the samples

The samples have been prepared according to synthesis developed in our laboratory by Berretti et al. [124]. Table 5-7 summarizes the electrochemical synthesis performed for this study. The cadmium sulphide was grown on the Ag(111)/Cu_xZn_yS substrate according to two different methodologies:

1) using the E-ALD method (samples ExCuZnS/CdS, Table 5-7)
2) checking the charge deposited at each cycle (samples QCuZnS/CuS, Table 5-7)

The E-ALD Ag(111)/Cu_xZn_yS substrates were prepared repeating 40 times the cycles described by Cinotti et al. [27,118]. The Cd deposition potential, -0.4 V, has been chosen assuming the peak at –0.3 V related to a SLR. The QCuZnS/CuS samples were prepared repeating cycles constituted by potentiostatic depositions under the control of our programmable automatic systems (paragraph 4.1) which integrate the current over time

and stops the deposition when the charge deposited reaches the set limit. In particular, the sample has been prepared according to the following procedure defining the cycle:

- Cd deposition at - 0.5 V until 75 μC/cm^2 charge are deposited
- Rinsing at - 0.5 V with ammonia buffer
- S deposition at -0.68 V until 75 μC/cm^2 charge are deposited
- Rinsing at - 0.68 V with ammonia buffer

These cycles where repeated 40 times in order to obtain the sample. The deposition potential of cadmium has been chosen as the beginning potential of Cd bulk deposition, as reported in literature [21].

The charge value set for the deposition has instead been chosen observing the deposited amount in the binary film of CdS grown on the Ag (1 1 1) by E-ALD method [21,51,52].

Label	Method	Deposition sequence	Layer scheme
Ag/Sad	*E-ALD*	*Ag/S*	*Ag/S*
Ex20	*E-ALD*	*Ag/(S/Cu/S/Zn)$_{20}$/S*	*Ag/p/S*
ExCuZnS/CdS	*E-ALD*	*Ag/(S/Cu/S/Zn)$_{20}$/(S/Cd)$_{40}$/S*	*Ag/p/n/S*
QCuZnS/CuS	*Charge control*	*Ag/(S/Cu/S/Zn)$_{20}$/(S/Cd)$_{40}$/S*	*Ag/p/n/S*
OpCuZnS/CdS	*E-ALD*	*Ag/(S/Cu/S/Zn)$_{20}$/(S/Cd)$_{40}$/S*	*Ag/p/n/S*

Table 5-7 List of the electrochemical synthesis presented in this paragraph.

5.3.2. Operando analysis at the end of the growth

In the reciprocal space maps (
Figure 5-24) at l=1.05 both Debye rings and Bragg peaks as for Cu_xZn_yS. The Bragg peaks of this phase, if compared with the results illustrated in the paragraph 5.2.3 can be safely assigned to the Cu_2S in the ternary Cu_xZn_yS. However, only the most intense peaks are present whereas most of the intensity diffracted form the deposit lies in the Debye rings.

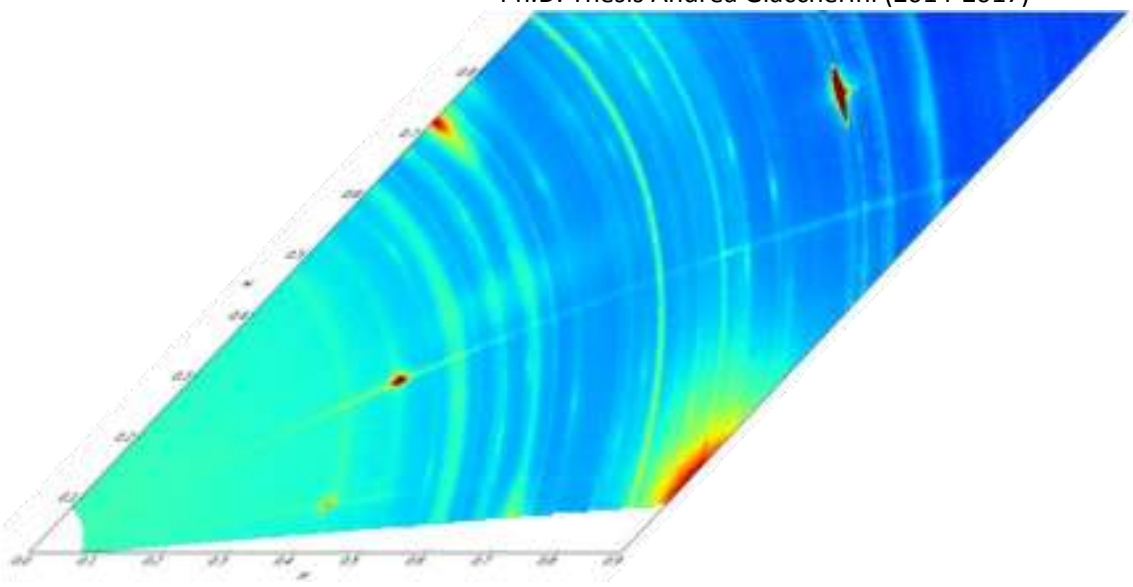

Figure 5-24 The reciprocal space maps (figure X) at l=1.05 for OpCdS/CuS

5.3.3. Micromorphology and semi-quantitative analysis

The secondary electrons (SE) micrographs of the ExCuZnS/CdS and QCuZnS/CuS samples are shown in the Figure 5-25, at different magnifications (3000x and 10000x). At low magnification, the ExCuZnS/CdS and QCuZnS/CuS samples reveal very similar features. In particular, a random distribution of particle aggregates is present on the top of both the investigated surfaces. At the highest magnification, a closer detail of the aggregates is obtained: they exhibit a prevailingly elongated habitus, the elongation dimension ranging between 1 and 2 µm, whereas the particle width is in the submicrometer range. Comparing this feature with the morphology of the ternary film reported in previous studies, we note that the ternary CuZnS film is always characterized by the presence of elongated nano to microstructures, the length of which depends on the number of the E-ALD cycles [67,119]. Accordingly, also in the present case the particle aggregates can be tentatively attributed to a specific feature of the p-layer. Below the aggregates, an almost homogeneous film is covering the Ag(111) electrode surface. The seldom presence of holes, already described for E-ALD films of metal sulphides [28], can be observed.

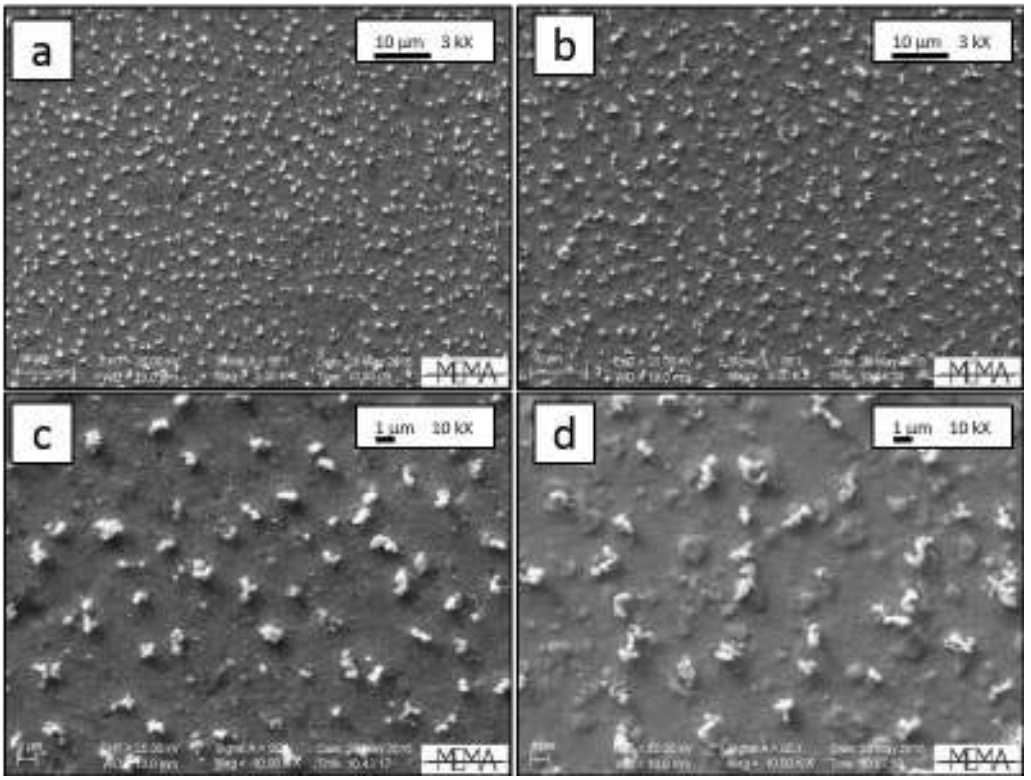

*Figure 5-25 Morphology of the thin films obtained in the two different methods at different magnifications: by E-ALD technique (**a** and **c**) and by checking the deposited charge (**b** and **d**).*

If the micrographs of the samples ExCuZnS/CdS and QCuZnS/CuS samples are compared, only minor differences can be highlighted. The first one (Figure 5-25c) consists in the concentration of aggregates, which appears slightly higher in the ExCuZnS/CdS sample than in the QCuZnS/CuS sample. Then, the Figure 5-25d reveals a higher roughness of the QCuZnS/CuS sample, where the presence of plate particles having an average diameter in the range 1-2 µm is apparent. EDX microanalysis was performed to gain a survey of the chemical composition of the two samples. The results are listed in Table 5-8. The main consideration deals with the Cd content, which can be only semi-quantitatively assessed in the present case through EDX. This is due to the closeness between L-edges of Cd and Ag (≈100 eV), especially taking into account the difference in relative amounts of the two elements (the first is occurring in few atomic layers on the top of a bulk crystal of the second). In this study the percentages were calculated without considering the Ag content, which was assessed from raw EDX data in the range of 90%. An approximated experimental appraisal of the Cd content in the sample can

be sorted out by comparing the (Cu+Zn) over S ratios of the sample before and after the CdS deposition, i.e. comparing the microchemical content of these elements in the ExCuZnS/CdS and QCuZnS/CuS samples, with respect to that of the B sample. Starting from the simple assumption that the addition of 40 layers of CdS over the 20 layers of CuZnS deposit yields in a dilution by a factor of ~2 in the EDS relative concentration, we would expect that the 1.2(2) (Cu+Zn)/S value become ~0.6. The values obtained for this ratio in Table 5-8 are thus consistent with this dilution process, indicating that almost one half of the total metal content of these samples is Cd. If directly evaluated, following the same assumption, 25 at% Cd would be expected. This value compares well with those reported in Table 5-8.

Moreover, Table 5-8 confirms that sample QCuZnS/CuS has a concentration of Zn and Cu consistent with sample B (before the deposition of CdS). Sample C has a lower concentration of Zn with respect to QCuZnS/CuS, while the discrepancy between Cu+Zn sulphides and S is lower, the concentration of Cd is higher than in sample QCuZnS/CuS.

Label	Cu	Zn	Cd	S	Cu/Zn	(Cu+Zn+Cd)/S	(Cu+Zn)/S
Ex20	43±4	12±2	N/D	45±4	3.5±0.9	1.2±0.2	1.2±0.2
ExCdS/CuS	23±6	<1	30±10	44±8	N/D	1.3±0.8	0.5±0.4
QCdS/CuS	17±1	3±1	27±2	53±2	7±3	0.9±0.1	0.37±0.05

Table 5-8 results of the SEM-EDX microanalysis, expressed as at% (atom of an element over 100 atoms in the EDX spot). A peak relative to Zn X-ray emission was observed, but the relative elemental amount remains undetermined because of the high relative uncertainty (6%). Consequently, ratio of Cu/Zn for sample C is undetermined.

5.3.4. XPS analysis

XPS data were acquired on sample ExCuZnS/CdS. Contamination from carbon and oxygen was determined in the order of 30% (surface atomic %), a range very common for a so small sample grown by means of E-ALD. In this context, the investigated depth can be considered roughly around 5 nm. One has to consider that this value probably represents a relevant fraction of the overall ExCuZnS/CdS sample thickness [51]. In , at% referred to Cu, Zn, Cd and S are reported excluding the contribution of contaminating

elements. Among the three transition elements, Cd is the most-abundant, followed by Zn and Cu. This can be explained by the effective formation of CdS above Cu_xZn_yS film underneath. The surface atomic ratios, Cu/Zn, (Cu+Zn)/S and (Cu+Zn+Cd)/S, were also calculated based on a quantitative analysis of XPS data, giving values of 0.3 ± 0.1, 1.8 ± 0.2, and 3.3 ± 0.5, respectively (Table 5-9). From the observation of Cu 2p HR region (Figure 5-26a) the Cu $2p_{3/2}$ photoelectronic peak falls at BE = 932.5 ± 0.1 eV and no shake-up signals between 940 and 945 eV (typical of Cu^{2+} species) can be found, indicating that this element is present as monovalent, as in Cu_2S [28,125].

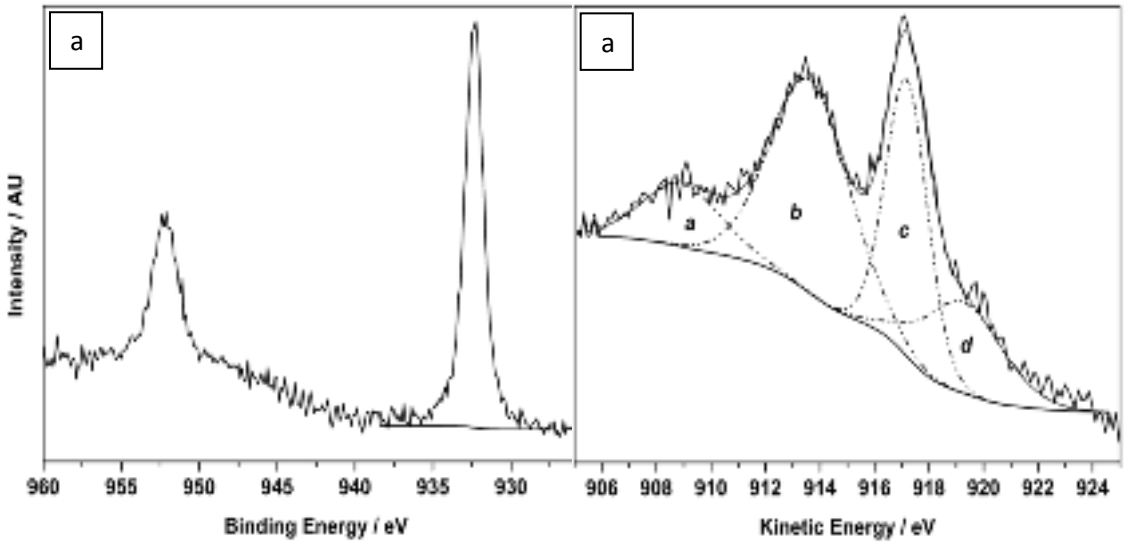

*Figure 5-26 Typical Cu2p (**a**) and Cu $L_3M_{45}M_{45}$ (**b**) regions acquired on thin films CdS/Cu_xZn_yS prepared by E-ALD technique.*

Moreover, Cu $L_3M_{45}M_{45}$ Auger signal (Figure 5-26) was studied performing suitable fit procedures as previously reported on similar films [79]. Position of "c" component, falling at Kinetic Energy (KE) equal to 917.1 ± 0.1 eV, confirms the attribution of copper signal to Cu_2S. Such results are in agreement with previous findings by Caporali et al. [28]. Interestingly, $Zn2p_{3/2}$ position is compatible with the presence of Zn(II) species, though the position of Zn LMM main signal (KE = 987.1 ± 0.1 eV) indicates the prevalence of zinc sulphate over sulphide [126]. Regarding Cd speciation, a single $Cd3d_{5/2}$ peak was found at BE = 405.5 ± 0.1 eV, that is compatible

Cu	Zn	Cd	S	Cu/Zn	(Cu+Zn+Cd)/S	(Cu+Zn)/S
9.5	31.6	35.8	23.2	0.3±0.1	3.3±0.5	1.8±0.2

Table 5-9 Surface abundance (expressed as at%) and element ratios, as determined by XPS analysis on sample ExCuZnS/CdS. Maximum error is ±0.5% for Cu, Zn and Cd; ±0.5% for sulfur.

5.3.5. Discussion

The operando SXRD results have to be considered as preliminary and qualitative, but they reveal that the deposition of CdS occurs, mostly, as a disordered phase. Hence, no CdS epitaxial phase can be registered in the sample OpCuZnS/CdS. It can be also observed an apparent increase between the Debye rings to Bragg peaks intensity ratio with respect to the ternary Cu_xZn_yS discussed in paragraph 5.2.2. This suggests a rearrangement of the Ag(111)/Cu_xZn_yS substrate while the CdS is grown by means of E-ALD. The spectroscopic characterization of the film revealed that it was not possible to assess correctly the elemental concentration of Zn in the ExCuZnS/CdS sample, due to the intrinsically high uncertainty of SEM-EDX at low concentrations. However, there is a substantial difference between sample ExCuZnS/CdS and QCuZnS/CuS, i.e. the lower amount of Zn (≤ 1%) in sample ExCuZnS/CdS. We attribute this difference to the operating potential for the deposition of Cd, which is closer to the oxidation potential of Zn in sample ExCuZnS/CdS than in sample QCuZnS/CuS. Thus, a partial re-dissolution of Zn from the film could likely occur. Preliminary XPS analysis corroborates this hypothesis, showing also that CdS, Cu_2S and Zn(II) are present. Further thermodynamic modelling of this process is in progress. It is worth noting that XPS and SEM-EDX elemental analyses are characterized by different sampling depths, between tens and hundreds of nm for SEM-EDX and few nm for XPS. This means that the film elemental composition as determined by these two techniques can result somehow different. As example, Ag% is dramatically higher in SEM-EDX than in XPS measurements, confirming that the former reckons the average elemental composition in the whole film while the latter investigates only its top layer. However, taking into account the typical thicknesses of the E-ALD deposits obtained after a similar number of cycles, we can state that at least one half of the whole sample is also investigated by XPS. On this ground, we can infer that: 1) CdS is more concentrated on the top of the sample, i.e. the CdS and Cu-Zn sulphide deposits are, at least approximately, layered; 2) Zn is more concentrated in the

top layers of the film while Cu in the bottom layers. This enrichment of Zn in the upper layers of the deposit could be related to both its higher solubility (under the operated physical and chemical conditions) and to its affinity for the CdS structure.

The diffusion of Zn from the inner through the CdS layer should be hindered by the experimental condition (room temperature and pressure) [127,128], however these data are consistent with the operando reciprocal space mapping suggesting a rearrangement of the underlying Cu_xZn_yS phase. The possible presence of Zn in the outer layer would not change its photovoltaic properties, since $Cd_{1-x}Zn_xS$ is a well know n-type semiconducting material [129].

A last consideration deals with the occurrence in ExCuZnS/CdS sample of some Zinc sulphate. Since there are not electrochemical evidences of the deposition of sulphate species, the sulphate layer is probably the results of an ageing process due to the oxidation of S^{2-} following the E-ALD process.

5.4. Ag(111)/CdS/Cu_2S

5.4.1. Preparation of the samples

No related E-ALD study of such system was known before this work, hence the synthesis has been developed by means of several different electrochemical measurements. Table 5-10 presents the electrochemical synthesis performed for this study according to the following protocol defined in this study.

In order to grow the Ag(111)/CdS substrate points 3-6 constitute a cycle repeated 60 times [21].

1. Deposition of S at -0.68 V for 60 s.
2. Rinsing at - 0.68 V with ammonia buffer.
3. Deposition of Cd at -0.65 V for 120 s.
4. Rinsing at -0.65 V with ammonia buffer.
5. Deposition of S at -0.68 V for 60 s.
6. Rinsing at -0.68 V with ammonia buffer.

In order to grow the Cu_2S substrate points 1-4 constitute a cycle repeated 30 times (see. paragraphs 5.4.2, 5.4.3 and 5.4.4):

1. Deposition of Cu at -0.425 V for 120 s.
2. Rinsing at -0.425 V with ammonia buffer.
3. Deposition of S at -0.68 V for 60 s.
4. Rinsing at -0.68 V with ammonia buffer.

Label	Method	Deposition sequence	Layer scheme
OpCdS/CuS	*E-ALD operando at ESRF*	$Ag/(S/Cd)_{60}/(S/Cu)_{30}/S$	*Ag/n/p*
ExCdS/CuS	*E-ALD ex-situ at UNIFI*	$Ag/(S/Cd)_{60}/(S/Cu)_{30}/S$	*Ag/n/p*

Table 5-10 *list of the electrochemical synthesis presented in this paragraph.*

5.4.2. EC study of the buffer solution on Ag(111)/$(S/Cd)_{60}$/S surface

The substrate consisting of the Ag(111) electrode covered by the CdS film was deposited according to the protocol reported in paragraph 5.4.1. The electroinactivity window of this new substrate was determined by means of cyclic voltammetry of the buffer solution. To avoid oxidation of the substrate (Ag), the cyclic voltammetry of the buffer solution on the Ag(111)/$(S/Cd)_{60}$/S electrode was performed starting from -0.680 V to -0.350 V, -0.400 V and -0.100 V at a scan rate of 50 mV/sec (Figure 5-27). As we can see from the anodic sweep ending at -0.100 V, metals start to dissolve at about -0.250 V. In the cathodic sweep, two cathodic currents are evident at -0.250 V and -0.625 V (Figure 5-27). Considering the previous works on the Cu_2S E-ALD on the Ag(111) substrate (see paragraph 5.1), we can thus preliminarily consider the range between -0.300 V and -0.65 V as a practicable potential window for the Cu deposition. However, it should be noticed that the oxidation of Cd from Ag(111)/CdS occurs at the same potential of the oxidation of Cu from Ag(111)/Cu_2S. Thus the growth of Cu_2S over Ag(111)/CdS cannot be studied by means of stripping voltammetries as often reported in literature for other systems.

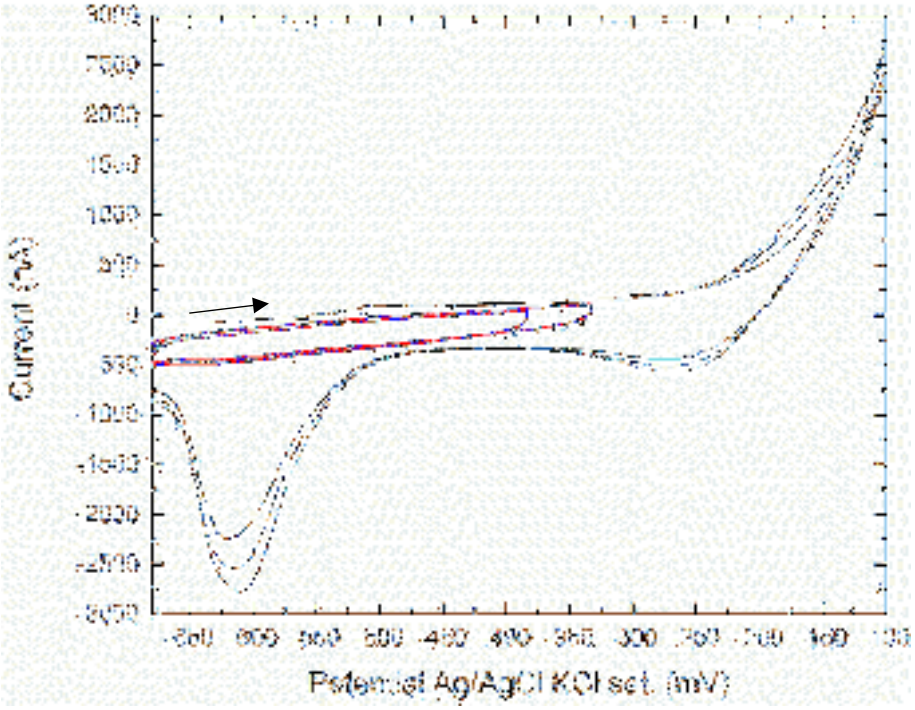

Figure 5-27 Cyclic voltammetries at different anodic vertex potentials (50 mV/s)

5.4.3. EC study of the Cu^{2+} solution on Ag(111)/$(S/Cd)_{60}$/S surface

In order to refine the viable potential for the electrodeposition of Cu, cyclic voltammetries of copper solution (0.5 mM $CuCl_2$) were performed on the Ag(111)/$(S/Cd)_{60}$/S substrate in the electroinactivity of the substrate (-0.650 V to -0.300 V). We repeated 5 cyclic voltammetries on Ag(111)/$(S/Cd)_{60}$/S at different cathodic vertex potentials without changing the solution (Figure 5-28 and Figure 5-29). In both the voltammetries of Figure 5-28 at the first cycle there is no evident peak, however a big cathodic current (up to -23 μA) is present, no anodic peak has been registered. In the following voltammetries the current deacreases and no peaks are shown again. Figure 5-28b is clearly showing an increase in cathodic current after -0.490 V associated with a peak at -0.350 V. Still, the current decreases after a few cathodic cycles.

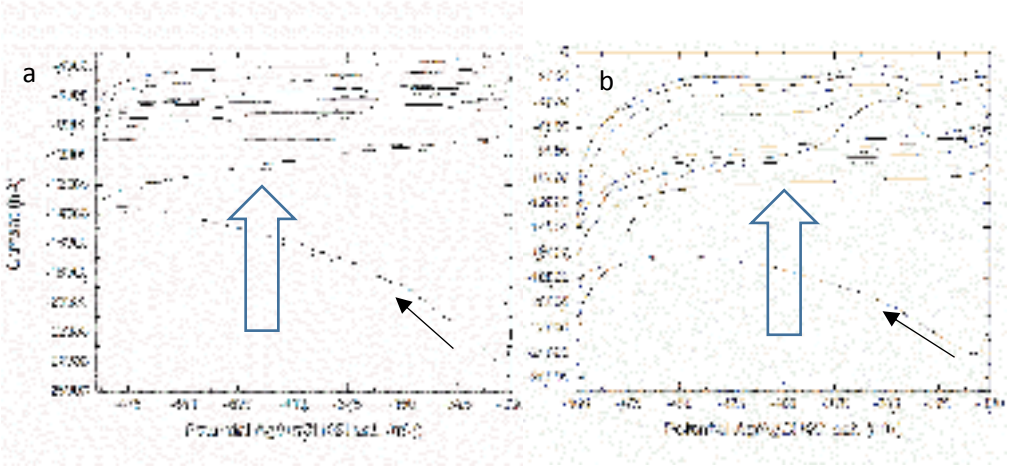

Figure 5-28 Cyclic voltammetries at different cathodic vertex potentials (a) -0.490 V (b) -0.500 V (50 mV/s).

To better understand the peaks in Figure 5-28 we repeated the set of 5 cyclic voltammetries for for smaller increase of the cathodic vertex potential. Figure 5-29a and 5-29b respectively depicts the results of the first and last cyclic voltammetries of each series. Figure 5-29 shows clearly how the first 5 voltammetries are not superimposable, since the solution is changed between each series there is a hysteresis of the system that has to be related to the modification of the surface. Moreover, the wide cathodic peak at -0.450 V appears only after a few voltammetric cycles. There are no associated anodic peaks, but a small current at -0.380 V appears. The emerging of this cathodic peak is probably related to the modification of the surface as well.

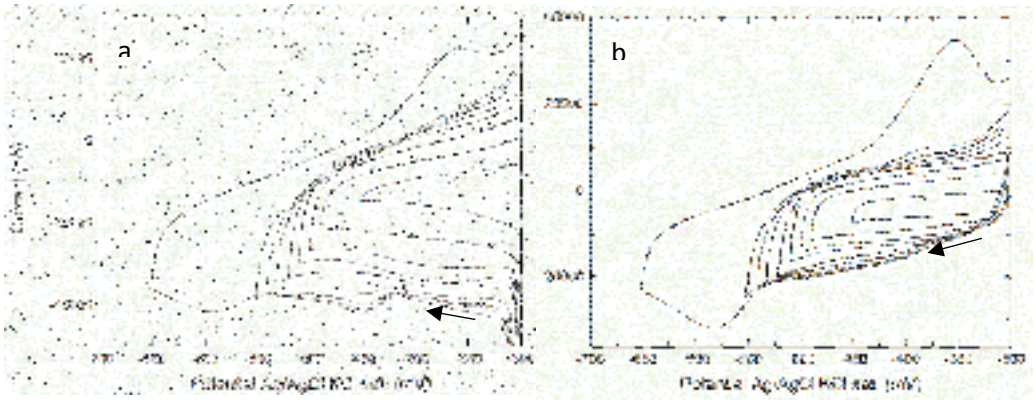

Figure 5-29 Cyclic voltammetries at different cathodic vertex potentials (a) first cyclic voltammetries (b) fifth cyclic voltammetries (50 mV/s).

Finally, while the cathodic peak at -0.600 V and the associated anodic peak at -0.380 V increases with the number of cycles the peak at -0.450 vanishes. Although, we cannot establish definitely the surface limited character of the process related to the cathodic peak at -0.450 V we can safely exclude that the process occurring at -0.600 V is not surface limited.

5.4.4. EC study of the Cu^{2+} solution on $Ag(111)/(S/Cd)_{60}/(S/Cu)_n/S$ surface

Linear sweep voltammetries of copper solution (0.5 mM) were performed on the $Ag(111)/(S/Cd)_{60}/(S/Cu)_n/S$ substrate to confirm that the viable potential found in paragraph 5.4.3 leads to a reproducible occurring of SLR over different potentiostatic treatment. The behaviour of the copper solution on the surface $Ag(111)/(S/Cd)_{60}/S$ is well described in paragraph 5.4.3, showing no peaks. However, it is found different after a potentiostatic treatments in copper solution at -0.425 for 120 seconds. Specifically, performing four consecutive cathodic scans (linear sweeps in the cathodic sense) we obtain the curves shown in Figure 5-30. If the following steps are repeated three times:

1. Deposition of Cu at -0.425 V for 120 s.
2. Rinsing at -0.425 V with ammonia buffer.
3. Deposition of S at -0.68 V for 60 s.
4. Rinsing at -0.68 V with ammonia buffer.

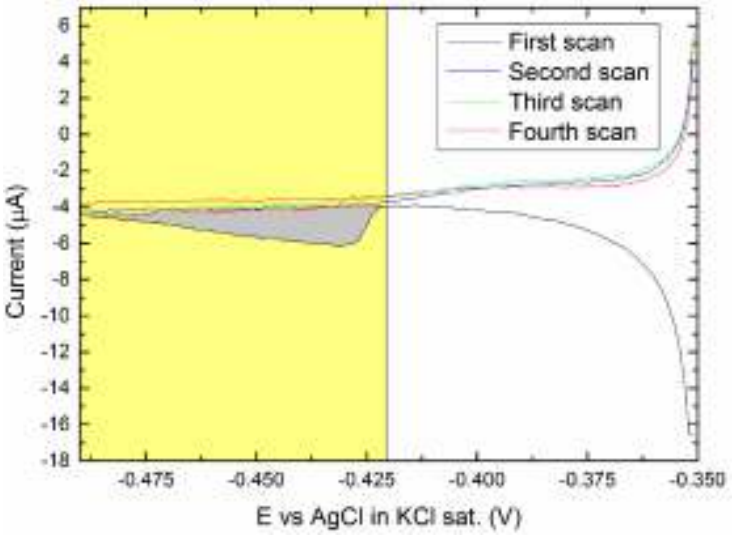

Figure 5-30 Four consecutive cathodic scan at 1mV/s, after the first cycle the grey area corresponf to the charge transfered (100.1 $\mu C/cm^2$) .

Then the four consecutive cathodic scans are consistently superimposable to the curves in Figure 5-30. This trend continues when reapeting the steps for several times. The peak is present in the first scan, vanishes if the scan rate is low enough, Figure 5-30 shows cathodic scans at 1 mV/s. For such slow scan rates the peaks can be considered a good estimation of the charge transferred by the associated process. The value of ~100 $\mu C/cm^2$ is comparable with a Cu_{ad} on Ag/S_{ad}.

5.4.5. Micromorphology and semi-quantitative analysis

The micrographs in Figure 5-31 show that the ExCdS/CuS surface is characterized by two main morphologies:

- a flat surface with some holes
- several small worm-like structures overgrowing the flat surface

The density if this worm-like structure is lower near the edges of the electrode as shown by Figure 5-31d. Table 5-11 reports the result of the semiquantitive EDX analysis. It should be reported that due to several interferences (i.e. Cd peaks with Ag) the results have just a qualitatively nature, suggesting that the process studied in paragraph 5.4.4 deposits effectively copper bearing phases on the substrate.

Label	Cu	Cd	S	Cu/S
ExCdS/CuS	55±4	N/D	45±4	1.2±0.2

Table 5-11 *results of the SEM-EDX microanalysis, expressed as at% (atom of an element over 100 atoms in the EDX spot). The peaks relative to Cd X-ray emission are superiomposed to the peaks of Ag. Consequently, the at% of Cd is not reported in the table.*

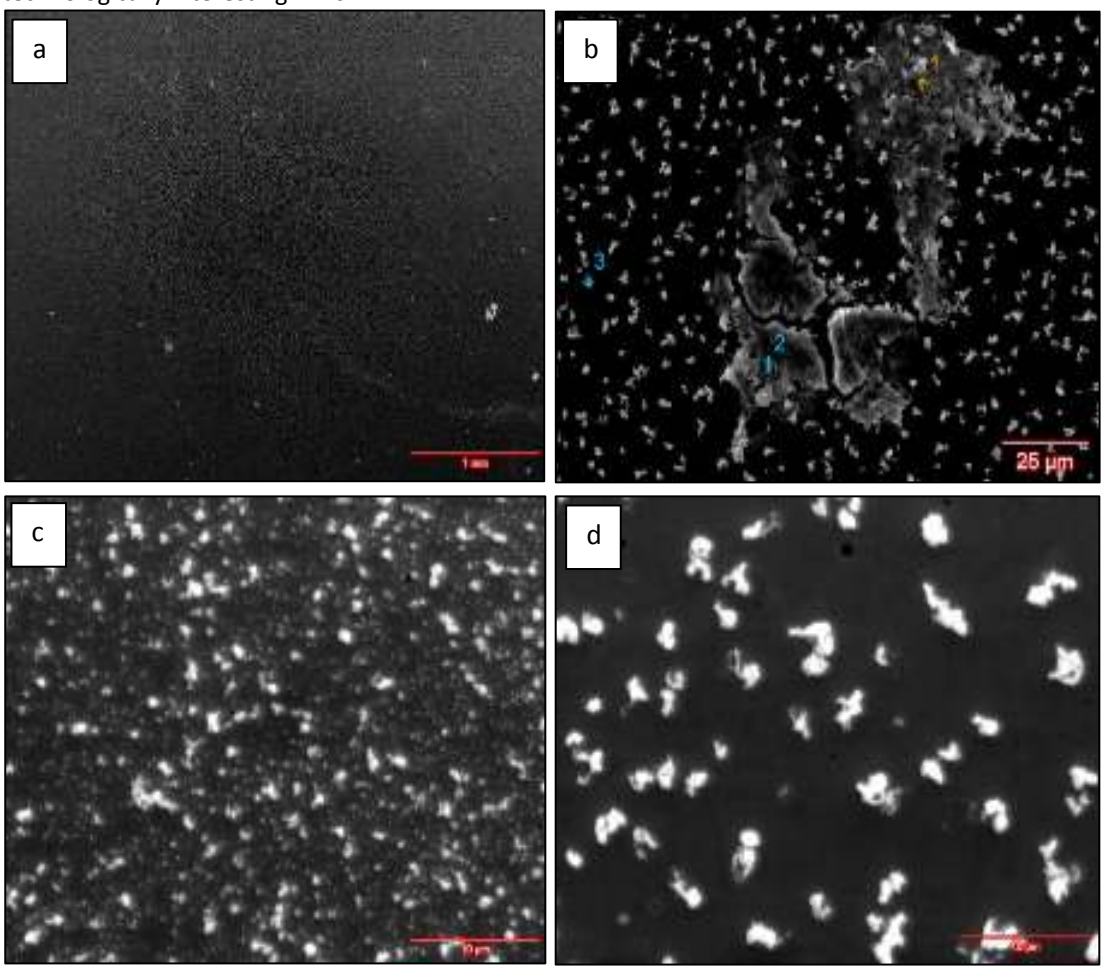

Figure 5-31 Micrographs of two representing portion of the sample ExCdS/CuS. In the center of the electrode at 30X (a), 800X(b), 3000X(c) and close the electrode edges at 3000X (d).

5.4.6. Operando analysis of the growth

SXRD analysis on selected peaks was performed every 6 cycles of Cu_2S E-ALD growth on $Ag(111)/(S/Cd)_{60}/S$ up to the 30^{th} cycles. The peaks approximately located at (0.73, 0.73, 1.05) and (0.67, 0.67, 2.32) allowed to monitoring eventual structural changes during the growth respectively for the CdS (greenockite) structure in the $Ag(111)/(S/Cd)_{60}/S$ substrate and the Cu_2S (chalcocite derived) structure expected in $Ag(111)/(S/Cd)_{60}/(S/Cu)_n/S$ overgrown (Figure 5-32). As shown by the related peak the

CdS layer does not change during the growth of Cu_2S. Moreover, the peak at (0.67, 0.67, 2.32) as FWHM of 0.08 while for (0.73, 0.73, 1.06) is 0.4-0.2 according to the growth stage.

Figure 5-33 depicts the trends of the 4 parameters obtained from the fit of the Voigt function on the peaks of Figure 5-32b. The plot in Figure 5-33a shows that the amount of deposited material increases with the deposition cycles. Still, we can see a possible saturation of the growth at the 30th cycle. Figure 5-33b show the position in the reciprocal space of the maximum of the observed peak, which is straightly related to the dimension of the unit cell. From the 12th onward the position of the Bragg peak is well defined but continuously increasing during the process. Interestingly, the position of the Bragg peaks (l=1.055) is slightly expanded with respect to Ag(111)/Cu_2S (l=1.045).

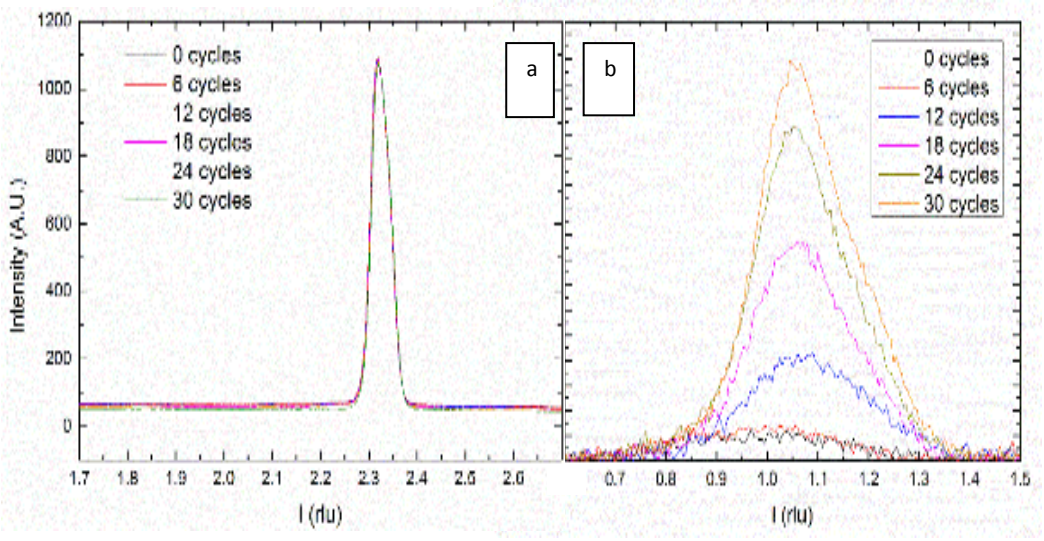

Figure 5-32 *Profiles of the Bragg peaks along the c* direction at (0.67, 0.67) (a) and (0.73, 0.73) (b).*

Figure 5-33c and Figure 5-33d depict the Gaussian and Lorentzian widths respectively, versus the growth cycles of Cu_2S. While Gaussian width seem to decrease during the growth, the Lorentzian width is roughly constant. Noticeably, the saturation of the

intensity of the Bragg peak coincides with the saturation of the Lorentzian width (30th cycle).

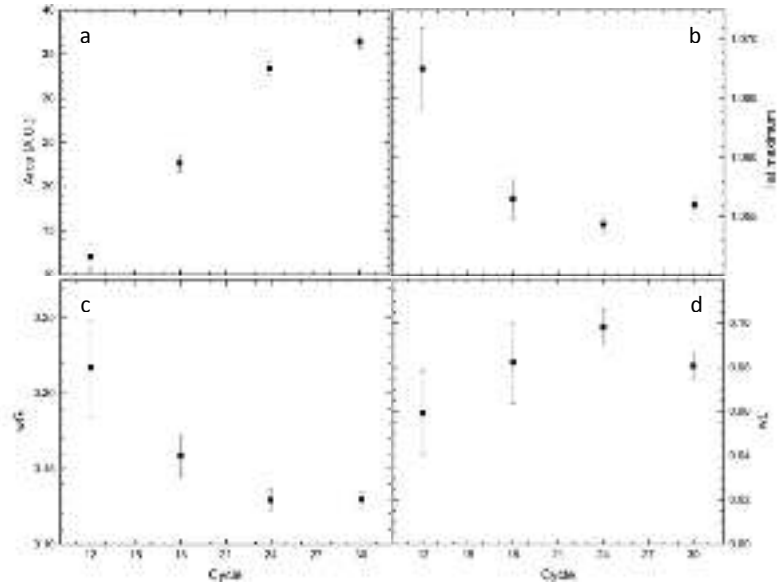

Figure 5-33 Growth curves for the peak area (a), the position at the maximum (b), the Gaussian breadth (wG) (d) and the Lorentzian breadth (wL) (d) along (0.73, 0.73, l). The experimental uncertainties are plotted as error bars corresponding to 3σ.

5.4.7. Discussion

The main achievement of this part of the study is the observation of the growth of Cu sulfide over Ag(111)/(S/Cd)$_{60}$/S by E-ALD. The Ag(111)/(S/Cu)$_{60}$/S and Ag(111)/(S/Cd)$_{60}$/(S/Cu)$_{30}$/S revealed the same structural arrangement concerning the Cu_2S phase (see paragraph 5.1.6). Similarly to the Ag(111)/(S/Cu)$_{60}$/S, the ratio Cu:S=2 in the Cu_2S layer of Ag(111)/(S/Cd)$_{60}$/(S/Cu)$_{30}$/S is justified by the crystal chemistry of the $Cu_{2-x}S$ system.

The electrochemical stability potential window of the Ag(111)/(S/Cd)$_{60}$/S was ascertained as occurring in the potential range between -0.300 V and -0.650 V (Figure 5-27). This represents a practicable potential window for the deposition of Cu. In fact, the potential value for the SLR on Ag(111)/S is -0.380 V and for the bulk deposition is roughly -450 V respectively (depending on the kinetics, see Figure 5-28). However, the straightforward determination of the amount of Cu deposited on Ag(111)/(S/Cd)$_{60}$/S is

impared by the superposition of the stripping currents related to the anodic dissolution of Cd.

Hence, a different approach had to be applied to check the occurrence of an SLR and eventually to refine its potential. Specifically, in the relative CVs only a peak related to the bulk deposition was revealed (Figure 5-28). Running several CVs in the potential range where the bulk deposition does not occur, a further peak at -0.450 V appeared (Figure 5-29). The vanishing of the peak at -450 V over several consecutive CVs suggests the surface limited character of the process while the increase of the cathodic peak at -0.580 confirm that it is consistent with a bulk deposition (e.g. from the comparison of the Figure 5-29a and Figure 5-29b). However, the fact that the peak at -0.580 V it is registered only after an adequate electrochemical treatment suggests a rearrangement of the Ag(111)/$(S/Cd)_{60}$/S surface. From a practical standpoint this means that the surface has to be "activated" before starting the growth.

Noticeably, the two registered cathodic peaks are dramatically shifted with respect to the bulk and SLR deposition peaks of Cu on Ag(111)/S respectively -0.430 V and -0.380 V. The potential shift of SLR peak when changing surface from Ag(111) to Ag(111)/S/$(Cd/S)_{60}$ is not surprising. However, the dramatic potential shift for the Bulk deposition is unusual and suggest a slower kinetics of the Cu deposition on Ag(111)/$(S/Cd)_{60}$/S with respect to the Ag(111)/S. Finally, the SLR nature of the Cu deposition on Ag(111)/$(S/Cd)_{60}$/S has been confirmed repeating the cathodic scans in Figure 5-30 every three cycles of potentiostatic treatment to deposit S (at -0.680 V in S^{2-} solution) and Cu (at -0.425 V in Cu^{2+} solution).

The micromorphology of the samples ExCdS/CuS presented in Figure 5-31 is consistent with the micromorphology of ExCuS suggesting an ordered growth of the former. The EDX analysis of the samples registered the presence of Copper confirming that the at -0.425 V in Cu^{2+} solution is in-fact leading to the deposition of copper

Electrochemical and spectroscopic evidences indicate the effective growth of Cu_2S on Ag(111)/CdS by means of E-ALD. Conversely, the question if this growth is ordered has not yet found a definite assessment. Moreover, the structure of the substrate can be altered by the growth of Cu_2S, although without exchanging electrons with the surface. The main peaks related to CdS and Cu_2S structures were monitored during the E-ALD growth of Cu_2S on Ag(111)/CdS confirming that while the Cu_2S grows, the intensity and position of the reflections due to the structure of CdS remains unchanged. This reveals that no intermixing/recombination is occurring during the growth. The process seems to reach a saturation of the growth at the 30th cycles but this has to be confirmed running more E-ALD cycles. However, the position of the Cu_2S along l is set after the 6th cycle as for the growth of Cu_2S on Ag(111) (paragraph 5.1.3) with a slightly expanded reciprocal coordinate if compared with Cu_2S on Ag(111). This is likely due to the epitaxial relationship between Cu_2S and CdS. Differently from Cu_2S on Ag(111) the epitaxial

growth of Cu_2S on Ag(111)/CdS occurs including defects during the growth on a more rough surface.

6. Conclusion

In the context of the bottom approach for the semiconducting materials and devices based on sulphides thin films, the E-ALD has been studied to answer the questions introduced in paragraph 2.5, emerging from the recent literature. It is worth to mention that, in the development of this study, the conditions for the growth of p-n junctions, based on the sulphides thin film technology, were set up, for the first time.

Exploiting the *operando* SXRD techniques, the first structural characterization of Cu and Zn-bearing sulphides semiconducting materials grown by means of E-ALD was carried out. With respect to previously reported CdS SXRD study, the hereby discussed Cu and Zn presented problems difficult to overcome:

- The Cu-S compositional field include 6 related structures close to the Cu_2S end-member, described by a much more complex elementary cell (e.g. Cu_2S chalcocite has 144 atoms in the unit cell). From a structural standpoint, the interpretation of diffraction data resulted more challenging than CdS especially when considering the possible epitaxial relationship with Ag(111).
- Cu and Zn have lower atomic scattering factors than CdS, hence a lower signal to noise ratio. This constituted a challenging problem from a technological standpoint.
- The smoothest of the films hereby discussed has an *operando* roughness higher than CdS, impairing a successful characterization through XRR, to reckoned the thickness. This rise a quest for a methodological approach to interpret the XRR data.

In the usual framework behind the E-ALD process, Cu_2S stoichiometry is not expected. In fact, the layer-by-layer growth, when at regime, should grow a CuS compounds "mimicking" the Ag(111) as happens for most of the binary discussed in chapter 2. On the basis of crystal chemistry considerations, we showed that this is not the case and the Cu:S ratio is 2:1, starting from the 4^{th} cycle. Moreover, the growth process is epitaxial although more complex that what has been proposed before. Since a constant amount of defects is included during the growing process, at the end of the growth the structure undergoes a structural rearrangement, which likely drives the formation of the small worm-like structure found by SEM investigation.

Similarly to Cu_2S ex-situ, but more evidently, the morphology of the Cu_xZn_yS, is characterized by a thread-like arrangement of worm-like structures of Cu_2S overgrowing a flat and epitaxial surface. The growth of the Cu_xZn_yS film is characterized by an epitaxial phase and a polycrystalline phase. The presence of zinc sulphide phases have been

confirmed by recording barely detectable wurtzite's Bragg peaks and Debye rings. However, these signals cannot explain completely the whole amount of Zinc found by SEM investigation, revealing a probable metastable inclusion of Zn in Cu_2S structure. Such inclusion should be referred as a defect, due to the immiscibility of copper and zinc sulphides [120]. Hence, this can explain the greater accumulation of stress of the Cu_2S phase in Cu_xZn_yS sample with respect to the Cu_2S sample. At this point, it is clear the role of the lattice strain due to inclusion of defects in the determination of the features of the final structure and morphology of Cu_xZn_yS. Regarding the zinc deficiency, the E-ALD growth of Cu_xZn_yS is not the only E-ALD process suffering of the deficiency of the less noble metal. In fact, a zinc deficiency in $Cd_xZn_{1-x}S$, and a Sn deficiency in Cu_xSn_yS have been reported in the past years, even if the Cd-Zn and Cu-Sn related ternary sulphides are well studied in the mineralogical literature. These results have been confirmed by chemical speciation models indicating the chemical equilibrium involved in the dissolution of the less noble phases (e.g. zinc sulphide phases) and the competitive precipitation of the more noble one (e.g. copper sulphide phases). We could say that the study of the growth of ternary compounds highlighted the role of the thermodynamic stability of the phases in the E-ALD growth.

The results gathered for the whole set of samples hereby reported suggest an unexpectedly complex growth mechanism underlying the E-ALD process in complex systems. The growth of these samples, in fact, is driven by the free energy of formation of the related compounds imposing stoichiometry and structure through a complex set of competitive processes. The surface limited equilibria induce the epitaxiality of the process, driving the ordering of the films. Still, other competitive factors (microcrystalline stresses and other chemical equilibria) concur to the final features of the film. For instance, the release of the stress accumulated is most likely the cause for the emerging of the worm-like structure observed ex-situ for the Cu_2S and astonishingly evident for both the in-situ and ex-situ Cu_xZn_yS films. On the other hand, the multiple competitive equilibria forecasted by chemical speciation models suggest that the stoichiometry is determined by the precipitation and re-dissolution of the chemical species as clearly discussed by paragraph 5.2.6. From a purely thermodynamic standpoint, these competitive processes can be described as discussed in Chapter 3. Likely, they have different influence on the thin film features according to the different stages of the growth. For instance, as discussed in paragraph 5.2, the strain and consequently the elastic energy clearly increases with the growth steps, until it becomes the predominant factor determining the morphology of the overlayer. On the other hand, the interaction with the surface, inducing the excess of the chemical species and the related absorption process driving the SLRs, becomes less important when the

thickness of the film increases. Finally, the SXRD on the Cu_2S revealed also at the first stages of the growth, in some cases, the free energy of formation of the semiconducting compound to potentially determine the stoichiometry of the sample. In this context, it is clarified that the process occurs within the boundaries established by thermodynamics, which cannot include solely the surface interactions, but also the strain and all the chemical equilibria involving the compounds grown during the process.

In this context, we answered to the last of the questions raised in paragraph 2.5 with a proof of concept. It is possible to apply the E-ALD process to grow devices? We proved that it is possible to grow with E-ALD two highly crystalline thin films, one on top of the other (Ag(111)/CdS/Cu_2S) without mixing the two phases. Electrical characterizations are in development, exploiting a dedicated setup to avoid dramatic surface modifications due to the interactions of a solid electric collector with the device. Several technological challenges have to be addressed to perform an electric characterization of such a ultra-thin layer device. Still, since the two thin films are, one n-type and the other p-type, we concluded to have grown the first p-n junction by means of E-ALD. The structural characterization confirmed that the two layers are highly ordered and epitaxial with barely strained crystallites. These last results prove that E-ALD is suitable for growing very ordered devices, characterized by an extremely low thickness to area factor controlling the thickness and structure of the layers.

In conclusion, although we confirmed that the E-ALD process cannot be described merely by a sequence of surface processes, we also showed that this does not constitute necessarily an impairing limit for the growth of nanoelectronic devices. Finally, we confirmed that E-ALD is a good candidate to grow, under the limitation of the complex thermodynamic description of the process, devices with high structural and chemical purity.

Bibliography

1. Nano and Giga Challenges in Microelectronics. (Elsevier, 2003).

2. Association, S. I. & others. International Technology Roadmap for Semiconductors 2015. Austin, TX (2015).

3. Frank, D. J. et al. Device scaling limits of Si MOSFETs and their application dependencies. Proc. IEEE **89,** 259–288 (2001).

4. Alhajji, A. F. Hubbert's peak: the impending world oil shortage. Resources Policy **28,** (Princeton University Press, 2002).

5. Bihouix, P. & De Guillebon, B. Quel Futur pour les Métaux ? - Raréfaction des Métaux : Un Nouveau Défi pour la Société. (EDP sciences, 2010).

6. Nozaki, H. et al. Crystal structure determination of solar cell materials: Cu_2ZnSnS_4 thin films using X-ray anomalous dispersion. J. Alloys Compd. **524,** 22–25 (2012).

7. Schorr, S. Structural aspects of adamantine like multinary chalcogenides. Thin Solid Films **515,** 5985–5991 (2007).

8. Bouaziz, M., Ouerfelli, J., Amlouk, M. & Belgacem, S. Structural and optical properties of Cu 3SnS 4 sprayed thin films. Phys. Status Solidi Appl. Mater. Sci. **204,** 3354–3360 (2007).

9. Ramasamy, K., Malik, M. A. & O'Brien, P. Routes to copper zinc tin sulfide Cu2ZnSnS4 a potential material for solar cells. Chem. Commun. **48,** 5703 (2012).

10. Terlemezo, M. Copper Zinc Tin Sulfide-Based Thin Film Solar Cells. (Wiley, 2015).

11. Delbos, S. Këwhile thin films for photovoltaics : a review. EPJ Photovoltaics **3,** 35004 (2012).

12. Wang, W. et al. Device characteristics of CZTSSe thin-film solar cells with 12.6% efficiency. Adv. Energy Mater. **4,** 1301465 (2014).

13. Jiang, F., Ikeda, S., Harada, T. & Matsumura, M. Pure Sulfide Cu_2ZnSnS_4 thin film solar cells fabricated by preheating an electrodeposited metallic stack. Adv. Energy Mater. **4,** 1301381 (2014).

14. Septina, W., Ikeda, S., Kyoraiseki, A., Harada, T. & Matsumura, M. Single-step electrodeposition of a microcrystalline $Cu_2ZnSnSe_4$ thin film with a kesterite structure. Electrochim. Acta **88,** 436–442 (2013).

15. Bernardini, G. P. et al. New data on the Cu_2FeSnS_4-Cu_2ZnSnS_4 pseudobinary

system at 750C and 550C. Eur. J. Miner. **2,** 219 (1990).

16. Deligianni, L., Ahmed, S. & Romankiw, L. T. The Next Frontier : Electrodeposition for Solar Cell Fabrication. Electrochem. Soc. Interface **20,** 47–53 (2011).

17. Riha, S. C., Parkinson, B. A. & Prieto, A. L. Compositionally tunable $Cu_2ZnSn(S_{1-x}Se_x)_4$ nanocrystals: Probing the effect of Se-inclusion in mixed chalcogenide thin films. J. Am. Chem. Soc. **133,** 15272–15275 (2011).

18. Lu, W. & Lieber, C. M. Nanoelectronics from the bottom up. Nat. Mater. **6,** 841–850 (2007).

19. Stickney, B. W. & Gregory, J. L. Electrochemical atomic layer epitaxy (ecale). J. Electroanal. Chem. **300,** 543–561

20. Innocenti, M. et al. Fabricating energy devices with low environmental impacts. SPIE Newsroom 2–4 (2016). doi:10.1117/2.1201512.006249

21. M. Innocenti, G. Pezzatini, F. Forni, and M. L. F. CdS and ZnS Deposition on Ag(111) by Electrochemical Atomic Layer Epitaxy. J. Electrochem. Soc. **148,** C357–C362 (2001).

22. Innocenti, M. et al. Electrochemical behavior of As on silver single crystals and experimental conditions for InAs growth by ECALE. J. Electroanal. Chem. **514,** 75–82 (2001).

23. Loglio, F. et al. Nickel sulfur thin films deposited by ECALE: Electrochemical, XPS and AFM characterization. J. Electroanal. Chem. **638,** 15–20 (2010).

24. Innocenti, M. et al. Electrochemical layer by layer growth and characterization of copper sulfur thin films on Ag(1 1 1). Electrochim. Acta **58,** 599–605 (2011).

25. Foresti, M. L. et al. Ternary CdS_xSe_{1-x} deposited on Ag(111) by ECALE: Synthesis and characterization. Langmuir **21,** 6900–6907 (2005).

26. Loglio, F. et al. Ternary $Cd_xZn_{1-x}Se$ deposited on Ag (1 1 1) by ECALE: Electrochemical and EXAFS characterization. Electrochim. Acta **53,** 6978–6987 (2008).

27. Innocenti, M. et al. Electrochemical growth of Cu-Zn sulfides. J. Electroanal. Chem. **710,** 17–21 (2013).

28. Caporali, S. et al. Sn-deficiency in the electrodeposited ternary $Cu_xSn_yS_z$ thin films by ECALE. Sol. Energy Mater. Sol. Cells **138,** 9–16 (2015).

29. Haissinsky, M. Recherche électrochimique sur le polonium (suite et fin). J. Chim. Phys. **30,** 27–46 (1933).

30. Haissinsky, M. & Danon, J. Isotherme d'adsorption dans la formation de dépots

électrolytiques inférieurs à une couche monoatomique. J. Chim. Phys. **48,** 106–107 (1951).

31. Coche, A. & Haissinsky, M. Electrochimie-Etude Du Depot Electrolytique De Polonium Sur Le Tantale, Le Tungstene Et Le Molybdene. Comptes Rendus Hebd. Des Seances L Acad. Des Sci. **222,** 1284–1286 (1946).

32. Haissinsky, M. Mécanisme des dépôts électrolytiques et expériences avec les radioéléments. J. Chim. Phys. **43,** 21–29 (1946).

33. Haissinsky, M. Recherche electrochimique sur le polonium. J. Chim. Phys. **29,** 453–473 (1932).

34. Danon, J. & Haissinsky, M. Role De La Polarisation Prealable Dans Lelectrolyse De Solutions Extrememement Diluees. J. Chim. Phys. Physico-Chimie Biol. **47,** 953 (1950).

35. Byrne, J. T., Rogers, L. B. & Griess, J. C. Electrodeposition Behavior of Traces of Silver III. Transition Region Between and Behavior. J. Electrochem. Soc. **98,** (1951).

36. Rogers, L. B., Krause, D. P., Griess, J. C. & Ehrlinger, D. B. The Electrodeposition Behavior of Traces of Silver. J. Electrochem. Soc. **95,** 33–46 (1949).

37. DeGeiso, R. C. & Rogers, L. B. Electrodeposition behavior of trace amounts of copper. J. Electrochem. Soc. **106,** (1959).

38. Kolthoff, I. M. & Tanaka, N. Rotated and Stationary Platinum Wire Electrodes: Residual Current-Voltage Curves and Dissolution Patterns in Supporting Electrolytes. Anal. Chem. **26,** 632–636 (1954).

39. Haenny, C. & Mivelaz, P. Recherches préliminaires effectuées à l'aide du radio-zinc 65. Helv. Chim. Acta **31,** 633–642 (1948).

40. Haenny, C. & Reymond, P. Etude du depot electrolytique du zinc en solutions diluees et tres diluees. Helv. Chim. Acta **37,** 2067–2083 (1954).

41. Bowles, B. J. Packing Density of Atoms in Metallic Monolayers on Platinum. Nature **212,** 1456–1457 (1966).

42. Bowles, B. J. Formation of monolayers of copper on platinum electrodes. Electrochim. Acta **15,** 589–598 (1970).

43. Bowles, B. J. Formation and desorption of monolayers of bismuth on a platinum electrode. Electrochim. Acta **15,** 737–747 (1970).

44. Bowles, B. J. Adsorption of cations on platinum—II. Charging curve studies for thallium. Electrochim. Acta **10,** 731–746 (1965).

45. Bowles, B. J. The specific adsorption of cations on electrodes—I. The adsorption of thallium on platinum at controlled potentials. Electrochim. Acta **10,** 717–729 (1965).

46. Hamilton, I. C. & Woods, R. An investigation of the deposition and reactions of sulphur on gold electrodes. J. Appl. Electrochem. **13,** 783–794 (1983).

47. Zell, C. A., Endres, F. & Freyland, W. Electrochemical insitu STM study of phase formation during Ag and Al electrodeposition on Au (111) from a room temperature molten salt. Phys. Chem. Chem. Phys. **1,** 697–704 (1999).

48. Aloisi, G. D. et al. In situ STM and electrochemical investigation of sulfur oxidative underpotential deposition on Ag(111). J. Phys. Chem. B **101,** 4774–4780 (1997).

49. Gao, X., Zhang, Y. & Weaver, M. J. Observing surface chemical transformations by atomic-resolution scanning tunneling microscopy: sulfide electrooxidation on gold(111). J. Phys. Chem. **96,** 4156–4159 (1992).

50. Demir, U. & Shannon, C. A Scanning Tunneling Microscopy Study of Electrochemically Grown Cadmium Sulfide Monolayers on Au(111). Langmuir **10,** 2794–2799 (1994).

51. Carlà, F. et al. Electrochemical atomic layer deposition of CdS on Ag single crystals: Effects of substrate orientation on film structure. J. Phys. Chem. C **118,** 6132–6139 (2014).

52. Foresti, M. et al. Electrochemical atomic layer epitaxy deposition of CdS on Ag (111): An electrochemical and STM investigation. J. Phys. Chem. B **102,** 7413–7420 (1998).

53. Fernandes, V. C. et al. Electrodeposition of PbS multilayers on Ag(111) by ECALE. J. Appl. Electrochem. **39,** 2191–2197 (2009).

54. Innocenti, M. et al. Underpotential Deposition of Sn on S-Covered Ag(111). ECS Trans. **50,** 1–7 (2013).

55. Lastraioli, E. et al. In Situ Scanning Tunneling Microscopy Investigation of Sulfur Oxidative Underpotential Deposition on Ag(100) and Ag(110). Langmuir **26,** 17679–17685 (2010).

56. Room temperature nano- and microstructure photon detectors. Microelectronics J. **40,** 507–511 (2009).

57. Brennan, T. P. et al. Efficiency enhancement of solid-state PbS quantum dot-sensitized solar cells with Al2O3 barrier layer. J. Mater. Chem. A **1,** 7566 (2013).

58. Lachenwitzer, A., Morin, S., Magnussen, O. M. & Behm, R. J. In situ STM study

of electrodeposition and anodic dissolution of Ni on Ag(111). Phys. Chem. Chem. Phys. **3,** 3351–3363 (2001).

59. In situ studies of the oxidation of nickel electrodes in alkaline solution. J. Electroanal. Chem. **587,** 172–181 (2006).

60. Innocenti, M., Cattarin, S., Cavallini, M., Loglio, F. & Foresti, M. L. Characterisation of thin films of CdS deposited on Ag(111) by ECALE. A morphological and photoelectrochemical investigation. J. Electroanal. Chem. **532,** 219–225 (2002).

61. Wyckoff, R. W. G. Crystal Structures. Interscience Publishers, New York, New York **1,** (1963).

62. A small angle scattering study of dendrimer–copper sulfide nanocomposites. Polymer (Guildf). **40,** 2537–2545 (1999).

63. Bencista, I. et al. Phase composition of Cu_xS thin films: spectroscopic evidence of covellite formation. Eur. J. Mineral. **24,** 879–884 (2012).

64. Di Benedetto, F. et al. Electrodeposition of ternary $Cu_xSn_yS_z$ thin films for photovoltaic applications. Prog. Photovoltaics Res. Appl. **22,** 97–106 (2014).

65. Benedetto, F. Di et al. Magnetic properties and cation ordering of nanopowders of the synthetic analogue of kuramite, Cu_3SnS_4. Phys. Chem. Miner. **38,** 483–490 (2011).

66. Innocenti, M. et al. Ternary cadmium and zinc sulfides: Composition, morphology and photoelectrochemistry. Electrochim. Acta **49,** 1327–1337 (2004).

67. Di Benedetto, F. et al. Physical Characterization Of Thin Films Of $Cu_xZn_yS_z$ For Photovoltaic Applications. ECS Trans. **58,** 59–65 (2013).

68. Loglio, F., Innocenti, M., Pezzatini, G. & Foresti, M. L. Ternary cadmium and zinc sulfides and selenides: Electrodeposition by ECALE and electrochemical characterization. J. Electroanal. Chem. **562,** 117–125 (2004).

69. Wyckoff, R. W. G. in Crystal Structures 1 7–83 (Interscience Publishers, 1963).

70. Pezzatini, G., Loglio, F., Innocenti, M. & Foresti, M. L. Selenium(IV) Electrochemistry on Silver: A Combined Electrochemical Quartz-Crystal Microbalance and Cyclic Voltammetric Investigation. Collect. Czechoslov. Chem. Commun. **68,** 1579–1595 (2003).

71. Electrochemical behaviour of tellurium and silver telluride at rotating glassy carbon electrode. Electrochim. Acta **33,** 991–996 (1988).

72. Aqueous electrochemistry of tellurium at glassy carbon and gold: A combined

voltammetry-oscillating quartz crystal microgravimetry study. J. Electroanal. Chem. Interfacial Electrochem. **252,** 441–451 (1988).

73. Oviedo, O. A., Reinaudi, L., García, S. G. & Leiva, E. P. M. Underpotential deposition : from fundamentals and theory to applications at the nanoscale.

74. Bockris, J. O. (John O. . Comprehensive treatise of electrochemistry. (Plenum Press, 1980).

75. Guggenheim, E. A. (Edward A. Thermodynamics : an advanced treatment for chemists and physicists. (North-Holland, 1986).

76. Jain, S. C. (Suresh C. ., Willander, M. & Overstraeten, R. van. Compound semiconductors strained layers and devices. (Kluwer Academic Publishers, 2000).

77. Foresti, M. L., Capolupo, F., Innocenti, M. & Loglio, F. Visual Detection of Crystallographic Orientations of Face-Centered Cubic Single Crystals. Cryst. Growth Des. **2,** 73–77 (2002).

78. Kurosawa, T. No Title. 35:5619 (1960).

79. Hamelin, A. in Modern Aspects of Electrochemistry, Vol. 16 (eds. Conway, B. E., White, R. E. & Bockris, J. O.) 1–101 (Plenum Press, 1985).

80. Balmes, O. et al. The ID03 surface diffraction beamline for in-situ and real-time X-ray investigations of catalytic reactions at surfaces. Catal. Today **145,** 220–226 (2009).

81. Von Dreele, R. B. & Rodriguez-Carvajal, J. The Intensity of a Bragg Reflection in Powder Diffraction 58–88 (Royal Society of Chemistry, 2008).

82. Scardi, P. Microstructural Properties: Lattice Defects and Domain Size Effects Powder Diffraction 376–413 (Royal Society of Chemistry, 2008).

83. Scardi, P., Leoni, M. & Delhez, R. Line broadening analysis using integral breadth methods: A critical review. J. Appl. Crystallogr. **37,** 381–390 (2004).

84. Giacovazzo, C. Fundamentals of crystallography. (Oxford University Press, 2011).

85. Robinson, I. K. & Tweet, D. J. Surface X-ray diffraction. Reports Prog. Phys. **55,** 599–651 (1992).

86. Felici, R. Surface X-ray diffraction in Characterization of Materials (John Wiley & Sons, Inc., 2012)

87. Pinchaux, R. et al. Surface X-ray diffraction.

88. Born, M. & Wolf, E. Principles of optics : electromagnetic theory of

propagation, interference and diffraction of light. (Cambridge University Press, 1999).

89. Ferrer, S. & Comin, F. Surface diffraction beamline at ESRF. Rev. Sci. Instrum. **66,** 1674–1676 (1995).

90. Lohmeier, M. & Vlieg, E. Angle calculations for a six-circle surface X-ray diffractometer. J. Appl. Crystallogr. **26,** 706–716 (1993).

91. Evans-Lutterodt, K. W., Tang, M. T. & IUCr. Angle Calculations for a `2+2' Surface X-ray Diffractometer. J. Appl. Crystallogr. **28,** 318–326 (1995).

92. Ponchut, C. et al. MAXIPIX, a fast readout photon-counting X-ray area detector for synchrotron applications. J. Instrum. **6,** C01069–C01069 (2011).

93. Roobol, S., Onderwaater, W., Drnec, J., Felici, R. & Frenken, J. BINoculars: Data reduction and analysis software for two-dimensional detectors in surface X-ray diffraction. J. Appl. Crystallogr. **48,** 1324–1329 (2015).

94. Drnec, J. et al. Integration techniques for surface X-ray diffraction data obtained with a two-dimensional detector. J. Appl. Crystallogr. **47,** 365–377 (2014).

95. Vinogradov, N. A. et al. The structural evolution of graphene/Fe(110) systems upon annealing. Carbon **111,** 113–120 (2017).

96. Patterson, A. L. The scherrer formula for X-ray particle size determination. Phys. Rev. **56,** 978–982 (1939).

97. Langford, J. I. The variance and other measures of line broadening in powder diffractometry. II. Determination of particle size. J. Appl. Crystallogr. **1,** 131–138 (1968).

98. Warren, B. E. & Averbach, B. L. The Effect of Cold-Work Distortion on X-Ray Patterns. J. Appl. Phys. **21,** 595 (1950).

99. de Keijser, T. H., Langford, J. I., Mittemeijer, E. J. & Vogels, A. B. P. Use of the Voigt function in a single-line method for the analysis of X-ray diffraction line broadening. J. Appl. Crystallogr. **15,** 308–314 (1982).

100. Olivero, J. J. & Longbothum, R. L. Empirical fits to the Voigt line width: A brief review. J. Quant. Spectrosc. Radiat. Transf. **17,** 23315 (1977).

101. Wells, R. J. Rapid approximation to the Voigt/Faddeeva function and its derivatives. J. Quant. Spectrosc. Radiat. Transf. **62,** 29–48 (1999).

102. Wojdyr, M. Fityk : a general-purpose peak fitting program Fityk: a general-purpose peak fitting program. J. Appl. Cryst. J. Appl. Cryst **43,** 1126–1128 (2010).

103. Björck, M., Andersson, G. GenX : an extensible X-ray reflectivity refinement program utilizing differential evolution. J. Appl. Crystallogr. **40,** 1174–1178 (2007).

104. Foresti, M. L. et al. In situ X-ray analysis under controlled potential conditions: An innovative setup and its application to the investigation of ultrathin films electrodeposited on Ag(1 1 1). Electrochim. Acta **51,** 5532–5539 (2006).

105. Henke., B. L., Gullikson., E. M. & Davis, J. C. Atomic Data and Nuclear Data Tables. At. Data Nucl. Data Tables **54,** 181–342 (1993).

106. Parkhurst, B. D. L. & Appelo, C. a J. User's Guide To PHREEQC (version 2) - a Computer Program for Speciation, and Inverse Geochemical Calculations. Exch. Organ. Behav. Teach. J. **D,** 326 (1999).

107. Helgeson, H. C., Delany, J. M., Nesbitt, H. W. & Bird, D. K. Summary and Critique of the Thermodynamic Properties of Rock-Forming Minerals. Am J Sci **278–A,** (1978).

108. Johnson, J. W., Oelkers, E. H. & Helgeson, H. C. SUPCRT92: A software package for calculating the standard molal thermodynamic properties of minerals, gases, aqueous species, and reactions from 1 to 5000 bar and 0 to 1000°C. Computers and Geosciences **18,** (1992).

109. Ball, J. W. & Nordstrom, D. K. User's Manual for WATEQ4F, with revised thermodynamic data base and test cases for calculating speciation of major, trace, and redox elements in natural waters. U.S. Geol. Surv. Water-Resources Investig. Rep. **91–183,** 1–188 (1991).

110. Skoog, D. A., West, D. M., Holler, F. J. & Crouch, S. R. Fundamentals of analytical chemistry.

111. Moulder, J. F. & Chastain, J. Handbook of x-ray photoelectron spectroscopy : a reference book of standard spectra for identification and interpretation of XPS data. (Physical Electronics Division, Perkin-Elmer Corp, 1992).

112. Evans, H. T. Crystal Structure of Low Chalcocite. Nat. Phys. Sci. **232,** 69–70 (1971).

113. Goble, R. J. Relationship Between Crystal Structure, Bonding and Cell Dimensions in the Copper Sulfides. Can. Mineral. **23,** 61–76 (1985).

114. Evans, H. T. The crystal structures of low chalcocite and djurleite. Zeitschrift fur Krist. - New Cryst. Struct. **150,** 299–320 (1979).

115. Miller, T. a et al. The mechanism of ultrafast structural switching in superionic copper (I) sulphide nanocrystals. Nat. Commun. **4,** 1369 (2013).

116. Giaccherini, a. et al. Synthesis and Technological Application of

Electrodeposited Semiconductors by EC-ALD. ECS Trans. **58,** 35–41 (2014).

117. Pattrick, R. a. D. et al. The structure of amorphous copper sulfide precipitates: An X-ray absorption study. Geochim. Cosmochim. Acta **61,** 2023–2036 (1997).

118. Innocenti, M. et al. Electrochemical Growth of Cu-Zn Sulfides of Various Stoichiometries. ECS Trans. **161,** D14–D17 (2014).

119. Giaccherini, A. et al. Operando SXRD of E-ALD deposited sulphides ultra-thin films: Crystallite strain and size. Appl. Surf. Sci. (2017).

120. Craig, J. R. & Kullerud, G. The Cu-Zn-S system. Miner. Depos. **8,** 81–91 (1973).

121. Giaccherini, A., Montegrossi, G. & Di Benedetto, F. Stability of Naturally Relevant Ternary Phases in the Cu–Sn–S system in Contact with an Aqueous Solution. Minerals **6,** 79 (2016).

122. Peters, E. The 1976 Extractive Metallurgy Lecture The Metallurgical Society of AIME Direct Leaching of Sulfides : Chemistry and Applications. (1976).

123. Huang, H.-H. The Eh-pH Diagram and Its Advances. Metals (Basel). **6,** 23 (2016).

124. Berretti, E. et al. Electrodeposition and Characterization of p and n Sulfide Semiconductors Composite Thin Film. J. Electrochem. Soc. **163,** D3034–D3039 (2016).

125. Perry, D. L. & Taylor, J. A. X-ray photoelectron and Auger spectroscopic studies of Cu_2S and CuS. J. Mater. Sci. Lett. **5,** 384–386 (1986).

126. NIST X-ray Photoelectron Spectroscopy DatabaseVersion 4.1. National Institute of Standards and Technology, Gaithersburg (2012).

127. Dzhafarov, T. D., Ongul, F. & Karabay, I. Formation of CdZnS thin films by Zn diffusion. J. Phys. D. Appl. Phys. **39,** 3221–3225 (2006).

128. Synthesis and processing of CdS/ZnS multilayer films for solar cell application. Thin Solid Films **474,** 77–83 (2005).

129. Mickelsen, R. A., Chen, W. S., Hsiao, Y. R. & Lowe, V. E. Polycrystalline thin-film $CuInSe_2$/CdZnS solar cells. IEEE Trans. Electron Devices **31,** 542–546 (1984).

Appendix

This appendix presented an extract of the works published during the development of my Ph.D., in the following a brief description of their content is summarized. Moreover, it is explained their relationship with the title of the thesis and the work developed during my Ph.D.:

- Paragraph A1 reports the first pages of the publications constituting the main part of the data discussed in the body of the thesis. Although several data non presented in these pubblications are reported in this thesis, such publications constitute the main development of this work.
- Paragraph A2 reports the publications regarding the characterization and modeling of both natural and synthetic sulphides. Specifically, the synthesis have been carried following a solvothermal pathway at reasonable temperature and room pressure. These papers contain several structural, crystal chemistry and thermodynamic considerations exploited for the discussion in this thesis. Moreover, it was developed the theoretical framework to model the speciation in the Cu-M-S system (where M is a generic chemical species). This theoretical framework has been exploited to model the E-ALD thermodynamics in paragraphs 5.2.5 and 5.2.6.
- Paragraph A3 reports the comparison between two experimental and one density functional method (DFT) to compute the band gap of semiconducting polymers as a test-bench for a more general application of these method. Comparing the optical and electrochemical method to extrapolate the band gap we found discrepancy which can be related to the binding energy of the exciton. This consideration is confirmed by the comparison with the DFT calculations.
- Paragraph A4 reports the publications related to the electrodeposition of metals from IL. Mainly concerning the aluminization, we gather information on the optimization of the process at the lab-scale and the thermal post treatment of some full-scale aluminized parts. Among other characterization techniques, we studied the microstructural features of the coatings exploiting the single line profile analysis exploited in paragraph 4.2.3. Additionally, it is presented a method developed to simulate the electrodeposition process based on the finite elements analysis (FEA) as implemented in Comsol©. Through the modeling of the transport, electrical and electrochemical process involved in the electrodeposition, it is possible to clarify most of the factors determining the quality of the coatings. Eventually, it is presented a model of the electrodeposition of aluminum from ionic liquids at the industrial scale.
- Paragraph A5 reports the chemical speciation model of the voltammetric scans performed on a Pd-based nanocatalyst in a Fixed Energy X-ray Absorption Voltammetry experiment. This approach, as a way for the interpretation of the

spectroelectrochemical data, has a wider application than the deactivation of Pd electrocatalyst. In fact, the same workflow has been applied to gather the data presented in paragraph 5.2.6.

Chapter 3

Operando Structural Characterization of the E-ALD Process Ultra-Thin Films Growth

Andrea Giaccherini, Roberto Felici and Massimo Innocenti

Additional information is available at the end of the chapter

http://dx.doi.org/10.5772/67355

Abstract

Spanning from nanoelectronics to new solar energy materials, technological development in the recent years requested highly controlled nanostructured surfaces, ultra-thin films, and 2D structured materials. In general, although very favorable from a full life cycle assessment (FLCA) standpoint, electrodeposition hardly allows to obtain the high order required by recent technologies. In particular cases, the electrodeposition enables the deposition of atomic layers by means of surface limited reactions (SLRs). By exploiting SLRs, it is possible to define layer-by-layer deposition scheme of different atomic layers; we refer to these schemes as electrochemical atomic layer deposition (E-ALD) and when the growth of the film is epitaxial with the substrate, the techniques are called electrochemical atomic layer epitaxy (ECALE). Aiming at characterizing structure and growth of materials grown by means of E-ALD, surface analysis techniques apply better. In particular, surface X-ray diffraction (SXRD) with high brilliance synchrotron sources enables the operando structural analysis in electrochemical environment. In recent years, several works on the operando surface characterization by means of SXRD have been reported. Thanks to novelties in the field of operando SXRD experiments, semiconducting systems were studied, such as single and multilayer of CdS and Cu_2S.

Keywords: ECALE, E-ALD, thin films, 2D materials, SXRD

1. Introduction

A fundamental aim of material research and surface science is the development of deposition techniques of compound semiconductors with low impact from either the energetic or environmental points of view. These techniques should ensure a high structural control for the

www.nature.com/scientificreports

OPEN

Operando SXRD study of the structure and growth process of Cu_2S ultra-thin films

Received: 5 September 2016
Accepted: 7 April 2017
Published online: 09 May 2017

Andrea Giaccherini[1,2], Serena Cinotti[1], Annalisa Guerri[1], Francesco Carlà[3], Giordano Montegrossi[4], Francesco Vizza[5], Alessandro Lavacchi[5], Roberto Felici[6], Francesco Di Benedetto[1,7] & Massimo Innocenti[1,2]

Electrochemical Atomic Layer Deposition (E-ALD) technique has demonstrated to be a suitable process for growing compound semiconductors, by alternating the under-potential deposition (UPD) of the metallic element with the UPD of the non-metallic element. The cycle can be repeated several times to build up films with sub-micrometric thickness. We show that it is possible to grow, by E-ALD, Cu_2S ultra-thin films on Ag(111) with high structural quality. They show a well ordered layered crystal structure made on alternating pseudohexagonal layers in lower coordination. As reported in literature for minerals in the Cu-S compositional field, these are based on CuS_3 triangular groups, with layers occupied by highly mobile Cu ions. This structural model is closely related to the one of the low chalcocite. The domain size of such films is more than 1000 Å in lateral size and extends with a high crystallinity in the vertical growth direction up to more than 10 nm. E-ALD process results in the growth of highly ordered and almost unstrained ultra-thin films. This growth can lead to the design of semiconductors with optimal transport proprieties by an appropriate doping of the intra metallic layer. The present study enables E-ALD as an efficient synthetic route for the growth of semiconducting heterostructures with tailored properties.

Present efforts of materials and surfaces science focus on the development of facile manufacturing techniques which either use processes with a low energy consumption or result in growth with high quality crystalline films. These two aspects of the process are important for semiconducting compounds involved in the development of several new technologies, spanning from nanoelectronics to energy conversion devices. For the last, it is crucial to improve low energy manufacturing techniques in order to increase the energy return of the invested energy, i.e. of the net energy associated with the use of the device in its whole life cycle. On the other hand, high crystallinity and low concentration of defect accumulated during the growth is the main focus in order to opportunely control the electronic and transport properties of the materials. In this context, our work proposes the use of thin layers of sulphides deposited by an electrodeposition technique that allows the deposition of single atomic layers with an accurate control of the crystal structure. Chalcogenide nanomaterials, interesting candidates as new semiconducting nanomaterial due to their tunable band gap and their peculiar transport properties[1], can be grown using several electrochemical methods[2–4]. Among them, the Electrochemical Atomic Layer Deposition (E-ALD) technique is able to build up monolayer-by-monolayer a film, under the bottom up scheme, by alternating the deposition of a monolayer of the metallic element with one of the nonmetallic element, in a cycle which can be repeated several times[5,6]. Deposition of the monolayers is obtained by means of a surface limited reaction (SLR), i.e. under-potential deposition (UPD). The method is also referred as ECALE (Electrochemical Atomic Layer Epitaxy)[7] when the deposits can be considered epitaxial. Previous studies[8–10] were successful in the realization by E-ALD of thin films with binary and ternary composition, as ZnS, CdS, Zn-Cd-S, Cu-S, Cu-Sn-S and Cu-Zn-S, with the aim of growing materials with controlled semiconducting gap properties tuned for photovoltaic applications. While

[1]Department of Chemistry, University of Florence, Via della Lastruccia 3-13, 50019, Sesto, Fiorentino (FI), Italy. [2]INSTM, Research Unit of Florence, Via della Lastruccia 3-13, 50019, Sesto, Fiorentino (FI), Italy. [3]ESRF, 6, Rue Horowitz, F-BP 220, 38043, Grenoble, Cedex, France. [4]IGG-CNR, via G. La Pira 4, 50121, Florence, Italy. [5]ICCOM-CNR, Via Madonna del Piano 10, 50019, Sesto, Fiorentino (FI), Italy. [6]SPIN-CNR, Area della Ricerca di Roma 2 - Tor Vergata, Via del Fosso del Cavaliere 100, 00133, Roma, Italy. [7]Department of Earth Sciences, University of Florence, Via La Pira 4, 50121, Firenze, Italy. Correspondence and requests for materials should be addressed to A.G. (email: andrea.giaccherini@unifi.it) or F.B. (email: francesco.dibenedetto@unifi.it) or M.I. (email: m.innocenti@unifi.it)

G Model
APSUSC-36828; No. of Pages 7
ARTICLE IN PRESS

Applied Surface Science xxx (2017) xxx–xxx

Contents lists available at ScienceDirect

Applied Surface Science

journal homepage: www.elsevier.com/locate/apsusc

Full Length Article

Operando SXRD of E-ALD deposited sulphides ultra-thin films: Crystallite strain and size

Andrea Giaccherini [a,*], Francesca Russo [a], Francesco Carlà [b], Annalisa Guerri [a], Rosaria Anna Picca [c], Nicola Cioffi [c], Serena Cinotti [d], Giordano Montegrossi [d], Maurizio Passaponti [a], Francesco Di Benedetto [d,e], Roberto Felici [f], Massimo Innocenti [a]

[a] Department of Chemistry, Università Degli Studi di Firenze, Via della Lastruccia 3-13, 50019, Sesto Fiorentino (FI), Italy
[b] ESRF, 6, Rue Horowitz, F-BP 220, 38043, Grenoble, Cedex, France
[c] Department of Chemistry, Università degli Studi di Bari, Via E. Orabona, 4-70125 Bari, Italy
[d] ICCOM-CNR, via C. La Pira 4, 50121, Italy
[e] Department of Earth Sciences, Università Degli Studi di Firenze, Via La Pira 4, 50121 Firenze, Italy
[f] SPINCNR, Area della Ricerca di Roma 2 – Tor Vergata, Via del Fosso del Cavaliere 100, 00133 Roma, Italy

ARTICLE INFO

Article history:
Received 8 March 2017
Received in revised form 21 July 2017
Accepted 31 July 2017
Available online xxx

Keywords:
SXRD
ECALE
E-ALD
Photovoltaics
Water-splitting
Ultra-thin films

ABSTRACT

Electrochemical Atomic Layer Deposition (E-ALD), exploiting surface limited electrodeposition of atomic layers, can easily grow highly ordered ultra-thin films and 2D structures. Among other compounds Cu_xZn_yS grown by means of E-ALD on Ag(111) has been found particularly suitable for the solar energy conversion due to its band gap (1.61 eV). However its growth seems to be characterized by a micrometric thread-like structure, probably overgrowing a smooth ultra-thin film. On this ground, a SXRD investigation has been performed, to address the open questions about the structure and the growth of Cu_xZn_yS by means of E-ALD. The experiment shows a pseudo single crystal pattern as well as a powder pattern, confirming that part of the sample grows epitaxially on the Ag(111) substrate. The growth of the film was monitored by following the evolution of the Bragg peaks and Debye rings during the E-ALD steps. Breadth and profile analysis of the Bragg peaks lead to a qualitative interpretation of the growth mechanism. This study confirms that Zn lead to the growth of a strained Cu_2S-like structure, while the growth of the thread-like structure is probably driven by the release of the stress from the epitaxial phase.

1. Introduction

The energy issue of modern society is linked to the limited availability of non-renewable fuels coupled to the increasing levels of global pollution, approaching an environmental overshoot. This implies the need for a rapid development in materials and techniques for renewable energy applications. An increase in efficiency and sustainability of the solar cells necessarily requires the use of materials consisting of elements whose availability will support the diffusion of the photovoltaic technology at a global level over the actual extent represented by the silicon-based solar cells. At the same time, the use of such materials should ensure a lower environmental impact, in a Full Life Cycle Assessment (FLCA), and the device production must be done through less-energy-intensive methods, thus increasing the Energy Return Over Energy Investment (EROEI). For these reasons, the scientific community is focusing its attention on new compounds based on economic and low-environmental impact elements such as Cu, Sn, Fe and Zn. A possibility to obtain high-quality thin film semiconductors relies on exploiting electrochemical deposition. This technique is a very attractive method to produce compound semiconductors with different stoichiometry and high crystallinity because of its easiness of implementation, its relatively low cost, its capability of growing the selected materials onto substrates of any shape and dimensions.

Chalcogenide nanomaterials are interesting candidates for photovoltaic applications due to the reasons well-explained by Innocenti et al. [1]. Chalcogenides can be grown by means of Electrochemical Atomic Layer Epitaxy (ECALE) [2]. This technique consists in the electrodeposition of alternating metallic and non-metallic monolayers in a cycle which can be repeated several times and which exploits reactions limited by the surface (SLR – Surface Limited Reactions), including UnderPotential Depositions (UPD). This method is also referred as E-ALD (Electrochemical Atomic Layer Deposition), when the deposit cannot be considered strictly epitaxial [3].

* Corresponding author.
E-mail address: andrea.giaccherini@unifi.it (A. Giaccherini).

http://dx.doi.org/10.1016/j.apsusc.2017.07.294
0169-4332/

Please cite this article in press as: A. Giaccherini, et al., Operando SXRD of E-ALD deposited sulphides ultra-thin films: Crystallite strain and size, Appl. Surf. Sci. (2017), http://dx.doi.org/10.1016/j.apsusc.2017.07.294

Journal of The Electrochemical Society, 163 (12) D3034-D3039 (2016)
0013-4651/2016/163(12)/D3034/6/$33.00 © The Electrochemical Society

FOCUS ISSUE ON ELECTROCHEMICAL DEPOSITION AS SURFACE CONTROLLED PHENOMENON

Electrodeposition and Characterization of p and n Sulfide Semiconductors Composite Thin Film

E. Berretti,[a] S. Cinotti,[a] S. Caporali,[a,b] N. Cioffi,[c] A. Giaccherini,[a,z] F. Di Benedetto,[b,d,z] M. L. Foresti,[d] G. Montegrossi,[e] A. Lavacchi,[f,z] F. Vizza,[f] R. A. Picca,[c] and M. Innocenti[a,b,f,z,*]

[a]Department of Chemistry, Università degli Studi di Firenze, Firenze 50019, Italy
[b]INSTM, Firenze 50121, Italy
[c]Department of Chemistry, Università degli Studi di Bari, Bari 70126, Italy
[d]Department of Earth Sciences, Università degli Studi di Firenze, Firenze 50019, Italy
[e]IGG, CNR, Firenze 50121, Italy
[f]ICCOM, CNR, Sesto Fiorentino 50019, Italy

In this article is proposed a new preparation method for composite ultra-thin films for photovoltaic application. Compounds such as Kesterites (CZTS, ternary and quaternary copper and zinc sulfides) could be used in virtue of their semiconductor behavior in conjunction with electrodeposition from aqueous media methodologies; in particular E-ALD (Electrochemical Atomic Layer Deposition) method seems a legitimate alternative to the high pressure and temperature methods used since today. We studied the feasibility of the electrodeposition process of two layers of semiconductors (Cu_xZn_yS, with p electronic proprieties, and CdS with n electronic proprieties), one above the other, by means of E-ALD. Preliminary electrochemical studies revealed the complex nature of the composite film, requiring the anodic stripping of Cd. In order to confirm that the Cd electrodeposition is surface limited, two sets of samples were compared using different conventional and charge controlled potentiostatic electrodeposition methodologies. SEM and XPS characterization was then performed to characterize morphologically and quantitatively the samples. Consequently, the conditions for the surface limited deposition of Cd over Cu_xZn_yS have been reckoned through the electrochemical and spectroscopical analysis. The layered (p-n) structure of the thin film has been confirmed.

Manuscript submitted April 20, 2016; revised manuscript received July 14, 2016. Published July 28, 2016. This paper is part of the JES Focus Issue on Electrochemical Deposition as Surface Controlled Phenomenon: Fundamentals and Applications.

The increasing worldwide energy consumption, combined to the decreasing of the availability of mineral resources, have moved the interest of governments[1,2] and scientists toward the research on renewable energies.[3] Among all the renewables, photovoltaic energy (PV) is one the most promising technologies, because of its prospective yield[4] (the sun everyday irradiates earth with an amount of energy much greater than the global human need) and of the possibility of a direct conversion of solar energy into electric energy. In fact, worldwide production of PV devices grew steeply in last years and more than 60% of all PV capacity in operation at the end of 2014 was added over the past three years.[5] Nowadays the main drawbacks to a ultimate diffusion of PV energy production consist in the need of rare and expensive elements, as well as the employment of difficult and energy expensive processes for their fabrication. In contrast, the full life cycle assessment (FLCA) could be more favorable while improving the production technigies involved in the industrial process and using less rare materials.[5,6] Therefore, research in the photovoltaic field needs to focus on alternatives to minimize the exploitation of rare elements and on more sustainable production processes, a task which does not appear mentioned in many publications on this subject. Concerning the abundance of raw materials, the scientific community in recent years started to focus on kesterites $Cu_2ZnSn(S,Se)_4$[6,8] and related materials as promising light absorbers. The relative abundance of the constituent elements, their scarce toxicity and low cost made them viable materials for next generation photovoltaics.[1,2,6,7]

Concerning the process optimization, electrodeposition techniques are highly considered to grow the constituents of the PV cell in a more energy-efficient way. In fact, they allow to work with diluted aqueous solutions, at atmospheric pressure and at temperatures lower than 100°C. Electrodeposition allows the synthesis of nanomaterials with a high degree of structural and compositional control.[9–11] Among electrodeposition techniques, one that best fits these key aims is Electrochemical Atomic Layer Deposition (E-ALD),[12,13] which is also called ECALE (Electrochemical Atomic Layer Epitaxy) when the growth can be considered epitaxial. E-ALD is a *layer by layer* technique, which exploits surface limited reactions (SLR), as Under Potential Deposition (UPD) phenomena, allowing the growth of a compound simply alternating the various SLR of the elements. E-ALD has been used to grow many binary and ternary compounds,[12–15] and particularly in the last years, to prepare p semiconductors belonging to the Cu-Zn-S system.[16–19]

In this work we aimed to test and verify the technical feasibility of growing, under laboratory conditions, a complete p-n junction through E-ALD. For this reason we decided to deposit a film of CdS on a film of Cu_xZn_yS that was chosen for its best bandgap value for PV applications.[20–23]

Both semiconductors have been chosen due to their bandgap which results narrow, making them appropriate materials for a p-n junction for solar cells.[21,22]

The deposition of CdS film on Ag (111) has been thoroughly studied by our group, both from a synthetic[12,13,17] and from a structural standpoint.[17,18] However, the deposition of CdS over a Cu_xZn_yS thin film required a reconsideration of the best conditions to perform the growth. Accordingly, in this paper we present the preliminary electrochemical study of this new step of the synthesis. Then, we describe the synthesis of the p–n junction and the final products that were characterized through Energy Dispersive X-Ray microanalysis (EDX), to assess the presence of CdS over the ternary compound, and Scanning Electron Microscopy (SEM) to study the morphology of the film surface. X-ray Photoelectron Spectroscopy (XPS) was also employed to determine the surface chemical speciation of the electrodeposited thin films.

Experimental

Reagents and electrochemical preparation.—The electrochemical measurements were performed using analytical grade reagents without further purification. $HClO_4$ 65% (Carlo Erba reagents) and NH_4OH 28% (VWR Chemical) were used to prepare the 50 mM [$HClO_4$] and 100 mM [NH_4OH] ammonia buffer at pH 9.2. Merck $CdCl_2 \cdot 2H_2O$, Merck $ZnSO_4 \cdot 7H_2O$, $3CuSO_4 \cdot 8H_2O$ and Aldrich $Na_2S \cdot 3H_2O$ were used as sources of Cu, Zn, Cd and S respectively to prepare 0.5 mM solution of each element in ammonia buffer.

*Electrochemical Society Member.
*E-mail: [redacted]

Eur. J. Mineral.
2016, 28, 611–618
Published online 1 April 2016

Paper presented at the
8th European Conference on Mineralogy and Spectroscopy,
Rome, September 9–11, 2015

Green synthesis of pyrite nanoparticles for energy conversion and storage: a spectroscopic investigation

ANDREA GIACCHERINI[1,*], IVAN COLANTONI[2], FRANCESCO D'ACAPITO[3], ANTONIO DE LUCA[1], FERDINANDO CAPOLUPO[1], GIORDANO MONTEGROSSI[4], MAURIZIO ROMANELLI[5], MASSIMO INNOCENTI[1] and FRANCESCO DI BENEDETTO[5]

[1] Chemistry Department, University of Firenze, Firenze, Italy
*Corresponding author, e-mail: andrea.giaccherini@unifi.it
[2] Department of Physics, Sapienza University of Rome, Rome, Italy
[3] CNR-IOM-OGG c/o ESRF, Grenoble, France
[4] The Institute of Geosciences and Earth Resources, CNR, Firenze, Italy
[5] Department of Earth Sciences, University of Firenze, Firenze, Italy

Abstract: Pyrite, FeS_2, nanoparticles were obtained through a one-pot solvothermal synthesis, without surfactants, carried out at room pressure and mild temperature (=180°C). A thorough characterization of the products was thus performed, including scanning-electron-microscope micromorphology, X-ray diffraction (XRD), diffuse reflectance spectroscopy, and X-ray absorption spectroscopy (both in the XANES and EXAFS regions).

Monophasic pyrite products are obtained as aggregates having an approximate dimension of few hundreds of nm. The Scherrer analysis of the Bragg reflections suggests that these aggregates are clusters of smaller units, having a mean size of ~25 nm. The XRD measurements point to a small but significant increase of the Fe–S bond distance (+1.7 %) with respect to reference data. The optical behavior of the pyrite nanoparticles is indistinguishable from that of the bulk pyrite.

These results point to the one-pot synthesis as an efficient and "green" way of obtaining pyrite nanoparticles exhibiting the same technological properties as bulk pyrite. Indeed these nanoparticles can be considered as a product viable for numerous technological applications in the solar-energy conversion and storage fields.

Key-words: sulfides; solvothermal synthesis; photovoltaics; pyrite; nanoparticles; XAS; diffuse reflectance spectroscopy.

Introduction

One of the most relevant challenges of the present-day society is associated to the conversion of the resources into materials through a more efficient and energy-saving way. In this field, pyrite (FeS_2) is a n-type semiconductor of relevant interest in materials science. In the photovoltaic technology, pyrite has been considered (MacPherson & Stoldt, 2012), due to its prominent attractive physical properties: the indirect band gap at ~0.95 eV, a direct transition at ~2.0 eV (Wadia *et al.*, 2009; Antonov *et al.*, 2009; Vadkhiya & Ahuja, 2011; MacPherson & Stoldt, 2012), the large optical absorption coefficient (>10^5 cm^{-1}, in the range 300–750 nm), and a minority carrier diffusion length in the range of 100–1000 nm.

In the energy-storage technology, pyrite, in the form of nanostructured polycrystalline material, was proven as a very efficient cathode in lithium-ion batteries, showing high Li-storage capacity, excellent performances at high temperature, low environmental impact, and affordable costs (Feng *et al.*, 2007). Pyrite nanoparticles were also considered for applications in rechargeable batteries (Chin *et al.*, 2005).

While the presence of pyrite in the environment is potentially harmful through the processes associated to the so-called acid mine drainage, this phase has been used in the field of waste treatment, for instance as a removal agent for chalcogenides ions from aqueous solution, achieving, in the case of Se^{4+}, an efficiency of more than 91 %, with a fairly low concentration of initial selenium (39.480 mg/L) (Han *et al.*, 2012; Wang *et al.*, 2014).

Different synthetic strategies have been proposed to obtain pure polycrystalline pyrite powders in micrometer and nanometer sizes. Other iron sulfides as marcasite (FeS_2), troilite (FeS) and pyrrhotite ($Fe_{1-x}S$) are commonly found in synthetic iron pyrite aggregates, affecting even in trace amounts their technological properties (e.g. the open circuit voltage of a PV device, Lazić *et al.*, 2013). Indeed, numerous solvothermal (Wang *et al.*, 2011; Kim *et al.*, 2014; Yoder *et al.*, 2014; Yu *et al.*, 2015), hydrothermal (Wu *et al.*, 2004; Feng *et al.*, 2007; Wadia *et al.*, 2009;

DOI: 10.1127/ejm/2016/0028-2534
0935-1221/16/0028-2534 $ 3.60

Gartman & Luther, 2013; Yuan *et al.*, 2015) and solid-state (Shi *et al.*, 2015) synthesis processes were exploited.

In this study, we propose a one-pot solvothermal synthesis of pyrite nanocrystals, carried out without the use of surfactants, at room pressure and at a mild temperature (180°C). This synthesis involves the co-generation of the sulfide anion. Moreover, the reduced number of phases involved assures a limited environmental concern: Fe and S are the only reactants in the process. A thorough characterization of the obtained products has been performed, including scanning electron microscopy (SEM) micromorphology, X-ray diffraction (XRD), diffuse-reflectance spectroscopy (DRS), and X-ray absorption spectroscopy (XAS).

Experimental procedures

Materials

In this study, pyrite nanoparticles are obtained through a one-pot method, based on the use of thiourea as a source of S^{2-} and ethylene glycol (EG) as a solvent. The temperature control is realized by maintaining the boiling conditions for the EG solvent at 180°C under reflux for 2 hours at room pressure.

In a typical batch, 2.4 mmol of thiourea (Merck), 1.2 mmol of $FeCl_2$ (Alfa-Aesar) where mixed with 50 ml ethylene glycol (Alfa-Aesar) in a two-neck flask. At the end of the synthesis, the dark brown precipitate is let spontaneously cool at room temperature. Products are then centrifuged, collected and washed for several times in ethanol. Finally, they are air-dried. Different synthetic conditions, such as the flask volume, the solvent filling, and the purity of the Fe^{2+} precursor were tested to optimize the synthesis strategy. The results are listed in Table 1. The sample labelled npy showed a lesser amount of impurities, hence it was chosen for the complete characterization of the product.

A commercial specimen of natural pyrite was also used in this study, as reference material for the XAS and DRS investigations.

X-ray diffraction

The phase determination of the synthetic products was carried out through powder XRD, performed using a PANalytical X'PERT PRO powder diffractometer and employing Ni-filtered Cu *Kα* (1.54187 Å) radiation. The powder XRD patterns were registered at 1,600 W (*i.e.* 40 kV, 40 mA) with a PIXcel detector on a rotating sample prepared on a silicon wafer (zero-background sample holder) in the 2θ range 5–100°, applying a step size of 0.026° 2θ and a step counting time of 0.27 s. The XRD data were refined by means of full-profile Rietveld algorithm, using the Fullprof software (Rodriguez-Carvajal, 1993). The same software was used to optimize the unit-cell parameter value, using a model in which the unit-cell parameter, the fractional coordinate of the sulfur in the pyrite structure, the line width and a preferred orientation parameter, along [200], were kept free.

Scanning electron microscopy

Particle morphology was checked by means of SEM, at three different magnification levels, from 10000× up to 45000×. The powder was mounted on standard aluminum sample holders covered by adhesive graphite tabs. To enhance the quality of the micrograph at high magnification, samples were gold coated. Secondary-electron micrographs were obtained using a SEM ZEISS EVO MA15, by applying a potential of 20 kV to the electron beam.

Diffuse-reflectance spectroscopy

The UV–vis-NIR diffuse reflectance spectrum of pyrite nanoparticles was measured using an Agilent Cary 300 spectrophotometer, equipped with a Labsphere PELA-1050 integration sphere. The DRS spectra were registered in the range 250–850 nm, at a step of 1 nm, counting 0.1 s per step.

X-ray absorption spectroscopy

The XAS data were collected at the Beamline BM25 operating at the European Synchrotron Radiation Facility (ESRF, Grenoble, France). Spectra were recorded, at room temperature, in the transmission mode, using two ion chambers to have roughly 10 % (I_0) and 80 % (I_1) of absorption at the Fe *K*-edge

Table 1. Summary of the samples used for this study.

Label	Name	Batch Formula	Source	
py	Pyrite (standard)	FeS_2	Natural	
npy	Pyrite (nanoparticles)	FeS_2	Solvent: 50 mL. Flask: 100 mL. Iron precursor: 1.2 mmol $FeCl_2$ (Analytical grade)	FeS_2
npy_1	Pyrite (nanoparticles)	FeS_2	Solvent: 50 mL. Flask: 100 mL. Iron precursor: 1.2 mmol $FeCl_2$ (Technical grade)	FeS_2 + FeO_x
npy_2	Pyrite (nanoparticles)	FeS_2	Solvent: 50 mL. Flask: 100 mL. Iron precursor: 1.2 mmol $FeCl_3$ (Analytical grade)	FeS
npy_3	Pyrite (nanoparticles)	FeS_2	Solvent: 150 mL. Flask: 500 mL. Iron precursor: 1.2 mmol $FeCl_2$ (Analytical grade)	FeS_2 + FeO_x

(7112.0 eV). The beamline monochromator was equipped with Si(111) operating in flat crystal mode. The XANES (X-ray near-edge spectroscopy) and EXAFS (Extended X-ray absorption spectroscopy) spectra of samples were normalized with respect to the high-energy side of the curve. Powdered samples were mixed with cellulose powder (amounts were calculated with XAFSmass software), pressed into pellets and sealed within two kapton foils. A minimum of four scans were executed and averaged for each sample. The EXAFS spectrum of nanopyrite was analyzed using IFEFFIT-1.2.9 (Newville, 2001) package. The edge position E_0 was determined using the maximum of the first-order derivative of the absorption spectrum.

The $\chi(k)$ (experimental data) EXAFS signal was Fourier transformed with a Hanning window in the range 3.50–12.50 $Å^{-1}$; fit was performed in the R-space in the range 1.20–4.40 Å, using FEFF8 (Ankudinov *et al.*, 1998) to generate EXAFS paths; refinement were performed using the structural model of standard pyrite (Brostingen, 1988).

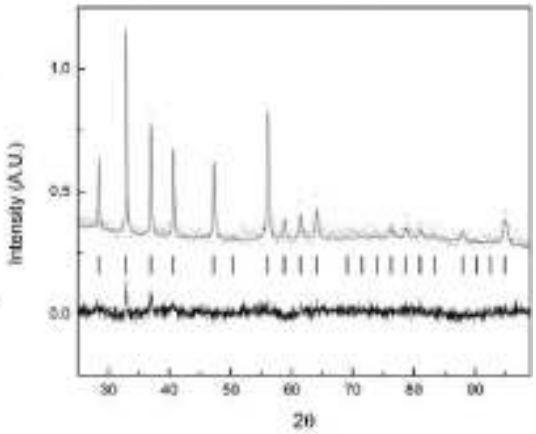

Fig. 1. Experimental XRD powder pattern of the synthetic pyrite nanoproducts. Dots represent the experimental data, the continuous line the best-fit calculated pattern, the darker line the difference spectrum and the segments the theoretical Bragg positions for the pyrite *Pa*-3 crystal structure.

Results

X-ray diffraction

The experimental XRD powder pattern of the sample npy is shown in Fig. 1. Apparently, all reflections are assignable to cubic pyrite (space group $Pa\bar{3}$, n° 205); no reflections due to spurious products or relics of the reactants are evident. Under the present experimental conditions, the minimum detection limit for the technique (taking also into account that products are nanocrystalline) is 1 wt%. Within this uncertainty, the patterns obtained point to a single-phase synthetic product. Repeated synthetic runs reproducing the best conditions (Table 1) resulted in similar XRD results.

The results from Rietveld refinement are shown in Table 2 along with the fitting error (3σ). The value of the cubic a_0 unit-cell parameter a 298 K is 5.4354(6) Å, which is larger than that reported for bulk pyrite in the literature, 5.4179 Å. Considering the unit-cell parameter and the S fractional coordinate values higher than the reference values (Table 2), the bond distance between Fe(4a) and S(8c) is 1.7 % longer than the value of reference FeS_2. The width of the best-fit line was used to assess a mean value of the crystallite size, by applying the Scherrer method (Scherrer, 1918; Patterson, 1939), resulting in an approximate average crystallite size of 25 nm.

Scanning electron microscopy

The irregular particle morphology of the synthetic pyrite products, with different aggregation patterns, can be observed on Fig. 2. The micrographs reveal microcrystalline aggregates, built by numerous smaller particles; their mean dimension can be estimated to a few hundreds of nanometers (150–300 nm), consistent with the 3–500 nm range proposed for similar solvothermal syntheses in the literature (Wu *et al.*, 2004; Wadia *et al.*, 2009; Wang *et al.*, 2011; Yuan *et al.*, 2015). A clear lack of a definite morphology in both the particles (which appear subhedral, with rounded corners) and the aggregates (resembling in some way the natural framboidal pyrite; Fukue *et al.*, 2003; Saikia *et al.*, 2014; Wang *et al.*, 2014) is evident. Moreover, a non-uniform morphology of the particles at the higher magnification reveal spheroids, rods and flat structures,

Table 2. Refined cubic *a* unit-cell parameter, S fractional coordinate, Bragg agreement factor (R) and mean particle size for the npy sample, compared with those of a natural reference standard. Uncertainties are reported in brackets. The Debye Waller factors for Fe and S, used during the refinement, are 0.280 and 0.330 $Å^2$, respectively (Bayliss, 1977).

	Unit-cell parameter, *a* (Å)	S fractional coordinate	Bragg R factor	Mean particle size (nm)	Reference
npy	5.4354(6)	0.3872(9)	3.231	22(6)	This study
pyrite	5.4179	0.3840	nd	nd	(Brostigen, 1988)

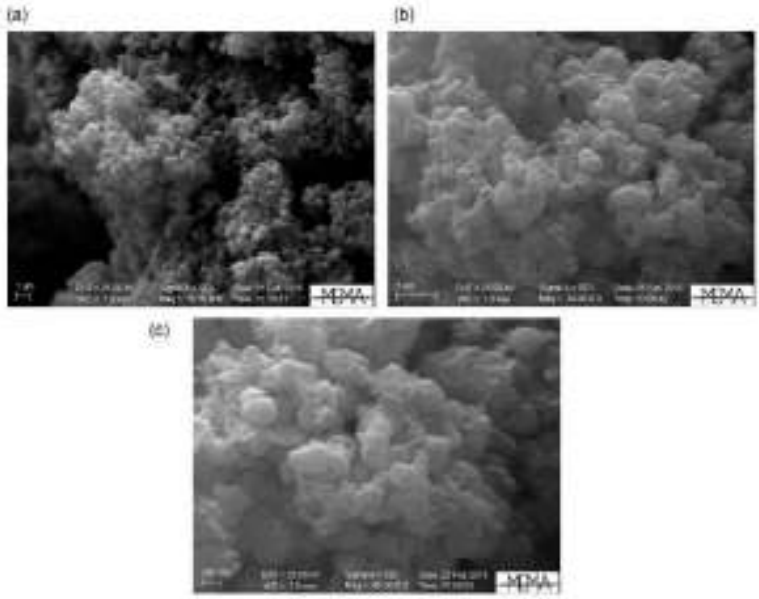

Fig. 2. SEM microscopy: secondary-electrons micrographs of the FeS_2 powder at different magnification: **a** 10 kX, **b** 30 kX and **c** 45 kX.

suggesting in some cases the occurrence of preferential growth directions. The SEM-EDS spectra, while confirming the pyrite stoichiometry, reveal the additional presence of a low amount of chlorine (0.93 at %) in the sample.

Diffuse-reflectance spectroscopy

The diffuse reflectance spectrum of the sample is shown in Fig. 3. A semiconductive material shows in the DRS an exciton peak related to its direct band-gap (Boldish &

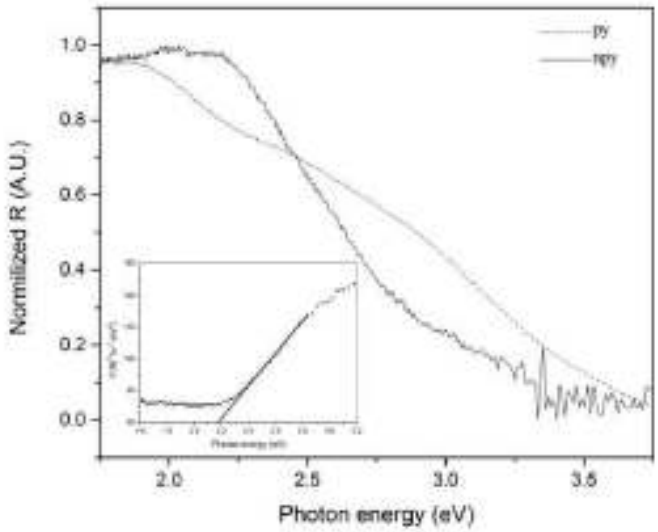

Fig. 3. Diffuse-reflectance spectrum *versus* photon energy (in eV) for Npy and standard Py; in the inset, the Tauc plot of npy, where experimental data and the linear extrapolation are compared.

White, 1998). The band gap of a semiconductive material can be extrapolated fitting the McLean analysis of the absorption edge (Boldish & White, 1998), *i.e.* by means of the extrapolation of the linear trends in the direct and indirect Tauc plots (J. Tauc, 1966). In the present study, the conversion of the DRS (Fig. 3) into the absorption spectrum was operated by means of the Kubelka-Munk equation (Boldish & White, 1998). The resulting spectrum was then converted into the Tauc plot (Fig. 3, inset), from which a direct band gap of 1.83(3) eV can be estimated. The allowed exciton transitions expected for bulk pyrite occur at 0.95 eV (corresponding to an indirect transition), and at ~2.0 and ~3.1 eV (corresponding to direct transitions; Lauer & Trautwein, 1984; Boldish & White, 1998; Ogawa, 1979; Antonov *et al.*, 2009; Vadkhiya & Ahuja, 2011). Concerning pyrite nanoparticles, numerous different estimations of the band gap are reported in the literature (in the range of 0.90-3.1 eV) depending on shape and size (Wu *et al.*, 2004; Chen *et al.*, 2005; Zhang *et al.*, 2005; Peng *et al.*, 2006; Feng *et al.*, 2007; Wadia *et al.*, 2009; Wang *et al.*, 2011; MacPherson & Stoldt 2012; Cabán-Acevedo *et al.*, 2012, 2014; Golsheikh *et al.*, 2013; Layek *et al.*, 2013; Akhoondi & Ziarati, 2014; Kim *et al.*, 2014; Kirkeminde *et al.*, 2014; Yoder *et al.*, 2014; Shi *et al.*, 2015; Yuan *et al.*, 2015). Accordingly, our results are fully in the range for the bulk and nanosized pyrite.

X-ray absorption spectroscopy

The XANES spectra of the nanoparticle pyrite sample and of the natural reference compound are shown in Fig. 4a. A close similarity is observed between natural pyrite and npy, in agreement with the long-range structural information provided by XRD (Table 2). The pre-edge analysis has been carried out by means of a standard method (Wilke *et al.*, 2001; Giuli *et al.*, 2011), consisting in the spline interpolation of the background, the background subtraction and a Gaussian fit of the isolated pre-edge peak. The position of the Gaussian peak (Fig. 4b) is in good agreement with literature data on natural pyrite (Petiau *et al.*, 1988). Indeed, the pre-edge analysis point to the octahedral coordination of Fe in the npy sample.

The result from the fit of the EXAFS nanopyrite data is listed in Table 3 and the best-fit curves are shown in Fig. 5a and b, in the χ and R spaces, respectively. The fit was carried out using the pyrite structural model (Brostigen, 1988), achieving a good R-factor (0.02). The amplitude factor S_0^2 was guessed and calculated during the fitting procedure, obtaining a value of 0.70. The best-fit results of the EXAFS data confirm the presence of four coordination shells at a mean distance still close to the literature value for pyrite (Brostigen, 1988). Remarkably, no evidence of structural modifications, as *e.g.* increase of the lattice constants or of the mean Fe–S distance are observed.

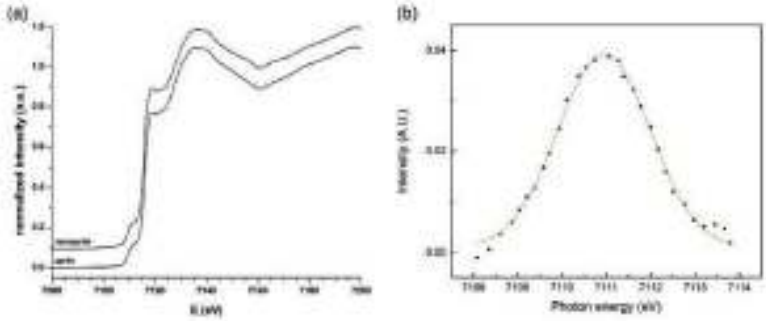

Fig. 4. (**a**) Comparison in the XANES range between the natural and synthetic pyrite; (**b**) spectrum in the pre-edge region and the relative fit. (online version in colour)

Table 3. X-ray absorption spectroscopy results. *N*, coordination number; *R*, distance between absorber and backscatter atoms (experimental and theoretical); σ^2, the Debye–Waller factor value; $\Delta\sigma^2$, the fitting uncertainties for the Debye-Waller. Fe-S_1, Fe-S_2, Fe-S_3 are the three first coordination shells. S_2 belongs to an adjacent corner sharing octahedron, S_3 to an adjacent non sharing octahedron. Uncertainties are reported in brackets.

Shell	N	R_{exp} (Å)	R_{theo} (Å)(Brostigen, 1988)	σ^2 (Å^2)	$\Delta\sigma^2$ (Å^2)
Fe-S_1	6	2.26(2)	2.25(6)	0.004	0.001
Fe-S_2	6	3.45(4)	3.44(4)	0.008	0.003
Fe-S_3	2	3.60(4)	3.59(4)	0.007	0.001
Fe-Fe_1	12	3.83(2)	3.82(1)	0.007	0.001

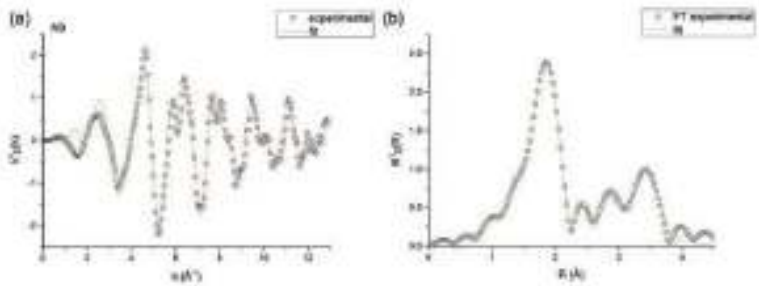

Fig. 5. Results of the fit of the EXAFS spectra: (a) experimental data; (b) Fourier-transformed experimental data. Data, blue solid line; fit, red solid line. (online version in colour)

Discussion

The main result of the present study is the successful synthesis of polycrystalline pyrite nanoparticles, having an approximate crystallite size of 25 nm. The adopted synthetic strategy minimizes duration, temperature and chemical reactants involved in the run. Thus, pyrite nanocrystals are obtained through a very easy and environmental friendly setup. The solvent, in fact, can be purified and re-used. The reaction mechanism proceeds through the co-generation of the sulfide anion during the thermal decomposition of thiourea (Kim *et al.*, 2014; Yoder *et al.*, 2014). Since studies about the process of thiourea thermal decomposition suggest the formation of H_2S at 180°C (Timchenko *et al.*, 2004), we suggest that this species can contribute to drive the selectivity of FeS_2 over FeS. The lack of surfactants can be considered the main factor causing the coalescence of the small nanoparticles into larger aggregates (150–300 nm in size) without a definite morphology. These results suggest that, under the adopted conditions, the nucleation process prevails on the growth of the pyrite crystals.

A remarkable difference between the solvothermal npy sample and the natural pyrite resides in the slight increase in the unit-cell parameter, clearly revealed by the Rietveld refinement of the XRD data. This observation appears as partially conflicting with the EXAFS results. However, one has to consider that discriminating changes in the bond distances of the order of 1–2 % is of the same amount as the estimated error bars (Table 3). Conversely, XRD data provide average over a long-range structural arrangement. Considering that the first surface layers of a nanoparticle account for at least 5 % of the total volume, the increase of the unit-cell parameter can be likely attributed to the surface effects.

The fate of the small but significant presence of Cl atoms in the npy deserves some discussion. The chlorine content either could be taken up by pyrite, or it could trace a co-precipitation process, where a slight part of Fe occurs in the npy sample as chloride, or it can represent a partial chlorination of the pyrite nanoparticle surface. If XRD and XAS probably would not detect a second Fe-bearing phase, due to its low amount, one has to point out that the chlorine content is detected by EDX inspection even at high magnification, thus suggesting it is occurring in a very dispersed mode. For this reason, the third hypothesis appears more consistent.

On the whole, the comparison of the crystal chemical and structural properties of the obtained nanoparticles with those of the natural microcrystalline pyrite point to a close similarity. The same holds true also for one of the most relevant technological properties, *i.e.* the band gap. Some authors suggested a size-dependent effect on the band gap of nanostructured pyrite (Peng *et al.*, 2006; Layek *et al.*, 2013; Shi *et al.*, 2015). The general theory of the size-dependent band gaps relates this effect to the quantum confinement of the excitons (Elliot, 1957; Brus, 1983; Enright & Donald, 1996), occurring when the radius of the smallest sphere, including the crystallite, is smaller than the Bohr radius of the exciton (Brus, 1983; Wilcoxon & Samara, 1995; Chukwuocha, 2012).

The Bohr radius of the exciton in a semiconductor can be calculated by means of the Elliot equation (Equation 1) (Enright & Fitzmaurice, 1996; Elliot, 1957)

$$r_b = \frac{h\varepsilon}{\pi e^2}\left(\frac{1}{m_e} + \frac{1}{m_h}\right) \qquad (1)$$

where r_b is the Bohr radius of the excitons in the pyrite, ε is the dielectric constant of the pyrite, m_e and m_h are respectively the effective mass of the electrons and of the hole. From the literature data in Table 4, the estimated upper limit for the Bohr radius is 6.1 nm, roughly two times smaller than the estimated radius of the smallest sphere including the average size crystallite. Accordingly, we exclude that size-dependent effects can occur in the npy nanoparticles obtained in the present investigation.

Table 4. Data for the effective mass approximation, m is the mass of the electron.

ε	–26 (Lazić *et al.*, 2013)
m_e	0.25 m (Altermatt *et al.*, 2002)
m_h	2.2 m (Altermatt *et al.*, 2002)

The achievement of pyrite nanoparticles using a "green" synthesis, and the absence of size-dependent properties for the main physical properties of the bulk FeS_2 can be considered two relevant goals for both the fundamental and application purposes, namely in the solar-energy conversion and storage field. From a mineralogical point of view, this study confirms that pyrite particles down to 25 nm in size maintain, with the only exception of the slight increase of the unit-cell parameter, their structural properties and crystallinity. The same result is of relevant interest also for the application purposes: with the present synthetic approach, we are able to provide pyrite nanoparticles with their unchanged technological properties in a form useful for its industrial application (*e.g.* inks, sprays, PVD) in technologically relevant devices. Finally, this synthetic route can be in principle scaled up.

References

Akhondi, A., Ziarati, M., Khandan, N. (2014): Hydrothermal production of highly pure nano pyrite in a stirred reactor. *Iran. J. Chem. Chem. Eng.*, **33**(1), 15–19.

Altermatt, P.P., Kiesewetter, T., Ellmer, K., Tributsch, H. (2002): Specifying targets of future research in photovoltaic devices containing pyrite (FeS_2) by numerical modelling. *Sol. Energ. Mat. Sol. C.*, **71**, 181–195.

Ankudinov, A.L., Ravel, B., Rehr, J.J., Conradson, S.D. (1998): Real-Space multiple-scattering calculation and interpretation of X-Ray-absorption near-edge structure. *Phys. Rev. B*, **58**, 7565–7576.

Antonov, V.N., Germash, L.P., Shpak, P., Yaresko, N. (2009): Electronic structure, optical and X-Ray emission spectra in FeS_2. *Phys. Status Solidi B*, **246**, 411–416.

Bayliss, P. (1977): Crystal structure refinement of a weakly anisotropic pyrite. *Am. Mineral.*, **62**, 1168–1172.

Boldish, S.I. & White, B.W. (1998): Optical band gaps of selected ternary sulfide minerals. *Am. Mineral.*, **83**, 865–871.

Brostigen, G. (1988): Redetermined crystal structure of FeS_2 (pyrite). *Acta Chem. Scand.*, **23**, 2186–2188.

Brus, L.E. (1983): A simple model for the ionization potential, electron affinity, and aqueous redox potentials of small semiconductor crystallites. *J. Chem. Phys.*, **79**, 5566.

Cabán-Acevedo, M., Matthew, S. F., Yizheng, T., Robert, J.H., Song, J. (2012): Synthesis and properties of semiconducting iron pyrite (FeS_2) nanowires. *Nano Lett.*, **12**, 1977–1982.

Cabán-Acevedo, M., Nicholas, S.K., Caroline, R.E., Dong, L., Blaise, J.T., Hong-En, C., Kyle, J.C., John, C.W., Robert, J. H., Song, J. (2014): Ionization of high-density deep donor defect states explains the low photovoltage of iron pyrite single crystals. *J. Am. Chem. Soc.*, **136**, 17163–17179.

Chen, X., Zhenghua, W., Xiong, W., Junxi, W., Jianwei, L., Yitai, Q. (2005): Single-source approach to cubic FeS_2 crystallites and their optical and electrochemical properties. *Inorg. Chem.*, **44**, 951–954.

Chin, P.P., Ding, J., Yi, J.B., Liu, B. H. (2005): Synthesis of FeS_2 and FeS nanoparticles by high-energy mechanical milling and mechanochemical processing. *J. Alloy. Compd.*, **390**, 255–260.

Chukwuocha, E.O. (2012): Theoretical studies on the effect of confinement on quantum dots using the brus equation. *World J. Cond. Mat. Phys.*, **2**, 96–100.

Elliot, R.J. (1957): Intensity of optical absorption by excitons. *Phys. Rev.*, **108**, 1384–1389.

Enright, B. & Donald, F. (1996): Spectroscopic determination of electron and hole effective masses in a nanocrystalline semiconductor film. *J. Phys. Chem.*, **100**, 1027–1035.

Feng, X., Xiangming, H., Weihua, P., Changyin, J., Chunrong, W. (2007): Hydrothermal synthesis of FeS_2 for lithium batteries. *Ionics*, **13**, 375–377.

Fukue, M., Yoshio, S., Mitsuaki, Y., Masahiro, Y., Yuichi, F. (2003): Change in microstructure of soils due to natural mineralization. *Appl. Clay Sci.*, **23**(1–4), 169–177.

Gartman, A. & Luther, W.G. (2013): Comparison of pyrite (FeS_2) synthesis mechanisms to reproduce natural FeS_2 nanoparticles found at hydrothermal vents. *Geochim. Cosmochim. Acta*, **120**, 447–458.

Giuli, G., Paris, E., Hess, K.U., Dingwell, D.B., Ciccone, M.R., Eeckhout, S.G., Fehr, K.T., Valenti, P. (2011): XAS determination of the Fe local environment and oxidation state in phonolite glasses. *Am. Mineral.*, **96**, 631–636.

Golsheikh, M., Huang, N.M., Lim, H.N., Chia, C.H., Harrison, I., Muhamad, M.R. (2013): One-pot hydrothermal synthesis and characterization of FeS_2 (pyrite)/graphene nanocomposite. *Chem. Eng. J.*, **218**, 276–284.

Han, D.S., Batchelor, B., Abdel-Wahab, A. (2012): Sorption of selenium(IV) and selenium(VI) onto Synthetic Pyrite (FeS_2): spectroscopic and microscopic analyses. *J. Colloid Interf. Sci.*, **368**, 496–504.

Kim, H.T., Thao, P.N.N., Chang-duk, K., Chinho, P. (2014): Formation mechanisms of pyrite (FeS_2) nano-crystals synthesized by colloidal route in sulfur abundant environment. *Mater. Chem. Phys.*, **148**, 1095–1098.

Kirkeminde, A., Phillip, G., Maogang, G., Huizhong, C., Shenqiang, R. (2014): Iron sulfide ink for the growth of pyrite crystals. *Nanotechnology*, **25**, 205603.

Lauer, S. & Trautwein, A.X. (1984): Electronic-structure calculations, photoelectron spectra, optical spectra, and Mössbauer parameters of the pyrites MS_2 (M = Fe, Co, Ni, Cu, Zn). *Phys. Rev. B*, **29**, 6774–6783.

Layek, A., Somnath, M., Partha, P.R. (2013): Increase in open circuit voltage by the incorporation of band gap engineered FeS2 nanoparticle within MEHPPV solar cell. *J. Mater. Sci. - Mater. Electr.*, **24**, 3749–3755.

Lazić, P., Armiento, R., Herbert, F.W., Chakraborty, R., Sun, R., Chan, M.K.Y., Hartman, K., Buonassisi, T., Yildiz, B., Ceder, G. (2013): Low intensity conduction states in FeS_2: implications for absorption, open-circuit voltage and surface recombination. *J. Phys. Condens. Matter*, **25**, 465801.

MacPherson, H.A. & Stoldt, C. R. (2012): Iron pyrite nanocubes: size and shape considerations for photovoltaic application. *ACS Nano.*, **6**, 8940–8949.

Newville, M. (2001): IFEFFIT: interactive XAFS analysis and FEFF fitting. *J. Synchrotron Radiat.*, **8**, 322–324.

Ogawa, S. (1979): Magnetic properties of 3d transition-metal dichalcogenides with the pyrite structure. *J. Appl. Phys.*, **50**(B3), 2308–2311.

Patterson, L. (1939): The Scherrer formula for X-Ray particle size determination. *Phys. Rev.*, **56**, 978–982.

Peng, G., Xie, Y., Ye, L., Chen, Y., Ying, C., Guo, Q. (2006): From 2D Nanoflats to 2D Nanowire networks: a novel hyposulfote self-decomposition route to semiconductro FeS_2 nanowebs. *Cryst. Growth Des.*, **6**, 583–587.

Petiau, J. & Calas, G. (1983): EXAFS and Near Edge Structure. *in* XANES of 3d Elements: Effects of Local Symmetry Evidenced Using High-Resolution Spectra. Vol. 27 of Springer Series in Chemical Physics, 144–46.

Petiau, J., Sainctavit, Ph., Calas, G. (1988): *K* X-ray absorption-spectra and electronic structure of chalcopyrite $CuFeS_2$. *Mat. Sci. Eng. B: Solid State Mat. Adv. Tech.*, **1**, 237–249.

Rodriguez-Carvajal, J. (1993): Recent Advances in Magnetic Structure Determination by Neutron Powder Diffraction. *Physica B: Condensed Matter*, **192**, 55–69.

Saikia, B.K., Colin, R.W., Marcos, L.S.O., James, C.H., Bimala, P. B., Marcel, B., Luis, F.S. (2014): Geochemistry and Nano-Mineralogy of Two Medium-Sulfur Northeast Indian Coals. *Inter. J. Coal Geol.*, **121**, 26–34.

Scherer, P. (1918): Bestimmung der Grösse und der inneren Struktur von Kolloidteilchen Mittels Röntgenstrahlen. *Göttinger Nachrichten Gesellschaft*, **2**, 98.

Shannon, R.D. (1976): Revised effective ionic radii and systematic studies of interatomic distances in halides and chalcogenides. *Acta Cryst.*, **A32**, 751–767.

Shi, X., Tian, A., Xue, X., Yang, H., Xu, Q. (2015): Synthesis of FeS_2 (pyrite) Nanotube through Sulfuration of Fe_2O_3 Nanotube. *Mater. Lett.*, **141**, 104–106.

Tauc, J., Grigorovici, R., Vancu, A. (1966): Optical properties and electronic structure of amorphous germanium. *Phys. Stat. Sol. B*, **15**, 627–637.

Timchenko, V.P., Novozhilov, L., Slepyshova, O. (2004): Kinetics of thermal decomposition of thiourea. *Russ. J. Gen. Chem.*, **74**, 1046–1050.

Vadkhiya, L. & Ahuja, B.L. (2011): Electronic and optical properties of iron pyrite. *J. Alloys Compd.*, **509**, 3042–3047.

Wadia, C., Wu, Y., Gul, S., Volkman, S.K., Guo, J., Alivisatos, P. (2009): Surfactant-assisted hydrothermal synthesis of single phase pyrite FeS_2 nanocrystals. *Chem. Mater.*, **21**, 2568–2570.

Wang, D., Wu, M., Wang, Q., Wang, T., Chen, J. (2011): Controlled growth of uniform nanoflakes-built pyrite FeS_2 microspheres and their electrochemical properties. *Ionics*, **17**, 163–167.

Wang, D., Hongfang, L., Tianwei, Q. (2014): Adsorption behavior of natural pyrite for removal of selenium ions from aqueous solution. *Huanjing Wuran Yu Fangzhi*, **36**, 30–34.

Wilcoxon, J.P. & Samara, G. (1995): Strong quantum-size effects in a layered semiconductor: MoS_2 nanoclusters. *Phys. Rev. B*, **51**, 7299–7302.

Wilke, M., Farges, F., Petit, P.E., Brown, G.E., Martin, F. (2001): Oxidation state and coordination of Fe in minerals: An Fe*K*-XANES spectroscopic study. *Am. Mineral.*, **86**, 714–730.

Wu, R., Zheng, Y.F., Zhang, X.G., Sun, Y.F., Xu, J.B., Jian, J.K. (2004): Hydrothermal synthesis and crystal structure of pyrite. *J. Crystal Growth*, **266**, 523–527.

Yoder, T.S., Cloud, J.E., Leong, G.J., Molk, D.F., Tussing, M., Micorelli, J., Ngo, C. (2014): Iron pyrite nanocrystal inks: solvothermal synthesis, digestive ripening, and reaction mechanism. *Chem. Mater.*, **26**, 6743–6751.

Yu, B.B., Zhang, X., Jiang, Y., Liu, J., Gu, L., Hu, J.S., Wan, L.J. (2015): Solvent-induced oriented attachment growth of air-stable phase-pure pyrite FeS_2 nanocrystals. *J. Amer. Chem. Soc.*, **137**, 2211–2214.

Yuan, B., Luan, W., Tu, S.T. (2015): Synthesis of air stable and pure phase pyrite FeS_2 nanoparticles in water. *Mater. Lett.*, **142**, 160–162.

Zhang, H., Wang, B., Zhang, Z., Wang, P., Wei, L., Jia, Q., Wang, Y. (2005): Experimental studies on FeS_2 films prepared on Si (100) substrates by synchrotron radiation surface X-Ray diffraction method. *High Energ. Phys. Nucl.*, **29**, 32–36.

Received 14 November 2015
Modified version received 22 January 2016
Accepted 15 February 2016

minerals

MDPI

Article

Stability of Naturally Relevant Ternary Phases in the Cu–Sn–S System in Contact with an Aqueous Solution

Andrea Giaccherini [1], Giordano Montegrossi [2,*] and Francesco Di Benedetto [2,3]

1 Department of Chemistry, University of Florence, via della lastruccia 3, Sesto Fiorentino 50019, Italy; andrea.giaccherini@unifi.it

2 National Research Council, Institute for Geosciences and Georesources, via G. La Pira 4, Firenze 50121, Italy

3 Department of Earth Sciences, University of Florence, via G. La Pira 4, Firenze 50121, Italy; francesco.dibenedetto@unifi.it

* Correspondence: montegrossi@igg.cnr.it; Tel.: +39-55-275-7495

Academic Editor: Federica Zaccarini

Received: 9 June 2016; Accepted: 22 July 2016; Published: 26 July 2016

Abstract: A relevant research effort is devoted to the synthesis and characterization of phases belonging to the ternary system Cu–Sn–S, mainly for their possible applications in semiconductor technology. Among all ternary phases, kuramite, Cu_3SnS_4, mohite, Cu_2SnS_3, and $Cu_4Sn_7S_{16}$ have attracted the highest interest. Numerous studies were carried out claiming for the description of new phases in the ternary compositional field. In this study, we revise the existing literature on this ternary system, with a special focus on the phases stable in a temperature range at 25 °C. The only two ternary phases observed in nature are mohite and kuramite. Their occurrence is described as very rare. A numerical modelling of the stable solid phases in contact with a water solution was underwent to define stability relationships of the relevant phases of the system. The numerical modelling of the Eh-pH diagrams was carried out through the *phreeqc* software with the lnll.dat thermodynamic database. Owing to the complexity of this task, the subsystems Cu–O–H, Sn–O–H, Cu–S–O–H and Sn–S–O–H were firstly considered. The first Pourbaix diagram for the two naturally relevant ternary phases is then proposed.

Keywords: Cu–Sn–S system; kuramite; mohite; thermodynamics; pourbaix diagrams

1. Introduction

Recent studies have pointed out interesting semiconducting performances in some terms of the ternary Cu–Sn–S system [1–5]. Namely, Cu_3SnS_4, Cu_2SnS_3 and Cu_4SnS_4 are considered as novel materials for the p-layer of thin film technology in solar energy conversion devices. Their energy gap and absorption coefficient, coupled to the fact that they consist of cheap and abundant elements, are studied as materials for next-generation thin film solar cells under the scheme of the thin film technology, together with other materials as the kesterite and $CuZnSn(S,Se)_4$. Moreover, the thermoelectric features of Cu_2SnS_3 and $Cu_4Sn_7S_{16}$ are also considered for the realization of new thermoelectric devices [4].

The economic exploitation of these substances in their future application asks for accurate knowledge about their stability in relation to the possible use. For instance, photovoltaic devices have to cycle, with a daily period, in a relatively wide temperature range, and should maintain their good performances over time. A second challenge is represented by the synthetic way to obtain them. These materials are usually synthesized by means of energy consuming pathways, requiring vacuum conditions, long run duration and high annealing temperatures. To minimize the energy costs of the synthesis, the research is moving towards mild hydro- and solvothermal approaches (e.g., [6,7]).

The present study is aimed to revise all information available on the ternary Cu–Sn–S system, and to explore the contribution that the thermodynamic modeling of the interaction of binary and ternary sulfide phases with a water solution could add to the knowledge about stability of these technologically relevant materials. The paper is organized as follows: in Section 2, a summary of the stability relationships in the ternary compositional field is provided; in Section 3, the details of the modeling are discussed; in Section 4, the numerical modeling is performed on some test systems (Cu–O–H, Sn–O–H, Cu–S–O–H, Sn–S–O–H); and, in Section 5, the results of the numerical modeling of the Cu–Sn–S–O–H system, not present in the literature, is reported.

2. State-of-the-Art in the Cu–Sn–S Compositional Field

The ternary Cu–Sn–S system and some of its most relevant pseudobinary joins have attracted a relevant interest during the 1970s, and then repeatedly studied [8–25]. Most of these studies focused on the Cu_2S–SnS_2 pseudobinary join, whose definitive assessment dates to Olekseyuk et al. [23]. Other pseudobinary joins (Cu_2S–SnS, Cu_2S–Sn_2S_3) were investigated by Khanafer et al. [10], whereas an isotherm section at 500 °C is due to Wu et al. [19].

Numerous phases were reported to occur in this system during more than 40 years of research. They are listed in the Table 1, together with their lower limits of the stability field. It is worth mentioning that a careful reconsideration of the existing literature leads to a reduction of the total number of phases. In the past, in fact, successive studies, carried out in phases of the ternary system, reported different chemical formulas, while describing the same crystalline phase [1]. This fact holds particularly true for the phases labelled as "c" and "d" in Table 1. "c" phases refer to the one corresponding to the formula $Cu_2Sn_4S_9$ [23] or $Cu_4Sn_7S_{16}$ [25]. For all phases belonging to the "c" group, Fiechter et al. [24] suggests that they could be represented by a small compositional field (at $T > 500$ °C) described by a general law: $Cu_2Sn_{3+x}Sn_{7+2x}$, which will also include the $Cu_2Sn_4S_9$ composition. "d" phases refer to the one corresponding to the formula Cu_4SnS_6. On the whole, the number of phases still considered valid in the Cu–Sn–S system reduces to six (corresponding to the a–f groups in Table 1). During the evolution of the knowledge about the stability fields in this system, some other phases were identified and successively discredited (see notes to Table 1).

Table 1. Phases of the Cu–Sn–S system described in the literature.

#	Formula	Lower Limit of the Stability Field	Reference(s)
a	Cu_4SnS_4	RT	[8,12,14,18,22,23]
b	Cu_2SnS_3	RT	[8,12,13,18,22,23]
c	$Cu_2Sn_4S_9$ $Cu_2Sn_3S_7$ $Cu_2Sn_{3.5}S_8$ $Cu_2Sn_{3.75}S_8$ $Cu_2Sn_{3.34}S_{7.68}$ $Cu_4Sn_7S_{16}$	RT	[9,22,23] [8,10,18,23] [12,23] [23] [12] [20,24]
d	$Cu_{10}Sn_2S_{13}$ $Cu_{9.67}Sn_{2.33}S_{13}$ Cu_4SnS_6	400 °C	[18,23] [11,18,23] [15,21,23]
e	$Cu_5Sn_2S_7$	600 °C	[13,18,23]
f	$Cu_7Sn_3S_{10}$	600 °C	[13,18,23]
g	Cu_3SnS_4	RT *	[16,23]

Other phases claimed to occur in the ternary Cu–Sn–S system but successively discredited: $Cu_4Sn_3S_8$ [22]; $Cu_2Sn_2S_5$ [18]; Cu_3SnS_4 [16]. * The stability of Cu_3SnS_4 was tested as this is a product of spontaneous reaction between Cu_4SnS_4 and S at $T < 300$ °C. RT, room temperature.

According to the most recent studies [19,23,24], only three ternary Cu–Sn–S compounds are stable at room temperature, i.e., Cu_4SnS_4, Cu_2SnS_3 and $Cu_2Sn_4S_9$ (Figure 1). Interestingly, they all belong to the pseudobinary join Cu_2S–SnS_2. In addition to the previously cited phases, high temperature terms are reported in the Figure 1: Cu_4SnS_6, above 400 °C, $Cu_5Sn_2S_7$ and $Cu_{10}Sn_2S_{13}$, above 500 °C.

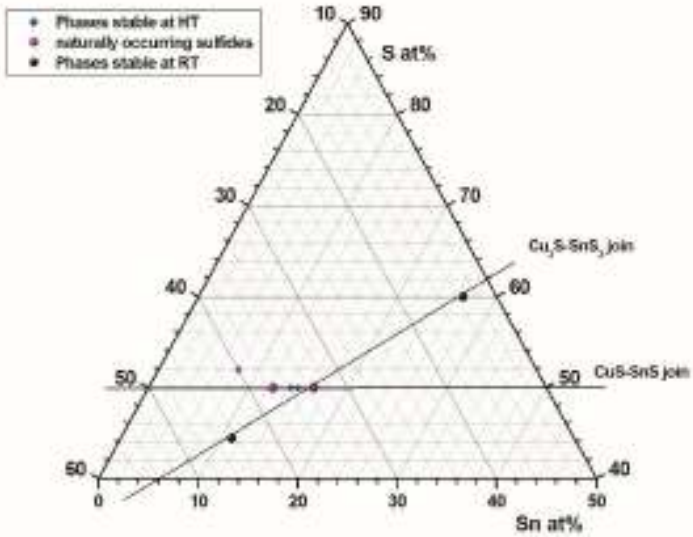

Figure 1. Ternary Cu–Sn–S system, reporting the phases found in nature (purple spheres), those reported as stable at room temperature (RT, black spheres) and those reported as stable at temperature values > 400 °C (HT, high temperature, blue diamonds).

A further relevant point resides in the consideration that none of the six cited phases are naturally occurring, except for Cu_2SnS_3. This latter phase corresponds to the mineral mohite. This mineral has been firstly described by Kovalenker et al. [26] and it was found in hydrothermal vein deposits (e.g., at Barquilla, Salamanca, Spain [27]) or associated with gold/silver deposits, included in sulfostannate assemblages (still of hydrothermal origin, at about 300–350 °C [28]). A peculiar case is represented by Cu_3SnS_4, kuramite, corresponding to the seventh group in Table 1. This phase represents the unique other naturally occurring ternary phase. Kuramite was firstly described by Kovalenker et al. [29], and it has also been reported in hydrothermal deposits, either in association with mohite (e.g., in gold-silver deposits [28]) or not (as e.g., at Agua Rica, Catamarca, Argentina [30,31]). The stability range of kuramite was studied on synthetic samples by Wang [17], who found it stable below 300 °C. This temperature range was studied through sulfidisation of Cu_4SnS_4 (i.e., through an out-of-equilibrium synthetic approach).

3. Modelling of the Equilibria in Aqueous Solutions

In the present study, the relationships between the main phases of the Cu–Sn–S system and a water solution are studied through the use of Eh versus pH (or "*Pourbaix*") diagrams, calculated according to the point-by-point mass balance method [32]. Under this approach, the predominant species at each given point of Eh and pH can be identified, taking into account other variables, as presence of ligand(s), temperature and pressure [32]. The predominant species is identified as the species with the highest content of the considered element. This predominance involves the absolute element content (in moles) considering both aqueous and solid species.

We performed our point-by-point mass balance calculation under the *phreeqc* formalism [33,34]. Aqueous phase equilibria are taken into account in a reference database file and the solid phases are

included through dissolution/precipitation reactions and reported as the logarithm of equilibrium constant (log K) at standard temperature and pressure condition (i.e., 25 °C and 1.0132 bar) [35,36]. Then, a Jacobian matrix including all the mass balance constants relative to the master species (Cu, Sn, S, H, O) is diagonalized obtaining the concentrations that satisfy the simultaneous solutions to all the considered equilibria.

Solid Phases Considered in the Calculations

Geochemical numerical models require comprehensive thermodynamic databases. Although today's geochemical databases are quite complete, including the most common reactions and reaction constants, some equilibria typical of specific environments may be not present. Accordingly, the thermodynamic properties of some minerals relevant to our model have been checked, and eventually added, to the *phreeqc* wateq4f.dat [37], and llnl.dat, for Sn, databases [38]. For the solid Cu oxides (cuprite, Cu_2O, and tenorite, CuO), calculations were performed using two different internally consistent sets of log K, one from the wateq4f.dat database [37], and the other from the JANAF tables [39]. The thermodynamic constants of the binary sulfides (chalcocite, Cu_2S, and covellite, CuS) arise from the wateq4f.dat database [37,40]. We included chalcocite, covellite and the crystalline defect $Cu_{2-x}S$ sulfides, i.e., djurleite, digenite and anilite.

A more detailed discussion deals with the ternary sulfide phases. As evinced from the previous paragraph, only two ternary phases, namely kuramite and mohite, are naturally relevant. Thus, we focused, in the calculation, only on these phases. However, experimental thermodynamic studies of mohite are lacking. Owing to this fact, an estimation of its log K respect to solvated ions is needed to refer to the *phreeqc* formalism and to evaluate their stability in contact with a solution.

A way to estimate the enthalpy of formation of mohite consists in obtaining it through the use of a Born-Haber cycle. The simplest way of designing a proper cycle should include the known binary compounds, as chalcocite, covellite, berndtite (SnS_2) and herzenbergite (SnS) and kuramite. However, starting from the binary sulfides, there is no chance of designing a cycle without including a phase in which disulfide groups are included. From a structural point of view, no disulfide groups are present in kuramite [7] nor in mohite [21]. This consideration rules out the possibility to extrapolate thermodynamic properties of the Cu–Sn–S ternary sulfides from the opportune mixing of those of the binary sulfides.

Since thermodynamic properties of crystals are strongly structure-dependent [41,42], we established a Born-Haber cycle including a close structural control on the mineral phases. This cycle is based on the thermodynamic properties of kesterite, Cu_2ZnSnS_4 [43], and kuramite. In kesterite, kuramite and mohite the crystal structure is organized on the same structural type, i.e., the tetrahedral arrangement of all cations within the framework derivative of that of sphalerite (ZnS) [44]. Thus, a close structural similarity between these phases is apparent. Following an approach similar to the linear additivity procedures developed by Yves Tardy and colleagues for other mineral types (e.g., [45,46]), the overall enthalpy of formation of kesterite can be hypothesized as consisting of the sum of the four MS_4 fragments (M = Cu, Zn, Sn). However, this should be done with some additional care due to the heterogeneity of sulphide structures, which may generate strong differences in group energy. In this context, an esteem of the enthalpy of formation of the ZnS_4 fragment can be obtained from the thermodynamic data of sphalerite, which also exhibit an arrangement of tetrahedrally coordinated Zn ions. Similarly, the enthalpy of formation of the SnS_4 fragment can be estimated from a cubic SnS polymorph, isostructural to sphalerite [47].

Accordingly, the enthalpy of formation of mohite can be derived from that of kesterite by subtracting the contribution due to the ZnS_4 fragment, or from that of kuramite by subtracting a CuS_4 fragment. Starting from kuramite, one has to first calculate the enthalpy of formation of a nominal cubic CuS phase having a sphalerite crystal structure, according to the following equation:

$$3\Delta H_{\text{cub. CuS}_4\text{-}} = \Delta H_{Cu_3SnS_4} - \Delta H_{SnS} \quad (1)$$

and then perform a summation of the CuS_4 and SnS_4 fragments in the opportune ratio. Thus, a Born-Haber cycle involving a hypothetical cubic CuS species can be performed in order to calculate the enthalpy of formation of mohite, and a similar procedure could be done starting from kesterite to check the consistency of the resulting values. We assume that the difference in mixing enthalpies for the three considered multinary compounds (kesterite, kuramite and mohite) is negligible [48]. The log k of formation of mohite is reported in Table 2. The data are in a good agreement with those evinced by the Zawadzki et al. [1] study. The discrepancies are in the range of 15%–20%, and they could be considered small if taking into account a non-homogeneous source for the thermodynamic data.

Table 2. Calculated log K for the dissolution reactions of the ternary species considered in this study.

Mineral	Log K	Reference
Cu_3SnS_4, kuramite	−73.14	This study, wateq4f.dat [37]
Cu_2SnS_3, mohite	−58.03	This study

4. Test Systems (Cu–O–H, Sn–O–H, Cu–S–O–H, Sn–S–O–H)

The predominance charts discussed in the following were computed in a grid limited by the water stability field from 0 to 14 pH units. The choice of the concentration of the master species (Cu, Sn, S) were dictated by the possibility of an immediate comparison with selected Pourbaix diagrams available in the literature. We used as reference diagrams those reported in the two Eh-pH atlantes by Brookins [49] and Takeno [50]. It is noteworthy to mention that the former refer to calculations performed in the "line method" [32], whereas the latter presents results obtained in the mass balance method, using up to five different databases.

Figure 2a shows the Eh-pH diagram for Cu in water. There is an almost perfect agreement between our diagram and that proposed by [49] and by [32]. If compared to those presented by [50], the major differences reside in the decrease of the stability field of cuprite, and in the appearance of a field or Cu^+. Both of these effects can be related to the different concentration used by these authors ($[Cu] = 10^{-6}$ and 10^{-10} mol/kgw). To verify this, we performed a calculation under their assumptions, still obtaining an excellent agreement. The comparison of diagrams obtained by different methods can yield slight differences in the boundaries as well as in the identification of the predominant species, and this can be due to the number and type of equilibria involved in the calculations [51]. In the present case, one has to highlight the presence (at high pH values) of a stability field of the $Cu(OH)_4^{2-}$ aqueous species, in perfect agreement with [32]: this field is not cited by [49] and [50], where a similar field was assigned to CuO_2^{2-}.

The Eh-pH diagram for Sn in water, shown in the Figure 2b, matches with a good agreement the data reported by [49]. Most of the diagram is dominated by cassiterite. The major differences reside in the absence of stability field of dissolved species at very low pH values (pH < 0.5) in the Brookins' [49] diagram. A better agreement is observed with the diagrams proposed by [50], even taking into account the difference in concentration. Again, we performed a calculation assuming $[Sn] = 10^{-10}$ mol/kgw, verifying an almost excellent agreement. The major difference between our diagram and that proposed by [49] can be attributed to the fact that in its line diagram, only few equilibria involving hydroxide complexes of Sn^{2+} were included, equlibria that are considered by our and Takeno's [50] calculations. The role of the complexing equilibria can obviously shift the boundaries between solid and aqueous species (as verified for the HS^- ligand by [44]). In contrast, both the line and mass balanced diagrams by [49,50] agree in pointing out a small field at negative Eh and high pH, where a soluble Sn^{2+} complex is more stable than cassiterite.

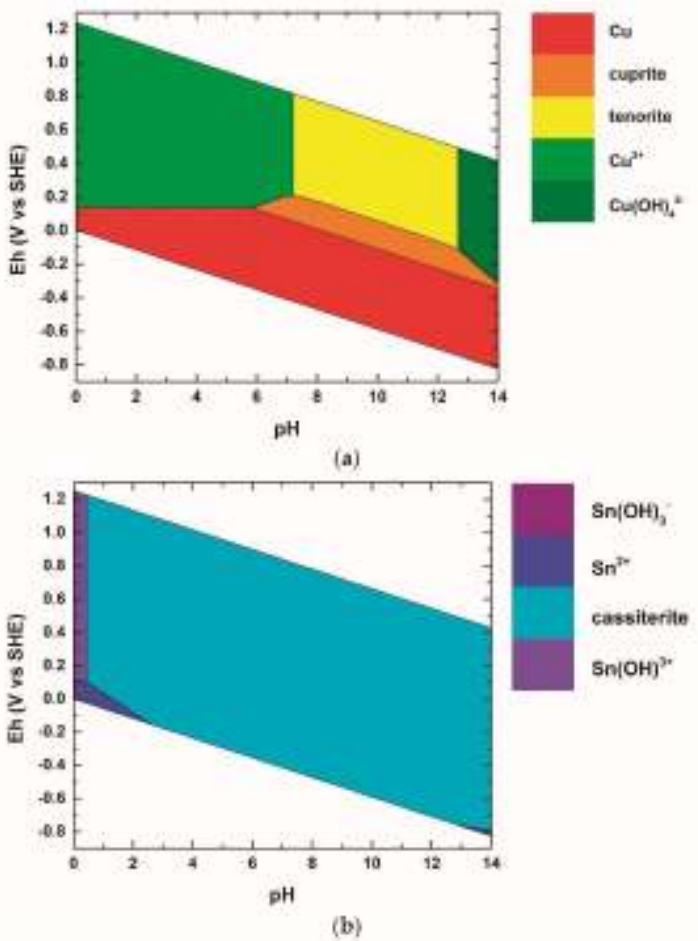

Figure 2. Eh-pH diagrams of: (**a**) the Cu–O–H system, calculated assuming [Cu] = 10^{-6} mol/kgw; (**b**) the Sn–O–H system, calculated assuming [Sn] = 10^{-5} mol/kgw.

Figure 3a depicts the diagram for the Cu–S system in water. In this case, the agreement of our calculation with the numerous available diagrams in the literature (e.g., [32,49,51,52]) is excellent, almost independently of the type of calculation (line or mass balanced methods) of the cited references. Concerning the defect $Cu_{2-y}S$ species, they were not included in Brookins' [49] calculations, but the present results fully agree with the fields proposed by the other authors. Concerning the results proposed by Young et al. [50], a marked difference regards the fields of the Cu(I) and Cu(II) thiocomplexes, which were not included in the present calculations (we reputed this detail beyond the aims of the present study). As already stated, the role of these thiocomplexes was revealed to be of some relevance in the definition of the proper stability fields and boundaries in the metal–sulfur–water Pourbaix diagrams [50].

Concerning the Sn–S–O–H– system, an exemplar diagram is shown in the Figure 3b. To the authors' knowledge, the unique reference diagram is provided by [49]. A good agreement between the two diagrams is observed: the diagram is dominated by the cassiterite stability field, limited at low pH values (pH < 0.5) by $Sn(OH)^{3+}$, and at high pH, low Eh values (pH > 13) by $Sn(OH)_3^-$. The remarkable difference with respect to the Sn–O–H system is the comparison of a large stability field for berndtite, while no herzenbergite fields are observed. A marked difference between our and

Brookins' [49] diagrams is the occurrence in the present calculation of a stability field for $SnSO_4$. Again, this fact is ascribed to the absence of this species in the calculations performed by [49].

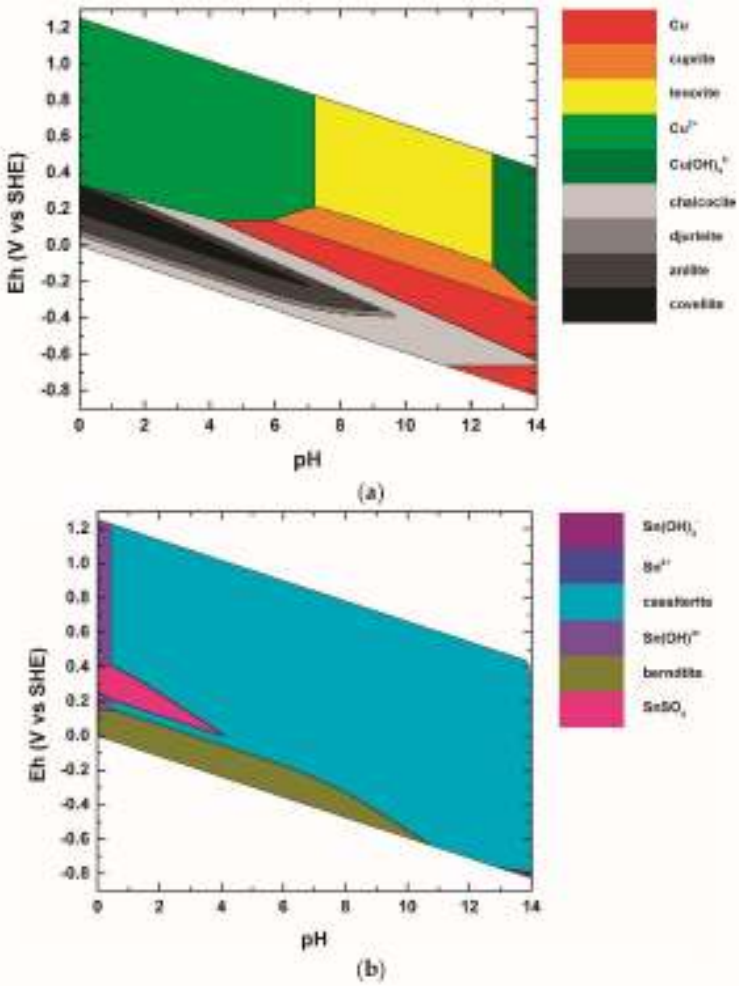

Figure 3. Eh-pH diagrams of: (**a**) the Cu–S–O–H system, calculated assuming $[Cu] = 10^{-6}$ mol/kgw and $[S] = 10^{-3}$ mol/kgw; (**b**) the Sn–S–O–H system, calculated assuming $[Sn] = 10^{-6}$ mol/kgw and $[S] = 10^{-3}$ mol/kgw.

5. The Study of the Cu–Sn–S–O–H System

The Eh-pH diagram for the Cu–Sn–S–O–H system (Figure 4) was calculated holding the 1:1 ratio between the initial concentrations of the metals ($[Cu] = [Sn] = 10^{-6}$ mol/kgw) and choosing 10^{-3} mol/kgw for [S], to let the graph comparable with those already presented in this study (i.e., Figures 2a and 3a). Only minor differences are observed comparing the Figures 3a and 4a. They mainly reside in a small increase of the covellite predominance field. Comparing the Figures 3b and 4b, the main differences consist in the disappearance of the fields relative to the species in solution at pH < 0.5 and pH > 13. Both fields are replaced by cassiterite. This change is not due to the different system analyzed, but it could be ascribed to the change in Sn concentration. In fact, at least under the adopted conditions for the calculations, the two systems Cu–S–O–H and Sn–S–O–H can be considered as

independent, owing to the fact that the ligand species (i.e., OH^-, HS^- and SO_4^{2-}) are abundant with respect to the concentration of Cu and Sn.

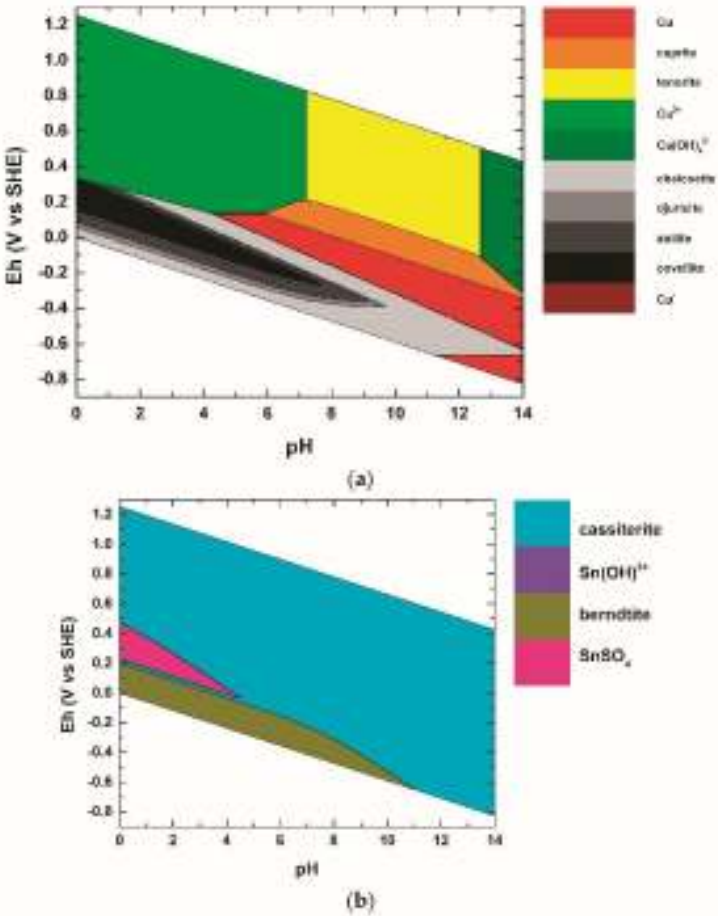

Figure 4. Eh-pH diagrams of the Cu–Sn–S–O–H system, calculated assuming [Cu] = 10^{-6} mol/kgw, [Sn] = 10^{-6} mol/kgw and [S] = 10^{-3} mol/kgw. (**a**) Diagram for the Cu species; (**b**) diagram for the Sn species.

A remarkable consideration point to the absence of predominance fields for either kuramite or mohite. This means that, at room temperature, these two minerals never attain a condition where they become the prevailing species in the system. This does not necessarily imply that the two minerals do not have a stability field at room temperature. For this reason, the stability fields of mohite and kuramite were plotted in Figure 5a,b, respectively. These fields were obtained allowing only mohite (or kuramite) to precipitate. The other, eventually concurring, precipitation mechanisms were not included in the mass balance. Accordingly, the fields reported in the Figure 5 represent the maximum stability field obtainable for the given mineral species, given the external (temperature, pressure, batch chemical composition) conditions. In the two figures, the black and red fields represent the stability field evaluated with respect to the Cu and Sn species, respectively. Accordingly, as mohite and kuramite are ternary compounds, both conditions have to be simultaneously satisfied. The actual stability field for mohite and kuramite are thus defined by the red (intersection) boundaries. Figure 5 is pointing to a definitely wider stability field for mohite than for kuramite, which is found stable

only in a limited range of Eh and pH. In contrast, mohite appears to be stable over a field more or less equivalent to that of chalcocite, which, of course, is always prevailing in terms of precipitated amount (in an unconstrained system, Figure 4a). Specific punctual tests carried out with *phreeqc* have verified that a subordinate amount of mohite is always occurring in association to the phases of the Cu–S system, in their stability fields of Figure 4a. It is worth mentioning that the partial superposition of the two stability fields is in a very good agreement with the evidence of coupled occurrence of the minerals in the low temperature hydrothermal genetic environment.

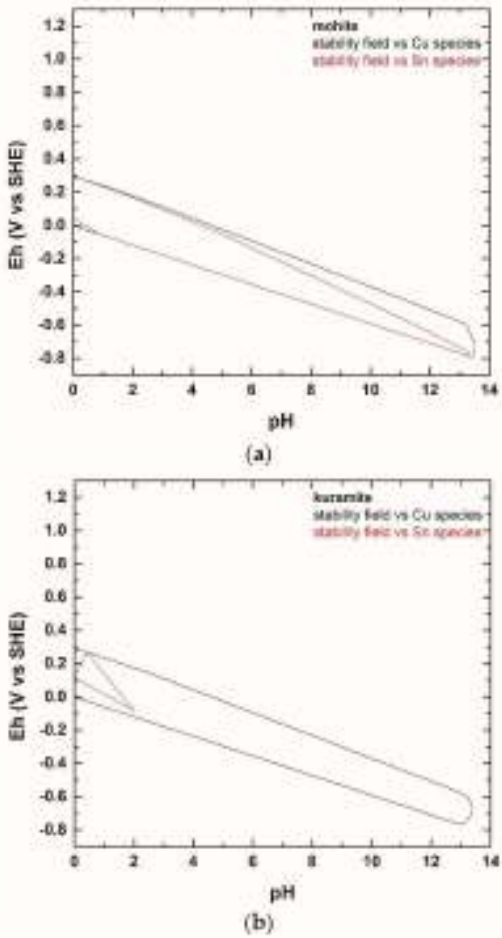

Figure 5. Stability fields for mohite (**a**) and kuramite (**b**) evaluated with respect to the Cu (**black** boundaries) and Sn (**red** boundaries) species. The calculation conditions are the same of the Figure 5.

The main result of this numerical modelling deals with the instability of the two phases, at room temperature, when kept in contact with a water solution. The presence of water, in fact, would favor their reaction towards more stable phases, as e.g., Cu and Sn binary sulfides. This fact has a fundamental consequence for application of these materials in technological devices, as their use has to be maintained in a water/moisture free environment. Similarly, we can expect that hydrothermal syntheses of mohite and kuramite will be less effective in providing good nanoparticle materials, than solvothermal syntheses.

6. Conclusions

The present study summarizes the state of the art concerning the stability of the ternary phases described in the Cu–Sn–S system. Moreover, a preliminary description of their stability at room temperature and pressure conditions is provided. According to our evaluation, mohite and kuramite, the only ternary Cu–Sn–S phases found in nature, can be considered relatively stable if under anhydrous conditions, and their presence in a mineral assemblage can be used to assess not only the temperature but also the Eh-pH window of precipitation.

As far as the materials science is concerned, our results can be considered at least in line with most of the synthetic results, who obtained kuramite and mohite preferring the solvothermal environment [2,6,7].

We are aware that this study is only preliminary, and future steps will involve the evaluation of the stability fields for the two minerals in relation to the temperature variable in a range from 25 to 350 °C, and the extension of the Eh-pH analysis also to non aqueous environment, to fully describe the solvothermal precipitation.

Acknowledgments: This manuscript was funded by the ex 60% 2013 (Department of Earth Sciences, University of Florence) funds to Francesco Di Benedetto.

Author Contributions: Giordano Montegrossi conceived and designed the numerical modelling strategy; Giordano Montegrossi and Andrea Giaccherini performed the *phreeqc* modelling; Francesco Di Benedetto conceived and realized the revision of the literature of the Cu–Sn–S system. All authors equally contributed to the interpretation of the results and to the development and writing of its sections.

Conflicts of Interest: The authors declare no conflict of interest.

References

1. Zawadzki, P.; Baranowski, L.L.; Peng, H.; Toberer, E.S.; Ginley, D.S.; Tumas, W.; Zakutayev, A.; Lany, S. Evaluation of photovoltaic materials within the Cu–Sn–S family. *Appl. Phys. Lett.* **2013**, *103*, 253902. [CrossRef]
2. Tipcompor, N.; Thongtem, S.; Thongtem, T. Effect of microwave radiation on the morphology of tetragonal Cu_3SnS_4 synthesized by refluxing method. *Superlattices Microstruct.* **2015**, *85*, 488–496. [CrossRef]
3. Chen, Y.; Ma, L.; Yin, Y.; Qian, X.; Zhou, G.; Gu, X.; Liu, W.; Wu, X.; Zhang, F. Strong quantum confinement effect in Cu_4SnS_4 quantum dots synthesized via an improved hydrothermal approach. *J. Alloy. Compd.* **2016**, *672*, 204–211. [CrossRef]
4. Tan, Q.; Sun, W.; Li, Z.; Li, J.-F. Enhanced thermoelectric properties of earth-abundant Cu_2SnS_3 via in doping effect. *J. Alloy. Compd.* **2016**, *672*, 558–563. [CrossRef]
5. Baranowski, L.L. Combinatorial Development of Cu2SnS3 as an Earth Abundant Photovoltaic Absorber. Ph.D. Thesis, Colorado School of Mines, Golden, CO, USA, 2015. p. 143.
6. Lokhande, A.C.; Gurav, K.V.; Jo, E.; Lokhande, C.D.; Hyeok Kim, J. Chemical synthesis of Cu_2SnS_3 (CTS) nanoparticles: A status review. *J. Alloy. Compd.* **2016**, *656*, 295–310. [CrossRef]
7. Di Benedetto, F.; Bencistà, I.; D'Acapito, F.; Frizzera, S.; Caneschi, A.; Innocenti, M.; Lavacchi, A.; Montegrossi, G.; Oberhauser, W.; Romanelli, M.; et al. Geomaterials related to photovoltaics: A nanostructured Fe-bearing kuramite, Cu_3SnS_4. *Phys. Chem. Miner.* **2016**, *2016*, 1–10. [CrossRef]
8. Moh, G.H. Tin-containing mineral systems. Part I: The Sn–Fe–S–O system and mineral assemblages in ores. *Chemie Der Erde* **1974**, *33*, 243–273.
9. Wang, N. The three ternary phases in the system Cu–Sn–S. *N. Jb. Miner. Mh.* **1974**, *9*, 424–431.
10. Khanafer, W.; Rivet, J.; Flahaut, J. Etude du ternaire Cu–Sn–S. Diagrammes d'equilibre des systèmes Cu_2S–SnS, Cu_2S–Sn_2S_3 et Cu_2S–SnS_2. Etude cristallographique des composés Cu_4SnS_4, Cu_2SnS_3, $Cu_2Sn_4S_9$, et $Cu_4Sn_7S_{16}$. *Bull. Soc. Chim. France* **1974**, *12*, 267–276. (In French)
11. Moh, G.H. Tin-containing mineral systems. Part II: Phase relations and mineral assemblage in the Cu–Fe–Zn–S system. *Chemie Der Erde* **1975**, *34*, 1–61.
12. Wang, N. Idaite and the synthetic phases $Cu_{4.33}Ge_{0.67}S_5$ and $Cu_{4.67}Sn_{2.33}S_{13}$. *N. Jb. Miner. Mh.* **1976**, *1976*, 241–247.

13. Sobott, R.J.G.; Teh, G.H. Investigations along the Cu_2S–SnS_2 join in the Cu–Sn–S system. *N. Jb. Miner. Abh.* **1977**, *131*, 23–26.
14. Wang, N. Structural variations of non-stoichiometric Cu_2SnS_3. *N. Jb. Miner. Abh.* **1977**, *131*, 26–27.
15. Jaulmes, S.; Rivet, J.; Laruelle, P. Cuivre–Etain–Soufre Cu_4SnS_4. *Acta Cryst. B Struct. Crystallogr. Cryst. Chem.* **1977**, *33*, 540–542. [CrossRef]
16. Wang, N. Covellite related phases within the Cu–Fe–Sn–S system. *N. Jb. Miner. Mh.* **1981**, *1981*, 337–343.
17. Wang, N. Sulfidization experiments performed at low temperatures. *N. Jb. Miner. Abh.* **1982**, *144*, 319–324.
18. Jaulmes, J.; Rivet, J.; Jumas, M. Structure Cristalline du Sulfure et D'Etain $Cu_{5.25}Sn_{2.75}S_8$. *Acta Cryst. B Struct. Crystallogr. Cryst. Chem.* **1982**, *38*, 51–54. (In French) [CrossRef]
19. Wu, D.; Knowles, C.R.; Chang, L.L.Y. Copper-tin sulphides in the system Cu–Sn–S. *Miner. Mag.* **1986**, *50*, 323–325. [CrossRef]
20. Osadchii, E.G. Solid solutions kesterite–Mn–stannite and sphalerite–alabandite in the pseudoternary system Cu2SnS3–ZnS–MnS at 820 °C and 700 °C. *N. Jb. Miner. Mh.* **1996**, *6*, 201–211.
21. Chen, X.; Wada, H.; Sato, A.; Mieno, M. Synthesis, Electrical Conductivity, and Crystal Structure of $Cu_4Sn_7S_{16}$ and Structure Refinement of Cu_2SnS_3. *J. Solid State Chem.* **1998**, *139*, 144–151. [CrossRef]
22. Chen, X.; Wada, H.; Sato, A. Preparation, crystal structure and electrical properties of Cu_4SnS_6. *Mater. Res. Bull.* **1999**, *34*, 239–247. [CrossRef]
23. Olekseyuk, I.D.; Dudchak, I.V.; Piskach, L.V. Phase equilibria in the Cu_2S–ZnS–SnS_2 system. *J. Alloy. Compd.* **2004**, *368*, 135–143. [CrossRef]
24. Fiechter, S.; Martinez, M.; Schmidt, G.; Henrion, W.; Tomm, Y. Phase relations and optical properties of semiconducting ternary sulfides in the system Cu–Sn–S. *J. Phys. Chem. Solids* **2003**, *64*, 1859–1862. [CrossRef]
25. Jemetio, J.P.F.; Zhou, P.; Kleinke, H. Crystal structure, electronic structure and thermoelectric properties of $Cu_4Sn_7S_{16}$. *J. Alloy. Compd.* **2006**, *417*, 55–59. [CrossRef]
26. Kovalenker, V.A.; Malov, V.S.; Evstigneeva, T.L.; Vyal'sov, L.N. Mohite, Cu_2SnS_3, a new sulfide of tin and copper. *Zapiski. Vses. Mineralog. Obshch.* **1982**, *111*, 110–114. (In Russian) [CrossRef]
27. Pascua, M.I.; Murciego, A.; Pellitero, E. Sn–Ge–Gd–Cu–Fe-Bearing Sulfides and Sulfosalts from the Barquilla Deposit, Salamanca, Spain. *Can. Miner.* **1997**, *35*, 39–52.
28. Kovalenker, V.A.; Nekrasov, I.Y.; Malov, V.S. Copper and iron sulfostannate minerals in gold-silver deposits. *Int. Geol. Rev.* **1986**, *28*, 1443–1459. [CrossRef]
29. Kovalenker, V.A. Kuramite, Cu_3SnS_4, a new mineral of the stannite group. *Int. Geol. Rev.* **1981**, *23*, 365–370. [CrossRef]
30. Franchini, M.; Impiccini, A.; O'Leary, S.; Rios, F.J.; Schalamuk, A.I. Distribución de las alteraciones y mineralizaciones en la sección central del yacimiento Agua Rica (27°22' S-66°16' O), Catamarca. *Rev. Asoc. Geol. Argent.* **2009**, *64*, 391–408. (In Spanish)
31. Franchini, M.; Impiccini, A.; Lentz, D.; Rios, F.J.; O'Leary, S.; Pons, J.; Schalamuk, A.I. Porphyry to epithermal transition in the Agua Rica polymetallic deposit, Catamarca, Argentina: An integrated petrologic analysis of ore and alteration parageneses. *Ore Geol. Rev.* **2011**, *41*, 49–74. [CrossRef]
32. Huang, H.H. The Eh-pH Diagram and Its Advances. *Metals* **2016**, *6*, 23. [CrossRef]
33. Parkhurst, D.L.; Appelo, C.A.J. *User's Guide to PHREEQC (Version 2)—A Computer program for Speciation, Batch-Reaction, One-Dimensional Transport, and Inverse Geochemical Calculations*; Water-Resources Investigations Report 99-4259; U.S. Geological Survey, Earth Science Information Center, Open-File Reports Section: Reston, VA, USA, 1999.
34. Kinniburgh, D.; Cooper, D. PhreePlot: Creating Graphical Output with PHREEQC. Available online: http://nora.nerc.ac.uk/19744/1/PhreePlot.pdf (accessed on 8 June 2016).
35. Helgeson, H.C.; Delaney, J.M.; Nesbitt, H.W.; Bird, D.K. Summary and critique of the thermodynamic properties of rock forming minerals. *Am. J. Sci.* **1978**, *278*, 1–229.
36. Johnson, J.; Oelkers, E.; Helgeson, H. SUPCRT92: A software package for calculating the standard molal thermodynamic properties of minerals, gases, aqueous species and reactions from 1 to 5000 bar and 0 to 1000 °C. *Comp. Geosci.* **1992**, *18*, 899–947. [CrossRef]
37. Ball, J.W.; Nordstrom, D.K. *User's Manual for WATEQ4F, with Revised Thermodynamic Data Base and Test Cases for Calculating Speciation of Major, Trace, and Redox Elements in Natural Waters*; USGS Numbered Series Open-File Report 91-183; U.S. Geological Survey: Reston, VA, USA, 1991; p. 193.

38. Delany, J.M.; Lundeen, S.R. *The LLNL Thermochemical Database: Revised Data and File Format for the EQ3/6 Package*; Lawrence Livermore National Laboratory: Livermore, CA, USA, 1991.
39. Stull, D.R.; Prophet, H. *JANAF Thermochemical Tables*, 2nd ed.; Office of Standard Reference Data, National Bureau of Standards: Washington, DC, USA, 1971; Volume 37, p. 1141.
40. Robie, R.A.; Waldbaum, D.R. *Thermodynamic Properties of Minerals and Related Substances at 298.15 K (25.0 °C) and One Atmosphere (1.013 Bars) Pressure and at Higher Temperatures*; U.S. Government Printing Office: Washington, DC, USA, 1968.
41. Moody, G.J.; Thomas, J.D.R. Lattice energy and chemical prediction: Use of the Kapustinskii Equations and the Born-Haber cycle. *J. Chem. Educ.* **1965**, *42*, 204–210. [CrossRef]
42. Donald, H.; Jenkins, B. Thermodynamics of the Relationship between Lattice Energy and Lattice Enthalpy. *J. Chem. Educ.* **2005**, *82*, 950–952.
43. Jackson, A.J.; Walsh, A. Ab initio thermodynamic model of Cu_2ZnSnS_4. *J. Mater. Chem. A* **2014**, *2*, 7829–7836. [CrossRef]
44. Onoda, M.; Chen, X.; Sato, A.; Wada, H. Crystal structure and twinning of monoclinic Cu_2SnS_3. *Mater. Res. Bull.* **2000**, *35*, 1563–1570. [CrossRef]
45. Vieillard, P.; Tardy, Y. Prediction of enthalpy of formation based on refined crystal structures of multisite compounds. 2. Application to minerals belonging to the system Li_2O-Na_2O-K_2O-BeO-MgO-CaO-MnO-FeO-Fe_2O_3-Al_2O_3-SiO_2-H_2O. Results and discussion. *Geochim. Cosmochim. Acta* **1994**, *58*, 4064–4107. [CrossRef]
46. Vieillard, P. Prediction of enthalpy of formation based on refined cyrstal structures of multisite compounds. 1. Theories and examples. *Geochim. Cosmochim. Acta* **1994**, *58*, 4049–4063. [CrossRef]
47. Burton, L.A.; Walsh, A. Phase Stability of the Earth-Abundant Tin Sulfides SnS, SnS_2, and Sn_2S_3. *J. Phys. Chem. C* **2012**, *116*, 24262–24267. [CrossRef]
48. Baranowski, L.; Zawadzki, P.; Christensen, S.; Nordlund, D.; Lany, S.; Tamboli, A.C.; Gedvilas, L.; Ginley, D.S.; Tumas, W.; Toberer, E.S.; et al. Control of Doping in Cu_2SnS_3 through Defects and Alloying. *Chem. Mater.* **2014**, *26*, 4951–4959. [CrossRef]
49. Brookins, D.G. *Eh-pH Diagrams for Geochemistry*; Springer Science & Business Media: Berlin, Heidelberg, Germany, 1988; p. 176.
50. Takeno, A. *Atlas of Eh-pH Diagrams: Intercomparison of Thermodynamic Databases*; Geological Survey of Japan Open File Report No.419; National Institute of Advanced Industrial Science and Technology, Research Center for Deep Geological Environments: Tokyo, Japan, 2005; p. 285.
51. Young, C.A.; Dahlgren, E.J.; Robins, R.G. The solubility of copper sulfides under reducing conditions. *Hydrometallurgy* **2003**, *68*, 23–31. [CrossRef]
52. Ma, R.; Stegemeier, J.; Levard, C.; Dale, J.G.; Noack, C.W.; Yang, T.; Brown, G.E., Jr.; Lowry, G.V. Sulfidation of copper oxide nanoparticles and properties of resulting copper sulfide. *Environ. Sci. Nano* **2014**, *1*, 347–357. [CrossRef]

Phys Chem Minerals
DOI 10.1007/s00269-017-0911-4

ORIGINAL PAPER

Mössbauer study of bornite and chemical bonding in Fe-bearing sulphides

M. Borgheresi[1] · F. Di Benedetto[1,2,3] · M. Romanelli[1,3] · M. Reissner[4] · W. Lottermoser[5] · R. R. Gainov[6,7] · R. R. Khassanov[6] · G. Tippelt[5] · A. Giaccherini[3,8] · L. Sorace[3,8] · G. Montegrossi[2,3] · R. Wagner[5] · G. Amthauer[5]

Received: 23 March 2017 / Accepted: 4 July 2017

Abstract The Mössbauer spectra of a nearly stoichiometric natural bornite, Cu_5FeS_4, specimen were reinvestigated between 295 and 4.2 K. There is no difference between the Neél temperature T_N as determined by the Mössbauer effect or by the susceptibility measurements (T_N = 67.5 K). No additional paramagnetic doublet can be observed in the low-temperature MS spectra. The valence state of Fe is $Fe^{(3-\delta)+}$ caused by a partial electron transfer from the Cu^+ ions to the Fe^{3+} ions which increases the shielding of the s-electrons by the d-electron density and by this increases the isomer shift to a value intermediate between tetrahedral high-spin Fe^{2+} and tetrahedral high-spin Fe^{3+}.

Keywords Magnetic properties · Bornite · Mössbauer spectroscopy · Chemical bond in sulphides

Introduction

Bornite, Cu_5FeS_4, is one of the most important copper ore minerals. Besides this aspect, bornite shows special semiconducting and magnetic properties used in several high-tech materials, such as diluted magnetic semiconductors or thermoelectrics provided that the metal ions are ordered in the structure (Qiu et al. 2014). Therefore, bornite is of potential interest for technological applications.

There are three different polymorphic phases of bornite with superstructure relationships (Koto and Morimoto 1975): a low-, an intermediate- and a high-temperature form. The low bornite is the only naturally occurring phase (Vaughan and Craig 1978).

High bornite is stable above 230 °C, has a cubic structure with space group Fm3m and a cell constant a = 5.50 Å. High bornite crystallizes in the antifluorite structure, where the S^{2-} ions occupy the positions of a face-centered cubic Bravais lattice and 5 Cu^+ ions, 1 Fe^{3+} ion, and 2 vacancies randomly occupy the centers of the 8 tetrahedral voids within that face-centered lattice (Fig. 1a).

With decreasing temperature, cations and vacancies entail order forming first intermediate bornite and finally low-temperature bornite. Their unit cells are multiple of that of high bornite with 2a2a2a for intermediate bornite, with partial ordering of cations and vacancies, and 2a4a2a for low bornite, with almost complete ordering.

Low bornite is orthorhombic (a = 10.950 Å, b = 21.862 Å, c = 10.950 Å) and belongs to the space group Pbca. The structure can be described consisting of 2 subcells: one has a sphalerite arrangement, with four metal ions and four vacancies in the eight available tetrahedral sites within a cubic face-centered S^{2-} lattice; the other one has again an antifluorite-type structure with all the tetrahedral voids within a cubic face-centered

F. Di Benedetto
francesco.dibenedetto@unifi.it

1 Dipartimento di Scienze della Terra, Università di Firenze, Florence, Italy
2 IGG-CNR, Florence, Italy
3 INSTM Unit of Florence, Florence, Italy
4 Institut für Festkörperphysik, TU Wien, Vienna, Austria
5 Fachbereich Chemie und Physik der Materialien, Universität Salzburg, Salzburg, Austria
6 Kazan Federal University, Kazan, Russia
7 Forschungszentrum Jülich, Jülich, Germany
8 Dipartimento di Chimica U. Schiff, Università di Firenze, Sesto Fiorentino, Italy

Published online: 17 July 2017

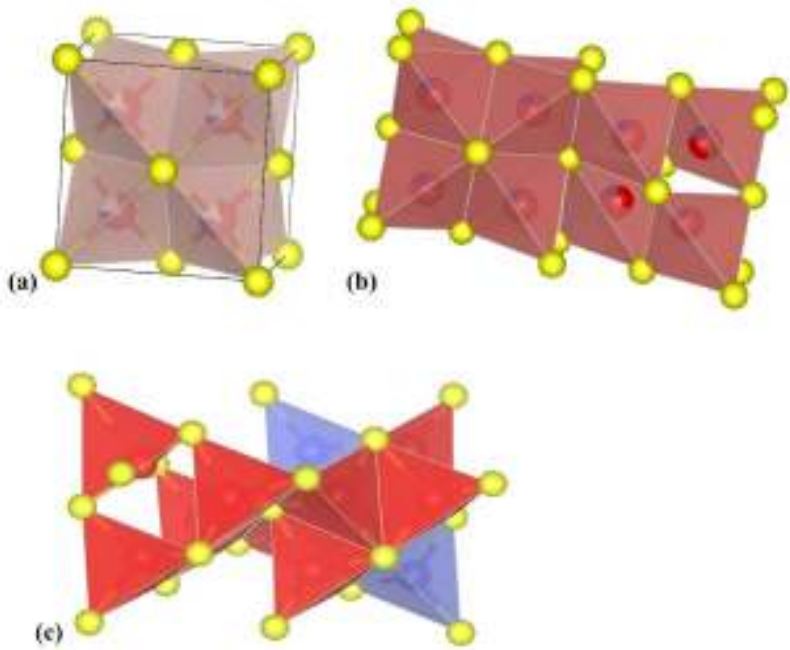

Fig. 1 **a** Structural model of high bornite: Cu atoms (*red*), Fe atoms (*blue*) and vacancies randomly occupy the tetrahedral voids of an antifluorite type unit cell; **b** detail of the low bornite structural model, exhibiting the antifluorite and the sphalerite subunits; **c** possible localisation of Fe sites in the structure, according to Collins et al. (1981) and Borgheresi et al. (2007)

S^{2-} lattice occupied by metal cations (Fig. 1b). Structural refinements suggest that 2 cation sites in the antifluorite subunit are occupied by Fe (Koto and Morimoto 1975).

The valence state of copper and iron in bornite as well as their distribution over the available metal sites are still a matter of discussion. Nominally, Cu should be Cu^{+} and Fe should be Fe^{3+}. ^{57}Fe Mössbauer studies assigned a single doublet in the Mössbauer spectra taken at room temperature to Fe^{3+} (Vaughan and Burns 1972). Because its isomer shift at room temperature IS = 0.39 mm/s is too high for pure tetrahedrally coordinated Fe^{3+} in sulphides, Vaughan and Craig (1978) suggested a dynamic electron exchange between Fe^{2+} and Fe^{3+} leading to a value of the IS, which is intermediate between tetrahedrally coordinated Fe^{2+} and Fe^{3+} in sulphides. This explanation was supported by Jagadeesh et al. (1981) by temperature-dependent Mössbauer studies and bulk magnetic susceptibility measurements. This electron hopping process between Fe^{2+} and Fe^{3+} should be accompanied by a similar process between Cu^{+} and Cu^{2+}, to achieve the charge balance. Because of uncertainty in some Mössbauer studies, a reexamination of bornites from different localities at room temperature has been done, which confirms finally the presence of one single doublet with isomer shift IS between 0.37 and 0.39 mm/s and quadrupole splitting QS between 0.20 and 0.23 mm/s (Gainov et al. 2014).

XAS studies by van der Laan et al. (2002), Patrick et al. (2004) and Mikhlin et al. (2005) confirmed the existence of Fe^{3+} and by that indirectly also the coexistence of Cu^{+} even though classical valence states are usually not suited to describe the metal bonding in sulphide minerals (Bente 1987). Q- and X-band cw-EPR measurements by Borgheresi et al. (2007) confirmed the presence of Fe^{3+} as fundamental valence state of iron in bornite in agreement with magnetic susceptibility measurements. The absence of Cu^{2+} signals in the EPR spectra within the whole paramagnetic regime suggested again the presence of Cu^{+} as main valence state of copper.

The same study confirmed that bornite undergoes a transition from the paramagnetic to the antiferromagnetic state at 64 K (already evidenced by many authors, e.g. Townsend et al. 1977; Collins et al. 1981; Jagadeesh et al. 1981; Oak et al. 1996; Przewoznik et al. 2013). The authors explained their results with magnetic coupling between Fe^{3+} in the antifluorite subunit located at the opposite corners of the distorted cube of tetrahedral positions (Fig. 1c) in agreement with the model of Collins et al. (1981) evidenced by a neutron diffraction study. Some discrepancies characterize the experimental studies dealing with the magnetic phase transition (e.g. Townsend et al. 1977; Jagadeesh et al. 1981; Collins et al. 1981; Oak et al. 1996; Borgheresi et al. 2007; Przewoznik et al. 2013). The Néel temperature (T_N), at which paramagnetic to antiferromagnetic transitions occur,

was determined by several authors as reported in Table 1. The higher values cluster around 76 K and are reported by Mössbauer studies (one of them coupled to neutron diffraction), whereas the lower values cluster around 65 K and are provided by magnetic susceptibility investigations. Additional changes of the magnetic behavior are reported to occur at lower temperatures (Table 1).

The effective magnetic moment μ_{eff} is always different from the theoretical free ion value for Fe^{3+} $\mu_{theor} = 5.9\ \mu_B$, indicating a more or less covalent nature of the chemical bond in this mineral (Townsend et al. 1977; Jagadeesh et al. 1981; Borgheresi et al. 2007; Przewoznik et al. 2013). The internal hyperfine field H_i as determined by Mössbauer spectroscopy is 350 kOe at 4.2 K (Collins et al. 1981; Jagadeesh et al. 1981; Przewoznik et al. 2013), i.e. much lower than the hyperfine field of 510 kOe (Hawthorne 1988) for high-spin Fe^{3+} in oxides and this again is explained by the strong contribution of covalent bonding in bornite (Przewoznik et al. 2013).

The aim of the present study was to collect additional Mössbauer data on an almost pure natural bornite sample, already characterized by magnetic studies (Borgheresi et al. 2007), at different temperatures in order to try to explain the following discrepancies and problems:

1. Which is the origin of the difference between the Neél temperature T_N as determined by the Mössbauer effect and T_N as determined by the susceptibility measurements?
2. Is the paramagnetic doublet sometimes observed in the Mössbauer spectra below T_N caused by superparamagnetism or by the presence of an additional paramagnetic phase or even to a trace of spin glass behaviour?

Table 1 List of the literature's magnetic transition temperatures

Transition temperature (K)	Method	References
76(2)	MS	Townsend et al. (1977)
76(2)	MS	Collins et al. (1981)
73	MS	Oak et al. (1996)
75	MS	Przewoznik et al. (2013)
67.5	Magnetometry, MS	Jagadeesh et al. (1981), this work
64	Magnetometry	Borgheresi et al. (2007)
35	Magnetometry	Jagadeesh et al. (1981)
35	Magnetometry	Borgheresi et al. (2007)
30	Magnetometry	Przewoznik et al. (2013)
8	Magnetometry	Townsend et al. (1977)
10	Magnetometry	Jagadeesh et al. (1981)

In addition, the chemical bonding and the valence states of Cu and Fe in Cu–Fe-sulphides including bornite which are still an open problem, will be discussed and interpreted on the basis of a comparison of the experimental Mössbauer data from the most common sulphide minerals which are typical examples for a special oxidation state and special coordination number.

Experimental methods

Chemical and mineralogical composition

Quantitative chemical analyses of the natural bornite specimen were performed using an electron microprobe (JEOL 8600 SUPERPROBE). Small grains were embedded in an epoxy holder and the surface was ground and then polished using diamond paste. Analytical measuring conditions were 15 kV accelerating voltage and a 10 nA beam current. The standards used were natural $CuFeS_2$ and synthetic CuS. Measuring times were 20 s for the peak maximum and 10 s for the background. Wavelength dispersive X-ray spectroscopy (WDS) measurements were made to characterize the sample in terms of its chemical homogeneity for the elements Cu and Fe. Twenty point analyses, distributed over five different grains, were carried out to obtain a representative composition for the natural sample.

X-ray powder diffraction patterns were recorded with CuK_α radiation using a Bruker D8 diffractometer. This was done to characterize the sample in terms of all present phases and to determine the symmetry and unit-cell dimension of the bornite. Data were collected between 10° and 70° 2θ. The lattice parameters a, b and c were obtained by Rietveld refinement using the program Topas V2.1 (Bruker AXS GmbH).

The chemical formula of the natural bornite specimen is calculated on the basis of 4 S^{2-} and can be reported as

$$Cu_{4.99}Fe_{0.99}Ag_{0.01}S_4,$$

and, therefore, corresponds to the almost ideal composition. No evidences of chemical inhomogeneity are found by the WDS point analyses within the experimental error.

All observed XRD reflections can be indexed by considering the low bornite crystal structure. The lattice parameters are a = 10.94(2) Å, b = 21.88(3) Å and c = 10.93(2) Å with space group Pbcu and 16 formula units per unit cell. According to these results, the investigated sample can be classified as an almost pure, chemically homogeneous, low bornite.

Mössbauer spectroscopy

Transmission ^{57}Fe Mössbauer experiments were carried out with a conventional Mössbauer apparatus, using a ^{57}Co/Rh matrix single line thin source with initial activity 50 mCi. The spectrometer is operated in constant acceleration mode with a symmetric triangular velocity shape and a multichannel analyzer with 1024 channels. The velocity range is either ±4 or ±12 mm s^{-1} calibrated to α-iron at RT. During the measurements, the source was kept at room temperature, whereas the absorber could be cooled down to low temperatures using a continuous flow vaporizer cryostat. Isomer shift values are reported relative to α-iron at room temperature. Line widths are reported as full widths at half peak maximum (FWHM).

For the absorber preparation, 100 mg of mineral grains, carefully hand-picked from fractions of dimensions 0.3–0.2 mm under a microscope, was ground under ethanol to avoid oxidation, mixed with epoxy resin and filled into Cu-rings of a 10-mm inner diameter, covered with a high-purity Al-foil on each side. The nominal absorber thickness was 10 mg Fe/cm^2. Complete thickness correction was applied to all Mössbauer spectra before analysis. The two symmetric spectra obtained, 512 channels each, were folded, calibrated to α-iron and evaluated assuming Lorentzian-shaped doublets or sextets and by solving the full Hamiltonian with both electrostatic and magnetic hyperfine interactions using the program Recoil (Lagarec and Rancourt 1998).

Results

Mössbauer spectroscopy

The room temperature (RT) Mössbauer spectrum of the absorber is presented in Fig. 2. It exhibits a single quadrupole split doublet with an isomer shift IS = 0.39(1) mm/s. The comparatively small half-widths FWHM = 0.24(1) mm/s of the doublet and its small quadrupole splitting QS = 0.22(1) mm/s in the RT spectrum suggest that most probably Fe occupies only one crystallographic equivalent position with minor distortion. The values of IS and QS are almost the same observed in former Mössbauer studies of bornite (Vaughan and Burns 1972; Townsend et al. 1977; Collins et al. 1981; Jagadeesh et al. 1981; Ouk et al. 1996; Przewoznik et al. 2013; Gainov et al. 2014). For instance, Gainov et al. (2014) reported in their room temperature Mössbauer study of natural bornites from different localities QS values in the range 0.20–0.23 mm/s and IS values in the range 0.37–039 mm/s with respect to α-iron at room

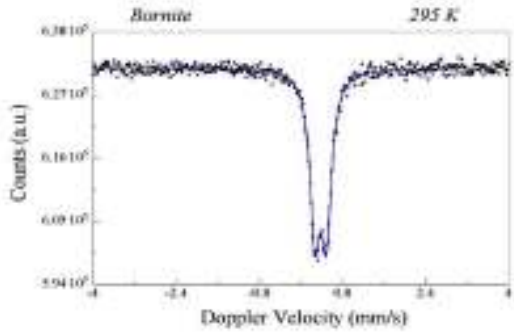

Fig. 2 ^{57}Fe-Mössbauer spectrum, taken at room temperature, of the absorber. The spectrum is evaluated by 1 doublet. The *dots* represent the experimental spectrum and the *solid line* the calculated spectrum

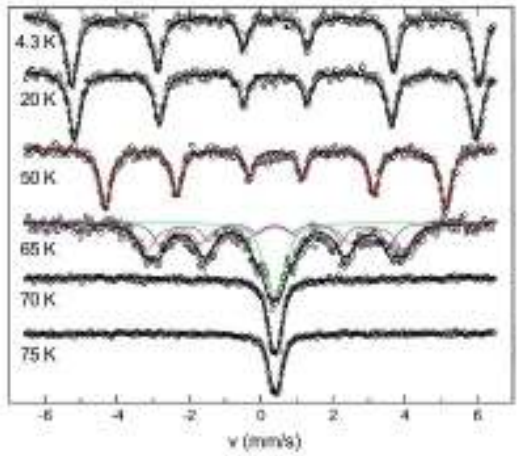

Fig. 3 Mössbauer spectra of bornite taken between 75 and 4.3 K absorber temperature

temperature. The current work shows almost the same Mössbauer parameters and this means that our sample is well suited for low-temperature studies as those carried out in the present study.

The Mössbauer spectra taken between 75 and 4.3 K are shown in Fig. 3 and the best-fit parameters used to reproduce the experimental Mössbauer spectra in the whole temperature range are reported in Table 2. Down to 70 K, a single doublet is observed with no evidence of magnetic hyperfine interaction. Accordingly, the Mössbauer parameters between room temperature and 70 K show the typical behavior expected for high-spin Fe^{3+}, i.e. a moderate increase of IS with decreasing temperature due to the second-order Doppler shift and almost no change of QS with

Table 2 ^{57}Fe Mössbauer parameters of natural bornite, Cu_5FeS_4, at different absorber temperatures

T (K)	IS (mm/s)	QS (mm/s)	H_i (kOe)	FWHM (mm/s)	A (%)
298	0.38(1)	0.22(1)	0	0.24(1)	100
80	0.51(1)	0.19(1)	0	0.26(1)	100
75	0.51(1)	0.18(1)	0	0.30(1)	100
70	0.51(1)	0.19(1)	0	0.33(1)	100
65	0.52(1)	0.00	222.7(1)	0.53(1)	35.3
65	0.50(1)	0.00	198.6(1)	0.40(1)	32.0
65	0.50(1)	0.00	13.8(1)	0.41(1)	32.7
50	0.52(1)	0.00	294.5(1)	0.33(1)	100
45	0.53(1)	0.01	311.6(1)	0.34(1)	100
22	0.54(1)	0.00	344.0(1)	0.24(1)	100
20	0.52(1)	0.00	347.0(1)	0.33(1)	100
4.3	0.53(1)	0.00	352.2(1)	0.33(1)	100

T absorber temperature, *IS* isomer shift referred to α-Fe at room temperature, *QS* quadrupole splitting, H_i internal magnetic field, *FWHM* full line width at half peak maximum, *A* area referred to the total resonant absorption area = 100%

decreasing temperature. Only the FWHM slightly increases from 0.24 mm/s at 80 K to 0.33 mm/s at 70 K.

The onset of magnetic hyperfine interaction was observed first at 65 K by the appearance of a six-line pattern with very broad lines, which required the consideration of 3 six-line patterns for a satisfactory reproduction of the spectrum. Therefore, we conclude that the antiferromagnetic ordering temperature T_N is between 70 and 65 K, i.e. 67.5 ± 2.5 K. This broadening of the lines is referred to some inhomogeneous distribution of magnetic fields in the proximity of a critical temperature, i.e. T_N. The 50 K spectrum can be fitted by a single six-line pattern with reasonable line widths. The same holds true for spectra at lower temperatures.

In the low-temperature range the isomer shifts continue to slightly increase from IS = 0.51 mm/s at 75 K up to 0.53 mm/s at 4.3 K. The line widths remain almost constant between 50 and 4.3 K with the exception of the transition zone near the magnetic ordering temperature indicating a decreasing distribution of magnetic fields at temperatures lower than T_N = 67.5 K. Surprisingly, the quadrupole splitting drops down to almost zero in the spectra of the magnetically ordered phase. This cannot be explained at the moment because no details of the crystal structure, such as the distortion of the tetrahedral sites, are reported for these low temperatures. The temperature dependence of the internal magnetic field $H_i(0)$ is displayed in Fig. 4. It increases from $H_i(0)$ = 294.4(1) kOe at 50 K to $H_i(0)$ = 352.2(1) kOe at 4.3 K.

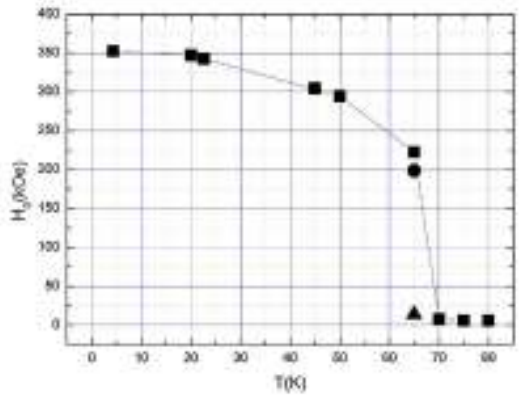

Fig. 4 Temperature dependence of the internal magnetic field $H_i(0)$ of bornite between 75 and 4.3 K. At T = 65 K, *three symbols* represent the three components used to fit the spectrum

Discussion

Magnetism of bornite (1): comparison of the Néel temperature T_N obtained from susceptibility measurements and Mössbauer spectroscopy

As discussed in the Introduction, the definition of the T_N for the magnetic transition of bornite is still an open problem. This transition is reported to occur between two recurring values, i.e. 76 and 67 K, and it can be in principle correlated to the preference by each author to rely either on MS or on susceptibility data; remarkably, the authors having performed both MS and susceptibility measurement always rely on the former (Townsend et al. 1977; Przewoznik et al. 2013).

A possible explanation of slight discrepancies between T_N values obtained by spectroscopy or by susceptibility measurements can be inferred by considering the different sensitivity of the two techniques to the onset of long-range order, and their intrinsically different timescale. Mössbauer spectroscopy provides indication of the AF coupling between neighbouring ions. According to Hawthorne (1988), the magnetic splitting of the Mössbauer spectra can be observed for substances in their long-range ordered ferromagnetic and antiferromagnetic configuration. Nevertheless, also paramagnetic states can exhibit magnetic splitting, provided that relaxation effects slow down such that their half-life becomes longer than that of the ^{57}Fe excited state ($\tau_{1/2}$ = 97.81 ns). On this basis, the onset of the Mössbauer magnetic splitting in bornite should be related to the slowing down of the relaxation processes,

while the susceptibility would trace the onset of the long-range arrangement of AF magnetic structure.

The present MS results point to a different situation: at 70 K a paramagnetic doublet still exists and at 65 K without any doubt a magnetic spectrum appears with very broad lines, which were evaluated by 3 different six-line patterns (Table 2). The magnetic ordering temperature occurs between 70 and 65 K, most probably at 67.5 K. This value is indeed very close to that obtained by EPR and magnetic susceptibility measurements of the same sample (Borgheresi et al. 2007). We thus suggest that in our sample the discrepancy between MS and susceptibility data falls in the range of the experimental uncertainty. Since, at variance with samples of previous reports, the sample of this investigation represent an almost pure bornite, the different values of T_N reported in the literature should then be attributed to varying chemical composition of the different samples and to their different thermal histories. This results in different cation order/disorder of the bornites and in different magnetic ordering temperature as observed by Mössbauer spectroscopy, whereas susceptibility data are apparently less sensitive to these differences.

Magnetism of bornite (2): comparison of the present Mössbauer results with previous data

The analogies between the present and previous results are clearly supported by studying the temperature dependence of the spontaneous magnetisation of the two ferromagnetic sublattices originating from the antiferromagnetic behaviour (Morrish 1980). The magnetic hyperfine field values, evaluated from the analysis of the MS spectral multiplets, arising from the magnetic splitting of the nuclear levels, are an excellent measure of the internal fields, H_i, in the absence of an externally applied magnetic field (Aharoni 1996). The magnetic fields, H_i, are originated by the existence of the opposite sublattice spontaneous magnetisations. Spontaneous sublattice magnetisation increases from zero at the T_N towards a maximum absolute value at 0 K as expected for Brillouin behaviour (Morrish 1980). In the Fig. 5, all the available literature's data are plotted in a graph of the reduced MS magnetic hyperfine field versus the reduced temperature. However, the differences in the whole dataset do not appear significant for the interpretation. All data obtained by different studies over at least four decades are fully comparable indicating the consistence of our data with previous reports. The experimental data can be adequately fitted by a theoretical function derived from a Brillouin plot of the reduced temperature, obtained in the mean field approximation (Aharoni 1996) and calculated for a spin-only d^5 high-spin system. The excellent agreement between the experimental data and the theoretical prediction is in line with previous EPR results on bornite

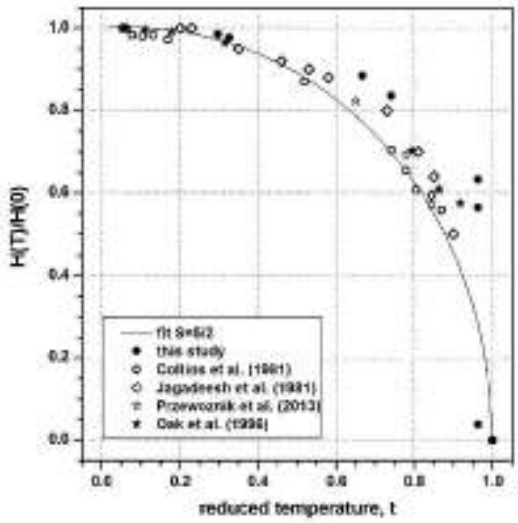

Fig. 5 Spontaneous magnetisation of bornite below the Neel temperature: plot of the reduced internal field, $H_i(T)/H_i$ ($T = 0$), versus the reduced temperature T/T_N. The data are reduced with respect to slightly different B_{hf} values, in a range between 34.5 T and 36.2 T, and for the different Néel temperatures, in the range between 67 and 76 K (Jagadeesh et al. 1981; Collins et al. 1981; Oak et al. 1996; Przewoznik et al. 2013)

(Borgheresi et al. 2007), definitely allowing to assess high-spin Fe^{3+} as the unique formal valence state for Fe.

The isomer shift and the nature of the Fe–S chemical bond

The isomer shifts of Fe in bornite at each measured temperature are much larger than expected for Fe^{3+} in tetrahedral positions in sulphides, as evidenced by Fig. 6a, which shows literature data of isomer shift at room temperature of Fe in various sulphides as function of the coordination number. Literature data were grounded on the fundamental dataset by Vaughan and Craig (1978), in which all IS data are comparable. Further IS data from other minerals needed for this discussion were also included.

IS data are grouped by coordination number, formal valence state of Fe and spin state. Only sulphides for which these three parameters are independently determined are plotted in Fig. 6a. Apparently, several sulphides group in homogeneous regions, identified as tetrahedral high-spin Fe^{3+}, tetrahedral high-spin Fe^{2+}, octahedral low-spin Fe^{2+} and octahedral high-spin Fe^{2+}, respectively. These groups are highlighted in the Fig. 6a by dot circles and we will discuss their relevant parameters in relation to bornite ones in the following.

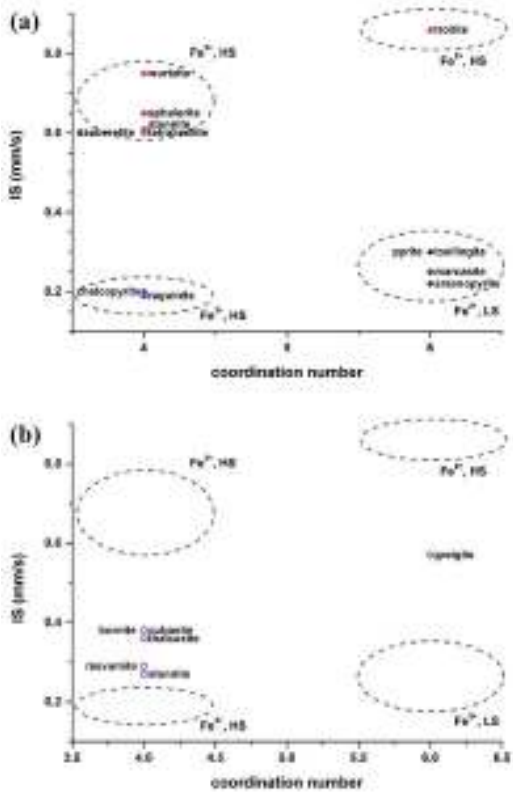

Fig. 6 Fe isomer shifts IS, evaluated from room temperature spectra and referred to α-Fe at room temperature, as function of the coordination number CN; IS data of **a** various reference sulphides and **b** for Cu^{+}-, Fe^{3+}-bearing tetrahedral sulphides, exhibiting anomalously high values, are plotted. The *dash ellipses* are used to mark grouped data

Chalcopyrite, $CuFeS_2$ and the isostructural raguinite, $TlFeS_2$, belong to the high spin Fe^{3+} group: their IS values are very close to each other [0.19 mm/s (Vaughan and Craig 1978) and 0.20 mm/s (Forcher et al. 1989), respectively], pointing to a close similarity of the chemical bonding in chalcopyrite and raguinite, and are distinctly lower than that of bornite. However, while in chalcopyrite Fe is associated with nominally Cu^{+}, in raguinite Cu is substituted by Tl at the tetrahedral sites and any kind of interactions between Cu and Fe can be excluded. Thus, Cu–Fe interactions are ruled out also in the case of chalcopyrite.

In the tetrahedral high-spin Fe^{2+} group are comprised daubréelite, $Fe^{2+}Cr_2S_4$, stannite, $Cu^{+}Fe^{2+}SnS_4$, tetrahedrite, $(Cu, Fe)_{12}(Sb,As)_4S_{13}$, sphalerite, cubic (Zn, Fe)S, and wurtzite, hexagonal (Zn, Fe)S. The IS values are in the range between 0.59 and 0.75 mm/s, distinctly larger than the IS of Fe in bornite (Vaughan and Craig 1978; Lepetit et al. 2003).

So far we have discussed Fe^{2+} and Fe^{3+} in high-spin configuration in sulphides. An example of low-spin Fe^{2+} in tetrahedral coordination is much unlikely to occur and is not known to us. Magnetic measurements ruled out the hypothesis that low-spin tetrahedral Fe^{3+} is occurring in bornite (Borgheresi et al. 2007). One can consider that this configuration in tetrahedral sites is highly improbable, as the spin pairing energy would be much larger than the Crystal Field Stabilization Energy CFSE (Cotton et al. 1999). Borgheresi et al. (2007) found in their susceptibility study on the same bornite sample of this study a Curie constant of 3.33 emu K/mol (and $\mu_{eff} = 5.16$ μB) corresponding to a value intermediate between HS Fe^{2+} ($C = 3.00$ emu K/mol) and HS Fe^{3+} ($C = 4.375$ emu K/mol). However, Fe^{3+} LS would be $S = 1/2$ (only one unpaired electron) corresponding to a Curie constant of 0.375 emu K/mol (and $\mu_{eff} = 1.74$ μB) and this is too low for the measured value.

One well-established example for diamagnetic low-spin Fe^{2+} is FeS_2, pyrite, with an isomer shift IS = 0.30 mm/s and Fe in octahedral coordination (Vaughan and Craig 1978; Schmid-Beurmann and Lottermoser 1993). According to these last authors, the same IS value is observed in at least one-third of the FeS_2–CuS_2 solid solution. Similar low-spin octahedral Fe^{2+}-bearing compounds are marcasite, orthorhombic FeS_2 and arsenopyrite, FeAsS, which fall in the same region of the plot of pyrite (Fig. 6a). The IS values of this group are similar to that of bornite (Vaughan and Craig 1978), but low-spin Fe^{2+} in bornite can be excluded, according to the magnetic susceptibility measurements exhibiting a paramagnetic behaviour at room temperature (Borgheresi et al. 2007).

Concerning high-spin octahedral Fe^{2+}, the case of troilite, FeS, can be considered. The IS value of this species, 0.86 mm/s, is definitely higher than that of bornite (Vaughan and Craig 1978).

Another group of sulphides, all characterised by peculiar IS values, is reported in Fig. 6b. They are rasvumite, KFe_2S_3, cubanite, $CuFe_2S_3$, greigite, Fe_3S_4, stannite, $Tl_2Cu_3FeS_4$, thalcusite and bornite, Cu_5FeS_4. Rasvumite, cubanite and greigite are compounds featuring mixed valent $Fe^{2.5+}$. As an example, the nature of this mixed valence of Fe will be discussed for the mineral rasvumite, which crystallizes with the orthorhombic space group Cmcm. According to its formula, one half of the iron should be Fe^{2+} and the other half Fe^{3+}. Both species occupy the same, crystallographic equivalent lattice positions, i.e. an infinite double chain of edge-sharing tetrahedra. Amthauer and Bente (1983) observed in the Mössbauer spectrum only one single doublet instead of the two expected, one for Fe^{2+} and one for Fe^{3+}. The existence of a single doublet (IS = 0.29 mm/s) can be explained by fast electron hopping between the Fe^{2+}- and Fe^{3+}-ions in neighbouring tetrahedra leading to an intermediate hyperfine interaction

in the Mössbauer spectrum. Therefore, the isomer shift IS in rasvumite is in between the values for "pure" ionic Fe^{3+} and Fe^{2+}. The electron exchange between neighbouring Fe ions through common edges is facilitated by the small average Fe–Fe distance of 2.71 Å. Similar electron exchange processes between Fe^{2+} and Fe^{3+} in neighbouring lattice sites are observed in greigite, Fe_3S_4, with an isomer shift of $Fe^{2.5+}$ at the octahedral sites IS = 0.57 mm/s (Coey et al. 1970) and in cubanite with an isomer shift of $Fe^{2.5+}$ in tetrahedral positions IS = 0.40 mm/s (McCammon et al. 1992). Goh et al. (2010) came to a similar interpretation of the valence state of Fe in cubanite by evaluating their X-ray absorption and photoelectron absorption spectroscopic investigation of the electronic structure of cubanite. Presently, we are performing a XAS and XPS study on bornite, the results of which will be presented in a forthcoming paper.

The situation is different for stannite (Di Benedetto et al. 2005) and thalcusite (Forcher et al. 1989): the anomalous values of IS for Fe^{3+} doublets cannot be explained by the occurrence of a Fe^{2+}–Fe^{3+} fast electron exchange, because of the specialisation of the cation sites in the relative structural model. Conversely, pairs of edge-sharing tetrahedral sites occupied by Cu and Fe are present.

Following this survey, we can conclude that the high IS value in bornite cannot be ascribed to some Fe–Fe electron exchange. In fact, the IS of Fe in bornite shows no discontinuity with temperature, i.e. a separation into Fe^{2+} and Fe^{3+} subspectra similar to that observed in magnetite, Fe_3O_4, below the Verwey transition at 123 K. Accordingly, we point out that a fast electron hopping between Fe^{2+} and Fe^{3+} can be excluded in bornite. As the IS depends on the s-electron density at the Fe nucleus an additional d-electron density transfer to Fe in bornite can be expected. An increased d-electron density at the Fe nucleus increases the shielding effect against the s-electrons and, therefore, the isomer shift increases distinctly compared to the pure ionic Fe^{3+} (Goodenough 1982). This means that the actual d-electron configuration of Fe in bornite is not $3d^5$ but rather $3d^{5+x}$ yielding an increased s-electron shielding by the $5 + x$ d-electrons. This d-electron density transfer can only arise from the copper ions, which formally are Cu^{1+} and occupy corner sharing tetrahedra. This influence of the Cu ions is the same observed in Cu-Fe-sulphides such as thalcusite and stannite (Fig. 6b). Interactions between neighbouring Cu- and Fe-ions were also mentioned by other authors. Townsend et al. (1977) referred the relatively high Neél temperature $T_N = 76$ K to a possible contribution to the overall exchange interaction from a small supertransferred spin density on Cu^+. Przewoznik et al. (2013) referred the distinctly smaller hyperfine field $H_t = 350$ kOe at 4.2 K in bornite compared to the hyperfine field of Fe^{3+} in oxides, i.e. 510 kOe, to Fe–S covalence and to a possible copper contribution to the effective magnetic moment of the compound. Nuclear magnetic resonance (NMR) or nuclear quadrupole resonance (NQR) spectroscopic methods applied on Cu nuclei could help to clarify the d-electron density transfer from Cu ions in bornite as well as in other sulphides (Gainov et al. 2009).

Concluding remarks

With respect to the aims declared in the introduction, this study was able to point out that

1. in a pure bornite sample the difference between the Neél temperature T_N as determined by Mössbauer spectroscopy and by the susceptibility measurements is not occurring; the discrepancies previously reported in literature have to be attributed to varying chemical compositions of the sample and/or different thermal histories;
2. in our investigation, no evidence of additional paramagnetic doublets either above or below the Neél temperature is observed; accordingly, we suggest that eventual additional doublets in earlier Mössbauer spectra of bornite below the Neél temperature are due to the presence of an additional paramagnetic phase;
3. the formal valence state of Fe in bornite is definitely assessed as $3 - x$; however,
4. bornite, together with thalcusite, Fe-bearing kuramite and other minerals, is characterized by a peculiar Fe–S chemical bond, where a partial transfer of d electron density occurs from Cu^+ ions; this transfer affects the IS of Fe in bornite, increasing it to a value intermediate between tetrahedral high spin Fe^{2+} and Fe^{3+};
5. this intermediate IS value is similar to that of mixed-valence Fe sulphides, as greigite, cubanite and rasvumite, but in their case the anomalous value is attributed to the occurrence of an high-frequency electron hopping.

Further studies, concerning the structural investigation of bornite below the Neél temperature are in progress.

Acknowledgements Authors acknowledge the Departments of Chemistry and of Earth Sciences of the University of Florence, for funding this research under the ex-60% programme, and the Italian CNR, for support.

References

Aharoni A (1996) Introduction to the theory of ferromagnetism. Clarendon Press, Oxford

Amthauer G, Bente K (1983) Mixed-valent iron in synthetic rasvumite, KFe_2S_3. Z Naturwissenschaften 70:146–147

Bente K (1987) Stabilization of Cu–Fe–Bi–Pb–Sn-sulfides. Mineral Petrol 36:205–217

Borgheresi M, Di Benedetto F, Cannechi A, Pratesi G, Romanelli M, Sorace L (2007) An EPR and SQUID magnetometry study of bornite. Phys Chem Minerals 34:609–619

Coey JMD, Spender MR, Morrish AH (1970) Magnetic structure of the spinel Fe_3S_4. Solid State Comm 8:1605–1608

Collins ME, Longworth G, Townsend MG (1981) Magnetic structure of bornite, Cu_5FeS_4. Can J Phys 59:535–539

Cotton FA, Wilkinson G, Murillo CA, Bochmann M (1999) Advanced inorganic chemistry, 6th edn. Wiley Interscience, Hoboken

Di Benedetto F, Bernardini GP, Borrini D, Lottermoser W, Tippelt G, Amthauer G (2005) ^{57}Fe- and ^{119}Sn-Mössbauer study on stannite (Cu_2FeSnS_4)–kesterite (Cu_2ZnSnS_4) solid solution. Phys Chem Minerals 31:683–690

Forcher K, Lottermoser W, Amthauer G (1989) Mössbauer study of rapaiuite, $TlFeS_2$, and thalcusite, $Cu_3Tl_2FeS_4$. In: Moh GH (ed) Ore minerals: an experimental approach and new observations. N Jb Miner Abh 160:25–28

Gabitov RR, Douglas AV, Pen'kov IN, Makhmedshin IR, Mozgova NN, Evlampiev IA, Bryzgalov IA (2009) Phase transition and anomalous electronic behavior in the layered superconductor CuS probed by NQR. Phys Rev B 79:075115

Gabitov RR, Vagizov FG, Golovanevskiy VA, Ksenofontov VA, Klingelhöfer G, Klekovkina VV, Shumilova TG, Pen'kov IN (2014) Application of ^{57}Fe Mössbauer spectroscopy as a tool for mining exploration of Bornite (Cu_5FeS_4) copper ore. Hyperfine Interact 226:51–55

Goh WG, Buckley AN, Skinner WM, Fan LJ (2010) An X-ray photoelectron and absorption spectroscopic investigation of the electronic structure of cubanite, $CuFe_2S_3$. Phys Chem Minerals 37:389–405

Goodenough JB (1982) Mössbauer ^{57}Fe isomer Shift as a measure of valence in mixed-valence iron sulphides. J Solid State Chem 41:1–22

Hawthorne F (1988) Mössbauer spectroscopy. In: Hawthorne FC (ed) Spectroscopic methods in mineralogy and geology, Rev Mineral 18:255–340

Jagadeesh MS, Nagarathna HM, Montano PA, Seehra MS (1981) Magnetic and Mössbauer studies of phase transitions and mixed valences in bornite $Cu_{5-x}Fe_{1+x}S_{4-y}$. Phys Rev B 23:2350–2356

Koto K, Morimoto N (1975) Superstructure investigation of bornite, Cu_5FeS_4, by the modified partial Patterson function. Acta Cryst B31:2268–2273

Lagarec K, Rancourt DG (1998) Extended Voigt-based analytic lineshape method for determining *N*-dimensional correlated hyperfine parameter distributions in Mössbauer spectroscopy. Nucl Instrum Methods 129:266–280

Lepetit P, Bente K, Doering T, Luckhaus S (2003) Crystal chemistry of Fe-containing sphalerites. Phys Chem Miner 30:185–191

McCammon C, Zhang J, Robert M, Hazen L, Finger W (1992) High pressure crystal chemistry of cubanite, $CuFe_2S_3$. Am Min 77:937–944

Mikhlin Y, Tomashevich Y, Tauson V, Vyalikh D, Molodtsov S, Szargan R (2005) A comparative X-ray absorption near-edge structure study of bornite, Cu_5FeS_4, and chalcopyrite, $CuFeS_2$. J Electron Spectrosc Relat Phenom 142:83–88

Morrish AH (1980) The physical principles of magnetism. RE Krieger Publishing Company Inc, Malabar

Oak HN, Baek KS, Jo Y (1996) Superparamagnetic relaxation in Cu_5FeS_4. Solid State Commun 100:467–470

Patrick RAD, van der Laan G, Charnock JM, Griguric BA (2004) Cu $L_{2,3}$ X-ray absorption spectroscopy and the electronic structure of minerals: spectral variations in non stoichiometric bornites, Cu_5FeS_4. Am Mineral 89:541–546

Przewoznik J, Zukrowski J, Gondek L, Gupka C, Lemański A, Kapusta C, Piestrzyński A (2013) Structural, magnetic, and Mössbauer effect studies of bornite. Nukleonika 58:43–46

Qiu P, Zhang T, Qiu Y, Shi X, Chen L (2014) Sulfide bornite thermoelectric material: a natural mineral with ultralow thermal conductivity. Energy Environ Sci 7:4000–4006

Schmid-Beurmann P, Lottermoser W (1993) ^{57}Fe-Moessbauer spectra, electronic and crystal structure of members of the CuS_2–FeS_2 solid solution series. Phys Chem Minerals 19:571–577

Townsend MG, Gosselin JR, Tremblay RJ, Ripley LG, Carson DW, Muir WB (1977) A magnetic and Mössbauer study of magnetic ordering and vacancy clustering in Cu_5FeS_4. Phys Chem Solids 38:1153–1159

Van der Laan G, Patrick RAD, Charnock JM (2002) Cu L-2, L-3 X-ray absorption and the electronic structure of nonstoichiometric Cu_5FeS_4. Phys Rev B 6604:135–139

Vaughan DJ, Burns RG (1972) Mössbauer spectroscopy and bonding in sulphide minerals containing four-coordinated iron. In: Proc 24th IGC, 21–30 September 1972, Montreal, 158–167

Vaughan DJ, Craig JR (1978) Mineral chemistry of metal sulfides. Cambridge University Press, London, p 494

molecules

MDPI

Article

An Integrated Experimental/Theoretical Study of Structurally Related Poly-Thiophenes Used in Photovoltaic Systems

Davide Vanossi [1], Luigi Cigarini [2], Andrea Giaccherini [3], Enrico da Como [4] and Claudio Fontanesi [4,5,*]

Received: 24 December 2015 ; Accepted: 14 January 2016 ; Published: 19 January 2016
Academic Editors: Nicola Cioffi, Antonio Monopoli and Massimo Innocenti

1 Department of Geological and Chemical Sciences, University of Modena and Reggio Emilia, Via G. Campi 183, Modena 41125, Italy; davide.vanossi@unimore.it
2 Department of Physics, University of Modena and Reggio Emilia, Via G. Campi 213, Modena 41125, Italy; luigi.cigarini@unimore.it
3 Department of Chemistry, University of Florence, Via della Lastruccia 3, Sesto Fiorentino 50019, Italy; andrea.giaccherini@unifi.it
4 Department of Physics, University of Bath, Claverton Down Bath BA2 7AY, UK; E.Da.Como@bath.ac.uk
5 Department of Engineering "Enzo Ferrari", University of Modena and Reggio Emilia, Via Vivarelli 10, Modena 41125, Italy
* Correspondence: claudio.fontanesi@unimore.it; Tel.: +39-059-2563-6170

Abstract: In this work, a series of eight thiophene-based polymers (exploited as "donors" in bulk heterojunction photovoltaics cells), whose structures were designed to be suitably tuned with the electronic characteristics of the [6,6]-Phenyl C61 butyric acid methyl ester (PCBM), is considered,. The electronic properties of the mono-, di-, trimeric oligomers are reckoned (at the Hartree-Fock and DFT level of the theory) and compared to experimental spectroscopic and electrochemical results. Indeed, electrochemical and spectroscopic results show a systematic difference whose physical nature is assessed and related to the exciton (electron-hole) binding energy (E_{eh}). The critical comparison of the experimental and theoretical band gaps, *i.e.*, the HOMO-LUMO energy difference, suggests that electrochemical and DFT values are the most suited to being used in the design of a polythiophene-based p-n junction for photovoltaics.

Keywords: polythiophenes; band gap; DFT; HF; exciton

1. Introduction

The electronic properties of eight thiophene-based polymers (Figure 1 shows the relevant structures), with a particular focus on the interfacial behavior, are rationalized within a "Lego-like sum approach": the electronic properties of the mono-, di-, trimeric species are calculated, and eventually the trimer results are selected (the differences between the dimer and trimer oligomers are almost negligible) and shown, in the following figures, to represent the electronic features of the polymer system well. Such a general modelistic approach spans extremely different worlds: from the Mott-Schottky barrier to Tafel plots in electrochemical systems [1–3]. It is noteworthy that when the field of linear conjugated polymers is considered, a number of non-linear effects concur to determine the final observed electronic properties (with a particular focus on conductivity), leaving this research topic still open to discussion and further development, because low dimensional structures such as polymers (polymers can be considered as electron one-dimensional conductive wires) are unstable, and, in these systems, the coupling between electrons and phonons wavefunctions (leading to the definition of the polaron [4,5]) determines a more tight localization of single- and double-bonds which

lifts molecular orbitals' degeneracy and finally induces the localization of π-electrons, leaving both the experimental and theoretical work a still-challenging field [4–8]. Within this field, the up-to-date frontier hot topic is the estimation and calculation of the so-called polaron dimension [9], which is thought to play a prominent role in determining the polymer electronic conduction.

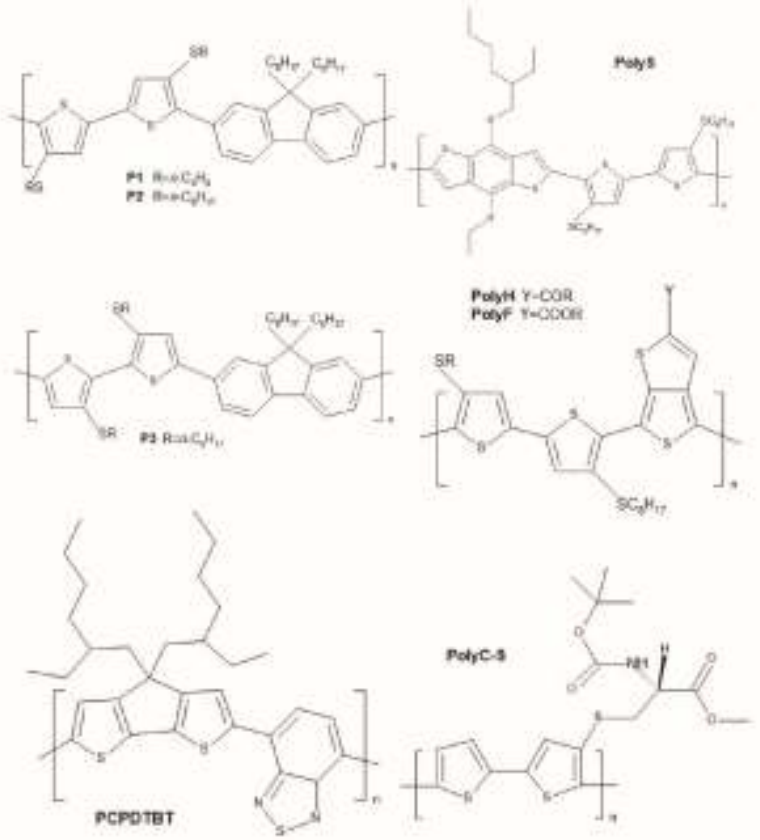

Figure 1. Polymer structures studied in this work.

Furthermore, a field of extremely relevant interest and expectations concerns thin-film polymer semiconductors exploited in hybrid systems, such as organic-based light-emitting diodes, photovoltaic cells and thin-film transistors, where the influence of the degree of order in the solid state plays a major role [10,11]. Indeed, the understanding of the interplay and relationship between the film morphology/electronic-structure and charge transport is of key importance for improving the performance of thin-film transistors [8].

In particular, in the field of organic semiconductors exploited to assemble photovoltaic devices, the open circuit potential is rationalized on the basis of the reciprocal HOMO-LUMO energy differences between the donor and the acceptor partners [11–13]. Although such an approach seems by far much too crude in its strategy, the straight comparison of HOMO-LUMO MOs energy levels, of the donor and acceptor building blocks, is still the most widespread tool exploited in the modelization of photovoltaic organic-based systems [14,15]. The electronic properties of the mono-, di-, trimeric oligomer species are considered and compared to the experimental spectroscopic and electrochemical results [16–19]. Among the different polythiophene structures investigated here, the peculiar characteristics of the chiral PolyC-S made it suitable for the realization of hybrid interfaces [20] exploited in the recently established field of "spin-dependent electrochemistry" [21,22].

2. Semiconductive Polythiophene Structures

In this work, a series of eight thiophene-based polymers (donors) are considered. Their structures were designed (both by the introduction of ring structures of various chemicals in the polymeric backbone structure—heteropolymers—and also by various lateral alkyl chains) to suitably tune the electronic properties of the PCBM (acceptor). The structures of the polymers studied here, are shown in Figure 1. PCPDTBT was purchased by Sigma-Aldrich (St. Louis, MO, USA) (754005 Aldrich, CAS Number 920515-34-0), while all of the other compounds are of original synthesis [16–19].

3. Experimental Setup

UV-vis spectra were recorded in ambient air at room temperature (25 °C), by means of a Perkin Elmer Lambda 900 spectrophotometer (Perkin Elmer, Waltham, MA, USA). Cyclic voltammetry (CV) measurements were performed both with a CHI 660A Electrochemical Workstation (CH Instruments, Inc., Austin, TX, USA) and an AUTOLAB PGSTAT20 (Metrohm Autolab B.V., Utrecht, The Netherlands). A three-electrode electrochemical cell configuration was adopted. A 0.1 mol/L *n*-tetrabutyl ammonium hexa fluorophosphate ($TBAPF_6$ > 99.9%, Sigma-Aldrich Chemie B.V., Zwijndrecht, The Netherlands) in acetonitrile (ACN) solution was used as the base electrolyte. The working electrode is obtained by drop-casting of polythiophene/CH_2Cl_2 solution applied on freshly polished Glassy Carbon (GC) electrodes (Metrohm Schweiz AG, Zofingen, Switzerland) and HTW Sigradur (HTW Hochtemperatur-Werkstoffe GmbH, Thierhaupten, Germany). Prior to polymer drop-casting, the GC surface was mechanically polished with emery paper, then with 0.05 μm alumina (Buheler, Lake Bluff, IL, USA), finally followed by a 5 min sonication cleaning in water. The GC surface was polymer-coated by casting one drop of a 0.1 mg/mL$_w$ in CH_2Cl_2, polymer solution on top of the GC surface and allowing it to dry [16]. A platinum wire was used as the counter electrode. A silver wire was used as a quasi-reference electrode, whose stability was checked (at the end of each measurement session) with respect to the ferrocene/ferrocenium reversible redox couple. In the following all potential values are referred to the Ag/Ag^+ couple. A large number of screening experiments were carried out, varying both the dose of the drop-casting as well as the drying time. Films obtained on repeating the sequence of a single drop-cast application three times, followed by 15 min drying, allowed for the best CV reproducibility. We estimate that our reduction and oxidation potentials are affected by a 30 mV absolute error (±15 mV error). The electrochemical cell was de-aerated with argon for 15 min before any measurement session. Figure 2 shows two examples of the cyclic voltammetry data treatment, in order to show in detail how the electrochemical onset potentials were determined. Two completely different experimental behaviors are considered: Poly H characterized by a rather hill-defined/sluggish cyclic voltammetry pattern (with particular reference to the positive potential range: polymer film oxidation), Figure 2a, and Poly F which shows a rather well-defined and neat cyclic voltammetry pattern, Figure 2b.

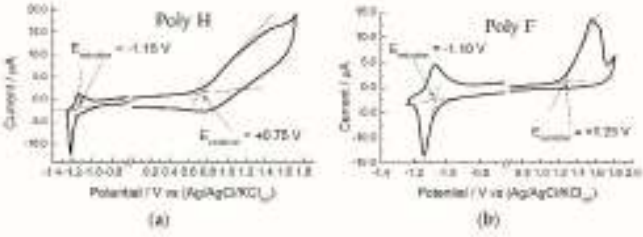

Figure 2. Cyclic voltametries (**a**,**b**) of the Poly H and Poly F polymer films on GC surfaces (obtained by drop-casting procedure), respectively. Showing the method adopted to determine the reduction and oxidation onset potentials, which are used to calculate the so-called electrochemical band gap (ΔE_{EC}). Onset values are obtained by the intercept of the lines interpolating the baseline and redox peak currents.

Figure 3 shows, as an example, the treatment of the UV-vis spectrum of Poly F, in order to show in detail how the onset wavelength is determined, which eventually leads to the calculations of the ΔE_{OPT} value.

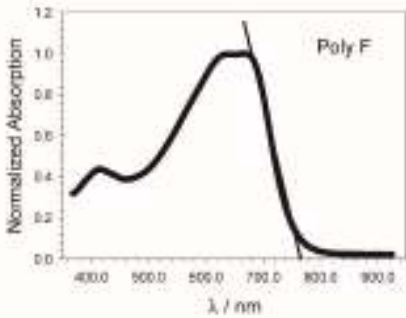

Figure 3. Poly F UV-vis spectrum, the line used to determine the onset wavelength is shown. The intercept with the absissa allows us to determine the optical band gap (ΔE_{OPT}).

4. Computational Details

In the present work, the overall calculations were performed in the framework of *ab initio* methods using the Gaussian and Firefly [23] QC packages, which are partially based on the GAMESS (US) source code. All calculations, unless otherwise indicated, were performed using C_1 symmetry and are of restricted nature. The results presented in this paper are obtained both at the very basic Hartree-Fock (HF) and Becke, three-parameter, Lee-Yang-Parr (B3LYP) exchange-correlation density functional levels of the theory; the all-electron split valence plus polarization basis set 6-31G(d) was used in both HF and DFT calculations. Preliminary screening calculations were carried out using less accurate basis sets: LanL2DZ, 3-21G*, with focus on the influence of the geometry optimization as well as of the number of repetitive units in the oligomer on the variation of the HOMO-LUMO energies and band gap. Moreover, periodic boundary condition (PBC) calculations were performed, the latter results well compare with the HOMO-LUMO band gap relevant to the dimeric and trimeric species, together with the systematic calculation (again involving the mono-, di-, trimer species) of TDDFT electronic spectra [24].

5. Theoretical Background

5.1. Orbital Energies: DFT vs. HF

It is well established [25] that the Kohn-Sham orbitals, $\varphi_i(\mathbf{r})$, do not have any particular physical meaning; they only serve as a tool to construct the exact (at least in principle) ground-state density for the actual system of interacting electrons. The same consideration is clearly also directed for the Kohn-Sham eigenvalues, ε_i, which, from a formal point of view, are simply lagrangian multipliers inserted *"ad hoc"* to perform the constrained variational minimization. Nevertheless, there is one important exception to this statement when the energy ε_N of the highest occupied orbital, for a finite system of N electrons, is considered: minus ε_N depicts, in fact (at least in the case of an exact exchange-correlation functional [25,26]), the ionization potential $I_p(N)$ of the system, *i.e.*,

$$\varepsilon_N(N) = E(N) - E(N-1) = -I_p(N) \quad (1)$$

where $E(N)$ and $E(N-1)$ are the total ground-state energies for the system with N and $N-1$ electrons. On the contrary, all the Hartree-Fock mono-electronic energies, thanks to the Koopmas theorem [27], correspond to electron removal energies once correlation and orbital relaxation effects are neglected.

It is also possible to write down an exact and equivalent relation to Equation (1) starting from the Kohn-Sham energy ε_{N+1} of the highest occupied orbital for a system with $N+1$ electrons:

$$\varepsilon_{N+1}(N+1) = E(N+1) - E(N) = -I_a(N) \tag{2}$$

Equations (1) and (2) can be considered the DFT Koopmans theorem, which, however, in comparison to the Hartree-Fock version, is exact because ε_N is endowed with a many-bodies nature. Equation (2) shows that minus ε_{N+1} is equal to the electron affinity $I_a(N)$ for the N-electron system (being $E(N+1)$, the total ground-state energy for the system with $N+1$ electrons).

Despite the soundness of Equations (1) and (2), differences in Kohn-Sham energy eigenvalues do not correspond, in general, to the exact excitation energies for the interacting N-electron system but, sometimes, they can be used as first, rather fairly acceptable approximations [28].

5.2. Computing the Band Gaps

When different types and states of matter are considered, it is well known [26,28,29] that energy band gaps may or may not occur. A gap is the direct manifestation of the existence of a finite energetic difference between two states of the system. In physics there are several type of gaps: the particle (or quasi-particle) gap, optical gap, superconducting gap [28]. For each one of these gaps, different experimental characterization methods exist. For example, the optical gap, which is related to the energy difference between the electronic ground state and the first excited state for a system with a fixed particle number N (neutral excitation), can be addressed by means of optical spectroscopy. Otherwise, the particle gap (which is of fundamental importance in an insulating periodic solid) is related to the ground-state energies of systems with different particle numbers (charged excitation) and can be typically probed using photoelectron spectroscopy. The particle gap is defined as [26,28]:

$$E_g(N) = I_p(N) - I_a(N) \tag{3}$$

In terms of KS energies, Equations (1) and (2) can be rearranged as:

$$E_g(N) = \varepsilon_{N+1}(N+1) - \varepsilon_N(N) \tag{4}$$

Equation (4) involves the energies of the highest occupied orbitals of two systems with a different number of electrons, so we are dealing with an excitation which does not conserve the number of electrons. Equation (4) can be clearly used when a finite system (such as a molecule) is considered, but becomes quite impractical when referring to a solid. In this last situation it is necessary to define a different particle gap, also known as a Kohn-Sham gap, by means of the following equation:

$$E_g^{KS}(N) = \varepsilon_{N+1}(N) - \varepsilon_N(N) = \Delta E_{DFT} \tag{5}$$

in which the lowest unoccupied (LUMO) and the highest occupied (HOMO) orbital energies, for the system with N electrons (neutral excitation), are considered. It is worthwhile to note that a relation formally equivalent to Equation (5) is commonly also adopted in the Hartree-Fock framework (even for finite systems):

$$E_g^{HF}(N) = \varepsilon_{N+1}^{HF}(N) - \varepsilon_N^{HF}(N) = \Delta E_{HF} \tag{6}$$

Equations (4) and (5) can be related to one another in this way:

$$E_g(N) = E_g^{KS}(N) + \Delta_{xc} \tag{7}$$

where Δ_{xc}, the many-bodies correction to the Kohn-Sham particle gap, can be casted as [28]:

$$\Delta_{xc} = \varepsilon_{N+1}(N+1) - \varepsilon_{N+1}(N) \tag{8}$$

5.3. Optical and Electrochemical Band Gaps

Absorption of a photon with energy equal to or greater than the band gap results in the excitation of an electron from the valence to the conduction band, leaving a hole in the valence band. Such an electron hole pair, or exciton, is bound by the electrostatic attraction between the collective state's electron in the conductive band and the hole in valence band. By means of optical excitation, four basic types of charge-transfer processes are proposed by Credi *et al.* [30], and we proposed them also for semiconducting polymers: electron injection into a neutral molecule (Figure 4a), electron extraction from a neutral molecule (or hole injection, Figure 4b), removal of an electron from one molecule and placing it into an identical molecule at a infinite distance, (Figure 4c), and generation of an electron-hole pair within the same molecule (Figure 4d).

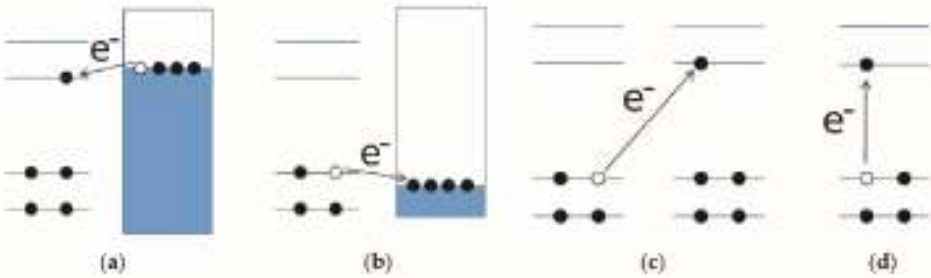

Figure 4. The white circles represent holes and the black circles electrons. In (**a**,**b**) the pseudo-fermi level of the polarized electrode is represented by the line on top of the dark rectangle representing the conduction band of the solid; (**c**,**d**) depicts the intermolecular and intramolecular electronic transitions, respectively. The other lines represent the orbitals in the polymer molecules while the arrows represent the electron transfer.

The electrochemically determined band gap (ΔE_{EC}) is operatively defined as the difference in energy between the first reduction and the first oxidation processes of the molecule, respectively, corresponding to the process in Figure 4a,b. Thus is equivalent to the energy required to produce a noninteracting electron-hole pair (quasi-particle gap). The optical band gap ΔE_{OPT} corresponds to the process in Figure 4d. In the ground of this theoretical model, the two band gaps are related by Equation (9):

$$\Delta E_{OPT} = \Delta E_{EC} + I_{e,h} \quad (9)$$

where $I_{e,h}$ is the binding energy of the exciton. Hence, for any given semiconducting molecule, the electrochemical energy gap is expected to be larger than the optical energy gap.

6. Results

Figure 5a shows the ΔE_{EC} *vs.* ΔE_{OPT} graph, obtained by the experimental band gap values. The latter are obtained (i) by means of spectroscopical measurements, ΔE_{OPT} (optical band gap, calculated by the onset of the absorption peak determined from the UV/Vis spectra), and (ii) by means of CV curves, ΔE_{EC} (note that the difference in the onset of potentials, V, relevant to the reduction and oxidation current peaks is straight transformed in a band gap energy, eV, on the basis of the work of Trasatti [31]).

All the points in this dataset are more positive than the "equivalence line": the electrochemical band gap is systematically larger than the optical band gap (about 0.45 eV), suggesting a bias in the difference between the two band gaps. In Figure 5b, the LUMO/HOMO energy difference, the HF band gap (ΔE_{HF}) has been compared with the DFT band gap (ΔE_{DFT}). Note the systematic large difference between ΔE_{HF} and ΔE_{DFT} values. Figure 5c,e patterns demonstrate that ΔE_{HF} are overestimated with respect to both the optical and electrochemical band gap, while in Figure 5d a comparison between the

DFT band gap and the optical band gap shows that DFT systematically overestimates the optical band gap. Eventually, the electrochemical band gap is compared with the DFT gap (Figure 5f), and ΔE_{DFT} values semi-quantitatively match the electrochemical band gap: the equivalence line is almost exactly placed in the middle of the dataset. Figure 6 shows the difference between the DFT, electrochemical and optical band gap values (*i.e.*, $(\Delta E_{DFT} - \Delta E_{EC})$, $(\Delta E_{EC} - \Delta E_{OPT})$ and $(\Delta E_{DFT} - \Delta E_{OPT})$ differences). Notably, the difference between electrochemical and DFT band gaps $(\Delta E_{DFT} - \Delta E_{EC})$ is scattered homogenously around zero, and the maximum deviation is 0.28 eV. However, the discrepancy between electrochemical and optical results is the same as the DFT and optical one: both ranging between 0.2 and 0.9 eV, highlighting that the DFT and electrochemical band gaps have the same quantitative trend.

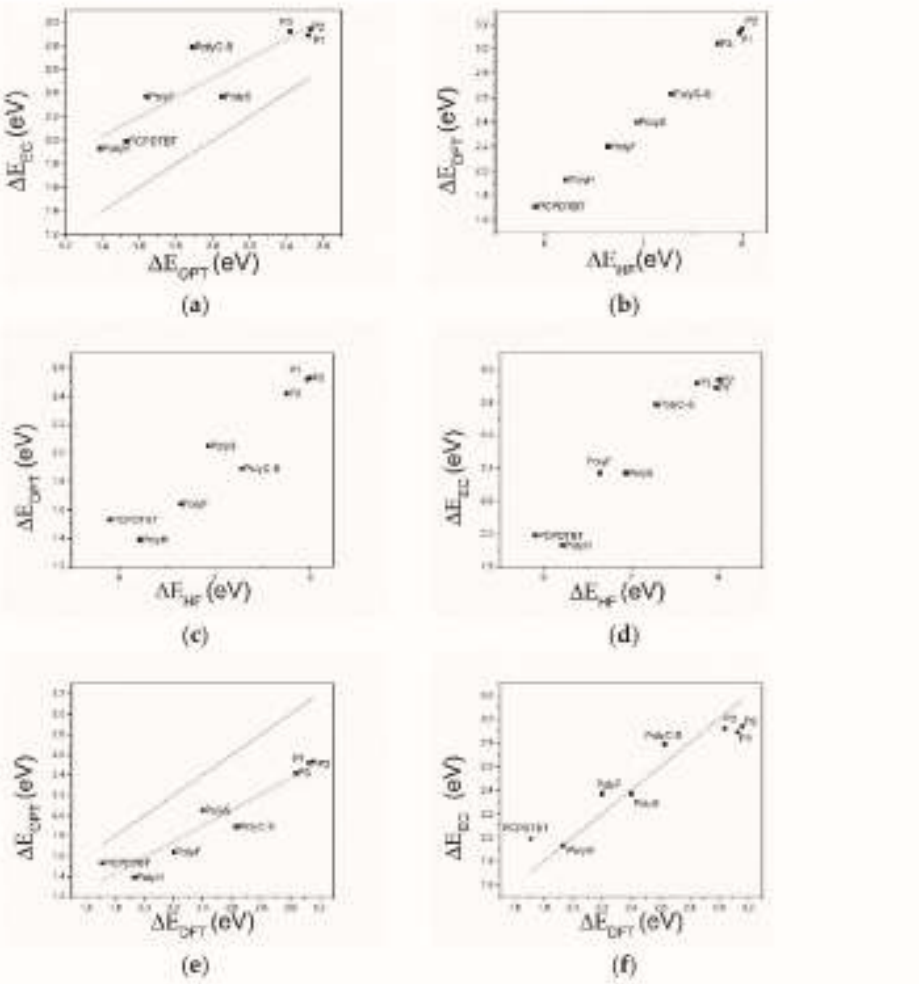

Figure 5. Comparison between (**a**) electrochemically determined and spectroscopically determined band gap; (**b**) band gap computed by means of DFT and HF methods; (**c**) band gap spectroscopically determined and computed by means of HF method; (**d**) band gap electrochemically determined and computed by means of HF method; (**e**) band gap spectroscopically determined and computed by means of DFT method; (**f**) band gap electrochemically determined and computed by means of DFT method. All data are reported in eV. The "equivalence line" shows the ideal line featuring slope = 1 and intercept = 0.

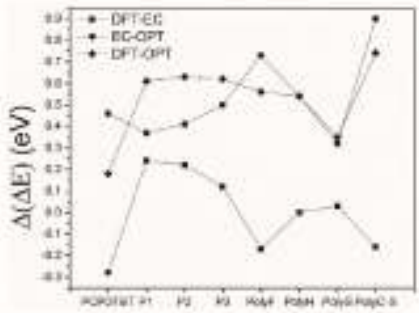

Figure 6. Discrepancies between band gaps computed by means of DFT method and electrochemically determined; band gaps electrochemically and spectroscopically determined; band gaps computed by means of DFT method and spectroscopically determined.

7. Conclusions

The electronic characteristics, with a focus on the band gap, of eight thiophene-based semiconducting polymers have been determined both experimentally (electrochemically, spectroscopically) and theoretically (at the Hartree/Fock and DFT level of the theory). Careful comparison between theoretical and experimental results allows us to draw some main line of action that is useful when dealing with problems of reciprocal coupling of hybrid donor/acceptor systems, where band gap features are thought to determine the ultimate performances of a system/device.

(1) The comparison of HF and DFT theoretical data, with both electrochemical and spectroscopic experimental band gap values, shows that the HF approach provides a dramatic overestimation of the band gap. The exchange-correlation and electron-correlation cannot be neglected; they have to be taken into account to assess the correct band gap energy. Indeed, ΔE_{DFT} values definitively show a better quantitative match with both the electrochemical and spectroscopic band gap values, as it is shown in Figures 5 and 6.

(2) Arguments, based both on the purely modelistic (Figure 4) and on the comparison between DFT and experimental data (Figures 5 and 6), show that the most effective approach to be used when assessing the band gap characteristics for photovoltaic materials is to make a reference to both the DFT and electrochemical methods to determine the HOMO-LUMO band gap.

(3) Eventually, an empirical quantitative value can be determined for the exciton stabilization energy (I_{eA}), *vide infra* relation 8. The close comparison of the physics underlying absorption in electronic spectra (Figure 4d) and reduction/oxidation current peaks in cyclic voltammetry measurements (Figure 4a,b) together with the systematic difference observed in Figure 5a (the least square fit yields $\Delta E_{EC} = 0.53 + 0.99\ \Delta E_{OPT}$) allow us to propose a value of about 0.5 eV (the intercept of the least square fit) as an average value for the exciton stabilization energy [30,32]. Such an estimate is further supported by the systematic shift observed in Figure 6 between the ΔE_{OPT} *vs.* ΔE_{DFT} pattern (red line represents the least square fitting of the ΔE_{OPT} *vs.* ΔE_{DFT} data) and the relevant equivalence line.

As a whole, the results presented in this paper strongly support the view of a tight equivalence between the DFT and electrochemically determined band gap values (a result consistent both in terms of the physics underlying the different processes involving electrons and of the purely measured and computed values). The electrochemical measurements, giving an insight in the relative energy of HOMO and LUMO in different systems, seem to provide the values best suited for designing and selecting optimum candidates for organic/hybrid photovoltaic systems.

Acknowledgments: DIEF (UniMORE), Department of Chemistry (UniFI) and Department of Physics (UniBATH) are kindly acknowledged.

Author Contributions: Davide Vanossi and Claudio Fontanesi conceived and designed the experiments; Luigi Cigarini and Andrea Giaccherini performed the calculations and analyzed the data; Enrico da Como contributed materials; Enrico da Como, Davide Vanossi and Claudio Fontanesi wrote the paper.

Conflicts of Interest: The authors declare no conflict of interest.

References and Notes

1. Tung, R.T. Chemical Bonding and Fermi Level Pinning at Metal-Semiconductor Interfaces. *Phys. Rev. Lett.* **2000**, *84*, 6078–6081. [CrossRef] [PubMed]
2. Mohilner, D.M. The electrical double layer, part I: Elements of double-layer theory. In *Electroanalytical Chemistry: A Series of Advances*; Bard, A.J., Ed.; CRC Press: Boca Raton, FL, USA, 1996; Volume 1.
3. Bard, A.J.; Faulkner, L.R. *Electrochemical Methods: Fundamentals and Applications*, 2nd ed.; Wiley: New York, NY, USA, 1980.
4. Bredas, J.L.; Street, G.B. Polarons, bipolarons, and solitons in conducting polymers. *Acc. Chem. Res.* **1985**, *18*, 309–315. [CrossRef]
5. Brédas, J.L.; Wudl, F.; Heeger, A.J. Polarons and bipolarons in doped polythiophene: A theoretical investigation. *Solid State Commun.* **1987**, *63*, 577–580. [CrossRef]
6. Roncali, J. Synthetic Principles for Bandgap Control in Linear π-Conjugated Systems. *Chem. Rev.* **1997**, *97*, 173–206. [CrossRef] [PubMed]
7. Pesant, S.; Boulanger, P.; Côté, M.; Ernzerhof, M. Ab initio study of ladder-type polymers: Polythiophene and polypyrrole. *Chem. Phys. Lett.* **2008**, *450*, 329–334. [CrossRef]
8. Lan, Y.-K.; Yang, C.H.; Yang, H.-C. Theoretical investigations of electronic structure and charge transport properties in polythiophene-based organic field-effect transistors. *Polym. Int.* **2010**, *59*, 16–21. [CrossRef]
9. Rawson, J.; Angiolillo, P.J.; Therien, M.J. Extreme electron polaron spatial delocalization in π-conjugated materials. *PNAS* **2015**, *112*, 13779–13783. [CrossRef] [PubMed]
10. Joseph Kline, R.; McGehee, M.D.; Toney, M.F. Highly oriented crystals at the buried interface in polythiophene thin-film transistors. *Nat. Mater.* **2006**, *5*, 222–228. [CrossRef]
11. Di Nuzzo, D.; Fontanesi, C.; Jones, R.; Allard, S.; Dumsch, I.; Scherf, U.; von Hauff, E.; Schumacher, S.; da Como, E. How intermolecular geometrical disorder affects the molecular doping of donor-acceptor copolymers. *Nat. Commun.* **2015**, *6*. [CrossRef] [PubMed]
12. Hallermann, M.; Como, E.D.; Feldmann, J.; Izquierdo, M.; Filippone, S.; Martin, N.; Jüchter, S.; von Hauff, E. Correlation between charge transfer exciton recombination and photocurrent in polymer/fullerene solar cells. *Appl. Phys. Lett.* **2010**, *97*, 023301. [CrossRef]
13. Veysel Tunc, A.; de Sio, A.; Riedel, D.; Deschler, F.; da Como, E.; Parisi, J.; von Hauff, E. Molecular doping of low-bandgap-polymer:fullerene solar cells: Effects on transport and solar cells. *Org. Electron.* **2012**, *13*, 290–296. [CrossRef]
14. Li, Y. Molecular Design of Photovoltaic Materials for Polymer Solar Cells: Toward Suitable Electronic Energy Levels and Broad Absorption. *Acc. Chem. Res.* **2012**, *45*, 723–733. [CrossRef] [PubMed]
15. Li, Y.; Calder, S.; Yaffe, O.; Cahen, D.; Haick, H.; Kronik, L.; Zuilhof, H. Hybrids of Organic Molecules and Flat, Oxide-Free Silicon: High-Density Monolayers, Electronic Properties, and Functionalization. *Langmuir* **2012**, *28*, 9920–9929. [CrossRef] [PubMed]
16. Parenti, F.; Morvillo, P.; Bobeico, E.; Diana, R.; Lanzi, M.; Fontanesi, C.; Tassinari, F.; Schenetti, L.; Mucci, A. (Alkylsulfanyl)bithiophene-alt-Fluorene: π-Conjugated Polymers for Organic Solar Cells. *Eur. J. Org. Chem.* **2011**, *2011*, 5659–5667. [CrossRef]
17. Morvillo, P.; Parenti, F.; Diana, R.; Fontanesi, C.; Mucci, A.; Tassinari, F.; Schenetti, L. A novel copolymer from benzodithiophene and alkylsulfanyl-bithiophene: Synthesis, characterization and application in polymer solar cells. *Sol. Energy Mater. Sol. Cells* **2012**, *104*, 45–52. [CrossRef]
18. Morvillo, P.; Diana, R.; Fontanesi, C.; Ricciardi, R.; Lanzi, M.; Mucci, A.; Tassinari, F.; Schenetti, L.; Minarini, C.; Parenti, F. Low band gap polymers for application in solar cells: Synthesis and characterization of thienothiophene-thiophene copolymers. *Polym. Chem.* **2014**, *5*, 2391–2400. [CrossRef]
19. Parenti, F.; Ricciardi, R.; Diana, R.; Morvillo, P.; Fontanesi, C.; Tassinari, F.; Schenetti, L.; Minarini, C.; Mucci, A. Polymers for application in organic solar cells: Bithiophene can work better than thienothiophene when coupled to benzodithiophene. *J. Polym. Sci. A Polym. Chem.* **2015**. [CrossRef]

20. Fontanesi, C.; Tassinari, F.; Parenti, F.; Cohen, H.; Mondal, P.C.; Kiran, V.; Giglia, A.; Pasquali, L.; Naaman, R. New One-Step Thiol Functionalization Procedure for Ni by Self-Assembled Monolayers. *Langmuir* **2015**, *31*, 3546–3552. [CrossRef] [PubMed]
21. Mishra, D.; Markus, T.Z.; Naaman, R.; Kettner, M.; Gohler, B.; Zacharias, H.; Friedman, N.; Sheves, M.; Fontanesi, C. Spin-dependent electron transmission through bacteriorhodopsin embedded in purple membrane. *Proc. Natl. Acad. Sci. USA* **2013**, *110*, 14872–14876. [CrossRef] [PubMed]
22. Mondal, P.C.; Kantor-Uriel, N.; Mathew, S.P.; Tassinari, F.; Fontanesi, C.; Naaman, R. Chiral Conductive Polymers as Spin Filters. *Adv. Mater.* **2015**, *27*, 1924–1927. [CrossRef] [PubMed]
23. Granovsky, A.A. Firefly Version 8.0.0. Available online: http://classic.chem.msu.su/gran/firefly/index.html (accessed on 18 January 2016).
24. Data available upon request to the corresponding author.
25. Koch, W.; Holthausen, M.C. *A Chemist's Guide to Density Functional Theory*, 2nd ed.; Wiley-VCH: New York, NY, USA, 1989.
26. Martin, R.M. *Electronic Structure: Basic Theory and Practical Methods*; Cambridge University Press: Cambridge, UK, 2004.
27. Szabo Ostlund Modern Quantum Chemistry Intro to Advanced Electronic Structure Theory 481s. Available online: http://www.scribd.com/doc/38501522/Szabo-Ostlund-Modern-Quantum-Chemistry-Intro-to-Advanced-Electronic-Structure-Theory-481s (accessed on 15 July 2013).
28. Ullrich, C.A. *Time-Dependent Density-Functional Theory: Concepts and Applications*; Oxford University Press: Oxford, UK, 2011.
29. Giuliani, G.; Vignale, G. Quantum Theory of the Electron Liquid. Available online: http://www.cambridge.org/us/academic/subjects/physics/condensed-matter-physics-nanoscience-and-mesoscopic-physics/quantum-theory-electron-liquid?format=PB (accessed on 22 December 2015).
30. Amelia, M.; Lincheneau, C.; Silvi, S.; Credi, A. Electrochemical properties of CdSe and CdTe quantum dots. *Chem. Soc. Rev.* **2012**, *41*, 5728–5743. [CrossRef] [PubMed]
31. Trasatti, S. The "absolute" electrode potential—The end of the story. *Electrochim. Acta* **1990**, *35*, 269–271. [CrossRef]
32. Strinati, G. Application of the Green's functions method to the study of the optical properties of semiconductors. *Riv. Nuovo Cim.* **2008**, *11*, 1–86. [CrossRef]

Sample Availability: Samples of the compounds are not available from the authors.

Current Density Distribution for a Full Scale Industrial Alluminization Process

Giaccherini, A.[1*], Martinuzzi, S.[2], De Luca, A.[1], Lavacchi, A.[3], Caporali, S.[2] and Innocenti, M.[1]
[1] Chemistry Department, University of Firenze, Firenze, Italy
[2] Consorzio INSTM, Firenze, Italy
[3] Institute of Chemistry of Organometallic Compounds, CNR, Firenze, Italy
Corresponding author: andrea.giaccherini@unifi.it

Abstract: The use of ionic liquids as electrolyte constitutes a challenging quest for galvanic industry. Their physical properties, i.e. viscosity, conductivity etc... strongly differ from aqueous solutions. Some aspects, such as high viscosity, negatively affect the electrochemical process, but some others such as the very wide electrochemical window, constitute unexpected and stimulating opportunities.
The main objective of this work is to formalize a complete computational model suitable for the description of the electrodeposition process takeing into consideration a time-dependant model of the continuous domains and variables playing active roles in the electrochemical process. A common approach is constituted by the Finite Elements Analysis (FEA) [1-3], which is a strategy to solve the governing partial differential equations by means of a suitable discretization.
Respect to the previous approaches, in this communication the electrochemical and chemical kinetics as well as the transport phenomena, were modelled at very high level of theory, taking into account all the parameters affecting the galvanic process, including turbulent convection fields. In particular, we considered tertiary current distribution, chemical equilibria and turbulence models, such as k-ε, to assess the electrodeposited layer thickness even on sharp edges.
Finally, the computational model has been applied to the classical Rotating Hull Cylinder (RHC) apparatus obtaining reasonable results.

Keywords: Electrodeposition, ionic-liquids, turbulence models, coupled problem.

1. Introduction

The electroplating technology from aqueous solutions has some limitations. In particular the little electrochemical window of water (1,23 V, limited respectively by hydrogen and oxygen discharge) impairs the electrodeposition of very electropositive elements [4,5]. In order to overcome this issue the use of non-protic solvents has been recently proposed. In particular, Ionic Liquids (ILs) have been applied to the electrochemical deposition of technical (several micron thick) coatings especially for anticorrosion purposes [6,7]. We refer to ionic liquids speaking of "Room temperature molten salts", which have been in their infancy more than 15 years ago, and are now assessed as viable alternative to the traditional electrochemical media. These liquids are able to join the low melting temperature (room temperature or below) typical of organic solvents with the high ionic conductivity of molten salts [8]. This paper presents the results of a Finite Elements Analysis (FEA) study aiming to determine the current distribution, which constitutes the driving force for the electrodeposition process from chloroaluminate-based ILs. In the field of FEA simulations, a typical aim is to obtain reliable models in order to "a priori" optimize the process setups [9]. We believe that this approach can be extended to electroplating industrial processes in order to determine the most favorable cell geometry [10], to achieve smooth and homogeneous aluminium coatings. The main focus of this paper is the analysis of the current density distribution at the electrodes boundaries. The calculation has been performed by means of the simulation program COMSOL Multiphysics® with the electrodeposition and the CFD (Computational Fluidynamics) modules.

2. Models

Previous studies approached this modelling problem taking into account the primary or secondary current distribution alone [11]. That allowed the design of a model able to account for the time-dependent evolution of the current density distribution, which can be related to the

change of the concentration distribution in the system. However, in the case of ILs, it fails to reproduce the current density distribution on sharp edges. In the present study we improve the reliability of the model takeing into account the tertiary current distribution and the effect of convection and homogenous chemical reactions. A simple 2D geometry, constituted by one cathode located between two anodes (Fig. 1a), has been used to investigate the electrodeposition under diffusion controlled condition; while the effect of a coupled convection field was evaluated by means RHC (Rotating Hull Cylinder) whose scheme is depicted in Figure 1b. That is constituted by an axialsymmetric 2D model, with the section of the cylindrical cathode, an insulant barrier and the anode. The symmetry axis coincides with the cathode axis.
The electrochemical media is constituted by a mixture of $AlCl_3$/BMIm(1:1.5), considering 1:1.5 as the molar ratio, characterized by chemical and physical proprieties reported in Table 1.

a b

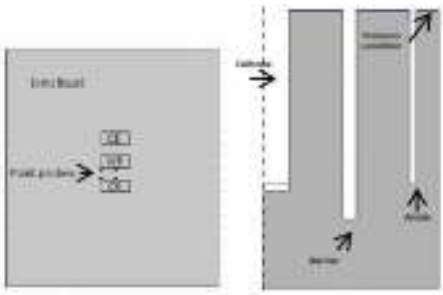

Figure 1. Scheme showing the cell geometry considered for (a) quiet and (b) fluidynamics conditions (rotating Hull cylinder).

2.1 Governing equations

Ohm's law, equation (1) takes into account for the electrical behavior of an electrochemical system [11-15].

$$\nabla^2 \phi_l = -\frac{Q_l}{\sigma_l} \tag{1}$$

ϕ_l is the electric potential in the electrolyte; σ_l is the conductivity of the electrolyte and Q_l is the electric charge. The Nernst-Plank equation describes the flux of the chemical species due to general transport phenomena including convection, diffusion and migration (2).

$$\underline{N_i} = -D_i \nabla c_i - z_i u_{m,i} F c_i \nabla \phi_l + \underline{u} c_i \tag{2}$$

Where c_i, D_i, u_i, and z_i are the concentration, the diffusion coefficient, the mobility and the charge of the of the i_{th} species, respectively; F the Faraday's constant; $\underline{u}$ the velocity field; R_i the reaction term for A and B. In order to calculate the change in composition of the electrolyte near the electrodes due to electron transfer, it's well established the validity of the following Faraday equation (3):

$$R_{i,m} = \frac{-\nu_{i,m} i_{loc,m}}{n_m F} \tag{3}$$

$i_{loc,m}$ is the faradaic current density for the m_{th} process, n_m is the number of electrons exchanged Finally, there are relation between electrochemical species, that can be depicted in the following equilibrium reaction:

$$Al_2Cl_7^- \rightarrow AlCl_4^- + AlCl_3 \tag{4}$$

Controlled by equation (5):

$$K_{eq} = \frac{C(AlCl_4^-)C(AlCl_3)}{C(Al_2Cl_7^-)} \tag{5}$$

On the other side electroneutrality, holds for the bulk electrolyte (6).

$$\sum_i z_i c_i = 0 \tag{6}$$

Turbulent advection has been coupled with the electrochemistry of the model, in order to take in to account for the mixing condition typical of the industrial galvanic baths. In a typical «Rotating Hull Cylinder» (RHC), the high rotation speed implies, in most cases, the turbulent swirl flow around the rotating cathode. We choose a typical k-ε model, due to its good convergence rate and relatively low memory requirements, though it does not very accurately compute flow fields that

exhibit strong curvature. However, the diameter of the Hull Cylinder can be considered to be large enough to make reliable his approximation.

2.2 Boundary conditions

Boundary conditions for the Nernst-Plank (2) can be defined as follow (7-9):

$$\underline{i_l} \cdot \underline{n} = i_{total} \tag{7}$$

$$i_{total} = \sum_i i_{loc,m} + i_{dl} \tag{8}$$

$$i_{loc} = i_0 \left(\frac{C_R}{C_R^0} e^{\frac{\alpha_a F \eta}{RT}} - \frac{C_O}{C_O^0} e^{\frac{-\alpha_c F \eta}{RT}} \right) \tag{9}$$

where, $\underline{i_l}$ is the current distribution vector; i_{dl} is the capacitive current density; $i_{loc,m}$ is the faradaic current density for the m_{th} process; i_0 is the exchange current; c_R/c_R^0 is the ratio of the concentration to the bulk concentration; α_a is the electron transfer coefficient; R is the perfect gasses constant; T is the temperature and η is the electrode overpotential defined by equation (10).

$$\eta = \phi_l + \phi_s - E_{eq} \tag{10}$$

Here, $\phi_l + \phi_s$ is the electrical potential drop across the electrode interface.

Recently, COMSOL Multiphysics® has implemented different mathematical approaches to model electrochemical systems. In particular, the electrodeposition module allows the use of different approximations of the Butler-Volmer boundary condition [16-20]. In the case of a negligible transport in the bulk electrolyte respect to the electron transfer process the ratio $C_O/C_O^0 = 1$, so that the local current can be described by equation (11).

$$i_{loc} = i_0 \left(e^{\frac{\alpha_a F \eta}{RT}} - e^{\frac{-\alpha_c F \eta}{RT}} \right) \tag{11}$$

When $\eta \approx 0$ the exponential term in the Butler-Volmer can be linearized as described in equation 12:

$$i_{loc} = i_0 \left(\frac{C_R}{C_R^0} \frac{\alpha_a F \eta}{RT} + \frac{C_O}{C_O^0} \frac{\alpha_c F \eta}{RT} \right) \tag{12}$$

In the case of a negligible transport in the bulk electrolyte respect to the electron transfer process the ratio $C_O/C_O^0 = 1$, so that the equation (12) becomes (13):

$$i_{loc} = i_0 \left(\frac{\alpha_a F \eta}{RT} + \frac{\alpha_c F \eta}{RT} \right) \tag{13}$$

For the case in study, we used a tertiary current distribution with boundary conditions (9,11-13). Regarding the RHC, boundary conditions for the Navier-Stokes equations had been considered, that the swirl flow imposing cathode rotation speed of 300 rpm. At the top vertex of the RHC 1 bar pressure condition has been imposed (Figure 1b).

2.3 Mesh

The two different problems have been 1investigated using a fine triangular mesh, in order to define the effect of the boundary conditions and of the homogenous chemical reaction (5).

2.4 Chemical and physical proprieties of the electrolyte

D(BMIm)	2.8 10^{-11} $m^2 s^{-1}$ [22]
D($AlCl_4$)	6.1 10^{-11} $m^2 s^{-1}$ [22]
D(Al_2Cl_7)	1.7 10^{-11} $m^2 s^{-1}$ [22]
c(BMIm)	3416 mol m^{-3} [23]
c($AlCl_4$)	1708 mol m^{-3} [23]
c(Al_2Cl_7)	1708 mol m^{-3} [23]
i_0	1 10^{-3} A m^2 [24]
K_{eq}	2.410^6 mol m^{-3} [25]
η	15 mPa s [26]

Table 1: Physical and chemical constant for the modelling of the $AlCl_3$/BMIm(1:1.5).

3. Results

3.1 Electrodeposition under diffusion control

That is the simplest electrochemical system (quiet solution), we approached this case study simulating the electrochemical cell as depicted in figure 1a. In principle, tertiary current distribution takes in to account the effect of the compositional variations of the electrolyte, and constitutes a reliable choice for the simulation of such systems [11]. The model has been solved for the four different boundary conditions (9,11-13). Figure 2 shows the compared results, in terms of deposited charge density after 120 minutes of potentiostatic electrodeposition (potential between the two electrodes 1.1V). Condition (9) constitutes our reference since conditions (11-13) are approximations. The solutions for the condition 9 compared with the results of condition (11) are depicted in figure 2a and 2b respectively. It suggests that condition (11) leads to an overestimation of the charge deposited by a 2%. Boundary conditions (12-13) give a tremendous drop of the charge deposited by a factor of 10^2 (Figure 2c,d). In principle for condition (11) and (13) it is possible to results in negative concentration for the depleted species at an electrode, that is physically impossible impairing the use of this conditions. Unfortunately condition (9) returns an unstable model that, in some cases, does not converge. To overcome this problem, for short time dependent simulation condition (11) can be used considering an error of 2%.

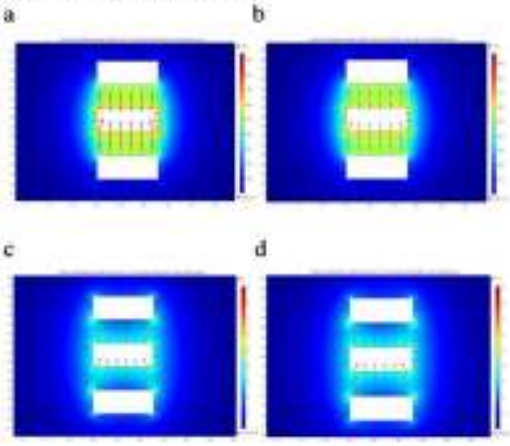

Figure 2. Effect of boundary condition approximations on charge density deposited.

In the light of these considerations the effect of homogeneous chemical equilibrium (5) has been applied only to the most reliable model: i.e. the one applying boundary condition (9). The results of this modeling are shown in figure 3. On the cathode the total current (figure 3a), and the current density on a point in the center (figure 3b) have been compared. The total current is not affected, as well as the current density in the central point. However, sensible differences has been observed in the edges (figure 3c).

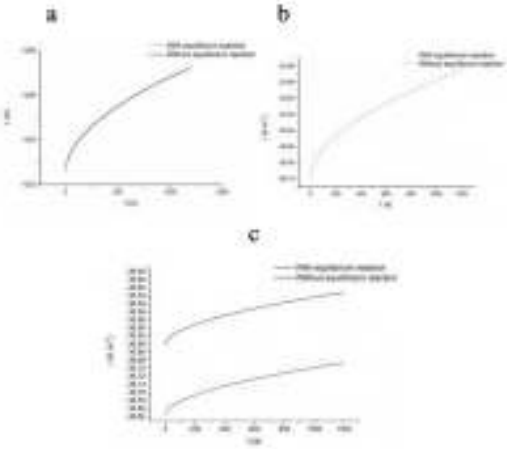

Figure 3. a) Total current on the cathode, b) normal current density on the center of the cathode and c) on the edge.

3.2 Electrodeposition under convection

The results of section 3.1 have been used to determine the current density on the cathode of the RHC. The electrolyte current density is shown in figure 4, confirming the effect of the barrier under the turbulent advection-diffusion condition.

The thickness of alluminium coating along the cathode, has been calculated and depicted in figure 5. After 600s of simulated potentiostatic electrodeposition (-1.1V between cathode and anode boundaries) the maximum thickness (2.8μm) have been observed in the terminal portion of the cylinder. As showed in figure 5 the

thickness decrease down to a minimum of 0.6μm in the uppermost portionof the chatode.

Figure 4. Streamline and modulus of the electrolyte current density for the RHC.

This trend has been confirmed by means of experimental investigations of the deposits, obtained in the same condition.

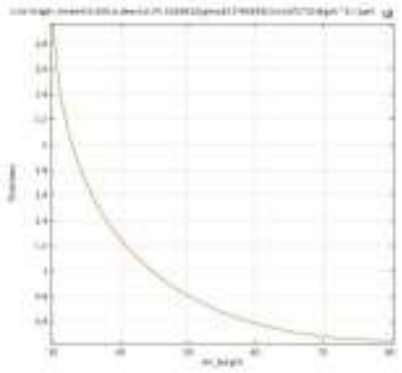

Figure 5. Thickness calculated along the cathode of the RHC.

4. Conclusions

The electrodeposition of Alluminum from $AlCl_3$/BMIm(1:1.5), under diffusion condition has been simulated with the electrodeposition module of COMSOL Multiphysics® applying different kind of approximations, resulting that the two acceptable boundaries condition for the electrode are the Butler-Volmer equation (9) and the closely related condition (11) which gives an overestimation of the deposited charge in the range of the 2%. The solution of the model with boundary condition (9), in some cases showed convergence problems that can be overcome by using condition (11) for short simulated time, in order to avoid negative concentration for the depleted species at the electrode. The equilibrium reaction can be used to refine the results since it make just a 1% difference on the current density at the edges. Finally the model has been coupled with turbulent advection field, by means of the investigation of the Rotating Hull Cylinder at 300rpm. The results show plausible values for the coating thickness distribution. Further studies will be necessary to validate the results at different rotating speed and extend the model to more complex geometry.

5. References

1. A. Lavacchi, U. Bardi, C. Borri, S. Caporali, A. Fossati, I. Perissi J. Appl. Electrochem., **39**, 2159 (2009)
2. C.T.J. Low, E.P.L. Roberts, F.C. Walsh Electrochim. Acta., **52**, 3831 (2007)
3. E.J.F. Dickinson, H. Ekstrom, Ed. Fontes Electrochem. Commun, **40**, 71 (2014)
1. F. Endres Elctrodeposition from Ionic Liquids, (2008)5. Armand, F. Endres, D. R. MacFarlane, H. Ohno and B. Scrosati, Nature Materials, **8**, 621, (2009).
6. Q.X. Liu, S. Zein El Abedin and F. Endres, Surf. Coat. Technol., **201**, 1352, (2006).
7. S. Takahashi, N. Koura, S. Kohara, M.-L. Saboungi, L.A. Curtiss, Plasmas and Ions, **2**, 91, (1992).
8. T. Jiang, M.J. Chollier Brym, G. Dubé, A. Lasia, G.M. Brisard, Surf. Coat. Technol, **201**, 1, (2006).
9. A.Lavacchi, U. Bardi, C. Borri, S. Caporali, A. Fossati, I. Perissi, J. Appl. Electrochem., (2009).
10. R. Li, L. Fang, Y. Deng, S. Liu, ICCDA, Nanjing, (2010).
11. I. Perissi, C. Borri, S. Caporali, and A. Lavacchi, "Current Density Simulations in the Electrodeposition from Ionic Liquids: Effects of the Conductivity", COMSOL Conference, Milan, (2009).
12. G. Richardson and J.R. King, J. of Math. Eng., **59**, 239, (2007).
13. C.T.J. Low, E.P.L. Roberts, F.C. Walsh, Electrochim. Acta., **52**, 3831, (2007).
14. D. Britz, Digital simulations in electrochemistry, Springer, (2005).
15. T.J. Davies, C.E. Banks, R.G. Compton, J. Solid State Electrochem., **9**,797, (2005).
16. W. Lu, X. Wang, X. Li, Y. Yin, Z. You, J. Nanoeng. Nanosyst., **228**, 93, (2014).

17. E.J.F. Dickinson, H. Ekstrom, Ed. Fontes, Electrochem. Commun., **40**, 71, (2014).
18. V. Ionescu, Romanian J. Phys., **59**, 285, (2014).
19. J. Vughan and D. Dreisinger, ECS Trans., **16**, 397 (2009).
20. A. Bonnefont, F. Argoul, M.Z. Bazant, J. Electroanal. Chem., **550**, 52, (2001).
21. J. Tang, K. Azumi, Electrochim. Acta., **56**, 1130, (2011).
22. Stijn Schaltin, Murugan Ganapathi, Koen Binnemans and Jan Fransaer, J. Electrochem. Soc., **158** (10), D634-D639, (2011)
23. S. Caporali, PhD thesis, Università Studi di Firenze, XVIII (2006) in italian
24. D. Pradhan, R.G. Reddy and A. Lahiri, Metallurgical and materials transactions B, **40B**, 114-122, (2009)
25. L. G. Joel and E. Gary Journal of American Chemical Society, **103**, 7147-7151, (1981)
26. Y. Zheng, K. Dong, Q. Wang, J. Zhang and X. Lu, J. Chem. Eng. Data **58**, 1, 32-42, (2013)

6. Acknowledgements

"The research leading to these results has received funding from the European Union Seventh Framework Programme (FP7/2007-2013) under grant agreement n°608698"

Modelling of the rotating disk electrode in Ionic liquids: difference between water based and ionic liquids electrolytes

A. Giaccherini[1], A. Lavacchi[2]
[1]INSTM, Firenze, Italy, [2]ICCOM - CNR, Firenze, Italy
*Corresponding author: via Lastruccia 3-13 50019, Sesto Fiorentino (FI), andrea.giaccherini@unifi.it

Abstract: The last few years experienced a rapid growth in the application of Ionic Liquids (IL's) to electrodeposition. ILs offer a variety of advantages over aqueous electrolytes. In general ILs show large chemical and thermal stability, high ionic conductivity and an electrochemical window much larger than water. These properties together with their negligible vapor pressure enabling their use at different temperatures without any risk of generating harmful vapors and joined to the absence of hydrogen discharge interfering with electrodeposition processes, as they are essentially hydrophobic, make them the best candidates to be used for the obtainment of homogeneous electrodeposited thin films. This study focuses on the silver electrodeposition from a silver tetrafluoroborate solution in 1-butyl-3-methyltetrafluoroborate BMImBF4. We notice that practical deposition rate at even concentrations were much lower in ionic liquids as compared to water electrolytes an investigation of mass transport has been undertaken. Hydrodynamic voltammetry with Rotating Disk Electrode (RDE) of ferrocene/ferrocinium solutions in BMImBF4 have been performed in order to estimate diffusion coefficient for the different systems. Eventually, simulation of the RDE voltammetry based on the FEA (Finite Elements Analysis) have been performed. Laminar flow has been imposed to compute the steady state solution of the Navier-Stokes equation (laminar flow) and then it has been solved the electrochemical process in the high conductivity regime. Thus solving only the transport proprieties neglecting the potential drop of the electrolyte. Two different process has been simulated: the actual voltammetries in IL and an equivalent voltammetries in water. The former allows to validate the model by means of comparison with the experimental voltammograms, the last allows to rationalize the peculiar mass transport properties of the Ils. In particular, thanks to the comparison of the concentration profiles and fluxes at the steady and quasi-steady states of the potential scan for both systems, we clarified the nature of the unexpected peaks show by the experimental voltammograms.

Keywords: Levich equation, Ionic Liquids, Transport proprieties, RDE, electroanalytical, CFD.

1. Introduction

Research on electrodeposition has recently focused on the quest for new electrolytes alternative to water. This was mainly driven by the need to develop new and green electrodeposition processes. Major breakthroughs were the discovery of Ionic Liquids which application to electrodeposition boomed in the first 2000's and deep eutectic solvents based on environmentally benign compounds (e.g choline and urea). The deposition of an extremely large variety of thin and thick films of metals and alloys from these novel electrolytes has been demonstrated at the lab scale.

The problem related to water-based galvanic bath are, among others, the limited electrochemical window (1.23V) imparing the deposition of many elements (eg. Aluminum, Silicon and Titanium etc…) and involving, in most cases, noxious or polluting chemical species. Oppositely, ionic liquids and DES have stability windows that in certain cases exceed 6V. Despite such definite advatange and the research effort,

IL's are still not fully exploited in the electrodeposition technologies, with only a few systems commercially available solutions for extremely specialized niches of application.

The cause for such slow development of this field is that extremely complex task constituted by the switching electrodeposition from water to IL's. Among several concerns such as the higher costs, stability of the solvents, necessity of dedicated galvanic lines (usually under controlled atmosphere) the transport proprieties affect definitely the stability of the coating process. We focus on this critical aspects of the electrochemical process. A significant difference in viscosity between water electrolytes and IL's exists. Water has a dynamic viscosity of 1 cp while most IL's range between one and two order of magnitude higher than that. By means of FEA (Finite Elements Analysis), as implemented in Comsol Multiphysics, we investigated the mass transport in highly viscous solvents to highlight the differences between electrodeposition in water and that in ionic liquids. Such complexity arises from the fact that viscosity affect both the diffusion coefficient of reacting species and the development of the velocity field in the electrolyte. Thus, things gets more difficult when convection is involved. In this work we report the results of an extensive investigation on convection in a highly viscous Ionic Liquid to unravel the elements that concur to the mass transport limitation of such electrolytes.

To do so we analyze the case the RDE voltammetries performed on the Ferrocene/Ferrocinium redox couple in $BMImBF_4$. This IL is known to have a viscosity of 100 cp that is ideal to emphasize the effect of viscosity on electrodeposition. We have realized a series of experiment in well-defined convective conditions (RDE experiments). These experiments have then be modeled by a finite element analysis to understand the concentration profile and to estimate the size of the boundary layers. The calculation have been performed both in water and in $BMImBF_4$ to highlight the differences between the two solvents.

2. Model

The necessity to understand the nature of the peak present in the RDE voltammetries performed in IL lead to definition of a numerical model of the RDE. The 3D geometry of the RDE has a cylindrical symmetry, thus the numerical domain can be reduced to a simple 2D axisymmetric geometry, constituted by an embedded disk electrode, located on the axis of symmetry of the system (Figure 1). For the purpose of perform a dedicated comparison with experimental data we designed a domain with the same volume and geometry of the real volume interested in the experiments (just the electrolyte under the level of the working electrode). The electrochemical media are constituted by Ferrocene (3.83 mol m^{-3}) in $BMImBF_4$ or water, characterized by chemical and physical proprieties reported in Table 1. The electrochemical reaction controlling the current in the RDE voltammetry is associated with the Ferrocene (FeCen)/Ferrocinium (FeCin) redox couple:

$$FeCen \longrightarrow FeCin + e^-$$

The calculation has been performed by means of the simulation program COMSOL Multiphysics® with the electroanalytical and the CFD (Computational Fluidynamics) modules.

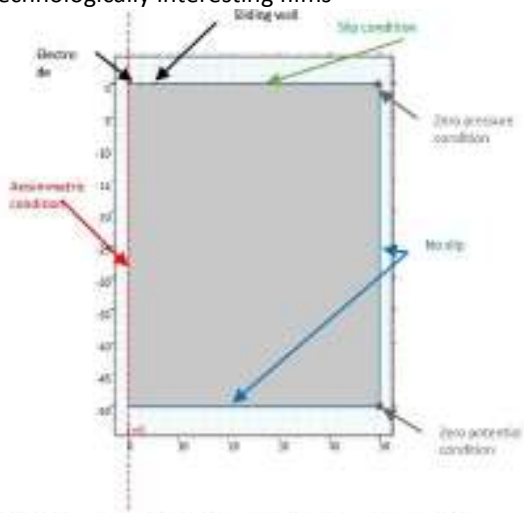

Figure 1. Scheme showing the cell geometry considered for the RDE with the set of boundary condition considered in this work. The electrolyte domain is a square with an edge of 50mm and the segments represent the radius of the embedded disk electrode (1.5mm) and the embedding cylinder (5mm).

2.1 Governing equations

The uncoupled problem has been solved in two step:

1. Solution for the stationary state of the Navier-Stokes equation(1). In a typical «Rotating Disk Electrode» (RDE), the cylindrical symmetry implies a laminar flow even at high rotation speed. Exploiting the symmetry of the system, we reduce the 3D RDE domain to a 2D axisymmetric domain as reported in figure 1. The 3D velocity is reproduced from the 2D velocity field thanks to the use of the "swirl flow" option in COMSOL Multiphysics® which solves implicitly for the azimuthal coordinate for an axisymmetric problem.

$$k\nabla^2 v - \rho(v\,\nabla v) - \nabla p = 0 \qquad \nabla \cdot v = 0 \tag{1}$$

2. The resulting laminar flow advection field has been given as input of the electroanalytical interface, to solve for the time dependent current in order to estimate the characteristic curve of the RDE voltammetry. Usually at the lab-scale, with such very high conducting electrolytes, the distribution of the electric potential can be neglected. In this context the Ohm's law, equation (2) is not considered, while the Nersat-Plank equation (3) constitute the only governing equation for this part of the model.

$$\nabla^2 \phi_l = -\frac{Q_l}{\sigma_l} \tag{2}$$

$$\underline{N_i} = -D_i \nabla c_i - z_i u_{m,i} F c_i \nabla \phi_l + \underline{u} c_i \tag{3}$$

ϕ_l is the electric potential in the electrolyte; σ_l is the conductivity of the electrolyte and Q_l is the electric charge. In the Nernst-Plank: Where c_i, D_i, u_i, and z_i are the concentration, the diffusion coefficient, the mobility and the charge of the of the i_{th} species, respectively; F the Faraday's constant; $\underline{u}$ the velocity field; R_i the reaction term for A and B. Due to the neglecting of equation (2), meaning that an homogenous distribution of the electric potential in the intermediate assumed, thus
the migration term in equation (3) has been not considered since. In order to calculate the change in composition of the electrolyte near the electrodes due to electron transfer, it's well established the validity of the following Faraday equation (3):

$$R_{i,m} = \frac{-\nu_{i,m} i_{loc,m}}{n_m F} \tag{3}$$

$i_{loc,m}$ is the faradaic current density for the m_m process, n_m is the number of electrons exchanged.

2.2 Boundary conditions

Boundary conditions for the Nernst-Plank (3) can be defined as follow (7-9):

$$\underline{i}_l \cdot \underline{n} = i_{total} \tag{7}$$

$$i_{total} = \sum_i i_{loc,m} + i_{dl} \tag{8}$$

$$i_{loc} = i_0 \left(\frac{C_R}{C_R^0} e^{\frac{\alpha_a F \eta}{RT}} - \frac{C_O}{C_O^0} e^{\frac{-\alpha_c F \eta}{RT}} \right) \tag{9}$$

where, $\underline{i}_l$ is the current distribution vector; i_{dl} is the capacitive current density; $i_{loc,m}$ is the faradaic current density for the m_m process; i_0 is the exchange current; C_R/C_R^0 is the ratio of the concentration to the bulk concentration; α_a is the electron transfer coefficient; R is the perfect gasses constant; T is the temperature and η is the electrode overpotential defined by equation (10).

$$\eta = \phi_l + \phi_s - E_{eq} \tag{10}$$

Here, $\phi_l + \phi_s$ is the electrical potential drop across the electrode interface.

2.3 Mesh

A dedicated approach to define the correct mesh for the Navier-Stokes equations and the Nernst-Plank equation has been followed. The convergence of the meshes has been tested plotting the algebraic residual of the module of the velocity and of the concentration, respectively for Navier-Stokes and Nernst-Planck equations. Independtly, a cross check of the effect of the mesh convergence was performed, checking the effect of the mesh size on the limiting velocity (Navier-Stokes) and on the limiting current (Nernst-Planck). For Navier-Stokes equations we chose a triangular mesh with the boundary layers on two of the edges, constituted by 50 quadrangular elements, a exponent of 1.05 and the thickness adjustment ratio of 1. The resulting algebraic residual is homogenously under 10^{-12}. For Nernst-Planck we chose a quadrangular mapped mesh with the boundary layers on one edge, constituted by 150 quadrangular elements, a exponent of 1.1 and the thickness of the first layer is adjustment ratio of 1nm. The resulting algebraic residual is homogenously under 10^{-8}.

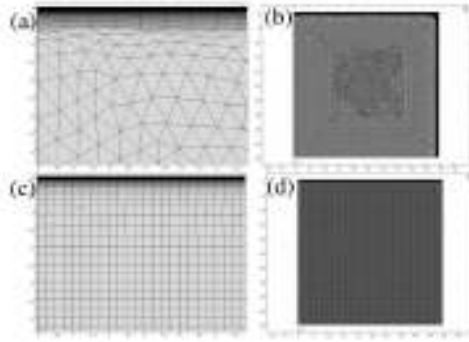

Figure 2. (a) close up (b) overall of the mesh for the Navier-Stokes. (c) close up (d) overall of the Nernst-Planck.

2.4 Chemical and physical proprieties of the electrolytes

	IL	Water
D(FeCen)	$1.3\ 10^{-11} m^2 s^{-1}$ [1]	$1.3\ 10^{-9} m^2 s^{-1}$ [1]
D(FeCin)	$1.3\ 10^{-11} m^2 s^{-1}$ [1]	$1.3\ 10^{-9} m^2 s^{-1}$ [1]
C_0(FeCen)	3.83 mol m^{-3}	3.83 mol m^{-3}
C_0(FeCin)	0 mol m^{-3}	0 mol m^{-3}
i_0	N/D	N/D
η	132 mPa s	0.894 mPa s

Table 1: Physical and chemical constant for the modelling of FeCen in $BMImBF_4$.

Where D are the diffusion coefficient, C_0 the bulk concentration of the electrolyte, i_0 the exchange current density and η the dynamic

viscosity of the IL. The exchange current density has been obtained as the solution of an inverse problem performed by means of comparison with the experimental curve in IL.

3. Results

3.1 Validation

The model has been validated by means of comparison with the experimental data, the comparison between the experimental and theoretical voltammetric curves at 2000rpm and different scan rate ($10mVs^{-1}$, $50mVs^{-1}$ and $100mVs^{-1}$) are depicted in Figure 3. We achieved a very good agreement at the steady state. The agreement at the peak have been achieved by sweeping the exchange current density.

The best agreement is achieved in every case with $1.8\ 10^{-1}$ A m^{-2}.

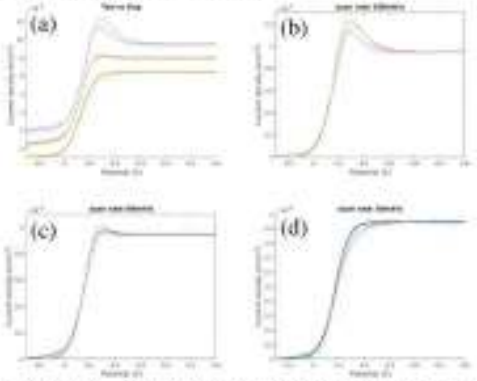

Figure 3. (a) close up (b) overall of the mesh for the Navier-Stokes. (c) close up (d) overall of the Nernst-Planck.

On the other hand using the Levich's law (11) to calculate the diffusion coefficient we obtain $1.6\ 10^{-11} m^2\ s^{-1}$ in contrast with the value obtained by Eisele with chronoamperometric and voltammetric measurements. [1,2]

$$i_L = \beta n F D_0^{2/3} \omega^{1/2} \nu^{-1/6} C_0 \qquad (11)$$

Where i_L is the average current density on the electrode at the steady state, β a constant related to the measure units, n number of electrons involved in the reaction, F the Faraday constant, D_0 the diffusion coefficient of the limiting species, ω the rotation rate, ν kinematic viscosity and C_0 the bulk concentration of the limiting species. Moreover, if we use $1.6\ 10^{-11} m^2\ s^{-1}$ a discrepancy, in the range of few percents, between the numerical and experimental data arises as expected. The cause for the peaks and for the discrepancies in the limiting current will be discussed in the following paragraphs.

3.2 Convection layers

The convection layers can be extrapolated by means of a graphical method from the concentration profiles, as depicted by blue lines in figure 4a,b. We report the concentration profiles for $10mVs^{-1}$, $50mVs^{-1}$ and $100mVs^{-1}$ at the steady state (0.6V) and the peak (0.12V). The three concentration profiles in figure 4a reported for the steady state in IL, are exactly superimposable. While the three concentration profiles for the peak in IL, are not superimposable and the higher the scan rate the higher the discrepancy with the steady state concentration profiles. In water all the six concentration profile (steady state and the peak) are perfectly matching each other. Figure 4c,d report the concentration as function of the distance from the electrodes and the potentials for IL (Figure 4c) and water (Figure 4d). The low potential side of the plot reports the concentration profiles for the kinetic controlled potential range. On the other hand, the high potential side report the mass transport controlled potential range, meaning that the black boxes highlight the transition potential ranges. Remarkably, the transition part of the voltammetry is not affected by the scan rate in water electrolyte, while in IL is scan rate dependent. Higher

the scan rate more extended the transition part is. Moreover, it is worth to notice that the transition part of the voltammetric scan for the 10 mVs^{-1} in IL resembles the transition part for water.

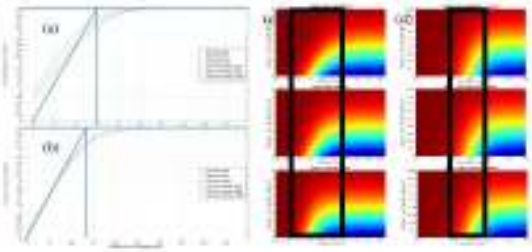

Figure 4. Concentration profiles in IL (a) and in water (b). Concentration as function of the distance from the electrodes and the potentials for IL (c) and water (d).

3.3 Velocity field

The velocity field for an embedded disk in an infinite domain has been analytically described by Von Karman. A popular solution to this problem has been proposed by Cochran. The solution has been used by Levich, obtaining the famous Levich's equation. The assumption that the Cochran solution holds, is necessary for the validity of the Levich's equation. Meaning that the velocity should be perpendicular to the electrode (left hand side of figure 5a,b) very closely to the upper boundary. The velocity field for water seems to be matching the Cochran's solution. A more precise picture is depicted in figure 5c,d, where the profile of the non-dimensional velocity field components calculated in this work are reported. The limiting velocity for water along the axis (V_z) is roughly 0.88, consistent with Cochran's solution (0.8847). For IL the limiting velocity component along z is remarkably lower. In general the non-dimensional velocity field components for water are perfectly matching the Cochran's solution, while for IL substantial difference can be reported. Thus for water the velocity field can be considered developed, in the sense of Cochran solution. On the contrary, for IL the velocity field is not completely developed. Hence, it is not consistent with Levich's equation. [2,3]

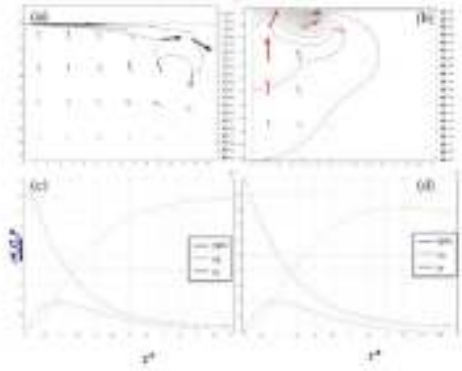

Figure 5. Velocity field near the electrode for water (a) and IL (b). Non dimensional velocity field components for water (c) and IL (d).

4. Conclusion

In this work we report a numerical model of a RDE voltammetry in a finite size domain allowed to understand two unexpected experimental results. Particularly, the peak at 0.12V is unexpected for RDE voltammetries at any practical rotating speed and scan rate. Moreover, the discrepancy of the diffusion coefficient obtained from the experimental rotating speed, with respect to the one calculated by Eisele by means of chronoamperometric and voltammetric measurements. In paragraph 3.1, is shown the very good agreement that we achieved at the limiting current and at the unexpected peak for the RDE voltammtries at 2000rpm and different scan rate ($10mVs^{-1}$, $50mVs^{-1}$ and $100mVs^{-1}$). Given that the exchange current density have been obtained by means of the comparison of the experimental data and several simulation carried at different exchange current density, in particular on

the kinetic controlled potential range. We successfully described the concentration profile, proving that at the peak the concentration profile is not completely developed, while in water it is matching perfectly the concentration profile at the steady state. Moreover, when the peak is not present (at $10mVs^{-1}$) the transition part of the voltammetric scan, depicted in figure 4c, is very similar to the one in water (Figure 4d). Eventually, we found that in this conditions the velocity field for IL (Figure 5b,d) is not well developed, in the sense of Cochran, while for water it is. Likely, this breaks the assumption that must hold to be able to rely on the Levich's equation validity in ionic liquid. We think that the velocity field cannot be well developed in IL since the dragged layer (1.6mm in this condition) is comparable with the radius of embedding cylinder, while for water is ten times smaller. Thus, new geometry should be study in order to be able to reliably apply Levich's equation in IL.

5. References

1. S. Eisele, M. Schwarz, B. Speiser, C. Tittel, Diffusion coefficient of ferrocene in 1-butyl-3-methylimidazolium tetrafluoroborate - concentration dependence and solvent purity, Electrochim. Acta. **51** (2006) 5304–5306.

2. Bard, Allen J.; Larry R. Faulkner, Electrochemical Methods: Fundamentals and Applications, 339, Wiley(2000)

3. Y. V. Pleskov, V. Y. Filinovski, The rotating disc electrode. Consultants Bureau, Studies in soviet science (1976)

materials

MDPI

Article

Aluminium Electrodeposition from Ionic Liquid: Effect of Deposition Temperature and Sonication †

Enrico Berretti [1], Andrea Giaccherini [1], Stefano M. Martinuzzi [1], Massimo Innocenti [1], Thomas J.S. Schubert [2], Frank M. Stiemke [2] and Stefano Caporali [3,*]

[1] Dipartimento di Chimica, Università di Firenze, Sesto Fiorentino 50019, Italy; enrico.berretti@unifi.it (E.B.); andrea.giaccherini@unifi.it (A.G.); stefano.martinuzzi@unifi.it (S.M.M.); m.innocenti@unifi.it (M.I.)

[2] IoLiTec Ionic Liquids Technologies GmbH, Heilbronn 74080, Germany; schubert@iolitec.de (T.J.S.S.); stiemke@iolitec.de (F.M.S.)

[3] Consorzio Interuniversitario Nazionale Per la Scienza e Tecnologia dei Materiali (INSTM) and Istituto Sistemi Complessi (ISC), Sesto Fiorentino 50019, Italy

* Correspondence: stefano.caporali@unifi.it; Tel.: +39-055-457-3119

† This paper is an extended and revised version of the paper published in Sciforum Electronic Conference Series, Proceedings of the 2nd International Electronic Conference Materials, 2–16 May 2016; Volume 2, 2016, C003; doi:10.3390/ecm-2-C003.

Academic Editor: Silvia Gross
Received: 17 June 2016; Accepted: 12 August 2016; Published: 24 August 2016

Abstract: Since their discovery, ionic liquids (ILs) have attracted a wide interest for their potential use as a medium for many chemical processes, in particular electrochemistry. As electrochemical media they allow the electrodeposition of elements that are impossible to reduce in aqueous media. We have investigated the electrodeposition of aluminium from 1-butyl-3-methyl-imidazolium chloride ((Bmim)Cl)/$AlCl_3$ (40/60 mol %) as concerns the effect of deposition parameters on the quality of the deposits. Thick (20 µm) aluminium coatings were electrodeposited on brass substrates at different temperatures and mixing conditions (mechanical stirring and sonication). These coatings were investigated by means of scanning electron microscope, roughness measurements, and X-ray diffraction to assess the morphology and the phase composition. Finally, electrochemical corrosion tests were carried out with the intent to correlate the deposition parameters to the anti-corrosion properties.

Keywords: ionic liquids; aluminium; electrodeposition; surface morphology; sonication; corrosion resistance; texture

1. Introduction

Since its invention, the Hall-Héroult process [1] has been the conventional process for the production of metallic aluminium. It is based upon the electroreduction of alumina in a cryolite melt by using graphite electrodes. The high temperature required (in the order of 900 °C) and the emission of toxic gaseous by-products, such as fluorine and carbon monoxide, rendered the research for greener and safer alternatives highly attractive [2]. The introduction of Ionic Liquids (ILs) (namely room temperature molten salts) as electrochemical media for the aluminium electrodeposition offered a very promising route to succeed in this goal. Since the first pioneeristic studies in the 1990s [3], a large number of investigations successfully reported the lab-scale electrodeposition of aluminium at room or nearly room temperature. Different types of ionic liquids [4–9] and additives [10,11] were proposed to achieve smooth and thick aluminium coatings. However, with the aim of the industrialization of the Al-plating process, the use of additive-free chloroaluminate ILs, seems to constitute the better compromise between the quality of the deposit and the durability of the electroplating bath. Beside the handling difficulties, mainly due to the vigorous reaction with atmospheric moisture, their high

aluminium content, reduced viscosity, and remarkable electrochemical stability allow for a high deposition rate, in the order of 10 $\mu m \cdot h^{-1}$, and a long working time without the need to replenish chemicals. The scheme of the Al-electroplating process is depicted in Figure 1.

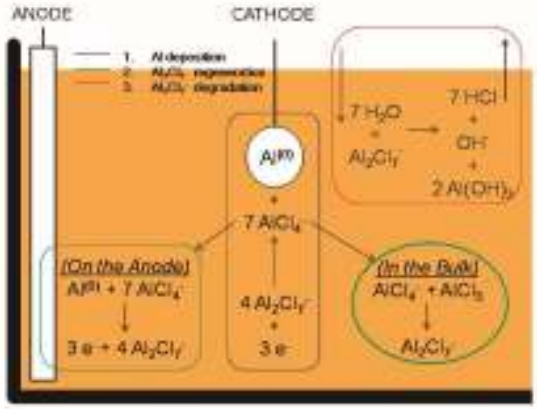

Figure 1. Scheme of the Al-electroplating process from chloroaluminated ionic liquids (ILs). Al is reduced at the cathode while at the anode the electroactive species is regenerated by aluminium dissolution and reaction with $AlCl_4^-$. The red box depicts the parasite reaction with moisture.

The Al-coatings obtained at lab scale by means of this technology were successfully employed as protective layers for structural materials such as carbon steel [10–12], magnesium alloys [13], and light weight alloys [14], just to name a few. The anticorrosion properties of the Al-coatings are based upon the formation of a dense passivation layer composed by aluminium oxide that prevents further corrosive action towards the metal beneath. Therefore, the anticorrosion ability requires the formation of a homogeneous, crack-free alumina layer.

In order to obtain high quality Al-coatings, the study of the effect of deposition parameters such as temperature and mixing conditions on the deposition rate, the crystalline structure, the surface morphology, and roughness is, therefore, mandatory. Electrodeposition in stirred solution has the advantage of reducing the thickness of the diffusion layer, thereby improving the deposition rate and the homogeneity of the deposit. However, even though some studies investigated the effect of temperature [12,15,16], very little work was reported on the effect of solution stirring [17,18] and, to the best of our knowledge, no one has addressed the effect of sonication so far.

For these reasons, with an aim to determine the better operative conditions for the industrialization of the Al-plating process, we investigated the effects of temperature and mixing conditions, both alone and combined, on the electrodeposition of Al from the ionic liquid (Bmim)Cl/$AlCl_3$ (40/60 mol %). Finally, the deposits were characterized by scanning electron microscopy (SEM) investigation, roughness measurement, X-ray diffraction, and electrochemical corrosion tests to assess the conditions more suited to achieving smooth, homogeneous, and thick aluminium coatings.

2. Materials and Methods

2.1. Chemicals

The electroplating bath was constituted by 1-butyl-3-methyl-imidazolium chloride ((Bmim)Cl)/$AlCl_3$ (40/60 mol %). It was supplied by IoLiTec Ionic Liquids Technologies GmbH (Heilbronn, Germany) and used as received without further purification.

2.2. Electrode Materials

12 mm diameter brass (Cu 63%, Zn 37%) tokens were employed for the study of temperature and mixing effect. Larger tokens (25 mm diameter) were used to study the combined effects. The tokens were grinded with SiC paper down to 1200 grit and polished with diamond suspension (Metadi 3 micron, Buehler, Uzwil, Switzerland), rinsed with tap water and sonicated in acetone (technical grade, VWR Chemicals, Leuven, Belgium) for 5 min. Before the electrodeposition they were rinsed again in tap water and soaked in HCl 1 M for 3 min, rinsed in distilled water, sonicated in acetone for 5 min and then dried under N_2. Inside the nitrogen filled glove box, prior to the start of electrodeposition, the working electrodes were electrochemically cleaned in the electroplating bath by applying a positive (oxidative) current (2.5 $mA \cdot cm^{-2}$) for 30 s.

2.3. Deposition Parameters

The plating process was carried out inside a nitrogen filled glove box (Iteco mod 10A, Castelbolognese, Italy), with water content below 20 ppm. The deposits were produced in current controlled (galvanostatic) conditions at 10 $mA \cdot cm^{-2}$ using a potentiostat (Model 7050 by Amel s.r.l., Milan, Italy), a circular anode constituted by a pure aluminium foil (Goodfellow, Huntingdon, UK, 99.0%) and brass tokens as cathodes. No reference electrode was used in this study, since the galvanostatic method requires only the control of the charge. The obtained potential vs. time curves refer to the absolute potential difference applied to the electrodes. Two different deposition set-ups were used with the same geometry but different anode/cathode surface ratio (see Figure 2a,b). Depositions were performed in quiet (no motion) or under mixing conditions by means of mechanical stirring (magnetic bar, 320 rpm) or sonication (Qsonica Sonicator Q500, Newtown, CT, USA, 500 W 20 kHz operating at 30% of maximum power). In the sonication experiments, the horn was placed on the cathode side as depicted in Figure 2b.

(a) (b)

Figure 2. Scheme of experimental set-ups used for temperature (**a**) and sonication (**b**) experiments.

2.4. Characterization of the Deposits

The morphology of the coatings was investigated by Scanning Electron Microscopy (S-2300, Hitachi, Tokyo, Japan) operating at 20 kV, while the average roughness was measured using a Hommel Tester W55 (Teplice, Czech Republic). The roughness measurements were obtained carrying out five different and independent tests in randomly chosen areas of the sample scanning 4.8 mm of surface at 0.2 $mm \cdot s^{-1}$ of scan rate. The parameters employed were λc = 0.8 mm and $\lambda c/\lambda s$ = 300 using a filter ISO 11562(MI). Different roughness parameters were calculated (see Appendix A) and the obtained values are summarized in Tables 1 and 2.

Table 1. Roughness parameters for the samples obtained at different temperatures and their relative yield.

Sample	Rt (μm)	Ra	RzISO (μm)	Rz (μm)	Yield (%)
Temp. 50 °C	32.9 ± 1.2	3.7 ± 1.1	25.5 ± 4.1	23.3 ± 2.8	79
Temp. 70 °C	21.7 ± 10.5	2.1 ± 0.2	14.9 ± 5.8	13.4 ± 4.8	86
Temp. 90 °C	4.2 ± 0.1	0.3 ± 0.1	3.1 ± 0.1	2.90 ± 0.1	88

Table 2. Roughness parameters for the samples obtained with different agitation modes and their relative yield.

Sample	Rt (μm)	Ra	RzISO (μm)	Rz (μm)	Yield (%)
Quiet deposit	4.2 ± 0.3	0.4 ± 0.1	3.6 ± 0.2	3.4 ± 0.2	60
Sonication 1 to 10	11.7 ± 1.3	0.7 ± 0.1	8.5 ± 0.8	7.2 ± 0.6	100
Sonication 1 to 1	17.0 ± 1.2	1.7 ± 0.1	13.6 ± 0.6	12.7 ± 0.4	100

2.5. Process Yield

Since the IL viscosity is much larger with respect to the aqueous solutions (thus limiting the mass transport of the electroactive species), the formation of dendritic deposits is favoured, especially when mild operative conditions (low temperature, no mixing) and high current densities are employed. If dendritic coatings are formed, the detachment of parts of the deposit during the rinsing operations cannot be neglected. To take into account this mass loss, process yield was calculated as the percent ratio between the effective mass of the obtained deposit and the theoretical mass calculated from the Faraday law (Equation (1)).

$$Yield = \frac{weighted Mass}{theoretical Mass} \times 100 \quad (1)$$

From the potentials reached in our experiments, there is no evidence that parasitic reactions can lower the cathodic efficiency of the deposition below a 100% yield. Therefore, considering the aluminium layer homogeneously distributed, the yield provides information about the thickness of the deposit.

2.6. XRD Analysis

The phase determination of the coatings was carried out through X-ray diffraction (XRD), performed using a XRD Bruker D8 Advance powder diffractometer (Bruker AXS GmbH, Karlsruhe, Germany) employing Cu Kα (1.54187 Å) radiation in the 2θ range 36°–80°, applying a step size of 0.022° 2θ and a step counting time of 0.27 s. XRD spectra deconvolution was performed by means of the single line profile analysis [19], involving the fitting of the peaks with two Voigt functions (one for the $K_{\alpha 1}$ and for $K_{\alpha 2}$). We are aware that for the complete assessment of the strain and size of the crystallites the Warren-Averbach method had to be used. However, the accurate assessment of these parameters requires tens of independent peaks and it is beyond the aim of this work. Still, the use of Voigt functions (convolution of Lorentzian and Gaussian functions) allows us to assess the average strain of the crystallites, related to the Gaussian width, and the crystallite size, related to the Lorentzian width, in a simple and reliable way as shown by several authors [19–21]. In such a way, information on the effect of the experimental conditions on the strain and size of the crystals as well as the texture coefficient were determined. The texture coefficient $T(hkl)$ for the (hkl) plane is defined in Equation (2):

$$T(hkl) = \frac{A(hkl) / A_0(hkl)}{\sum_{hkl} A(hkl) / A_0(hkl)} \quad (2)$$

where $A(hkl)$ is the experimental area under the Voigt curve of the (hkl) plane and $A_0(hkl)$ is the respective theoretical area simulated by using the program Mercury and Wycoff structural parameters [22–24].

2.7. Electrochemical Corrosion Test

The electrochemical corrosion tests were performed using a corrosion cell from Princeton Applied Research (Flat cell KO235, Oak Ridge, TN, USA) in aerated 3.5% NaCl (>99.5% from Merck, Darmstadt, Germany) solution at room temperature (20–23 °C). The potentiostat (Princeton Applied Research model 2273, Oak Ridge, TN, USA) was controlled by PowerSuite 2.58 software (Princeton Applied Research, Oak Ridge, TN, USA). The classical three electrode set-up was employed using a platinum grid as counter electrode and a standard calomel electrode (SCE) reference electrode separated from the solution with an ions conducting glass frit, the working electrode surface was always 1.0 cm^2. The tests were performed on the aluminized samples without further treatment. Every sample was kept in the saline solution for at least 16 h in order to allow the stabilization of the open circuit potential (OCP); then, potentiodynamic (PD) experiments were recorded starting from −0.250 V with respect to the OCP at the scan rate of 0.4 $mV \cdot s^{-1}$.

3. Results

3.1. Effect of Temperature

Even though the effect of temperature on the morphology of the Al-coatings has been previously reported for this IL up to 55 °C [14], we extended the investigation at higher temperatures. In this set of experiments, while maintaining quiet the electroplating bath, the Al deposition was performed at three different temperatures: 50 °C, 70 °C and 90 °C. During the deposition the potential-time curves (Figure 3) were recorded in order to extrapolate the induction time (the time needed to reach a stable deposition potential) and the equilibrium potential. The last one provides direct insight about the overpotential needed to obtain the Al-reduction and, therefore, the energy consumed.

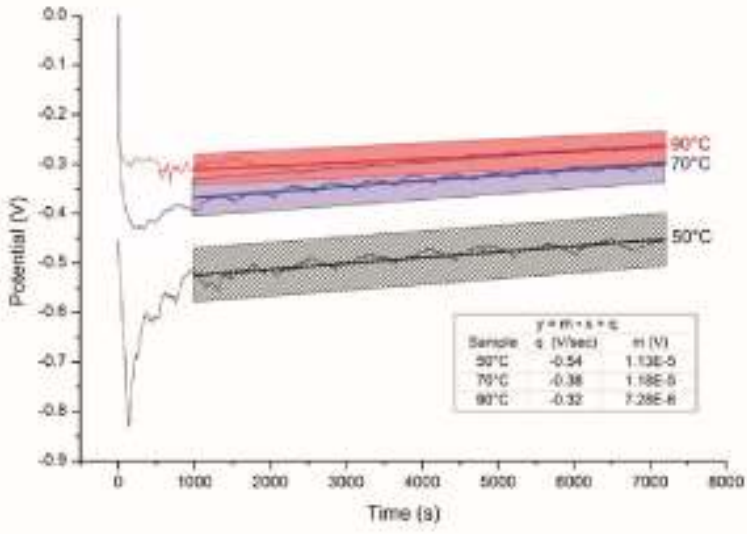

Figure 3. Potential-time curves obtained at different temperatures. Galvanostatic deposition 10 $mA \cdot cm^{-2}$, deposition time 2 h. The inset depicts the results of data linear fitting. The slope of the curves decreases with increasing temperature.

In accordance with previous investigations in similar ionic liquids [14], higher temperature favours the electroreduction process. Increasing temperature reduces the induction time, promotes higher process yield, and requires less negative potentials. It is noteworthy that the curves are characterized by smaller slopes indicating, on the whole, a lower surface increase as a consequence of the formation of smoother deposits. This qualitative observation was supported by more quantitative roughness measurements. The data summarized in Table 1 show that the surface roughness decreased and more homogeneous deposits (lower relative error in the roughness measurement) were obtained as a function of temperature increase.

SEM investigation (Figure 4) strengthen this trend evidencing the change of morphology from pinnacle type deposits at 50 °C to homogeneous crystalline structure at 90 °C.

Unfortunately, repeated experiments demonstrate that for temperatures higher than 70 °C the ILs undergo very rapid degradation. This impairs the use of higher temperatures for industrial and applicative purposes. The recommended maximum temperature can be considered 60 °C. All the following experiments were carried out at temperatures not exceeding 60 °C.

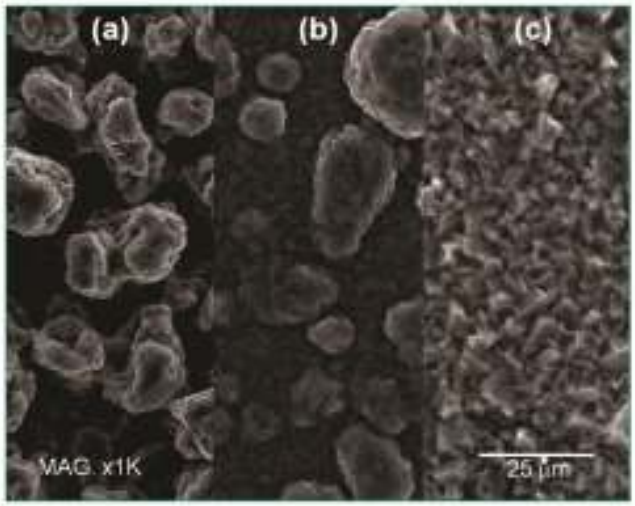

Figure 4. Scanning electron microscopy (SEM) images of the samples obtained at different temperatures: (**a**) 50 °C; (**b**) 70 °C; and (**c**) 90 °C. Deposition time was 2 h.

3.2. *Effect of Sonication*

By using the larger set-up (Figure 2b) necessary to immerse the sonication horn in the electroplating bath, two series of samples were produced at 20 °C employing different sonication duty cycles. The first one, namely mild sonication, consisted of 1 s on (30% power) for every 10 s off; the second, stronger sonication, consisted in a 1 s on (30% power) for every 1 s off. We refer to these conditions as "Sonication 1 to 10" and "Sonication 1 to 1" respectively. Quiet depositions were also carried out for comparison.

The potential-time curves depicted in Figure 5 show long induction time and the serious effect of sonication on the equilibrium potential; stronger sonication leads to less negative deposition potentials and, in turn, an easier deposition process. On the other side, the roughness measurements summarized in Table 2 depict an opposite trend with respect to the temperature series indicating, on the whole, the increase of surface roughness as a function of sonication. This counter intuitive behaviour is explained by SEM investigation (Figure 6). Even if the nucleation and growth mechanism remain unchanged, increasing the sonication power leads to the formation of larger crystals that account for the increased surface roughness. It is also worth noting that by using sonication a 100% yield is achieved.

On the other hand, the deposit obtained at 20 °C without sonication presents a massive deposit loss (yield about 60%, Table 2). That is reasonably due to the formation of dendrites that were removed during sample rinsing. As a consequence of the reduced thickness, the surface roughness decreases.

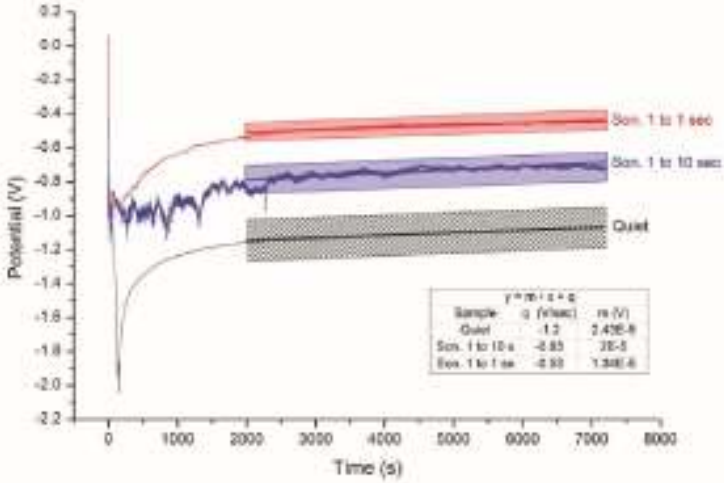

Figure 5. Potential-time curves obtained at different sonication levels. Galvanostatic deposition 10 mA·cm^{-2}, deposition time 2 h. The inset depicts the results of data linear fitting; shadow areas represent the confidence interval.

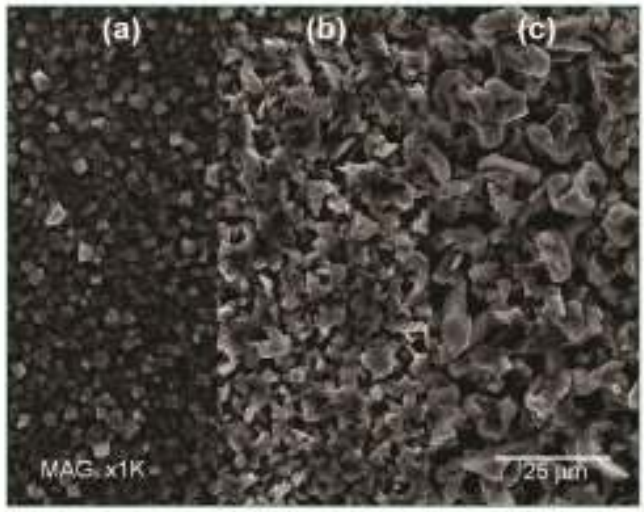

Figure 6. SEM images of the samples obtained using different sonication: (a) Quiet solution; (b) Sonication 1 to 10; and (c) Sonication 1 to 1.

Corrosion Tests

The Al-coatings obtained at different temperatures and mixing conditions were investigated to assess their anticorrosion properties in 3.5% NaCl aerated aqueous solution. Figure 7 shows the potentiodynamic curves relative to the samples obtained at different temperatures (a) and mixing conditions (b). There were no substantial variations among the free corrosion potentials. Only a modest

decrease in the corrosion current (i_c) is detectable in the temperature series. That is reasonably due to the decrease in sample roughness and, therefore, the reduction of the active surface. On the whole, all the curves but one present very similar anodic branches thereby confirming a similar corrosion mechanism. The different curve shape displayed by the sample obtained at room temperature in quiet conditions is reasonably due to the lower thickness, about 12 μm accordingly to a 60% yield, with respect to the 20 μm of a 100% yield (Table 2).

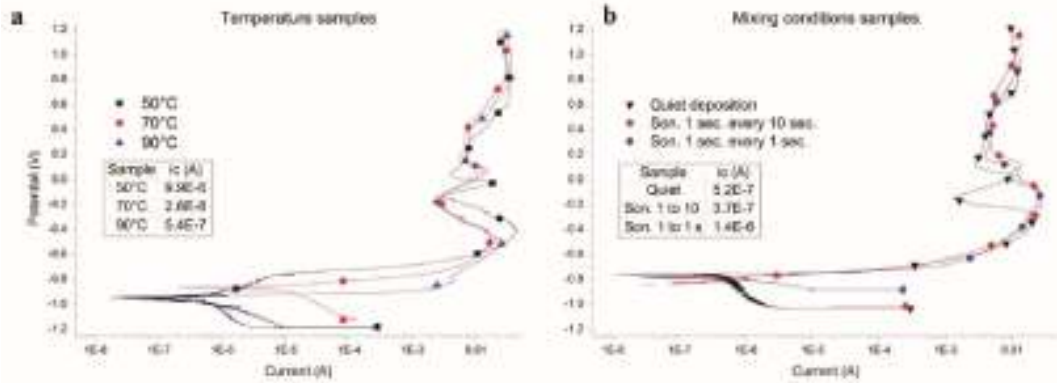

Figure 7. Potentiodynamic curves in 3.5% NaCl aerated aqueous solution on samples obtained at different temperatures (**a**) and mixing conditions (**b**). Scan rate 0.4 $mV \cdot s^{-1}$. The inset depicts the corrosion current values.

3.3. *Combined Effects*

In order to study the influence of both temperature and sonication, a new set of Al-deposits were obtained. Three temperatures (20 °C, 40 °C, and 60 °C) and three mixing parameters (quiet bath, stirring at 320 RPM, and sonication 1 to 10) were chosen to deposit aluminium on 25 mm diameter disks. Table 3 summarizes the tested combinations, while the electrochemical set-up used is depicted in Figure 2b. The sample at 20 °C in quiet was not studied since it required a very negative potential (close to −4 V), well below the IL cathodic limit.

Table 3. Summary of the samples obtained by means of combined experimental conditions and, within brackets, their relative process yield.

Yield %	20 °C	40 °C	60 °C
Quiet Deposits	–	A (45%)	B (69%)
Stirring 320 RPM	C (82%)	D (100%)	E (100%)
Sonication 1 to 10	F (100%)	G (100%)	H (100%)

Deposition at high temperature combined with strong sonication duty cycle (30%, 1 to 1) is not of practical interest since the heating effects of sonication cause local temperatures to rise, which leads to quick degradation of the IL. As expected, the yield increases as a function of temperature (samples A and B) and mixing (Table 3).

Roughness and morphological investigation on the Al-deposits are depicted in Figures 8 and 9. A substantial increase of the crystal size of the deposits obtained at higher temperatures accounts for the observed increased roughness.

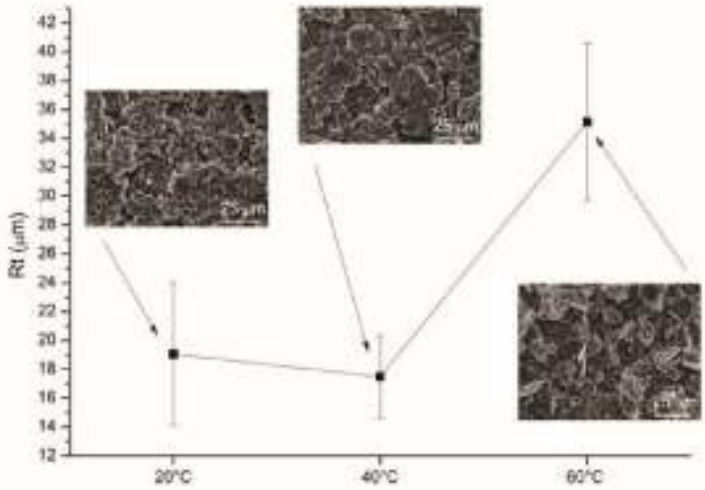

Figure 8. Roughness and SEM micrograph (scale bar is 25 μm) of the samples obtained by mechanical stirring (320 RPM) at different temperatures.

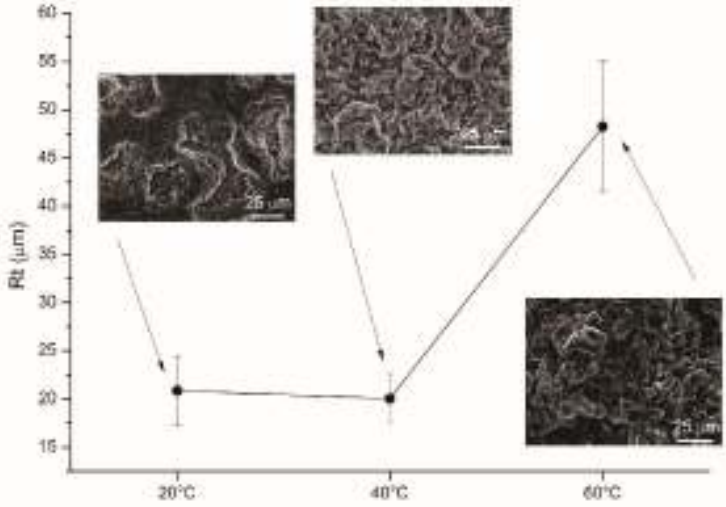

Figure 9. Roughness and SEM micrograph (scale bar is 25 μm) of the samples obtained via sonication (1 to 10 cycle) at different temperatures.

Structural Investigation

The XRD patterns of the Al-coated samples (from A to H) compared with the simulated Al metal pattern are depicted in Figure 10 (PDF 85-1327). The substrate (63% Cu, Zn 37% brass alloy) is an α–β biphasic alloy (Alloy Phase Diagrams, ASM international, page 48), the α-brass pattern is labelled as "Brass" according to the PDF 50-1333 card, while the β-phase pattern (PDF 02-1231) is hindered by the pattern of the Al coating.

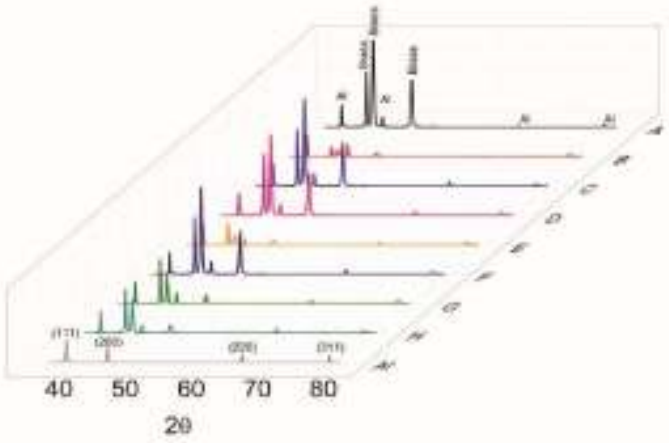

Figure 10. X-ray diffraction (XRD) patterns of the samples (A–H) in Table 3 compared with the simulated powder aluminium pattern (Al).

The diffraction peaks have been fitted with a R^2 always higher than 0.987. Figure 11 depicts the resulting fits of the $K_{\alpha 1}$ and $K_{\alpha 2}$ diffraction peaks for the sample B.

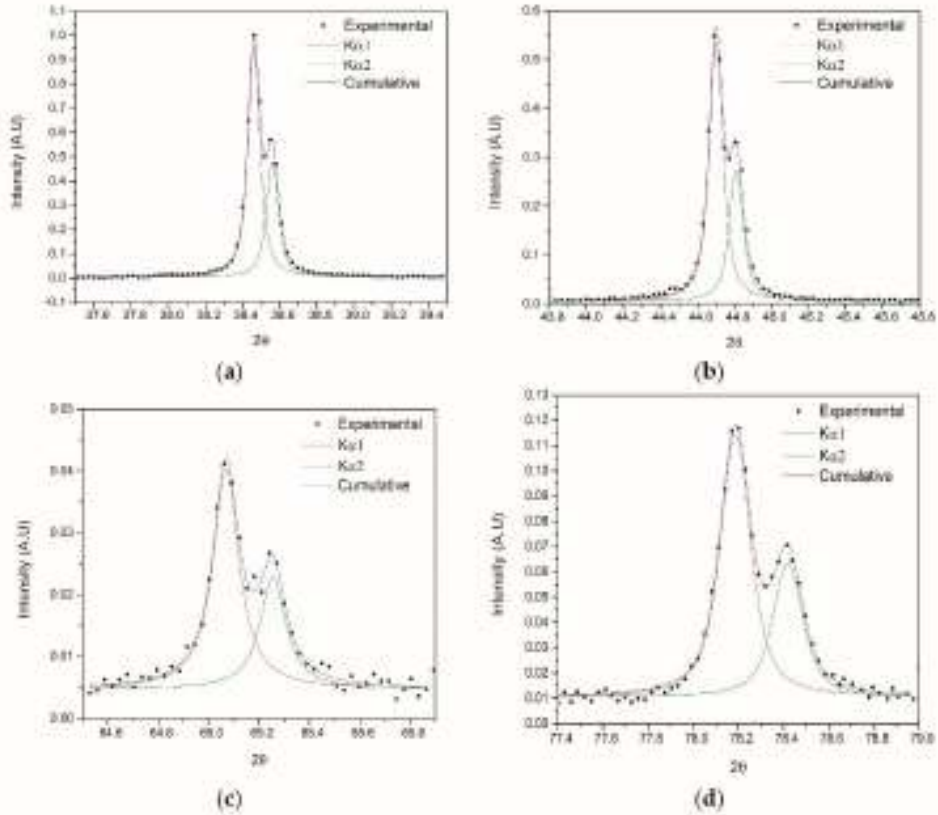

Figure 11. An example of the fitted double Voigt for the sample B: plane (111) (**a**); (200) (**b**); (220) (**c**); and (311) (**d**).

The texture coefficients obtained from these spectra (Figure 12a) clearly show the effect of deposition parameters on the growth of the deposits. In the samples obtained by using mechanical stirring (samples C to E), the texture along (111) and (311) planes increases as a function of the temperature. On the contrary, texturing of planes (200) and (220) decrease with rising temperatures. Samples obtained by means of sonication (samples F to H) show a similar but less enhanced texturing as a function of the temperature. Moreover, the (220) plane is characterized by a significant increase of texturing for the sample obtained at 60 °C.

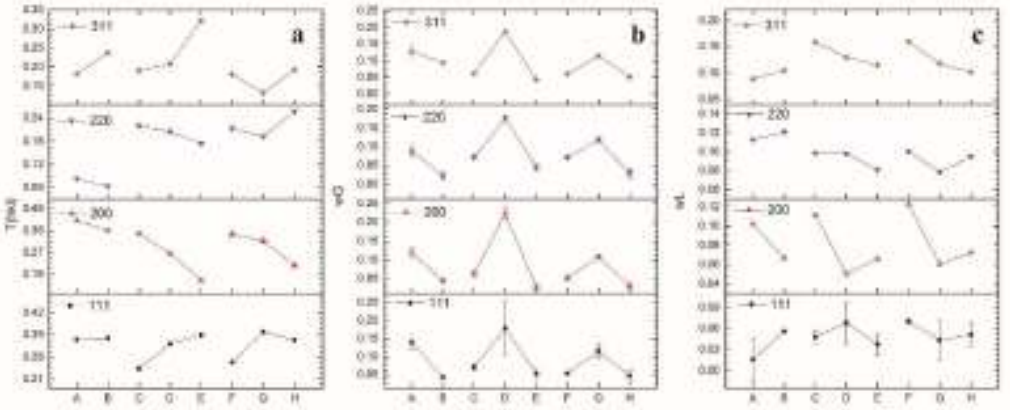

Figure 12. Trends of the fits for the assigned peaks over the three different sets of results: (**a**) the texture coefficient (no error bars); (**b**) the Gaussian width (proportional to the average strain); and (**c**) the Lorentzian width (proportional to the average size of the crystallites). The missing error bars in panels b and c are related to errors smaller than 0.5%.

Figure 12b reports the Gaussian widths of the XRD peaks. These values are considered to be related to the average strain of the crystallites. It is worth noting that for each plane the maximum Gaussian width, hence the maximum lattice strain, was achieved in the deposits obtained at 40 °C. Regarding the Lorentzian width of the peaks, which is inversely related to the average crystal size, the obtained values are depicted in Figure 12c. The average crystallite size presents trends that are more complex with respect to the texture. Generally speaking, improving the mixing conditions does not dramatically affect crystallite size along (111), (200), and (220) planes. In particular, the temperature does not consistently change the size along the zonal axis of the (111) plane. Along the zonal axis corresponding to the (200) and (220) planes, the crystallites size reaches its maximum at 40 °C under sonication. On the other hand, along the zonal axis of the (311) plane, the average crystallite size increases consistently with the temperature.

4. Conclusions

We have successfully prepared thick coatings of metallic aluminium on brass substrates by electrodeposition from (Bmim)Cl/$AlCl_3$ 40:60 ionic liquid. The investigation of the surface morphology, the crystal orientation, as well as the process yield evidenced the effects of temperature and mixing conditions.

Particularly, the process yield proved useful to assess the optimal deposition conditions to achieve compact and dense deposits. Yield lower than 100% can be related to the formation of dendritic coatings due by mass transfer limitations. Regarding the effect of operative conditions, temperature increase plays a positive role enhancing the deposition yield and smoothing the roughness of the deposits. On the other hand, sonication greatly improves the mobility of the species inside the IL allowing 100% yield, but also forcing a slight increase in roughness [25].

The combined effects of the experiments demonstrated that for temperatures above 60 °C, mixing has a larger effect with respect to temperature in reducing the roughness of the deposits. Below 40 °C, temperature affects the morphology of the coatings more effectively. It is reasonable to suppose that the two effects have a competitive role in growing the layer, with a threshold assessed between 40 °C and 60 °C. Compared to the sonication, stirring shows a lower yield at nearly room temperatures, but at higher temperatures the morphological and roughness studies show similar trends between these two mixing systems.

Regarding XRD analysis, the texturing of the Al coating is related to the temperature of the deposition process, favouring the orientation along the (111) and (311) axis. That is confirmed by the crystallite size analysis which demonstrated the preferential growth along different zonal axis according to different mass transport conditions [26]. In general, the mixing conditions do not affect the crystallites' size, while increasing the temperature does. Moreover, the maximum of the crystallite strain at 40 °C, in each set of mixing conditions, can be explained as a higher concentration of defects in the crystallites. This phenomenon cannot be confirmed in this study and the reason for its occurrence has to be understood. We suggest that it can be considered a trade-off between the nucleation-growth mechanism and the improvement of the mass transport of the active species.

In conclusion, higher temperatures and stronger mixing conditions promote the deposition of smoother and thicker aluminium deposits. However, in order to move towards the industrialization of the process and to increase the durability of the IL, temperatures above 60 °C should be avoided. In order to speed up the electrodeposition process, mechanical stirring or mild sonication can be successfully adopted.

Acknowledgments: The research leading to these results has received funding from the European Union Seventh Framework Programme (FP7/2007-2013) under grant agreement no. 608698.

Author Contributions: Stefano Caporali and Massimo Innocenti conceived and designed the experiments. Enrico Berretti and Stefano M. Martinuzzi obtained and characterized the deposits; Andrea Giacherini performed the XRD characterization and analysed the data. Thomas J.S. Schubert and Frank M. Stiemke supplied the ILs used in this study. Stefano Caporali also wrote the paper.

Conflicts of Interest: The authors declare no conflict of interest.

Abbreviations

The following abbreviations are used in this manuscript:

IL	Ionic liquid
Bmim	1-Butyl-3-methyl-imidazolium
SCE	Standard calomel electrode
WG	Gaussian width
WL	Lorentzian width
OCP	Open circuit potential
PD	potentiodynamic

Appendix A. Roughness

Four different roughness parameters are considered in this article: Rt, Ra, Rz ISO, and Rz [27,28].

Rt is the so called total roughness, the height between the deepest valley and the highest peak extrapolated from the entire evaluation length.

Ra is the average roughness, the arithmetic mean of the profile from a mean line.

Rz ISO and Rz are similar to the Rt value; in fact, they are expressed as the mean of the sum of the maximum value of profile peak height and the maximum profile valley depth taken in various sampling lengths within the evaluation length (ten for the Rz ISO and five for the Rz).

While Ra and Rt alone may be of very limited value in assessing the overall surface roughness of a sample (particularly Rt which can be seriously affected by a single spurious scratch or particle of dirt on the surface), their conjunction with the two Rz values could greatly boost our comprehension of the homogeneity of the obtained deposits. In addition, the variance related to the roughness

measurements helped us to visualize the surface homogeneity of the obtained deposits. In fact, roughness parameters were collected considering five measurements within three samples for each experiment. Larger errors are related to higher inhomogeneity of the surfaces, while smaller ones represent more homogeneous surfaces.

References

1. Grjotheim, K.; Halvor, K. *Introduction to Aluminium Electrolysis: Understanding the Hall-Héroult Process*, 2nd ed.; Aluminium-Verlag: Düsseldorf, Germany, 1993.
2. Markiewicz, M.; Hupka, J.; Joskowska, M.; Jungnickel, C.H. Potential application of ionic liquids in aluminium production—Economical and ecological assessment. *Physicochem. Probl. Miner. Process.* **2009**, *43*, 73–84.
3. Takahashi, S.; Koura, N.; Kohara, S.; Saboungi, M.L.; Curtiss, L. Technological and scientific issues of room-temperature molten salts. *Plasmas Ions* **1999**, *2*, 91–105. [CrossRef]
4. Abbott, A.P.; Harris, R.C.; Hsieh, Y.T.; Ryder, K.S.; Sun, I.W. Aluminium electrodeposition under ambient conditions. *Phys. Chem. Chem. Phys.* **2014**, *16*, 14675–14681. [CrossRef] [PubMed]
5. Fang, Y.; Yoshii, K.; Jiang, X.; Sun, X.G.; Tsuda, T.; Mehio, N.; Dai, S. An $AlCl_3$ based ionic liquid with a neutral substituted pyridine ligand for electrochemical deposition of aluminum. *Electrochim. Acta* **2015**, *160*, 82–88. [CrossRef]
6. Pulletikurthi, G.; Bödecker, B.; Borodin, A.; Weidenfeller, B.; Endres, F. Electrodeposition of Al from a 1-butylpyrrolidine-$AlCl_3$ ionic liquid. *Prog. Nat. Sci. Mater. Int.* **2015**, *25*, 603–611. [CrossRef]
7. Su, C.J.; Hsieh, Y.T.; Chen, C.C.; Sun, I.W. Electrodeposition of aluminium wires from the Lewis acidic $AlCl_3$/trimethylamine hydrochloride ionic liquid without using a template. *Electrochem. Commun.* **2013**, *34*, 170–173. [CrossRef]
8. Endo, A.; Miyake, M.; Hirato, T. Electrodeposition of aluminium from 1,3-dimethyl-2-imidazolidinone/$AlCl_3$ baths. *Electrochim. Acta* **2014**, *137*, 470–475. [CrossRef]
9. Hadi, M.A.; Abood, N.L.D. Morphology of electrodeposited aluminium metal from aluminium chloride-urea room temperature ionic liquid (RTIL) at variable parameter. *Int. J. Sci. Res.* **2015**, *4*, 753–760.
10. Wang, Q.; Chen, B.; Zhang, Q.; Lu, X.; Zhang, S. Aluminium deposition from lewis acidic 1-butyl-3-methylimidazolium chloroaluminate ionic liquid ((Bmim)Cl/$AlCl_3$) modified with methyl nicotinate. *ChemElectroChem* **2015**, *2*, 1794–1798. [CrossRef]
11. Wang, Q.; Zhang, Q.; Chen, B.; Lu, X.; Zhang, S. Electrodeposition of bright Al coatings from 1-butyl-3-methylimidazolium chloroaluminate ionic liquids with specific additives. *J. Electrochem. Soc.* **2015**, *162*, D320–D324. [CrossRef]
12. Yue, G.; Lu, X.; Zhu, Y.; Zhang, X.; Zhang, S. Surface morphology, crystal structure and orientation of aluminium coatings electrodeposited on mild steel in ionic liquid. *Chem. Eng. J.* **2009**, *147*, 79–86. [CrossRef]
13. Chang, J.K.; Chen, S.Y.; Tsai, W.T.; Deng, M.J.; Sun, I.W. Electrodeposition of aluminium on magnesium alloy in aluminium chloride ($AlCl_3$)–1-ethyl-3-methylimidazolium chloride (EMIC) ionic liquid and its corrosion behavior. *Electrochem. Commun.* **2007**, *9*, 1602–1606. [CrossRef]
14. Bardi, U.; Caporali, S.; Craig, M.; Giorgetti, A.; Perissi, I.; Nicholls, J.R. Electrodeposition of aluminium film on P90 Li–Al alloy as protective coating against corrosion. *Surf. Coat. Technol.* **2009**, *203*, 1373–1378. [CrossRef]
15. Zheng, Y.; Zhang, S.; Lu, X.; Wang, Q.; Zuo, Y.; Liu, L. Low-temperature electrodeposition of aluminium from lewis acidic 1-allyl-3-methylimidazolium chloroaluminate ionic liquids. *Chin. J. Chem. Eng.* **2012**, *20*, 138–139. [CrossRef]
16. Guikuan, Y.; Suojiang, Z.; Yanli, Z.; Xingmei, L.; Shucai, L.; Zengxi, L. A promising method for electrodeposition of aluminium on stainless steel in ionic liquid. *AIChE J.* **2009**, *55*, 783–796.
17. Pradhan, D.; Reddy, R.G. Dendrite-free aluminium electrodeposition from AlCl3–1-ethyl-3-methyl-imidazolium chloride ionic liquid electrolytes. *Metall. Mater. Trans. B* **2012**, *43*, 519–531. [CrossRef]
18. Choudhary, R.K.; Kain, V.; Hubli, R.C. Stirring effects on aluminium coatings electrodeposited in ionic liquids. *Surf. Eng.* **2014**, *30*, 562–567. [CrossRef]
19. De Keijser, T.H.; Langford, J.I.; Mittemeijer, E.J.; Vogels, A.B.P. Use of the Voigt function in a single-line method for the analysis of X-ray diffraction line broadening. *J. Appl. Crystallogr.* **1982**, *15*, 308–314. [CrossRef]

20. Scardi, P.; Leoni, M.; Delhez, R. Line broadening analysis using integral breadth methods: A critical review. *J. Appl. Crystallogr.* **2004**, *37*, 381–390. [CrossRef]
21. Balzar, D. Voigt-function model in diffraction line-broadening analysis, in defect and microstructure analysis from diffraction. *Int. Union Crystallogr. Monogr. Crystallogr.* **1999**, *10*, 94–126.
22. Macrae, C.F.; Bruno, I.J.; Chisholm, J.A.; Edgington, P.R.; McCabe, P.; Pidcock, E.; Rodriguez-Monge, L.; Taylor, R.; van de Streek, J.; Wood, P.A. Mercury CSD 2.0—New features for the visualization and investigation of crystal structures. *J. Appl. Crystallogr.* **2008**, *41*, 466–470. [CrossRef]
23. Wyckoff, R.W.G. *Crystal Structures*; Wiley: New York, NY, USA, 1963; pp. 7–83.
24. Downs, R.T.; Hall-Wallace, M. The American mineralogist crystal structure database. *Am. Mineral.* **2003**, *88*, 247–250.
25. Costa, C.; Doche, M.; Hihn, J.; Bisel, I.; Moisy, P.; Léveque, J. Hydrodynamic sono-voltammetry of ferrocene in $(Tf_2N)^-$ based ionic liquid media. *Ultrasonics* **2010**, *50*, 323–328. [CrossRef] [PubMed]
26. Zheng, Y.; Dong, K.; Wang, Q.; Zhang, J.; Lu, X. Density, viscosity, and conductivity of lewis acidic 1-butyl- and 1-hydrogen-3-methylimidazolium chloroaluminate ionic liquids. *J. Chem. Eng. Data* **2013**, *58*, 32–42. [CrossRef]
27. Stout, K.J. Surface roughness—Measurement, interpretation and significance of data. *Mater. Eng.* **1981**, *2*, 260–265. [CrossRef]
28. Gadelmawla, E.S.; Koura, M.M.; Maksoud, T.M.A.; Elewa, I.M.; Soliman, H.H. Roughness parameters. *J. Mater. Process. Technol.* **2002**, *123*, 133–145. [CrossRef]

coatings

MDPI

Article

Aluminizing via Ionic Liquid Electrodeposition and Pack Cementation: A Comparative Study with Inconel 738 and a CoNiCrAlY

Luca Tagliaferri [1], Enrico Berretti [2], Andrea Giaccherini [2], Stefano M. Martinuzzi [2], Francesco Bozza [1], Martin Thoma [3], Ugo Bardi [2] and Stefano Caporali [4,5,6,*]

1 Turbocoating s.p.a., Via Mistrali 7, 43040 Rubbiano di Solignano, Italy; LucaTagliaferri@turbocoating.it (L.T.); Francesco Bozza@turbocoating.it (F.B.)
2 Dipartimento di Chimica, Università di Firenze, via della Lastruccia 3, 50019 Sesto Fiorentino, Italy; eberretti@gmail.com (E.B.); andrea.giaccherini@unifi.it (A.G.); ste.martinuzzi@gmail.com (S.M.M.); ugo.bardi@unifi.it (U.B.)
3 MT Consulting, Mainzerstrasse 15, 80804 Munich, Germany; martin.thoma@forumt.com
4 Dipartimento di Ingegneria Industriale, Università di Firenze, via di S. Marta 3, 50139 Firenze, Italy
5 Consorzio Interuniversitario Nazionale per la Scienza e Tecnologia dei Materiali, via Giusti 9, 50123 Firenze, Italy
6 Istituto Sistemi Complessi (ISC-CNR), via Madonna del Piano 10, 50019 Sesto Fiorentino, Italy
* Correspondence: stefano.caporali@unifi.it; Tel.: +39-055-457-3119

Received: 1 May 2017; Accepted: 15 June 2017; Published: 19 June 2017

Abstract: A novel aluminizing process based upon room temperature Al-electrodeposition from Ionic Liquids followed by diffusion heat treatment was applied on bare- and CoNiCrAlY-coated Inconel 738 (IN738). The aluminized samples were tested by isothermal oxidation at 1000 °C in air. The microstructural and chemical evolution of the samples were determined as function of oxidation time and compared with the currently applied coatings obtained via pack cementation. The newly proposed method is suitable for the CoNiCrAlY coating, but not for the bare IN738. In the latter, the formed Al-enriched layer is much thinner and the anticorrosion properties resulted in being reduced. This is probably due to the presence of precipitates, which slow down the aluminum inward diffusion impairing the formation of a well-developed interdiffusion zone (IDZ). Traces of the electrolyte, embedded during the Al-electrodeposition process, can be seen as the origin of these precipitates.

Keywords: ionic liquids; electrodeposition; aluminum; isothermal test; NiAl; Ni superalloys; gas turbine; SEM-EDX; coatings

1. Introduction

Inconel 738 (IN738) is a nickel-based superalloy widely used as a high temperature material for gas turbine and aerospace applications. Its industrial success is based on the superior creep resistance with respect to other alloys at the high operating temperatures employed in gas turbine engines (up to 1300 °C). However, this alloy is not without drawbacks. In particular, it presents low resistance to hot corrosion and high temperature oxidation. For this reason, surface modifications are mandatory in order to improve the durability of IN738 parts in the hot sections of gas turbines.

The oxidation and corrosion resistance of high-temperature alloys and coatings is dependent on the formation and retention of a thin, dense, continuous external oxide scale, which serves as a diffusion barrier preventing oxygen diffusion and therefore the rapid oxidation of the metal beneath. Alumina is typically the preferred protective scale for applications above 900 °C. Thus, two types of alumina-forming coatings are currently used as oxidation-resistant systems on gas turbine superalloy: nickel aluminide diffusion coatings (NiAl) [1–6] and MCrAlX alloys (where M = Ni, Co and/or Fe

and X = Y, Hf, Zr and/or Si). The diffusion aluminide coatings are based on β-NiAl phase; the MCrAlY (M = Ni, Co, or NiCo) overlay coatings are based on a mixture of β-NiAl and γ′-Ni_3Al or γ phases. One important advantage of the overlay coatings is the extra freedom in the choice of coating composition. A further over-aluminizing step on MCrAlX coatings is generally performed in order to enhance their oxidation protection at high temperatures [7–11].

Due to many merits such as low cost, convenient operation and mature techniques, diffusion aluminide coatings have been extensively applied on the surface of gas turbine blades and vanes [12]. Pack cementation is the principal industrial methodology to produce diffusion aluminide coatings. It is based on the deposition of aluminum from Al-halides (typically $AlCl_3$) created from a powder mix containing an Al-source (CrAl or CoAl), an halide activator (typically NH_4Cl) and an inert filler to avoid particles sintering [2,12,13]. At high temperatures (from 650 to 1100 °C), a reaction takes place with the creation of volatile, Al-rich halides that finally lead to the diffusion of metallic Al into the Ni/Co base [12] forming the Ni–Al intermetallic compounds and secondary phases.

Nickel-aluminide diffusion coatings can also be achieved by diffusing pure aluminum—layered on the surface—into the nickel-based alloy. The process is well known and models for Al and Ni-diffusion have been proposed [14,15]. This method requires the deposition of a pure aluminum layer and, recently, a new method to create Al-enriched coatings has been proposed on the basis of the electrodeposition of metallic aluminium from Ionic Liquids (ILs) [16]. ILs, and in particular chloroaluminated-based ILs, are a well known family of non-protic compounds from which layers of aluminum can be obtained by electrodeposition at room temperature. Even though the process must be carried out in moisture-free environments, it has several advantages over vacuum-based techniques such as: high deposition rate (10–20 μm/h), simple and cheap instrumentation, and low energy consumption [17–22]. For these reasons, the industrialization of the Al-plating process for automotive and aerospace applications is of great technological interest and it is currently under industrial development [23,24].

The present work deals with a two-step aluminizing process based on (a) the electrodeposition of aluminum and (b) the formation of Ni–Al intermetallics by means of thermal treatment. The results of this new process in terms of microstructural investigation and isothermal oxidation test were compared with the currently employed pack cementation process over bare IN738 (aluminizing) and CoNiCrAlY-coated IN738 (over-aluminizing). The results show comparable oxidation resistance for the over-aluminizing process while on bare IN738 (aluminizing) the sample produced with the two-step process resulted less performing respect to the ones produced by pack cementation.

2. Materials and Methods

Flat samples of IN738 (16 wt % Cr, 8.5 wt % Co, 3.4 wt % Ti, 2.6 wt % W, 2.65 wt % Ta, 1.75 wt % Mo, 0.11 wt % C, Ni balance) were prepared by casting and machining 7 × 7 cm^2 tokens. Al-rich coatings were prepared on bare and CoNiCrAlY-coated IN738 via IL double step and pack cementation and will be called from now on, respectively, as: IL or Pack "aluminizing" and IL or Pack "over-aluminizing".

Five types of sample were prepared as listed below:

- "IL aluminizing": IN738 + Al by Ionic Liquids + Heat treatment (1100 °C in vacuum).
- "IL over-aluminizing": IN738 + CoNiCrAlY + Al by Ionic Liquids + Heat treatment (1100 °C in vacuum).
- "Pack aluminizing": IN738 + pack cementation process (1000 °C) + Heat treatment (1100 °C in vacuum).
- "Pack over-aluminizing": IN738 + CoNiCrAlY + pack cementation process (1000 °C) + Heat treatment (1100 °C in vacuum).
- "Reference coating": IN738 + CoNiCrAlY + Heat treatment (1100 °C in vacuum).

Furthermore, 200 ± 50 μm thick CoNiCrAlY coatings (38.1 wt % Co, 32 wt % Ni, 21 wt % Cr, 8 wt % Al, 0.5 wt % Y) were deposited, prior to the aluminizing processes on IN738, by HVOF (High

Velocity Oxygen Fuel) thermal spray using a JP5000 HVOF gun, manufactured by Artec s.r.l (Parma, Italy) working in an oxygen/kerosene configuration.

Aluminum coatings were electrodeposited from 1-butyl-3-methylimidazolium chloride/Aluminum chloride ([Bmim]Cl/$AlCl_3$) 40/60 mol % supplied by IoLiTec Ionic Liquids Technologies GmbH (Heilbronn, Germany) and used without further purification. The process was carried out inside a N_2 filled glove box (Iteco mod 10A, Castelbolognese, Italy), with a moisture content below 30 ppm using a PAR model 2273 potentiostat (Oak Ridge, TN, USA) controlled by PowerSuite 2.58 software (v. 2.58, Princeton Applied Research, Oak Ridge, TN, USA). A pure aluminum foil (Goodfellow, Huntingdon, UK, 99.0) was used as counter electrode.

The Al-deposits were produced by direct deposition in current controlled (galvanostatic) conditions at 10 mA·cm^{-2} for 2 h at room temperature, and then rinsed with acetone and distilled water to remove traces of the adsorbed electroplating bath. Figure 1 depicts the cross sections of the Al layer deposited on bare IN738 and CoNiCrAlY-coated IN738.

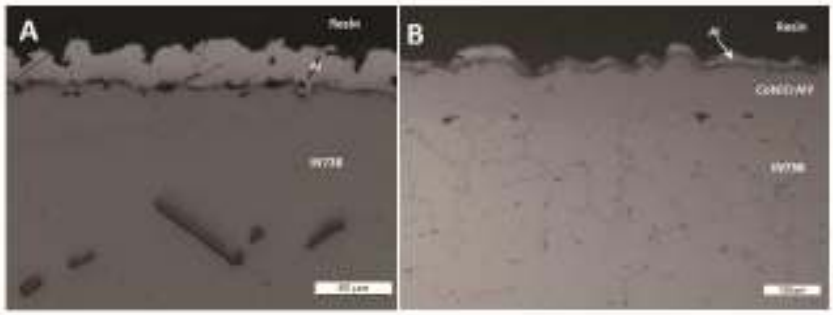

Figure 1. SEM images (SE signal) of the aluminum coating on bare IN738 (**A**) and CoNiCrAlY coated IN738 (**B**) before the heat treatment. In both cases, a pure Al layer about 20 µm thick is detectable on the top of the sample.

The heat treatment was finally performed at 1100 °C for 2–5 h in vacuum (range 10^{-1}–10^{-3} mbar) allowing the Al diffusion inwards the substrates but avoiding its high temperature oxidation (for process details, see Ref. [14] and citations therein).

Samples of bare IN738 and CoNiCrAlY-coated underwent the same treatment, while replacing the two-step process with the pack aluminizing process (for process details, see Ref. [8] and citations therein). The process was carried out by covering the surface to be Al-enriched with a powder mix containing an Al source (CoAl or CrAl alloy), an activator (NH_4Cl) and an inert filler (Al_2O_3 powder). The process was carried out in Ar atmosphere at 1000 °C for 2–5 h. At this temperature, a reaction took place within the powder mix, creating the Al chloride vapour phase, able to let the inward diffusion of Al into both IN738 and CoNiCrAlY.

For each of the 5 systems, three samples were prepared applying a post treatment at 1100 °C in vacuum (range 10^{-1}–10^{-3} mbar) for 2–5 h as final step. The obtained samples were tested under isothermal conditions (air atmosphere, 1000 °C) and characterized before oxidation test (0 h) and after 500 and 1000 h (end of the test) by means of Scanning electron microscope (SEM), X-ray diffraction (XRD) and micro-hardness analyses. Since Ni–Al intermetallic phases are materials harder than the Ni superalloy, a micro-hardness profile evaluation can be profitably used as indirect indication of the formation of these compounds.

Metallographic cross sections of the samples were prepared and investigated by using a Hitachi 2300 SEM microscope (Tokyo, Japan). Compositional profiles were determined by means of an Energy Dispersive Microanalysis (EDS) system (NORAN NSS 300, Thermo Fisher Scientific, Waltham, MA, USA) using 20 kV acceleration and 34.7° take off angle. The peaks were fitted by Gaussian curves applying the ZAF (atomic number absorption fluorescence) correction.

The crystalline phases present in the coatings were determined through XRD, using a XRD Bruker D8 Advance powder diffractometer (Bruker, Billerica, MA, USA) employing Cu Kα (1.54187 Å) radiation covering a 2θ range between 36° and 80°, applying a step size of 0.022° and a step counting time of 0.27 s.

Hardness measurements were carried out by using a HX1000 micro-hardness tester (Remet, Bologna, Italy) equipped with a Vickers indenter. The measurements were performed using a load of 25 g and repeated at least 4 times for every sample on randomly chosen profiles of the cross section.

3. Results

3.1. Comparison between Pack Aluminizing and IL Aluminizing over IN738

The evolution of the base material (IN738) aluminized, via both pack cementation and ILs electrodeposition, was evaluated and compared as a function of the isothermal test duration.

Figure 2 depicts the SEM-BSE (backscattered electron mode) micrographs of the cross sections obtained on both the type of samples as function of test duration.

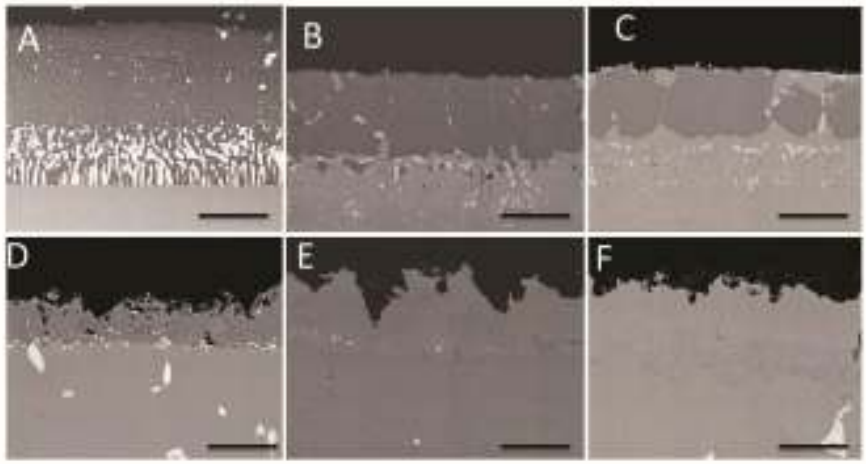

Figure 2. SEM images (BSE signal) of the aluminized IN738 as function of the isothermal test duration (**A**,**D** = 0 h; **B**,**E** = 500 h; **C**,**F** = 1000 h) for IN738 + pack aluminizing + heat treatment (**A**–**C**) and IN738 + IL Aluminizing + heat treatment (**D**–**F**). Scale bar 25 µm.

The coatings substantially differ in terms of thickness and microstructure even before the thermal tests. The one obtained via pack aluminizing (Figure 1A) is thicker (up to 40 µm) and presents a well-developed interdiffusion zone (IDZ) compared to the sample obtained via IL aluminizing process (Figure 1D). Clues about the reduced thickness of the diffusion layer were investigated analyzing the interphase between the IL aluminide coating and the IN738 substrate. Figure 3 displays the backscattered electron (BSE) magnification of this zone. It shows the presence of a large number of bright particles which imply a high electron scattering power generated by high atomic number elements. The EDS analysis performed on these particles shows the presence of W, Nb, Mo, Ti and Ta, probably as carbides or nitrides (Table 1). It seems reasonable that these precipitates, absent in the sample prepared via pack cementation, slow down the Al inward diffusion. As a consequence of the reduced inward diffusion rate, at the severe condition of the heat treatment (vacuum, 1100 °C), aluminum sublimation could become a relevant process leading to the loss of part of the deposit. The most likely explanation for the presence of these compounds is the presence of traces of the electrolyte embedded in the growing Al-layer. Carbon and/or nitrogen present in the cation of the

IL may have reacted with the metals present in the base material (W, Ta, Nb, Ti, Mo) during the heat treatment (1100 °C) in vacuum, leading to the formation of carbides and/or nitrides.

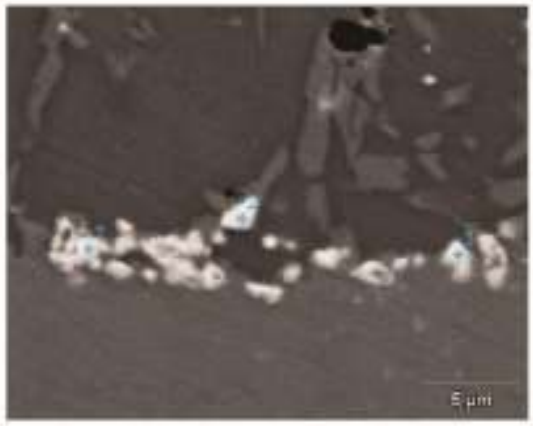

Figure 3. SEM image (BSE signal) of the interphase between IL aluminide coating and IN738 substrate. Numbers indicate the spots on which EDS analysis was performed. Scale bar 25 µm.

Table 1. EDS spot analysis over the points depicted in Figure 2.

Element	Point 1	Point 2	Point 3
Al	0.2	0.4	0.3
Ti	3.7	1.7	15.5
Cr	50.4	45.9	3.3
Co	2.1	3.8	2.5
Ni	13.2	25.3	20.7
Mo	12.0	9.3	–
W	18.4	13.6	–
Nb	–	–	4.7
Ta	–	–	53.0

EDS compositional analysis, micro-hardness profiles and XRD patterns have been realized to better characterize the samples. Figures 4–6 show the elemental profile concentration, the hardness profiles and the XRD pattern of these coatings, respectively.

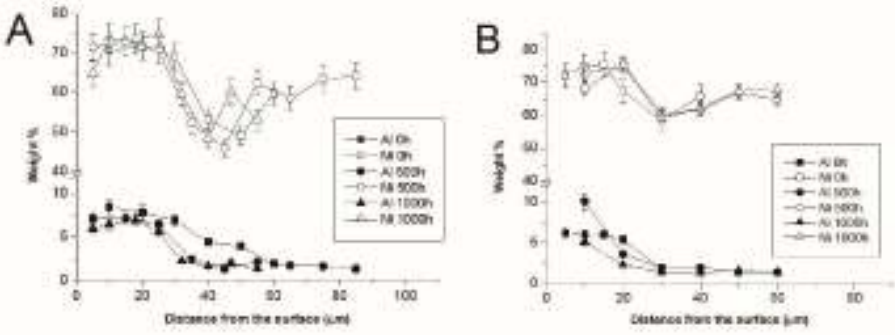

Figure 4. Compositional profiles of Al (full symbols) and Ni (empty symbols) for the cross sections depicted in Figure 1 as determined by EDS measurement. (**A**) and (**B**) panels depict data for IN738 + pack aluminizing + heat treatment and IN738 + IL aluminizing + heat treatment, respectively.

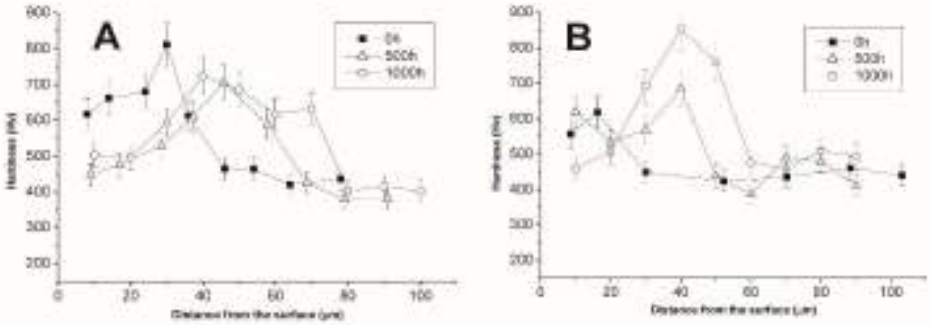

Figure 5. Hardness profile measurement for IN738 + Pack aluminizing + Post treatment (**A**) and IN738 + IL aluminizing + post treatment (**B**), respectively, at 0, 500 and 1000 h of isothermal test (1000 °C).

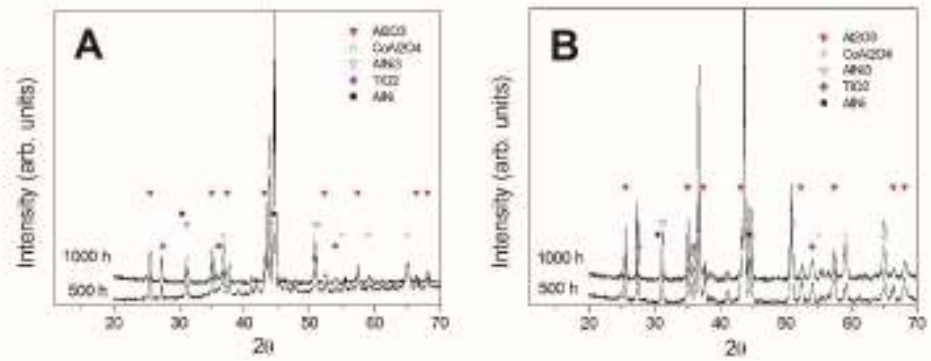

Figure 6. Surface XRD pattern of IN738 + Pack aluminizing + Post treatment (**A**) and IN738 + IL aluminizing + post treatment (**B**), respectively, after 500 and 1000 h of isothermal test (1000 °C).

Compositional and hardness profiles depicted in Figures 4 and 5 present a clear trend: pack aluminizing generates a higher concentration of aluminum and, consequently, we observe the formation of Ni–Al intermetallic compounds within the coating cross section. On the other hand, the IL aluminizing performed over IN738 resulted in a lower and more shallow Al inward diffusion leading to the formation of a different microstructure depleted in Ni–Al as proved by the lower hardness (compare the curves at 0 h of Figure 5A,B). The consequence was a lower oxidation resistance (also detectable from results at 500 and 1000 h of isothermal test). The surface of the sample obtained via ILs aluminizing also results much rougher (Figure 2E,F) and richer in oxidation byproducts such as rutile (TiO_2) (see Figure 6), providing direct evidence of severe oxidation of the base material (IN738).

On the contrary, the surface of samples obtained via pack cementation, is dominated by α-Al_2O_3, which is the oxidation product of the aluminide coating that plays a protective role toward the Ni-base superalloy (see Figure 6).

3.2. Tests on the Reference Coating: HVOF Sprayed CoNiCrAlY on IN738 with No Aluminizing Process + Heat Treatment (1100 °C in Vacuum).

To determine the oxidation resistance of the CoNiCrAlY alone, the IN738 samples coated with CoNiCrAlY, but without any over-aluminizing process, underwent oxidation tests in isothermal conditions. Figure 7 shows SEM-BSE micrographs of the cross section as a function of the test duration while Figure 8 displays the Ni and Al concentration profiles as determined by EDS.

Figure 7. SEM micrographs for the HVOF sprayed CoNiCrAlY + heat treatment at 0 h (**A**), 500 h (**B**) and 1000 h (**C**) of isothermal test. Scale bar 50 μm.

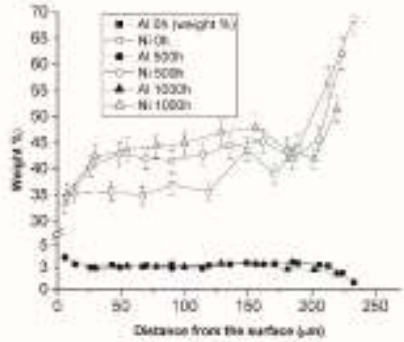

Figure 8. Ni and Al concentration profile for HVOF sprayed CoNiCrAlY on IN738 at 0, 500 and 1000 h of isothermal test.

During the high temperature test, aluminum diffuses toward the surface and oxidizes: creating the protective Al_2O_3 scale. At the same time, nickel migrates outward from the base material. Figure 8 shows the increase of Ni amount from 0 h in which Co concentration is higher than Ni, to 500 and 1000 h, where Ni becomes the dominant element in the coating. The migration of Ni at high temperature also brings changes within the microstructural composition of the CoNiCrAlY coating. Higher amounts of Ni are observed in the coatings at 500 and 1000 h. This leads to the decrease of β NiAl and the parallel increase of γ' Ni_3Al. This process has detrimental effects on the anticorrosion properties of the treatment. The microstructural evolution is clearly detectable from the micrographs depicted in Figure 7 as well as the compositional profiles depicted in Figure 8. Ni diffusion from substrate towards the bond coat leads the transformation from β to γ phase reducing the overall coating hardness (Figure 9).

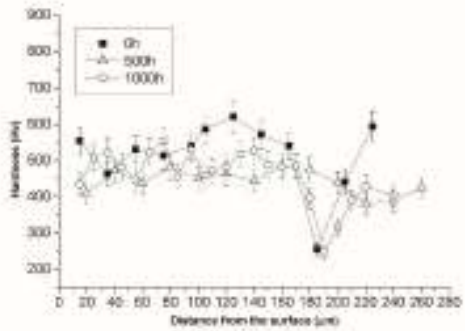

Figure 9. Micro-hardness profiles of HVOF sprayed CoNiCrAlY on IN738 + heat treatment at 0, 500 and 1000 h of isothermal test.

The evolutionary trend of CoNiCrAlY during oxidation test was finally confirmed by XRD analysis (Figure 10) on which Al2O3 and the mixed oxide CoAl2O4 result as the main oxidation byproducts [7,8].

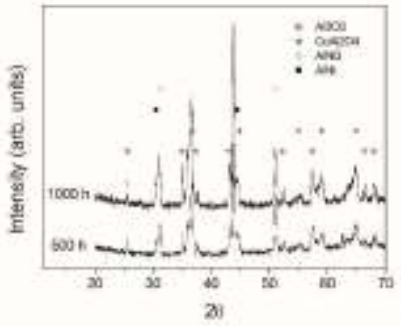

Figure 10. XRD analysis performed on HVOF sprayed CoNiCrAlY on IN738 + heat treatment at 500 and 1000 h of isothermal test.

3.3. Comparison between Pack- and IL Over-Aluminizing

As a final evaluation, the results of isothermal tests for the two over-aluminizing processes (pack aluminizing and IL aluminizing) were compared.

Microstructural investigation of the cross sections (Figure 11) provides evidence of the different behavior and trends of the double-step coated and heat treated samples with respect to the standard aluminizing process over IN738 (see Section 3.1). In this case, no formation of carbides is detected and aluminum diffuses much deeper into the metallic coating with respect to the pack aluminizing.

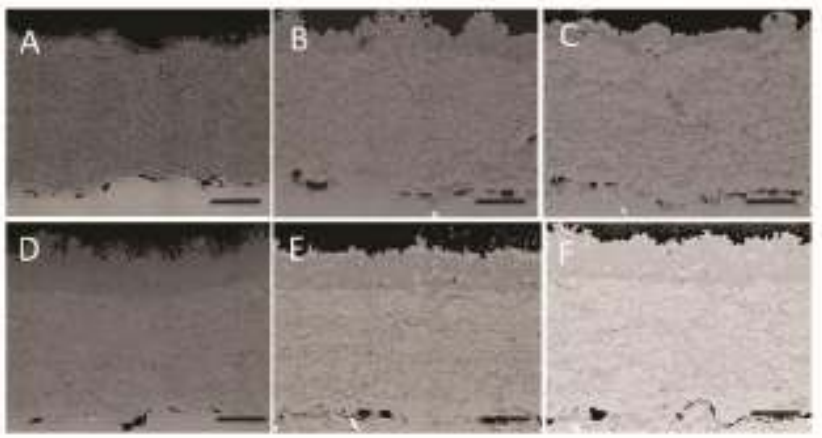

Figure 11. SEM images (BSE signal) of the over-aluminized IN738 + CoNiCrAlY as function of the isothermal test duration (**A**,**D** = 0 h; **B**,**E** = 500 h; **C**,**F** = 1000 h) for IN738 + CoNiCrAlY + pack aluminizing + heat treatment (**A**–**C**) and IN738 + CoNiCrAlY + IL Aluminizing + heat treatment (**D**–**F**). Scale bar 50 μm.

These trends are also confirmed by the compositional profiles (Figure 12): Al in the IL over-aluminized CoNiCrAlY diffuses deeper than in the case of the pack aluminizing process increasing the β NiAl phase within a thicker CoNiCrAlY section. Figure 13 depicts the hardness variation across the coating of both the over-aluminized samples: little but detectable differences in the micro-hardness values

indicate that it generally increases in the outermost portion of the coating due to the higher amount of Al diffused from the over-aluminized process. However, among the two over-aluminizing processes, the sample obtained via IL electrodeposition is characterized by larger hardness increase (from an average of 450 HV up to 700 HV in the more external portion of the coating, Figure 13B) due to the higher thickness of the over-aluminide coating itself with respect to the pack over-aluminide coatings.

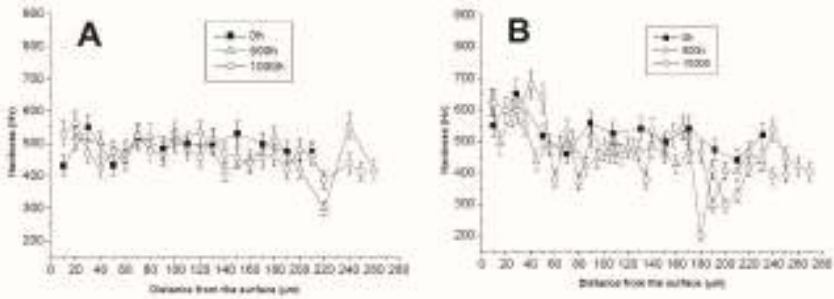

Figure 12. Compositional profiles of Al (full symbols) and Ni (empty symbols) for the cross sections depicted in Figure 10 as determined by EDS measurement. (**A**) and (**B**) panels depict data for IN738 + CoNiCrAlY + IL aluminizing + heat treatment and IN738 CoNiCrAlY + Pack aluminizing + heat treatment, respectively.

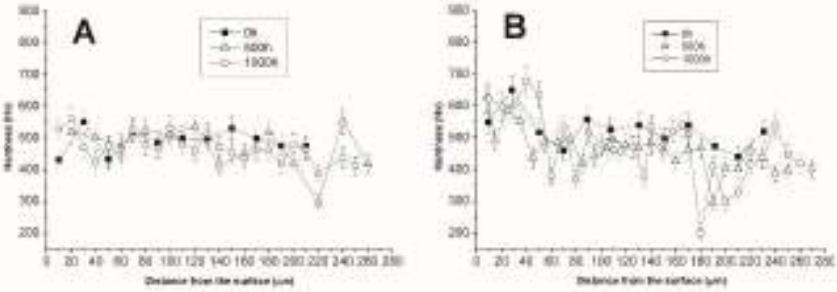

Figure 13. Hardness profile measurement for IN738 + CoNiCrAlY + Pack aluminizing + Post treatment (**A**) and IN738 + CoNiCrAlY + IL aluminizing + post treatment (**B**), respectively, at 0, 500 and 1000 h of isothermal test (1000 °C).

XRD data (Figure 14) confirm the good resistance for both types of over-aluminized samples.

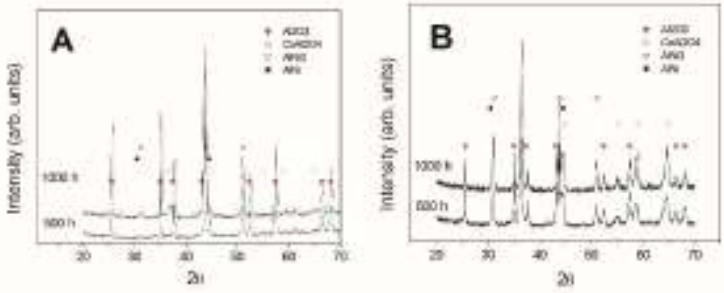

Figure 14. Surface XRD pattern of IN738 + CoNiCrAlY + Pack aluminizing + Post treatment (**A**) and IN738 + CoNiCrAlY + IL aluminizing + post treatment (**B**), respectively, after 500 and 1000 h of isothermal test (1000 °C).

4. Conclusions

The results obtained in the present study can be summarized as follows:

- Apparently, the two-step aluminizing process by Al-electrodeposition and consequent diffusion heat treatment (IL aluminizing) is not suitable for the direct application over IN738. Al inward diffusion seems to be inhibited by the possible formation of carbides or nitrides. These precipitates were observed after the diffusion post treatment, and they could result from the reaction of traces of ionic liquid entrapped in the growing Al layer with the base material. A further cleaning process could be attempted after the electroplating step in order to avoid the presence of IL residuals.
- Over-aluminizing of CoNiCrAlY is beneficial in order to create a viable anti-corrosion coating. This is due to the high Ni interdiffusion from the base material to the coating. This behavior causes the transformation of the β NiAl into γ Ni_3Al, which is less protective under oxidative and corrosive environment. For this reason, a further aluminizing step (over-aluminizing) is required for these types of metallic coatings in order to enhance the oxidation resistance at high temperatures.
- Being virtually free of W, Ta, Ti, there is no formation of carbides in the CoNiCrAlY coat; therefore, IL over-aluminizing on CoNiCrAlY allows a better and deeper diffusion of the Al toward the coating with respect to the pack over-aluminizing process.

Overall, the IL aluminizing process results in being feasible and suitable as an over-aluminizing step onto CoNiCrAlY metallic coatings for high temperature oxidation protection but not for direct aluminizing of IN738.

Acknowledgments: The research leading to these results has received funding from the European Union Seventh Framework Programme (FP7/2007-2013) under Grant No. 608698. We wish to thank the IoLiTec Ionic Liquids Technologies GmbH (Heilbronn, Germany) for supplying the Ionic Liquid used in this study.

Author Contributions: Luca Tagliaferri and Stefano Caporali conceived and designed the experiments, analyzed the data, and wrote the paper; Stefano M. Martinuzzi realized the Al-electrodeposition from ionic liquid and Francesco Bozza via pack cementation. Enrico Berretti performed and analyzed the hardness profiles, and Andrea Giaccherini analyzed the XRD data. Martin Thoma and Ugo Bardi analyzed the data and contributed to the paper writing.

Conflicts of Interest: The authors declare no conflict of interest.

References

1. Bozza, F.; Bolelli, G.; Giolli, C.; Giorgetti, A.; Lusvarghi, L.; Sassatelli, P.; Scrivani, A.; Candeli, A.; Thoma, M. Diffusion mechanisms and microstructure development in pack aluminizing of Ni-based alloys. *Surf. Coat. Tech.* **2014**, *239*, 147–159. [CrossRef]
2. Xiang, Z.D.; Burnell-Gray, J.S.; Datta, P.K. Aluminide coating formation on nickel-base superalloys by pack cementation process. *J. Mater. Sci.* **2001**, *36*, 5673–5682. [CrossRef]
3. Kim, D.; Sah, I.; Lee, H.J.; Hong, S.; Jang, C. Development of an aluminide coating layer on Alloy 617 by Al sputtering and inter-diffusion heat treatments. *Surf. Coat. Technol.* **2014**, *244*, 15–22. [CrossRef]
4. Wang, Y.; Chen, W.; Wang, L. Micro-indentation and erosion properties of thermal sprayed NiAl intermetallic-based alloy coatings. *Wear* **2003**, *254*, 350–355. [CrossRef]
5. Wang, Y.; Chen, W. Effect of ceria on the erosion resistance of HVOF thermal sprayed NiAl intermetallic coatings. *J. Mater. Sci. Lett.* **2003**, *22*, 845–851. [CrossRef]
6. Deevi, S.C.; Sikka, V.K.; Liu, C.T. Processing, properties, and applications of nickel and iron aluminides. *Prog. Mater. Sci.* **1997**, *42*, 177–192. [CrossRef]
7. Lih, W.; Chiang, E.; Wu, B.C.; Chao, C.H. The effect of pack-aluminisation on the microstructure of MCrAlY and the performance of thermal barrier coatings. *Surf. Coat. Technol.* **1992**, *50*, 277–288. [CrossRef]
8. Chang, S.F.; Chao, C.H.; Wu, B.C.; Leu, R.Q.; Chang, E. Zirconia/pack-aluminized Co-29Cr-6Al-1Y thermal barrier coatings. *J. Vac. Sci. Technol. A* **1991**, *9*, 2099–2106. [CrossRef]
9. Tong, L.; Dengzun, Y.; Chungen, Z. Low-temperature formation of aluminide coatings on Ni-base superalloys by pack cementation process. *Chin. J. Aeronaut.* **2010**, *23*, 381–385. [CrossRef]

10. Svensson, H.; Angenete, J.; Stiller, K. Microstructure of oxide scales on aluminide diffusion coatings after short time oxidation at 1050 °C. *Surf. Coat. Technol.* **2004**, *177–178*, 152–157. [CrossRef]
11. Fossati, A.; Ferdinando, M.; Lavacchi, A.; Scrivani, A.; Giolli, C.; Bardi, U. Improvement of the oxidation resistance of CoNiCrAlY bond coats sprayed by high velocity oxygen-fuel onto nickel superalloy substrate. *Coatings* **2011**, *1*, 3–16. [CrossRef]
12. Choy, K.L. Chemical vapour deposition of coatings. *Prog. Mater. Sci.* **2003**, *48*, 57–170. [CrossRef]
13. Thoma, M.; Scrivani, A.; Giolli, C.; Giorgetti, A. Aluminizing turbine parts—Processes and coatings. In Proceedings of the ASME Turbo Expo 2011, Vancouver, BC, Canada, 6–10 June 2011.
14. Mishin, Y. Atomistic modeling of the γ and γ'-phases of the Ni–Al system. *Acta Mater.* **2004**, *52*, 1451–1467. [CrossRef]
15. Wu, K.; Chang, Y.A.; Wang, Y. Simulating interdiffusion microstructures in Ni–Al–Cr diffusion couples: A phase field approach coupled with CALPHAD database. *Scripta Mater.* **2004**, *50*, 1145–1150. [CrossRef]
16. Bardi, U.; Caporali, S.; Craig, M.; Lavacchi, A.; Nicholls, J. A Method for Making a Protective Coating on a Metal Substrate. European Patent No 2330233 A1, 1 December 2009.
17. Abbott, A.P.; Harris, R.C.; Hsieh, Y.T.; Ryder, K.S.; Wen-Sun, I. Aluminium electrodeposition under ambient conditions. *Phys. Chem. Chem. Phys.* **2014**, *16*, 14675–14681. [CrossRef] [PubMed]
18. Fang, Y.; Yoshii, K.; Jiang, X.; Sun, X.G.; Tsuda, T.; Mehio, N.; Dai, S. An $AlCl_3$ based ionic liquid with a neutral substituted pyridine ligand for electrochemical deposition of aluminum. *Electrochim. Acta* **2015**, *160*, 82–88. [CrossRef]
19. Wang, Q.; Chen, B.; Zhang, Q.; Lu, X.; Zhang, S. Aluminium deposition from lewis acidic 1-butyl-3-methylimidazolium chloroaluminate ionic liquid ([Bmim]Cl/$AlCl_3$) modified with methyl nicotinate. *ChemElectroChem* **2015**, *2*, 1794–1798. [CrossRef]
20. Wang, Q.; Zhang, Q.; Chen, B.; Lu, X.; Zhang, S. Electrodeposition of bright Al coatings from 1-butyl-3-methylimidazolium chloroaluminate ionic liquids with specific additives. *J. Electrochem. Soc.* **2015**, *162*, D320–D324. [CrossRef]
21. Zheng, Y.; Zhang, S.; Lu, X.; Wang, Q.; Zuo, Y.; Liu, L. Low-temperature electrodeposition of aluminium from lewis acidic 1-allyl-3-methylimidazolium chloroaluminate ionic liquids. *Chin. J. Chem. Eng.* **2012**, *20*, 130–139. [CrossRef]
22. Berretti, E.; Giaccherini, A.; Martinuzzi, S.M.; Innocenti, M.; Schubert, T.J.S.; Stiemke, F.M.; Caporali, S. Aluminium Electrodeposition from Ionic Liquid: Effect of Deposition Temperature and Sonication. *Materials* **2016**, *9*, 719. [CrossRef]
23. Project Scail-Up. Scaling-Up of the Aluminium Plating Process from Ionic Liquid. Available online: http://scailup.eu (accessed on 25 February 2017).
24. Caporali, S.; Martinuzzi, S.M.; von Czarnecki, P.; Schubert, T.J.S.; Bardi, U. Effects of metal ions on the aluminum electrodeposition from ionic liquids. *J. Mater. Eng. Perform.* **2017**, *26*, 685–691. [CrossRef]

E3690 *Journal of The Electrochemical Society*, **164** (11) E3690-E3695 (2017)

JES Focus Issue on Mathematical Modeling of Electrochemical Systems at Multiple Scales in Honor of John Newman

Computational Speciation Models: A Tool for the Interpretation of Spectroelectrochemistry for Catalytic Layers under Operative Conditions

G. Montegrossi,[a] A. Giaccherini,[b,z] E. Berretti,[b] F. Di Benedetto,[a,z] M. Innocenti,[b,z] F. d'Acapito,[d] and A. Lavacchi[c]

[a]*IGG, CNR, Florence 50121, Italy*
[b]*Department of Chemistry, Università degli Studi di Firenze, Florence 50019, Italy*
[c]*Department of Earth Sciences, Università degli Studi di Firenze, Florence 50019, Italy*
[d]*IOM, CNR, c/o ESRF, Grenoble 38043, France*
[e]*ICCOM,CNR, Florence 50019, Italy*

In this study, the first coupled FEXRAV and chemical speciation modelling study of the Pd deactivation is presented. Due to the high brilliance of synchrotron light, FEXRAV can investigate deeply buried surfaces. More specifically, we directly analyzed the evolution of the Pd/C catalytic layer during a voltammetric cycle, through a specifically designed electrochemical cell. Still, we observed a complex interfacial chemistry of Pd, which impairs a straightforward interpretation of FEXRAV data. Exploiting thermodynamic chemical speciation modelling we were able to overcome this issue. The study leads to three main results: 1) the confirmation of the relationship between the charge of the Pd/Pd(II) ratio and the charge of the Fluorescence intensity 2) the investigation of the deactivation mechanism 3) the identification of the relevant species leading to the electrodissolution of Pd under operative conditions. This study opens new perspectives for the application of the chemical speciation modelling to the study of the deactivation mechanism of Pd in Pd/C catalytic layers under operative conditions in different electrolytes.

Manuscript submitted April 3, 2017; revised manuscript received July 21, 2017. Published August 11, 2017. *This paper is part of the JES Focus Issue on Mathematical Modeling of Electrochemical Systems at Multiple Scales in Honor of John Newman.*

In recent times, Palladium-based electrocatalysts proved to be able to promisingly substitute Pt in several electrocatalytic applications due to their lower cost and higher availability.[1] Moreover, Pd catalysts resulted very effective in direct alcohol fuel cell (DAFC). One of the benefits consists in the bypass of the deactivation process occurring in Pt catalysts due to reaction with CO.[2,3] Nowadays, the main issue still preventing full exploitation of such electrodic materials is their anodic deactivation, which is not fully understood and manageable. In fact, although the origin of the deactivation has been related to the formation of an oxide layer on the Pd surface, its formation mechanism is still an open question.[4] Moreover, other studies suggested that Pd electrodes are also subjected to electrodissolution under operative condition.[5] In principle, the latter process is competitive with the formation of the oxide layer and it is not observable by means of ex-situ techniques. In this context, a natural follow-up of the conventional ex-situ experiments are in situ/operando spectroelectrochemical measurements, performed to investigate the competition between these two processes under operative conditions. For operative conditions, we refer to the strongly anodic and basic conditions usually applied to the catalytic layer for the electrooxidation of alcohols. In the same context, the catalytic layer is usually intended as the place where the interaction between the electrolyte, the catalysts and the support occurs.[6] Several in-situ/operando techniques applied to catalysts are reported in literature, most of them are carried out on model systems with specific surface preparation or they require concentrated materials (i.e. on Pd electrodes).[7–10] As shown by Minguzzi et al., the Fixed Energy X-ray Absorption Voltammetry[11] enables the direct study of the oxidation state for chemical species under operando conditions. Recently, our group reported an operando study of Pd half-cell through FEXRAV.[12] Our results pointed out that FEXRAV alone is not able to clearly distinguish the different species of the same valence state (i.e. Pd(II)). Hence, even considering only the contribution due to the formation of the oxide layer (PdO) and the electrodissolution of Pd (Pd^{2+} solvated species) to the deactivation process of Pd/C electrocatalyst, the analysis of the experimental data could not identify which process is prevailing. On this basis, our aim is to present an integrated theoretical-experimental method to draw a conclusion on this subject.

[z]Electrochemical Society Member.
*E-mail: andrea.giaccherini@unifi.it; minnocenti@unifi.it

Methods

Details of the FEXRAV experiment.—Recording the time evolution of the sample response to X-rays at a fixed energy close to the absorption edge of an element, FEXRAV reckons the valence states of each element even in a complex matrix under an electrochemical stimulus (i.e. during a cyclic voltammetry).[11,13] Thanks to the high penetration of X-rays, it delivers information on X-ray absorption data through the walls of an electrochemical cells, with only minor design changes with respect to a standard electrochemical cell. Thus, it constitutes an ideal tool to investigate standard catalytic layers in operative conditions. In the setup hereby discussed, the lower detection limit is evaluated to be approximately 10^{13} atoms/cm^2. In order to perform our experiments we used a standard three electrode cell, specifically designed (3D model in Figure 1a) to be mounted in the experimental XAS chamber of the LISA beamline at ESRF.[14] The schematic of the experimental setup is presented in Figure 1b.

In the FEXRAV study of the Pd half cell, Pd/C nanostructured catalysts were involved. The Pd/C catalysts were synthesized according to the procedure reported in Refs. 15,16. The anode catalytic ink was prepared by mixing and sonicating the Pd/C catalyst (100 mg) with water (400 mg) and a 5 wt% nafion solution. The final charge of Pd on the electrode is approximately 4 mg/cm^2, a target loading selected to achieve the optimal sensitivity in the FEXRAV experiment. The electrochemical measurements have been performed by means of a PAR263 potentiostat installed at the BM08 beamline. The results obtained studying two different electrolytic solutions are presented in this paper: 1) KOH 2 M and 2) EtOH 2 M + KOH 2 M.

Concerning the beamline set up, the monochromator was equipped with Si(311) flat crystals, with an energy resolution $\Delta E/E \approx 10^{-5}$, a spot size of about 2*0.5 mm and a flux at the sample position up to

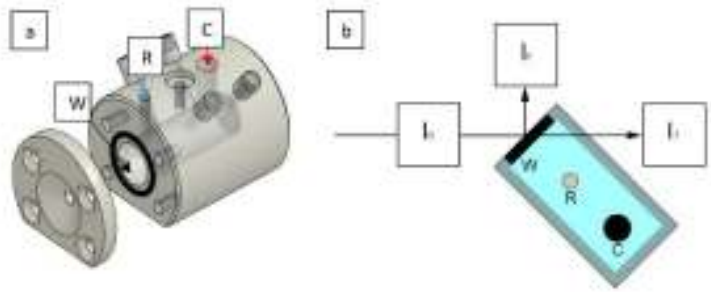

Figure 1. a) 3D model of the electrochemical cell used during the PEXRAV measurements with the position of the working electrode (W), reference electrode (R) and counter electrode (C); b) experimental setup for fluorescence (If) and transmission (It) measurements. I0 is the incoming monochromatic X-ray radiation.

10^{16} ph/s. All spectra were registered at room temperature, with reference to a metal foil, simultaneously analyzed in a second chamber located after the former. According to this procedure, the energy calibration was let available during the whole measurement. Reference materials were: elemental Pd under the form of a metal foil (Goodfellow) and PdO (Sigma Aldrich). This latter sample was prepared dispersing and homogenizing an appropriate amount of microcrystalline powders in cellulose, and pressing the mixture to a self-supporting half inch pellet.

Numerical modelling.—*Phreeqc formalism.*—We performed our calculation under the *phreeqc* formalism,[17] taking into account aqueous species equilibria in a reference database. The solid phases are considered through dissolution/precipitation reactions, and their stability is reported as the logarithm of equilibrium constant of formation (log K) at standard temperature and pressure condition (i.e. 25°C and 1.0132 bar) from the master species.[16,18] Only one master species is associated to each element or element valence state (for instance Fe^{3+} for ferric iron), one to the hydrogen ion, one to water and (formally) one to the aqueous electron. In this work, $Pd^{2+}{}_{(aq)}$ acts as master species while all the other species coming from the dissolution of metallic Pd in the half cell are secondary species ($Pd(OH)^{+}{}_{(aq)}$, $Pd(OH)_2$, $Pd^{+}{}_{(aq)}$, etc.). The master species are the "building blocks" used in the *phreeqc* formalism to write all chemical equations: they are related to the secondary species, in fact, by means of formation reactions involving the master species as a reactant (e.g. $Pd^{2+} + 2OH^{-} = Pd(OH)_2$, $Pd^{2+} + e^{-} = Pd^{+}$, etc.) and the relative equilibrium constant logarithms are included in the calculation (as a function of temperature). These species are present in a single phase, an aqueous solution. On this ground, the aim of the *phreeqc* formalism is the definition of a system of algebraic homogeneous equations describing the equilibrium conditions for different thermodynamics variables such as the activities of aqueous species (including water), ion-exchange species, surface-complexation species, gas-phase components, solid solutions, pure phases, aqueous charge balance, gas-phase equilibria and ionic strength. Such algebraic system is assembled taking into considerations all the residual function (denoted by *f*) describing the relevant equilibria. The residual functions are defined as the difference between a global constant and the combination of specific variables for each species or phases. Hence, for each set of values of the thermodynamics variables, defining a certain state of the system, the residual functions describe the "distance" of the state from the equilibrium. On this basis, the equilibrium condition corresponds to the set of values for the thermodynamics variables that let all the residual functions equal to zero. To compute the results, each residual function is reduced to contain a minimum number of variables (called the unknown masters), so that the number of functions equals the number of variables. The unknown masters for aqueous solutions are the natural log of the activities of master species ($\ln a_m$), the natural log of the activity of water ($\ln a_{H_2O}$), the ionic strength (μ), and the mass of solvent water in an aqueous solution (W_{aq}). The system is then computed and solved by means of the Newton-Raphson technique, which proceeds through the assembling of a Jacobian matrix containing the derivatives of the residual functions by the unknown master. Thus, this matrix describes the thermodynamics of the multi-equilibria system and its diagonalization leads to the equilibrium conditions. The analytic expression of each residual function and of the related derivatives has been developed and implemented in the *phreeqc* software. For instance, the equilibrium between the aqueous phase and pure solid phases is described under the following assumptions:

1) The activity of the pure phase is 1.0
2) The additional unknown master for each pure solid phase is the mole of the pure phase present in the system (n_p where p refers to the p^{th} phase)
3) The mass-action law holds

Under this assumptions the pure phase equilibria are described by the mass-action law:

$$K_p = \prod_{m}^{M_{aq}} a_m^{C_{m,p}}$$

Where K_p is the equilibrium constant with the p^{th} phase, $c_{m,p}$ is the stoichiometric coefficient of the aqueous master species (positive if the product of the desorption reaction and negative otherwise), a_m is the activity of the m^{th} species (it is an unknown master). Eventually, M_{aq} is the number of aqueous master species.

On this basis a new residual function can be defined:

$$f_p = \ln K_p - \sum_{m}^{M_{aq}} C_{m,p} \ln a_m$$

The total derivative of the residual function in terms of the unknown master is:

$$d f_p = \sum_{m}^{M_{aq}} c_{m,p}\, d \ln a_m$$

Chemical speciation in aqueous solutions is not uniquely defined but depends on the theoretical formulation of mass-action equilibria and activity coefficients (e.g. Davis, Pitzer or Debye-Hückel activity model);[17] in other words, the numerical solution of the system is model-dependent. Some aqueous speciations can be analytically determined, but operational definitions and assumptions are still unavoidable. Accordingly, the equilibrium is computed with a reaction-path calculation, i.e. a sequence of mass-transfer calculations that follows defined phase (or reaction) boundaries during incremental steps of reaction progress.

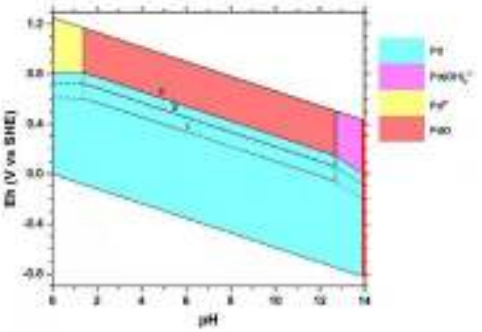

Figure 2. Pourbaix diagrams of the Pd-O-H system a) $[Pd] = 1 \cdot 10^{-3}$ mol/kgw b) $[Pd] = 1 \cdot 10^{-6}$ mol/kgw c) $[Pd] = 1 \cdot 10^{-10}$ mol/kgw.

In this study, the considered gas species, i.e. $H_{2(g)}$ and $O_{2(g)}$, are computed defining the corresponding partial pressures, and in the database are present the dissolution reactions (e.g. $O_{2(g)} = O_{2(aq)}$) and the corresponding constants. Accordingly, the presence of oxygen or hydrogen in any redox reaction is linked to their partial pressures. These latter are monitored as the result of an evolving chemical system in any given thermodynamic conditions.

The Pd-O-H system.—Numerical models for the chemical speciation require comprehensive thermodynamic databases. Although today's geochemical databases are quite complete, including the most common reactions and reaction constants, some equilibria typical of specific environments may be not present. Accordingly, the thermodynamic properties of some chemical species relevant to our model have been checked, and added, to the *phreeqc* wateq4f.dat database.[20] Specifically, Palladium hydroxylates have been added according to the work of Mountain and Wood.[21]

Modelling of the predominance charts and of the FEXRAV signals.—In the present study, the relationships between the main phases of the Pd-O-H system (Pd and water solution) are studied through the use of Eh versus pH (or "*Pourbaix*") diagrams, calculated according to the point-by-point mass balance method (referred also as the grid method).[22,23] Under this approach, a grid is defined by the span of the potential (Eh – with respect to the standard hydrogen electrode), pH and the chosen resolution (0.01 logarithmic units in both the Eh and pH axes, in the present case). Then, the chemical speciation for a given total amount of the element of interests is computed according to the *phreeqc* formalism[20] for each given point of the grid. The results are rendered directly by coloring each species differently and plotting each point of the grid with the color of the predominant species (as depicted in Figure 2). The predominant species (in the aqueous or solid phase) is identified as the species with the highest amount (moles) at the equilibrium.

The modelling of the FEXRAV signal relies on its dependence on the Pd chemical speciation in the Pd-O-H system. For a given amount of Pd, the chemical speciation is computed at each potential applied during the voltammetric scan. Thus, the Pd-bearing species exhibiting the higher amount of moles is considered prevalent, whereas species with an amount less than 10^5 times lower than the former are neglected in the presentation of the results.

Results

Pourbaix predominance charts.—The predominance charts were computed in a grid limited by the conventional water stability field from 0 to 14 pH units. The choice of the concentration of the master species were dictated by the possibility of an immediate comparison with selected Pourbaix diagrams available in the literature: Mountain and Wood,[21] Nuzzo[24] and Pourbaix et al.[25] It is noteworthy to mention that the former articles refer to calculations performed using the mass balance method, and including results calculated by using up to five different databases, whereas the latter presents results obtained using the "fine method" (i.e. depicting the boundary defined by Nernst equations). Figure 2 shows the Pourbaix diagram for the Pd-O-H system, where our point-by-point mass balance approach leads to very close agreement with all the cited works. Only a small difference can be evidenced between the Pourbaix et al.[25] study and the present one, and near the stability boundary of water, where our calculations predict the predominance of $Pd(OH)_4^{2-}$ (Palladium tetrahydroxilate), whereas Pourbaix et al. reports PdO_2^{2-}.[25]

As the total amount of Pd assumed in the calculation increases, the only changes in the plot deal with the Pd/Pd(II) boundary, because higher Pd contents stabilize the solid phases. This is due to fact that Pd solubility, dependent on speciation, is in any case limited. Under the operative conditions (pH = 14 and anodic potential), the relevant boundary is $Pd/Pd(OH)_2^{2-}$ while the fractional amount of PdO is generally two orders of magnitude lower with respect to both Pd and $Pd(OH)_4^{2-}$.

Fluorescence.—The simultaneous acquisition of the electrochemical and FEXRAV signals from the electrodic layer required a specific choice of the energy of the incident X-ray beam. Figure 3a depicts two X-ray Absorption Near Edge Spectroscopy (XANES) spectra of the reference materials, Pd and PdO. The difference between the XANES spectra of Pd and PdO is apparently maximized at 24370 eV. It is worth to notice that at this energy, the higher is the signal intensity, the lower is the fraction of Pd(0) contributing to the signal. On this ground, FEXRAV signals have been registered by means of the Fluorescence detector, while performing a cyclic voltammetry from –0.2 V to 1.2 V (RHE) with a scan rate of 1 mV/s, irradiating the electrochemical cell with a monochromatic persistent beam set up at 24370 eV. Apparently, at anodic potential we observe an increased signal intensity, and at the end of the cathodic scan the fluorescence signal is lower than at the beginning of the anodic scan (Figure 3b).

Speciation.—The chemical speciation modelling of this system under the voltammetric stress can be efficiently implemented defining analytical fractional amount readily usable. To this end, we calculated a 'slice' of the Pourbaix diagram in operative condition (red vertical line in Figure 2) corresponding to the range of potential applied to the electrode. Then a polynomial function has been fitted on the numerically calculated fractional amounts against Eh. Such function constitute the esteem of the fractional amount, as a function of Eh, used to follow the chemical speciation during the voltammetry. The speciation models revealed that Pd and $Pd(OH)_4^{2-}$ are the most relevant species. In fact, the third species by abundance (PdO) has a fractional amount not higher than $3 \cdot 10^{-3}$ while the other Pd-bearing species are always lower than 10^{-7}. Regarding the effect of ethanol on the equilibrium speciation the results for a KOH 2 M and EtOH 2 M solution are equivalent to the one for the solution KOH 2 M since the only effect of the EtOH at the equilibrium is to be oxidated to CO_2 and H_2O. However the reaction is so slow that it has no practical meaning in our context. Hence, for our purposes the Pd-O-H and Pd-C-O-H systems are equivalent.

Comparison between experiment and modelling.—Figure 4 shows the FEXRAV data for a KOH 2 M solution together with the corresponding calculated speciation distribution. The FEXRAV signal shows a periodic oscillation in response to the potential ramps. A further apparent feature of Figure 4, is that the oscillation between maxima and minima in the FEXRAV signal (whose shape, amplitude and phase are almost constant throughout the whole experiment) are combined with a general linear trend decreasing the signal intensity. This suggest that FEXRAV intensity is eventually not only determined by alternation of different redox states of solid Pd-bearing species.

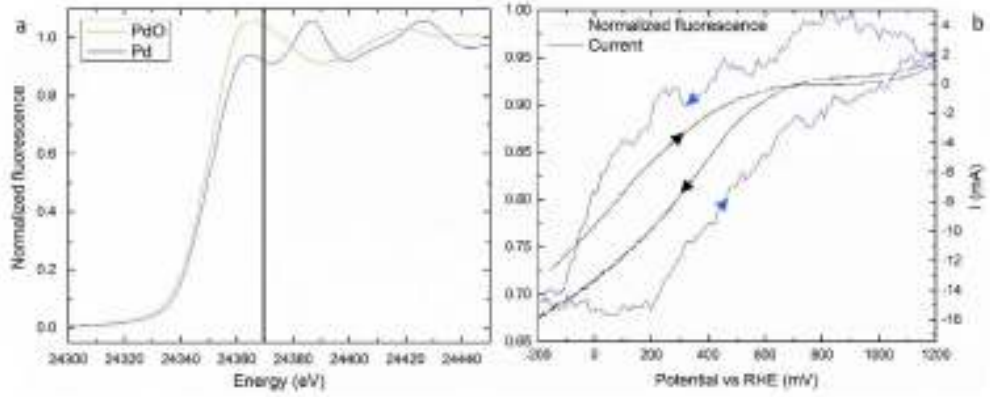

Figure 3. a) XANES spectrum for Pd and PdO standards b) The black curve is the current measured and the blue curve is the fluorescence signal from the electrode interface in a KOH 2 M solution.

The speciation model is in close agreement with the FEXRAV signal. Since the fractional amounts result from the equilibrium computation, their maxima and minima correspond, as expected, to the maxima and minima of the potential ramps. One can notice that the maxima of the FEXRAV occur after (approximately 0–200s) the maxima of the fractional amount of $Pd(OH)_4^{2-}$ in the catalytic layer. In the same way, the minima of the FEXRAV occur after (approximately 1000–1400s) the maxima of the fractional amount for Pd. This pattern is constantly reproduced for all the performed voltammetric cycles.

Figure 5 depicts the comparison between the results of a FEXRAV experiment (KOH 2 M and EtOH 2 M) solution with the speciation calculations for a KOH 2 M. Again, a good agreement between experimental data and the speciation model is achieved for all the voltammetric cycles. If compared to Figure 4, the main difference is the shape of the oscillations. For the solution of KOH and ethanol, the oscillation amplitude appears wider than with a solution of KOH only. Regarding the general trend of decreasing intensity observed in the FEXRAV of the half-cell filled with KOH, an almost linear decrease is observed also in the case of KOH and ethanol, but it is limited up to the 4th voltammetric cycle, whereas after the 5th cycle a pseudo-steady state is established. Interestingly, the ethanol in the electrolyte seems to make the maxima (or minima) of the FEXRAV signal occurring before the maxima (or minima) of the fractional amount for $Pd(OH)_4^{2-}$ along all the voltammetric cycles. This trend is clearly opposite to what observed in Figure 4.

Discussion

The Pourbaix diagrams of Figure 2, used to model the chemical speciation of the Pd-O-H, reveal an excellent agreement with the literature. No differences between the present and the latest published stability fields[29,34] are observed. The only small difference was found in the comparison with the Pourbaix et al. findings,[25] who couldn't take in account the chemistry of hydroxypalladates at the time. In their paper, these authors reported the diagrams with the hypothetical predominance of PdO_2^{2-} ions where we find the predominance of $Pd(OH)_4^{2-}$. As discussed by Pourbaix et al. themselves, the confirmation of their hypothesis was impaired by the lack of a thorough thermochemical characterization of hydroxypalladates. However, the predominance of $Pd(OH)_4^{2-}$ was firstly predicted by Mountain and Wood[31] exploiting the thermochemical characterization published by Chandrasekharam in 1974.[28] The latter was not accounted before 1988 when Mountain and Wood[31] applied the mass balance method to describe hydrothermal processes involving Pd species. An almost perfect agreement occurs between the present and Mountain and Wood's[31] charts. It is our opinion that the reproducibility of the literature's predominance charts by our approach enables its use as a tool to predict the evolution of chemical speciation in the Pd-O-H system during a voltammetric scan. Following the Mountain and Wood's calculation, the role played by the $Pd(OH)_4^{2-}$ species appears crucial for the interpretation of FEXRAV data.

Regarding the comparison between simulated and experimental FEXRAV data, the first part of this discussion is focused on the analysis of the chosen electrochemical and spectroscopic operating conditions. These conditions were, in fact, dictated by a mediation between the requirements of both voltammetry and XAS spectroscopy. At least two main choices are relevant:

1) The choice of monitoring FEXRAV through the Fluorescence detector is due to the sampling depth of the relative signal. At 24370 eV, the attenuation length of X-rays in the catalytic layer is estimated around 10 μm (i.e. smaller than the layer thickness).[4,37] Hence, the signal received by the Fluorescence detector is relative only to the catalytic layer.
2) The very low scan rate (1 mV/s) was aimed at improving the sampling time and to achieve the best possible signal-to-noise ratio (SNR) in the Fluorescence detector. As a side consequence, at this rate the system approaches the Nernstian equilibrium. Thus, the results of our thermochemical description based on the mass balance method (i.e. at the thermodynamic equilibrium) can provide an appropriate description of the chemical environment at the electrodic interface. This reflects the excellent agreement we found between the FEXRAV measurements and the calculated chemical speciation of Pd.

According to the recent literature, the spectral feature at 24370 eV, although being chosen in the present study from the comparison of Pd and PdO XANES spectra, is not specifically diagnostic for PdO, and can be safely used to assess only the generic oxidation of Pd to Pd(II).[28–31] In fact, the XANES signals are mostly sensitive to the oxidation state of an element, and less sensitive to its local coordination and structure.[32] Hence, from the spectroscopic point of view, PdO and $Pd(OH)_4^{2-}$ cannot be easily discriminated, whereas the redox change from Pd to Pd(II) can be easily monitored, even using a single fixed energy of 24370 eV (Fig. 3a).

The comparison between the trend of the current and FEXRAV as a function of the potential in the Figure 3b qualitatively suggests that Pd undergoes the same oxidation process reported in References 28–31

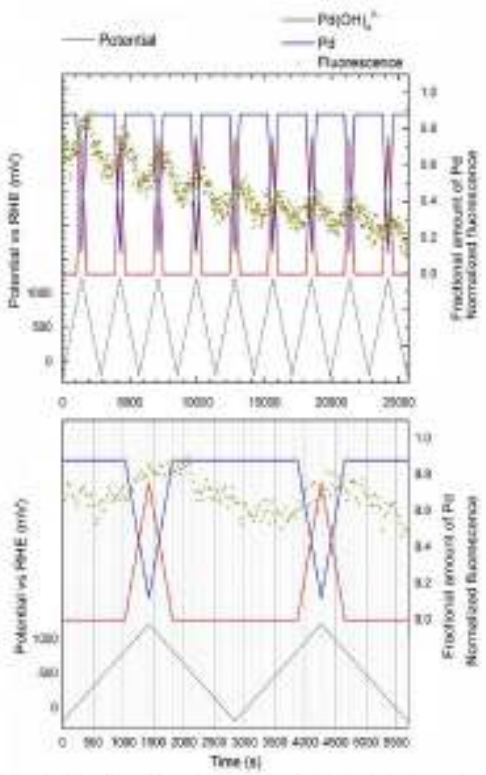

Figure 4. Experimental FEXRAV signal and calculated fractional amount of the relevant species, Pd and $Pd(OH)_4^{2-}$, during a potential scan rate of 1 mV/s. The electrochemical cell was mounted in the three electrode scheme, and filled with a KOH 2 M solution. FEXRAV signal was detected through the Fluorescence detector. (a) is the overview of the entire voltammetric scan (b) is a closeup of the first two cycles.

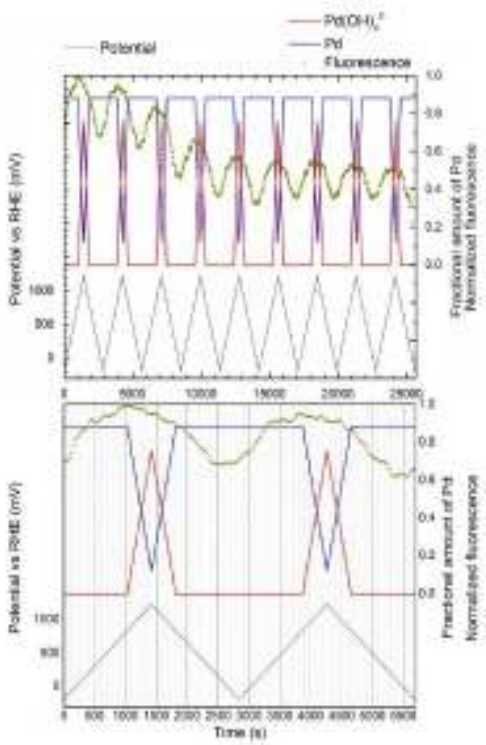

Figure 5. Experimental FEXRAV signal and calculated fractional amount of the relevant species, Pd and $Pd(OH)_4^{2-}$, during a potential scan rate of 1 mV/s. The electrochemical cell was mounted in the three electrode scheme, and filled with a KOH 2 M and EtOH 2 M solution. FEXRAV signal was detected through the Fluorescence detector. (a) is the overview of the entire voltammetric scan (b) is a closeup of the first two cycles.

However, these works are related to catalytic processes completely different with respect to the oxidation process, observed in the anodic half-cell of a DAFC. Hence, although we expect the oxidation of Pd to Pd(II), we cannot safely confirm that the increase of the FEXRAV intensity in Figure 3b is linked to this phenomenon without a speciation model. The calculated speciation as a function of time (Fig. 4) allowed to conclusively state that the relevant species are Pd and $Pd(OH)_4^{2-}$ and that the fractional amount of PdO is negligible. Indeed, the oscillatory increase of FEXRAV, when applied potential values approach 1000 mV vs RHE, is explained in terms of a temporary predominance of the oxidized $Pd(OH)_4^{2-}$ species over the reduced Pd species.

The explanation of the general decreasing trend, observed in the full experiment with KOH (Fig. 4) and only partially in the experiment with KOH and EtOH (Fig. 5) deserves a further discussion. Since the $Pd(OH)_4^{2-}$ is soluble, the total amount of Pd in the catalytic layer progressively decreases due to the diffusion process. To approximately quantify the effect of the diffusion, we should consider that roughly a quarter of the total time of the voltammetric scan ($t \approx 700$ s) is spent under diffusion limited condition. In addition, the diffusion coefficient for $Pd(OH)_4^{2-}$ is assumed to be $D \approx 6.14 \cdot 10^{-6}$ m^2/s.[32,34] On this basis, the thickness of the diffusion layer is 13 mm ($\delta = \sqrt{4Dt}$ [35]).

Thus, both the thickness of the catalytic layer (roughly 100 μm) and the sampling depth for Fluorescence (roughly 10 μm) signal are negligible if compared to the thickness of the diffusion layer. Therefore, the increasing of the diffusion layer thickness over time, depletes the total Pd content from the catalytic layer (hence also the sampling volume), resulting in a net and progressive decrease of the average FEXRAV signal revealed by the Fluorescence detector. These results are in line with the considerations provided by the review study of Grden.[3] Two main differences between the experimental data for the KOH 2 M solution (Figure 4) and the KOH 2 M + EtOH 2 M solution (Figure 5) where revealed:

1) the fluorescence peaks for the KOH 2 M occur after the correspondent peaks in the speciation model (after the inversion of the potential), whereas the peaks KOH 2 M + EtOH 2 M solution occur before the calculated peaks (before the inversion of the potential);
2) the decrease of the averaged fluorescence signal is linear for KOH 2 M solution while it stops after the 4th cycle for the KOH 2 M + EtOH 2 M solution.

These discrepancies are probably related to mechanistic and kinetics differences between the process occurring in the two electrolytes, and deserve further investigations, still in progress.

Conclusions

In this paper we present a modelling procedure of the chemical speciation (namely the mass balance method) which proved to be very useful in the interpretation of the results recorded by means of a new application of the FEXRAV technique.

Basically, we have shown that while experimental FEXRAV data registered through the Fluorescence detector can easily correlate with the potential applied to a Pd-bearing catalytic layer, an attribution of the changes in the chemistry responsible of the the changes in the FEXRAV signal cannot be appropriately reached. The proposed numerical modelling approach clearly points out a chemical speciation dependent on the applied potential where changes of the relative amounts of Pd and Pd(II) are responsible for the change of FEXRAV intensity during the voltammetric scan. Moreover, we were able to identify the main Pd(II) species involved in the process was identified as $Pd(OH)_4^{2-}$. On this ground, our study was able to confirm the prevalence, under the operative conditions, of the electrodissolution processes of Pd over the formation of the oxide layer.

It is opinion of the authors that this approach is of general interest in helping the analysis of data coming from spectroscopic techniques used to detect speciation features, in particular when working near equilibrium.

Acknowledgments

The authors warmly acknowledge Carlo Bartoli (ICCOM-CNR) for his technical assistance in the realization of the Electrochemical cell, as well as Dr. Alessandro Puri and Dr. Giovanni Orazio Lepore (IOM-CNR), for their contribution in the adaptation of the cell to the experimental set up of the BM08 LISA beamline. Their high skills and their motivation were fundamental to the success of the experimental part of this study. Dr. Claudio Zafferoni is also acknowledged for having supported the initial stages of this study. XAS data were performed at the BM08 "LISA" beamline (ESRF, Grenoble, France) during the MA-2153, 08-01-996, MA-2936 and MA-3173 experimental beamtimes. ESRF is gratefully acknowledged for provision of synchrotron radiation and for provision of the technical infrastructure. FDB and MI benefited for departmental funding (ex 60%). Gabbrielli Technology and Bluclad srl are acknowledged for contributing to fund this study, as well as is acknowledged the Italian CNR, for support.

References

1. European Commission, *Critical Raw Materials for the EU* (2010).
2. V. Barbagiovi et al., *ChemSusChem*, 5, 1266 (2012).
3. C. Bianchini and P. K. Shen, *Chem. Rev.*, 109(9), 4183 (2009).
4. L. Wang et al., *Electrochim. Acta*, 177, 193 (2015).
5. M. Grdeń, M. Łukaszewski, G. Jerkiewicz, and A. Czerwiński, *Electrochim. Acta*, 53, 7583 (2008).
6. A. Lasia, R. Miller, and F. Vitta, *Nanotechnology in Electroanalysis for Energy*, 115, (2013).
7. F. Zaera, *Chem. Soc. Rev.*, 43, 7624 (2014).
8. B. L. Mojet, S. D. Ebbesen, and L. Lefferts, *Chem. Soc. Rev.*, 39, 4643 (2010).
9. E. Campbell et al., *J. Phys. Chem. C*, 120, 14027 (2016).
10. L. Wang et al., *J. Power Sources*, 195, 3096 (2010).
11. A. Minguzzi et al., *Anal. Chem.*, 85, 7089 (2013).
12. D. G. Montagnini, D. A. Giaccherini, D. F. Di Benedetto, D. W. Gherlet, and D. A. Lanzarini, in *MSC*, (2016).
13. E. Achilli et al., *Journal of Spectroscopy*, 2014 (2014).
14. A. Balerna et al., *Nat Neurosci Lett Neuroscience*, 39, 34 (2014).
15. P. K. Shen and C. Xu, *Electrochem. commun.*, 8, 184 (2006).
16. C. Xu, P. kang Shen, and Y. Liu, *J. Power Sources*, 164, 527 (2007).
17. B. D. L. Purchase and C. a J. Appelo, *Etch. Organ. Reduct. Geoch. J.*, 11, 326 (1999).
18. H. C. Helgeson, J. M. Delany, H. W. Nesbitt, and D. K. Bird, *Am J Sci*, 278–A (1978).
19. J. W. Johnson, E. H. Oelkers, and H. C. Helgeson, *Computers & Geosciences*, 18(7), 899 (1992).
20. J. W. Ball and D. K. Nordstrom, *U.S. Geol. Surv. Water-Resources Investig. Rep.*, 91–183, 1 (1991).
21. B. Mountain and S. A. Wood, *Economic Geology*, 83(3), 492 (1988).
22. H. Huang, *Metals*, 6 (1), 23 (2005).
23. A. Giaccherini, G. Montagnani, and F. Di Benedetto, *Minerals*, 6, 78 (2016).
24. N. Takano, *Natl. Inst. Adv. Ind. Sci. Technol. Tokyo*, 285 (2009).
25. M. J. N. Pourbaix, J. Van Muylder, and N. de Zoubov, *Pacific. Mar. Rev.*, 3, 47 (1959).
26. M. Chandrasekharaiah, M. R. Udupa, and G. Aravamudan, *Perm. Bergamon Britain, Gt. Division. Exp.*, 36, 1317 (1974).
27. R. L. Hoxby, C. M. Gulbransen, and J. C. Davis, *At. Data Nucl. Data Tables*, 34, 181 (1985).
28. J. B. Brazier et al., *Catal. Struct. React.*, 3, 54 (2017).
29. D. Kirsch et al., *Phys. Chem. Chem. Phys.*, 11, 8620 (2009).
30. G. L. Chiarello and D. Ferri, *Phys. Chem. Chem. Phys.*, 17, 10579 (2015).
31. J. Nilsen et al., *ACS Catal.*, 5, 2481 (2015).
32. M. Nyman Jr., *Rev. Mineral. Geochemistry*, 78, 33 (2014).
33. W. P. Griffith, S. D. Robinson, and R. Snaith, *Gmelin Handbook of Inorganic Chemistry - Pd*, (1989).
34. R. Vracimirović and Y. L. Morgantsev, *Izv. VSR Mekst. Akad. Darbaz.*, 5, 89 (1966).
35. A. J. Bard et al., *Electrochemical Methods: Fundamentals and Applications*, (2000).